Laser-Driven Neutron Sources - A Compact Approach to Non-Destructive Material Analysis

Zimmer, Marc

(2020)

Laser-Driven Neutron Sources - A Compact Approach to Non-Destructive Material Analysis

Lasergetriebene Neutronenquellen - ein Kompakter Ansatz zur Zerstörungsfreien Materialanalyse

Zur Erlangung des Grades eines Doktors der Naturwissenschaften (Dr. rer. nat.)
genehmigte Dissertation von Marc Zimmer aus Heppenheim
Tag der Einreichung: 11. Februar 2020, Tag der Prüfung: 04. Mai 2020

1. Gutachten: Prof. Dr. Markus Roth
2. Gutachten: Priv. Doz. Dr. Vincent Bagnoud
Darmstadt - D 17

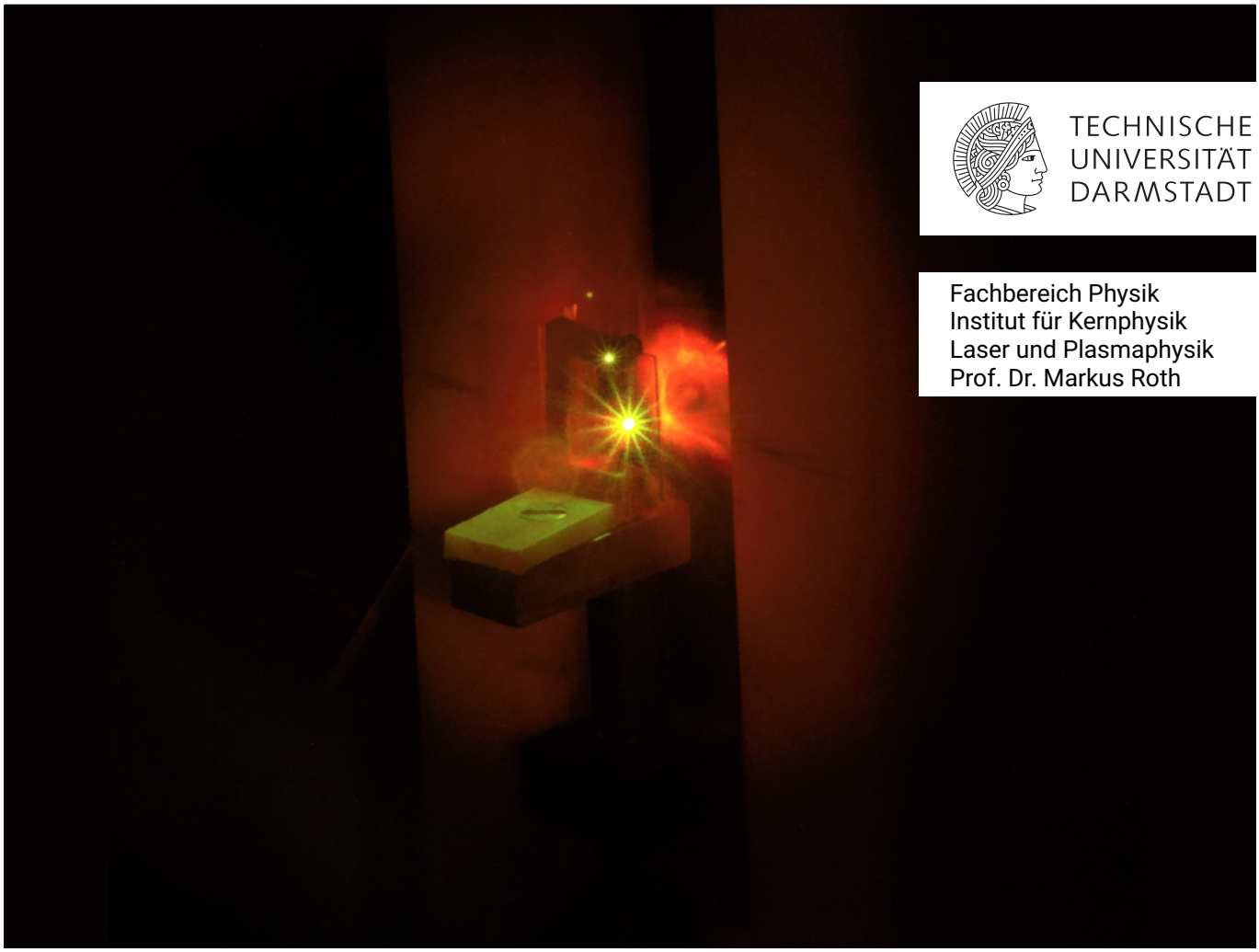

TECHNISCHE UNIVERSITÄT DARMSTADT

Fachbereich Physik
Institut für Kernphysik
Laser und Plasmaphysik
Prof. Dr. Markus Roth

Laser-Driven Neutron Sources - A Compact Approach to Non-Destructive Material Analysis
Lasergetriebene Neutronenquellen - ein Kompakter Ansatz zur Zerstörungsfreien Materialanalyse

Genehmigte Dissertation von Marc Zimmer aus Heppenheim

1. Gutachten: Prof.Dr. Markus Roth
2. Gutachten: Priv. Doz. Dr. Vincent Bagnoud

Tag der Einreichung: 11.02.2020
Tag der Prüfung: 04.05.2020

Darmstadt — D 17

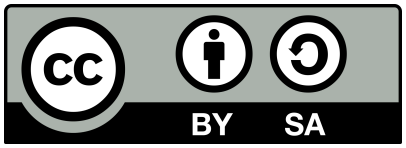

Erklärung zur Abschlussarbeit gemäß § 23 Abs. 7 APB der TU Darmstadt

Hiermit versichere ich, M. Zimmer, die vorliegende Dissertation ohne Hilfe Dritter und nur mit den angegebenen Quellen und Hilfsmitteln angefertigt zu haben. Alle Stellen, die Quellen entnommen wurden, sind als solche kenntlich gemacht worden. Diese Arbeit hat in gleicher oder ähnlicher Form noch keiner Prüfungsbehörde vorgelegen.

Mir ist bekannt, dass im Fall eines Plagiats (§ 38 Abs. 2 APB) ein Täuschungsversuch vorliegt, der dazu führt, dass die Arbeit mit 5,0 bewertet und damit ein Prüfungsversuch verbraucht wird. Abschlussarbeiten dürfen nur einmal wiederholt werden.

Bei der abgegebenen Thesis stimmen die schriftliche und die zur Archivierung eingereichte elektronische Fassung überein.

Bei einer Thesis des Fachbereichs Architektur entspricht die eingereichte elektronische Fassung dem vorgestellten Modell und den vorgelegten Plänen.

Datum / Date: Unterschrift / Signature:

_____ _____

Abstract

Neutrons have become a unique tool for non-destructive testing of materials but despite the increasing interest from science and industry, the number of accessible neutron sources has decreased in the last years due to the phasing out of nuclear research reactors. This creates a strong discrepancy between supply and demand for access to neutron facilities. Laser-Driven Neutron Sources (LDNS) have the potential to fill this gap but so far research on this topic is mostly focused on the neutron production and not on their utilization for material testing. This shortcoming is addressed by this thesis through the development of a setup designed to conduct Neutron Resonance Spectroscopy (NRS) on a laser-driven source. In this process, the question is answered how the involved components have to be optimized to enable this source type to be competitive with established neutron sources. This is accomplished via a meta-analysis on laser ion acceleration, a systematic review process of targetry solutions as well as Monte Carlo (MC) simulations for the neutron generation, moderation and transport. This is followed by an experimental verification of this technique through the identification of the isotopes ^{182}W and ^{183}W inside a tungsten sample. In addition, it was shown that the same setup was capable of determining the sample thickness of a 1 mm indium plate behind a 2 mm thick lead shield via a thermal neutron radiography. By using MC simulations for state of the art laser systems it was possible to predict the performance of LDNS to be comparable to existing sources while being orders of magnitude smaller in size. These results close the gap between LDNS as a theoretical concept and their application as a tool for material identification.

Zusammenfassung

Neutronen sind zu einem wichtigen Werkzeug der zerstörungsfreien Materialanalyse geworden, doch trotz des steigenden Interesses seitens der Wirtschaft und der Forschung, sinkt die Anzahl der Verfügbaren Neutronenquellen weiter ab. Die Ursache dafür, ist das allmähliche Abschalten alter Forschungsreaktoren, was zu einer starken diskrepanz zwischen Angebot und Nachfrage führt. Laser-Neutronenquellen haben das Potential diese Lücke zu füllen, jedoch hat sich der Großteil der bisherigen Forschung in diesem Bereich darauf konzentriert, die Neutronenerzeugung zu untersuchen und nicht darauf, die Neutronen für Materialuntersuchungen nutzbar zu machen. Dieser Mangel wird von der vorliegenden Thesis adressiert, indem ein Aufbau entwickelt wird, um an einer Laser-Neutronenquelle Neutronen-Resonanzspektroskopie durchzuführen. Innerhalb dieses Prozesses wird die Frage beantwortet, inwieweit vorhandene Komponenten optimiert werden können, damit ein derartiges System mit etablierten Neutronenquellen konkurrieren kann. Dies geschieht unter Anderem, durch das Erstellen einer Metaanalyse über den Einfluss des Lasers auf die Ionenerzeugung, eine systematische Übersichtsarbeit über existierende Targetsysteme, sowie Monte Carlo Simulationen zur Neutronenerzeugung und deren Transport. Mithilfe eines Experimentes wurde die Anwendbarkeit des entwickelten Aufbaus durch den simultanen Nachweis der Isotope ^{182}W und ^{183}W innerhalb einer Wolframprobe bestätigt. Darüber hinaus, konnte die Dicke einer 1 mm Indium Probe hinter einer 2 mm Bleiabschirmung bestimmt werden. Durch Monte Carlo Simulationen für moderne Lasersysteme konnte gezeigt werden das vergleichbare Neutronenflüsse wie bei etablierten Quellen erzielt werden können, jedoch mit einem um Größenordnungen kleineren Aufbau. Diese Ergebnisse schließen die Lücke zwischen der Betrachtung von Laser-Neutronenquellen als theoretisches Konzept und deren tatsächlichen Nutzung als Werkzeug zur Materialanalyse.

Contents

1 Introduction

The utilization of neutrons for non-destructive material testing has proven to be a powerful tool and their unique interaction properties make them a valuable research instrument. They become especially important when other non-invasive diagnostic techniques such as charged particle irradiation or X-rays reach their limitations, as it is the case in high-Z materials [IAEA-TECDOC, 2008]. This has made neutron-based analysis methods a meaningful asset to a wide range of fields ranging from medicine over material science and engineering to the security sector. Despite the gaining popularity of the neutron as a tool, more and more research reactors are phased out, partly driven by the fear of reactor related events in the past [Nature Editorial Comment, 2019]. This causes an increasing discrepancy between the demand and the supply of neutron beamtime in Europe and all over the world. Although flagship projects like the European Spallation Source (ESS) [Connaster, 2019] try to tackle this imbalance with localized high flux sources, they can only provide access to a limited number of users and the demand for small and medium-sized neutron sources still prevails.

LDNS have the potential to fill this demand. They operate through the acceleration of protons and deuterons via the interaction of high-intensity ($>10^{18}\,\mathrm{W/cm^2}$) laser irradiation with sub-μm thick targets. These ions are then directed on a "catcher" material which emits neutrons through nuclear processes. With this technique neutrons with initial energies between 100 keV and up to 100 MeV have been observed [Roth et al., 2013]. Even though LDNS are a relatively new concept, recent experiments have demonstrated short neutron pulses with up to 10^{10} n/sr and a pulse duration below 1 ns [Kleinschmidt et al., 2018]. With the recent developments of modern laser technology, these sources can be operated in the Hz to kHz regime in the near future posing a huge increase in average flux compared to the previous laser generation with repetition rates in the regime of one shot per hour [Eli Beamlines, 2019]. At these high repetition rates and with such pulses, LDNS have the potential of providing similar fluxes as established neutron production facilities. Their advantage is their drastically smaller size and costs. While a spallation source is hundreds of meters long and costs billions of Euros, an LDNS can fit into a larger room and costs on the order of 10s of million Euro. The development and construction of an LDNS could enable access to neutron beams to a much wider range of users and even on-site material testing facilities become feasible for companies.

With laser neutron generation still being in its early stages, most research conducted in this field has focused on the characterization of the emitted neutron beam. The potential of these sources for applications has so for not been exploited. Especially material analysis techniques that rely on short neutron pulse lengths like NRS can have large benefits from the sub-ns pulses of an LDNS. Even though some attempts have been made into this direction no systematic approach has been undertaken to develop an optimized setup for utilizing LDNS as an epi-thermal source for material analysis based on NRS.

This is the declared goal of this presented scientific thesis and to demonstrate its applicability in an experiment at a high-intensity laser. Such a demonstration will move LDNS from a conceptual idea of an alternative way of neutron production to a proven technique of non-destructive material identification. The following introduction into the structure of the thesis will outline the approach that was taken to get to this design.

1.1 Thesis Structure

After this first introduction, the second chapter is laying the theoretical foundations necessary to comprehend the underlying physical principles. This includes the laser-matter interaction required for the particle acceleration, an explanation of the nuclear processes responsible for the creation of neutrons as well as the slowing down process of neutrons and their detection.

With the basic principles introduced, chapter three can focus on a comparison of existing neutron sources. The strengths of an LDNS are pointed out and matching applications are introduced. It is pointed out why NRS is especially promising for an LDNS and how such a measurement would be done.

Section four then goes into detail of such a setup and introduces the obstacles that have to be taken and shows how to overcome them to detect neutron resonances with sufficient accuracy and resolution. This is done by going step by step through all involved components, discussing their influences and limitations to find an optimal solution, either by the use of simulations or by the utilization of experimental data from other groups to create empirical models for a given problem.

Section five uses this optimized setup to conduct an NRS experiment on a tungsten sample to demonstrate its applicability. To achieve this goal, the setup is first characterized by a description of the neutron flux conditions, the source spectrum as well as a determination of the signal to noise ratio. To examine if the setup is limited to NRS or can also be applied to Neutron Resonance Imaging (NRI) two gated thermal neutron radiographies are made to determine a minimal required neutron flux.

To evaluate the potential of this kind of neutron source, section 6 uses simulations derived from the experimental data of other experiments to predict the neutron output of laser-driven neutron sources when they are used with existing modern laser technology. As an example for the different applications three most promising concepts are chosen. This includes a small mobile combined neutron and X-ray source, a LDNS for high average neutron flux with intermediate energies and repetition rates as well as a high peak flux neutron source with high laser energies and low repetition rates.

2 Theory

This section will introduce the fundamental theoretical concepts necessary to understand laser-driven neutron generation as well as the required neutron interactions with matter and their mechanisms of detection.

2.1 Plasma

Besides the three states solid, liquid and gaseous, there is a fourth state, called plasma. While its occurrence is rare on the surface of the earth, more than 99% of the visible matter in the universe is in this condition [Alfven, 1986]. This fourth state consists of partly or fully ionized matter with an equal number of positive and negative charges making it quasi-neutral on macroscopic scales. This ionization allows the material to display a collective behavior as the electromagnetic forces allow the interaction of charged particles inside the plasma over larger distances [Elizer, 2002]. There are certain key properties of plasma which are vital for the understanding of laser ion acceleration, therefore a short introduction into plasma physics will be given.

2.1.1 Plasma Frequency

If an external force is applied to a plasma in its equilibrium state, the local neutrality can be disturbed on the microscopic scale resulting in a perturbation of the electron density. These changes in the electron distribution will create an electric field that acts as a restoring force on disturbed electrons. The force of the field is proportional to the displacement which creates a harmonic oscillator. From the Maxwell equations the solution for this conditions for a plasma with $T = 0\,K$ will give the oscillation frequency [Elizer, 2002]:

$$\omega_p = \sqrt{\frac{e^2 n_e}{\epsilon_0 m_e}} \tag{2.1}$$

with the elementary charge e, the electron density n_e the electric field constant ϵ_0 and the electron mass m_e. This ω_p is called the plasma frequency which is an integral parameter for the adequate description of a plasma as it describes the movement of the electrons.

2.1.2 Debye Length

For free charge carriers the electric potential is inversely proportional to the distance r between neighboring particles which enables interactions across large distances. In a plasma this long-distance interaction

is screened by the superposition of the potentials of neighboring ions and electrons. This modifies the Coulomb potential to the Debye potential [Elizer, 2002]:

$$\phi(r) = \frac{Ze}{4\pi\epsilon_0}\frac{1}{r}\exp(-\frac{r}{\lambda_D}) \tag{2.2}$$

where λ_D is called the Debye length or Debye radius:

$$\lambda_D = \sqrt{\frac{\epsilon_0 k_B T_e}{e^2 n_e}} \tag{2.3}$$

Where T_e is the electron temperature, the charge state Z, k_B the Boltzmann constant, e the elementary charge, the electric field constant ϵ_0 and the electron density n_e. The term Debye-radius originates from the fact that it defines the radius of a sphere around an inserted test charge at which the potential has decreased to 1/e through this screening effect [Elizer, 2002]. This concept requires to have a sufficient number of particles inside the Debye-sphere to make the screening possible [Gallagher and Bloomfield, 2013].

2.1.3 Critical Density

So far for the calculation of the plasma frequency, the temperature was assumed to be T = 0 K. If the temperature is included in the consideration then a displacement will cause electron plasma waves with co-moving electric fields [Elizer, 2002]. The dispersion relation of these waves is given by:

$$\omega = \omega_p^2 + \frac{3}{2}k^2 v_e^2 \tag{2.4}$$

in which case ω is the frequency of the electron plasma wave and k is the wave number. v_e is the mean electron velocity in the plasma. If the perturbation is caused by electromagnetic waves entering the plasma a similar dispersion relation can be derived by solving the Maxwell equations for this case [Elizer, 2002]:

$$\nabla^2\vec{E} - \frac{\epsilon}{c^2}\frac{\partial^2}{\partial t^2}\vec{E} = 0 \tag{2.5}$$

In this case ϵ = 1 - ω_p^2/ω_L^2 with the laser frequency ω_L, resulting in the dispersion relation:

$$\omega_L^2 = \omega_p^2 + k^2c^2 \tag{2.6}$$

It becomes evident that for the case $\omega_p > \omega_L$, k becomes imaginary and reduces the propagation inside the plasma to an evanescent wave. This defines a critical density for which $\omega_p = \omega_L$ is fulfilled. If an electro-magnetic (EM) wave reaches a region inside a plasma with this density, then it cannot propagate further. For laser radiation with a given wavelength λ_L this critical density can be calculated via:

$$n_c = \frac{\epsilon_0 m_e \omega_L^2}{e^2} \approx 1.1 \cdot 10^{21}\left(\frac{\mu\text{m}}{\lambda_L}\right)^2 cm^{-3} \tag{2.7}$$

Plasmas with $n_e < n_c$ are called underdense and allow laser propagation inside the plasma. For $n_e > n_c$ the plasma is overdense and becomes opaque for laser radiation. As a reference point, the critical density for a system like the PHELIX laser [Bagnoud et al., 2010] is at $1{\cdot}10^{21}$ cm^{-3} and therefore below solid-state density of regular targets which is on the order of $3{\cdot}10^{23}$ cm^{-3} [Sanyal et al., 1996]. This implies that those targets become opaque once they enter the plasma state.

2.2 Laser Plasma Interaction

It is vital to discuss the different interaction mechanisms between laser and target, to explain how the laser is capable of transferring its energy to the ions in the target. The direct acceleration of ions in a laser field requires intensities in the range of $10^{24}\,\mathrm{W/cm^2}$ [Yandow et al., 2019] which is still out of reach for modern laser systems with current record intensities of $5.5{\cdot}10^{22}\,\mathrm{W/cm^2}$ [Yoon et al., 2019]. Therefore the laser energy is first transferred to hot electrons which then are capable to accelerate ions via the generation of quasi-static electric fields. Before this is possible, the target first has to be ionized to be in a plasma state.

2.2.1 Target Ionization

As discovered by Einstein [Einstein, 1905] light exists only in packages of discrete amounts of energy. This energy is given through the relation $E = hc/\lambda$ with the plank constant h and the photon wavelength λ. For a laser in the visible or infrared region, this energy is around 1 to 3 eV. Most materials have a photo-effect ionization threshold of 5 to 20 eV [Tipler and Mosca, 2004] making single photon ionization impossible for a large fraction of materials.

If the intensity of the light is increased, the chance of two or more photons being absorbed at the same time is rising and can lead to an effect called multi-photon ionization. This can start at intensities of $10^{10}\,\mathrm{W/cm^2}$ and ranges to $10^{12}\,\mathrm{W/cm^2}$, benefiting from an increase in the absorption cross section with further increasing photon numbers [Gibbon, 2004] [Elizer, 2002]. For modern short pulse lasers, these intensities can already be reached by Amplified Spontaneous Emission (ASE) creating a pedestal of several ps or ns before the main pulse arrives. Also, pre-pulses caused by amplified reflections inside the laser system preceding the main pulse can reach these values. Both effects can ionize the target and are capable of launching shock waves through the material causing damage to the structural integrity of the target [Kaluza et al., 2004].

At higher intensities, the electric field, generated by the laser is strong enough to cause field ionization in the target. Thereby the superposition of the bounding electric potential of the atom and the potential created through the laser is causing a potential suppression. This lowers the potential barrier for electrons in the field of a nucleus. The electrons can either leave the atom through the tunnel effect or if the barrier is suppressed below the ground state, the atom is directly ionized. The first effect is called tunnel ionization and start around $10^{13}\,\mathrm{W/cm^2}$ while the latter is observed at intensities surpassing $10^{13}\,\mathrm{W/cm^2}$ and is called barrier suppression ionization [Elizer, 2002].

If a free electron is already present in the target, either created by background radiation or early pre-pulses, it can also be accelerated directly in the laser field at intensities of $10^{9}\,\mathrm{W/cm^2}$. The accelerated electron is then capable of ionizing surrounding atoms creating a chain reaction.

2.2.2 Regime of Relativistic Electron Motion

As a first step to understanding the energy transfer of an electromagnetic wave to a plasma, only a single electron inside an EM field is considered. The force acting on this particle is the Lorentz force [Gerthsen, 2013]:

$$F_L = m_e \frac{d\vec{v}_e}{dt} = -e(\vec{E} + \vec{v}_e \times \vec{B}) = -e\left[\vec{E} + \vec{v}_e \times \left(\frac{1}{c}\vec{e_B} \times \vec{E}\right)\right] \tag{2.8}$$

with the electric field $\vec{E}$, the magnetic field $\vec{B}$, the elementary charge e and $\vec{e_B}$ is the unity vector in $\vec{B}$ direction. For low and intermediate intensities, the main contribution comes from the electric field and the solution to the equation of motion is a harmonic oscillation with an electron quiver velocity [Gibbon, 2004] of:

$$v_{os} = \frac{eE_0}{m_e \omega_L}. \tag{2.9}$$

If the intensity is further increased the electric field rises as well and causes v_{os} to approach relativistic velocities. At this point, the influence of the magnetic field can not longer be neglected. This is the case for electric field amplitudes $E_0 > 3.2{\cdot}10^{12}$ V/m or intensities above $1.37{\cdot}10^{18}$ W/cm^2 [Borghesi et al., 2006]. To classify the form of laser-matter interaction the dimensionless electric field amplitude is used:

$$a_0 = \frac{eE_0}{m_e \omega_L c} = \sqrt{\frac{I_0[\mathrm{W/cm^2}] \cdot \lambda_L^2[\mu\mathrm{m}]}{1.37 \cdot 10^{18}\,\mathrm{W/cm^2}}}. \tag{2.10}$$

Interactions become relativistic when a_0 is larger than one. In this regime of relativistic electron motion, resonance absorption and inverse bremsstrahlung are contributing to the electron heating as well. At higher intensities vacuum heating occurs when the laser drives an electrostatic wave at the critical density. In addition, $\vec{j} \times \vec{B}$ heating contributes significantly [Elizer, 2002]. The laser electron heating process is a complex and wide topic and has been intensely discussed by [Mulser and Bauer, 2010]. Therefore only the ponderomotive force will be discussed here as it has the highest relevance for this work as it directly affects the electron temperature [Schollmeier, 2009].

2.2.3 The Ponderomotive Force

For a homogeneous plane EM-wave the electron oscillates in the electric field but remains on average in the same position and no net energy is transferred. In an experiment, the laser is focused down to several μm to reach maximum intensities. This leads to strong field gradients across the Gaussian shape of the laser spot with the highest intensity in the center. From equation 2.8 for $v_e \ll$ c it can be derived that an electron close to the center will experience the acceleration:

$$\frac{\partial v_y}{\partial t} = -\frac{e}{m_e} E_y(\vec{r}). \tag{2.11}$$

Electrons in the center will consequently experience the highest acceleration. An electron that moves during the first half of a laser cycle to a region that is further away from the beam center will encounter a lower field at this position. This leads to a lower acceleration in the second half of the laser cycle. The

resulting force averaged over one laser cycle is called the ponderomotive force and can be derived from a Taylor expansion of the electric field over an averaged cycle [Bauer et al., 1995]:

$$F_P = -\frac{e^2}{4m_e\omega_L^2}\frac{\partial E_0^2}{\partial y}. \tag{2.12}$$

This force accelerates electrons out of areas with high laser intensity towards regions with lower intensity. For relativistic velocities, the magnetic field again cannot be neglected anymore and the full ponderomotive force has to be rewritten as [Bauer et al., 1995]:

$$\vec{F_P} = -\frac{c^2}{\gamma}\left(\vec{\nabla}m_{\text{eff}} + \frac{\gamma-1}{v_0^2}\left(\vec{v_0}\cdot\vec{\nabla}m_{\text{eff}}\right)\vec{v_0}\right) \tag{2.13}$$

with the space-time dependent mass m_{eff} and the relativistic gamma factor $\gamma = (1 - v^2/c^2)^{-1/2}$. The solution to this equation of motion is rather complex and discussed in [Bauer et al., 1995] and [Schollmeier, 2009] therefore the result is directly presented. Through the relativistic ponderomotive force, an additional component of acceleration into the forward direction is applied and the resulting acceleration will be at an angle:

$$\theta = \arccos\left(\sqrt{(\gamma-1)/(\gamma+1)}\right). \tag{2.14}$$

All mechanisms discussed above transfer energy from the laser to the electrons resulting in a distribution of hot electrons at the rear surface. For the ion acceleration the most important attributes of these electrons are the electron temperature [Schollmeier, 2009]:

$$T_{hot} = \frac{m_e c^2}{k_B}\left(\sqrt{1+a_0^2}-1\right) \tag{2.15}$$

and the hot electron surface density:

$$n_{e,0} = \frac{\eta E_L}{c\tau_L\pi(r_0 + d\tan\theta/2)^2 k_B T_{\text{hot}}} \tag{2.16}$$

with the laser pulse width τ_L, the focal spot radius r_0, target thickness d, the angle θ from equation 2.14, and the fraction of transferred energy [Schollmeier, 2009] [Wilks et al., 1992]:

$$\eta = 1.2\cdot 10^{-15} I^{0.74}. \tag{2.17}$$

this can be rewritten as:

$$n_{e,0} = 1.5\cdot 10^{19}\frac{r_0^2}{(r_0 + d\tan\theta/2)^2}\frac{I_{18}^{7/4}}{\sqrt{1+0.73\cdot I_{18}\lambda_{\mu\text{m}}^2}-1}[\text{cm}^{-3}]. \tag{2.18}$$

With a higher hot electron density, more ions can be accelerated and with an increased electron temperature the maximum ion energy rises as well. The mechanisms behind the acceleration will be discussed in the following section.

2.3 Laser Ion Acceleration

The acceleration of ions via the usage of a laser is, in comparison to classical accelerators, a rather novel concept and was only recently discovered in 1999 [Snavely et al., 2000]. This section will discuss the most promising laser acceleration mechanisms that are currently accessible and will debate the main advantages and disadvantages for neutron generation.

2.3.1 Target Normal Sheath Acceleration

The target normal sheath acceleration (TNSA) process was first described by [Wilks et al., 2001]. If a laser with $a_0 > 1$ is focused on a solid target with a thickness in the range of 1 to 100 μm, then the target surface is ionized by the rising edge of the laser pulse and a pre-plasma is created. In this plasma the laser can transfer energy to the electrons via the mechanisms discussed above, heating them into the MeV-regime [Mulser and Bauer, 2010]. The process is displayed in figure 2.1 for a better understanding. The hot electrons travel through the target until they reach the rear surface. There they either leave the target or move back to the front surface via a return current. There they can interact once more with the laser field and be accelerated, further increasing the temperature. This return current is necessary since the hot electron current would otherwise by far exceed the Alfvèn limit [Roth and Schollmeier, 2017] but the recirculating electrons compensate the magnetic field in that region. After several electron acceleration cycles, a dense electron sheath is building up at the rare side of the target forming an electric field on the order of TV/m or MV/μm [Elizer, 2002]. This large potential gradient field ionizes the atoms at the surface. Once ionized they are accelerated in the electric field.

Typically for solid TNSA targets, the rear-surface is covered by a contamination layer of water and hydrocarbons that are deposited through its exposure to air. These materials are rich in hydrogen and since protons have the highest charge to mass ratio, they are accelerated most efficiently. The protons from the contamination layer modify the electric field with their Debye-potential and create a shielding effect for other ions further inside the target. This causes an exponentially decaying spectrum towards higher energies as well as a less efficient acceleration of ions from the bulk material. For neutron generation, often deuterated targets are used as deuterons have a higher neutron yield than protons [Rücker et al., 2016]. Since deuterons are only present in deeper layers of the target, they are therefore accelerated less efficient in this process. The large advantage of TNSA is, that it is well explored and delivers reproducible results [Roth and Schollmeier, 2017]. This mechanism is suitable for laser neutron generation but it is not the most efficient acceleration process in terms of ion energies and conversion efficiency. With an increase in intensity, contrast and a reduction of the target thickness, it is possible to access an acceleration regime that is more efficient for neutron production.

2.3.2 Ion Acceleration from Relativistic Induced Transparency

As mentioned in the previous section, the laser can only propagate in a plasma until the critical density $n_c = \frac{\epsilon_0 m_e \omega_L^2}{e^2}$ is reached. For sufficiently high intensities, the movement of the electrons in the laser field approaches the speed of light, resulting in a relativistic increase of the mass $m_{\text{rel}} = \gamma m_e$ with

$\gamma = 1/\sqrt{1-(v/c)^2}$. This higher mass decreases the plasma frequency and therefore the critical density. Once the modified plasma frequency drops below the laser frequency the plasma becomes transparent again even though the density would be classically overdense. This enables the laser light to propagate further into the target until the new critical density is reached. This effect leads to the name Relativistic Induced Transparency Acceleration (RITA) [Sahai et al., 2014] [Fuchs et al., 1998][Hoffmeister, 2014]. As the position of the critical density moves from the front surface further into the target, ions are accelerated in the process. If the expansion through the pre-pulse heating leads to a reduction in the electron density at the laser facing surface, the penetration depth is further increased. For a target that is chosen thin enough (sub-μm), so that those two effects enable a laser propagation through the entire target until the rear surface, the laser ion energy coupling is increased and ions are accelerated to higher maximum energies and a larger fraction of bulk material is accelerated than via TNSA [Wagner, 2014]. Details of this acceleration mechanism are still under investigation and the increase in ion energy and bulk material has been linked to the formation of a Buneman instability that drives resonant waves in a process called break out afterburner (BOA) [Yin et al., 2006]. Other sources explain this through the increase in relativistic self-focusing [Hoffmeister, 2014] or a more effective laser coupling.

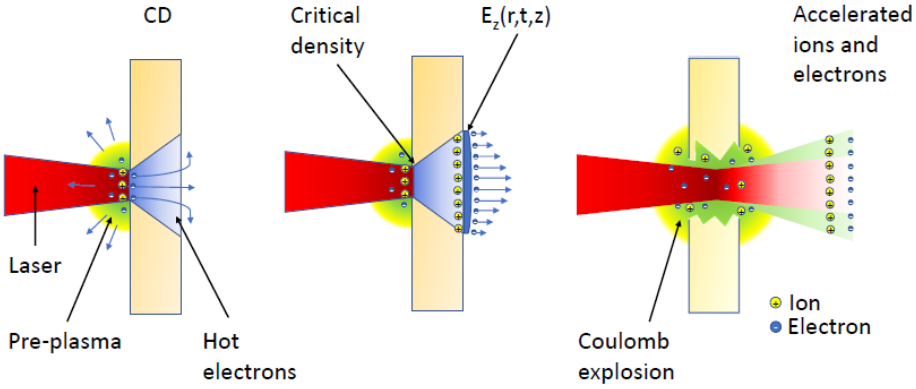

Figure 2.1: The process of laser-driven ion acceleration. A laser pulse impinges on a target and creates a plasma. Energy is transferred to the electrons which create a sheath at the rear surface. This charge separation creates a strong electric field that is capable of accelerating ions from the surface. If the target is thin enough the laser can propagate through the target via RITA and enhance the acceleration.

The major advantage of this acceleration process is the resulting higher ion energy as well as the increased fraction of accelerated deuterons, both resulting in higher neutron numbers. Section 4.3.2 will discuss this in further detail. The disadvantage of RITA is, that the thin targets are very susceptible to damage by pre-pulses. If the target is too thin or the laser contrast to low, then the plasma does not couple efficiently with the laser and the acceleration is decreased [Kaluza et al., 2004]. If the target is too thick or the laser not intense enough then the acceleration enters the TNSA regime. Therefore there is an optimal target thickness for every laser system that has to be identified experimentally [Hegelich et al., 2013].

2.4 Nuclear Physics of the Neutron

In this section, the most important nuclear reactions will be discussed that lead to the emission of neutrons, as well as the reaction of neutrons with other materials and thereof resulting consequences.

2.4.1 Neutron Production via Direct Nuclear Reactions: Break-Up and Stripping

For the production of neutrons, it is useful to classify the reactions according to the delay between interaction and neutron emission. Direct nuclear reactions appear on a timescale that is similar to the time an ion needs to pass by the nucleus and are typically on the order of 10^{-22} s. Inelastic scattering of incoming particles is a good example for these reactions, where the projectile can knock out nucleons or break the target nucleus into fragments. These reactions appear without the formation of a compound nucleus and do have a strong forward orientation of their neutron emission. For deuteron projectiles, there are two direct reactions that play a significant role in the neutron generation and are discussed in detail.

Deuteron break-up is one of the most commonly referred reaction [Roth and Schollmeier, 2017] [Guler et al., 2016] [Kleinschmidt, 2017] in the topic of neutron generation below 100 MeV. Despite its frequent use, the name often refers to different nuclear processes which can lead to confusion. Therefore here, the term deuteron break-up will refer to the dissociation of a deuteron in the presence of the electric field of a target nucleus. As a classical analog, it can be viewed as rapid deceleration of the deuteron in the field of the nucleus. The decelerating force is only affecting the proton while the inertia of the neutron forces it to maintain its momentum. If the asserted force becomes larger than the binding force between proton and neutron both are split and the neutron continues its trajectory with the momentum it had during the separation.

This effect has been theoretically studied by [Gold and Wong, 1963] via perturbation theory in the dipole approximation. They concluded that the cross section for the deuteron break-up can be calculated via:

$$\sigma = \int_0^\infty \frac{16\hbar^2}{3m} n_1^2 \frac{\epsilon_0^{1/2}\epsilon^{3/2}}{(\epsilon+\epsilon_0)^4} ln\left(\frac{2n_1}{n_2-n_1}\right) d\epsilon \tag{2.19}$$

with

$$n_1 = \frac{Ze^2}{\hbar|v_1|} \quad \text{and} \quad n_2 = \frac{Ze^2}{\hbar|v_2|}. \tag{2.20}$$

Z is the target nucleus atomic number, $\hbar$ is the reduced Planck's constant, m the nucleon mass, v_1 and v_2 are the initial and final velocity of the internal center of mass of the deuteron in comparison to the center of the potential. ϵ is the internal disintegration energy and $\epsilon_0 \approx 2.225$ MeV the binding energy of the deuteron. In this equation it becomes evident that the break-up cross section increases quadratically to Z of the target nucleus. Using this equation to calculate the cross section of beryllium in the low MeV range delivers values around 10 mb. Even though the elastic coulomb break-up is often referred to as a main source of neutrons as mentioned earlier, 10 mb are rather an insignificant contribution to the neutron yield of deuteron beams on low Z targets. This break-up effect only contributes for catcher materials with a high Z number like copper where it leads to high cross sections of around 500 mb for deuteron energies above 25 MeV.

For materials with low Z like beryllium and lithium, the coulomb potential is rather weak in comparison to the ion energies. This, on the one hand, explains the low break-up cross section and on the other hand, enables interactions via the strong nuclear force as the deuteron can approach closer to the nucleus. This increases the likelihood of the deuteron stripping processes. Thereby the deuteron is getting close to the target nucleus and their wave functions start to overlap. In that configuration, either the proton or the neutron can form a compound nucleus with the target while the other half of the deuteron does maintain

its momentum. This stripping cross section for beryllium can have up to 350 mb for deuteron energies between 3-4 MeV [Koning et al., 2009] and is consequently important for neutron generation with low cut off energies

2.4.2 Compound Nuclear Reactions

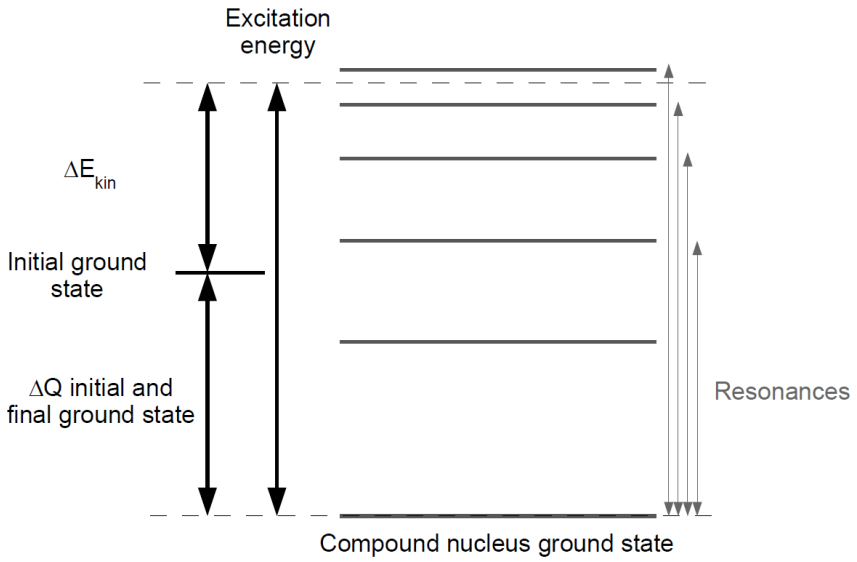

Figure 2.2: Excitation states after the formation of a compound nucleus. The energy state of the compound is the sum of the kinetic energy and the increase in energy from the lower ground state. If the sum of E_{kin} and ΔQ is equal to a new excited state of the compound, then a resonance is formed.

In contrast to the direct nuclear reactions mentioned above that are defined by the neutron production via a single nuclear reaction, the compound nuclear reactions consist of many interactions between nuclei. The idea of the formation of a compound nucleus goes back to Niels Bohr in 1936 [Ghoshal, 1950] and assumes that a projectile and a target nucleus become indistinguishable from another and the new compound nucleus is only characterized by its number of nucleons and its energy state. These states usually exist for a comparably long time on a nuclear scale on the order of 10^{-16} s to 10^{-18} s where the nucleus has already reached thermal equilibrium. This leads to a loss of all information of the entrance channel, therefore there is no preferred neutron emission direction. The decay of a compound nucleus only depends on its excitation energy and the probability of the decay channels. The neutrons spectrum which is emitted from these reactions via evaporation can be described by [Bertsch et al., 1996]:

$$\Phi(E)dE = \sqrt{\frac{E}{\pi(k_B\mathrm{T})^3}} \cdot \exp\left(-\frac{E}{k_B\mathrm{T}}\right)dE \tag{2.21}$$

where T is the nucleus temperature and k_B the Boltzmann constant. This evaporation process releases energy from the nucleus and can happen until the nucleus reaches a stable state.

If a neutron is emitted, before the nucleus has reached its thermal equilibrium, the process is called pre-equilibrium reaction [Griffin, 1966]. This can happen when the projectile energy is large in comparison

to the binding forces. In this case, the information of the entry channel is partly maintained and the neutrons emitted will have an increased forward orientation.

The laws of quantum mechanics do predict for a compound nucleus discrete quantum states. A schematic view of these states can be seen in figure 2.2. If the energy of the previous ground state plus the added kinetic energy from the ion are equal to a distinct excitation state of the formed compound nucleus, then the cross section for this reaction is drastically increased and so-called resonances are formed.
These resonances are unique to every isotope as well as to the incoming projectile and can be used to the material identification via NRS. If an incoming projectile interacts with a nucleus or not is probabilistic and is therefore described best by an attenuation model as discussed in the following section.

2.4.3 Propagation of Neutrons Inside Material

The microscopic reaction cross section σ can classically be seen as an effective surface area the nucleus appears to have for a given reaction. The larger the surface area, the more likely it is that it is hit by a neutron and a reaction occurs. The total cross section of a material is the sum of the cross sections of all available reaction channels r, therefore:

$$\sigma = \sum_{r}^{n} \sigma_r. \tag{2.22}$$

σ only describes the interaction probability with a single nucleus. To calculate the interaction rate inside a material, the macroscopic cross section is used as a product of the number of nuclei per unit volume or also called atomic number density N with the microscopic cross section σ [Ragheb, 2011]:

$$\Sigma_i = N_i \cdot \sigma_i \tag{2.23}$$

N_i is thereby the density of atoms of type i in the material. It can be calculated by:

$$N_i = \frac{\rho}{M} \cdot A_v f_i \tag{2.24}$$

Where ρ is the material density and A_v is the Avogadro constant. If a material composition is given by molecular composition like H_2O then, M is the molecular weight in atomic weight units u and f is the fraction of nuclei of the type i inside the material. In the case of isotopic compositions, M represents the average atomic weight in u and f is the fraction of the isotope i inside the material. therefore, the macroscopic scattering cross section of for example polyethylene (PE) at 1 MeV would be:

$$\Sigma_{\mathrm{PE}}(E) = \frac{\rho_{\mathrm{PE}}}{M_{\mathrm{PE}}} \cdot A_v \left(\cdot 2 \cdot \sigma_{H_{\mathrm{scat}}}(E) + \cdot 1 \cdot \sigma_{C_{\mathrm{scat}}}(E)\right) = 0.456\,\mathrm{cm}^{-1} \tag{2.25}$$

To calculate the attenuation of a neutron beam, the intensity of the neutron beam at the depth x inside the material is defined as $I(x)$ [Forget, 2013]. By increasing $\mathrm{d}x$ deeper into the material, the intensity is decreased by

$$-\mathrm{d}I(x) = I(x) \cdot \Sigma \cdot \mathrm{d}x \tag{2.26}$$

An integration over the entire beam path yields:

$$I(x) = I_0 \cdot e^{-\Sigma \cdot x} \tag{2.27}$$

A closer look at equation 2.26 shows that $dI(x)/I(x)$ is the fraction of neutrons that will interact in the next dx. Therefore, Σ is the probability per unit path length for an interaction. With this information the mean free path between two collisions can be calculated by:

$$\lambda = \Sigma \int_0^\infty x \cdot e^{-\Sigma \cdot x} dx = 1/\Sigma \tag{2.28}$$

This path length is equal to the distance it takes until the initial neutron beam decreased to 1/e of its intensity. For the 1 MeV polyethylene example, the mean free path is 2.2 cm, and therefore, every structure aiming to have a significant moderation or shielding effect needs to be larger than this value.

2.5 Neutron Moderation

Neutrons are usually produced with energies in the MeV-regime. This is desirable for applications like fast neutron radiography since they have a high penetration depth and therefore, can probe thick material samples. In contrast to that, many material analysis techniques like NRS or neutron resonance imaging require much lower energies in the range of several eV to keV. To decrease the energy of more than 6 orders of magnitude, moderators are used to transfer the momentum via elastic collisions.
To describe this process correctly the average logarithmic energy decrement ξ is introduced. It describes the change of the neutron energy before and after a scattering event [Forget, 2013]:

$$\xi = 1 - \frac{(A-1)^2}{2A} ln\left(\frac{A+1}{A-1}\right). \tag{2.29}$$

On average after every collision, the neutron gains ξ per collision which is measured in "lethargy"-units. This can be used to find an average number of collisions n for the neutron to reach an energy E_n:

$$ln(E_n) = ln(E_0) - n\xi \tag{2.30}$$

$$n = \frac{1}{\xi} ln\left(\frac{E_0}{E_n}\right) = \frac{u}{\xi}. \tag{2.31}$$

The product of $\xi n = \mathrm{u}$ will therefore represent the total lethargy [Narita and Narita, 1989]. It is desirable to have a low number of collisions to reach a certain energy because this reduces the time a neutron needs to be moderated and results in a shorter neutron pulse length and a Time-Of-FLight (TOF) uncertainty. Besides the high energy loss per collision, the collision rate is also important to keep the moderation time low. This requires a large scattering cross section Σ_s. The product of ξ and Σ_s is called the moderating power M_P and describes how fast a neutron can be moderated.

Although a fast moderation is desirable, a good moderator also has to have a low neutron absorption cross section Σ_a. Otherwise, the neutron losses during the moderation process would negatively impact the usable neutron numbers for the material analysis. Therefore it is helpful to use the moderation ratio:

$$M_R = \frac{\xi \cdot \Sigma_s}{\Sigma_a}. \tag{2.32}$$

A good moderator needs to have a high moderation ratio to be effective. In table 2.1 several common moderator materials are compared to find the best candidate. Water has a high M_P but a rather low M_R

Table 2.1: Various important parameters for different moderation materials. An efficient moderator needs to have a high moderation power and a high moderation ratio to minimize the moderation time t_{mod}. n_{mod} is the average number of collisions to thermalize and t_{diff} is the diffusion time before neutrons are absorbed. The data is either calculated via PHITS simulations (PE) or extracted from [Forget, 2013] and [Dabruck, 2018]

Material	Moderating Power $\xi\Sigma_{el}$	Moderating Ratio $\xi\Sigma_{el}/\Sigma_{abs}$	$t_{mod}\,[\mu s]$	n_{mod}	$t_{diff}\,[s]$
Water	1.36	62	10	20	2e-4
Heavy Water	0.18	5000	46	27	2e-1
Beryllium	0.16	145	67	86	4e-3
Graphite	0.06	165	150	114	1e-2
Polyethylene	3.26	122	5-10	20	1e-4

therefore it is good at slowing down neutrons but a large number of neutrons is absorbed. Heavy water on the other hand has a lower M_P but through the lower neutron absorption cross section of deuterium compared to hydrogen, the moderating ratio is at 5000 and therefore very effective. Despite their high M_R deuterated moderators are often not used due to their high cost. In addition, the diffusion time of D_2O is with 0.2 s to high causing successive pulses to overlap at high repetition rate. Water as a moderator is mostly used in cases where heat has to be transported away from the neutron source like in nuclear reactors, where its liquid state provides a benefit since a steady water flow is simultaneously cooling the fuel rods. In the case of laser neutron sources or accelerator-driven sources, a solid moderator is preferred as they have a higher compatibility with the required vacuum systems. Beryllium and graphite both have high M_R but have a comparably low M_P value. This is caused by their heavier atomic weight which causes neutrons to be moderated more slowly. This becomes evident in the higher moderation time t_{mod} and the higher required collisions N_{mod}. The optimal candidate is high-density polyethylene as it has high M_P and M_R values and a low diffusion and moderation time.

Besides the moderator composition, the moderator shape also plays a role in the neutron emission. Directly at the neutron source, the percentage of fast moving neutrons is highest as they did not have a chance to scatter and to reduce their energy. Further away from the source the number of neutrons that did not undergo any scattering has decreased and the ratio has shifted from predominantly fast neutrons to slow neutrons. For every energy E_n and source distance r therefore, it is possible to calculate a probability that the neutron reaches this point via diffusion or without scattering. A theoretical prediction of this behavior of neutrons in moderators is given by the Fermi age theory [M. Ragheb, 2019].

For any lethargy interval Δu, $\frac{\Delta u}{\xi}$ is the probability of a neutron colliding in Δu. Let q be the number of neutrons passing through Δu per unit time and unit volume, then $q\frac{\Delta u}{\xi}$ is the number of collisions per unit volume and unit time in Δu. Replacing Δu with du and using equation 2.31 one arrives at:

$$\frac{\frac{n_{col}}{dE}}{dV \cdot dt} = q\frac{du}{\xi} = -\frac{q}{\xi E}dE \tag{2.33}$$

With $\frac{n_{col}}{dE}$ the number of collisions in the interval dE and dV the unit volume. Neglecting the absorption in the material, this can be rewritten as:

$$\Sigma_s \Phi dE = \frac{q}{\xi E}dE \rightarrow \Phi = \frac{q}{\xi\Sigma_s}\frac{1}{E} \tag{2.34}$$

With the neutron flux Φ. The important result of this equation is, that the flux Φ is proportional to $\frac{1}{E}$ for non-absorbing, infinite moderators. If weak absorption and limited size is taken into account, then the neutron balance equation has to be fulfilled:

$$[\textit{neutrons produced in dE}] - [\textit{neutrons absorbed in dE}] - [\textit{neutrons leaking out of dE}] = 0 \tag{2.35}$$

or

$$SdE - \Sigma_a \Phi dE + D\nabla^2 \Phi dE = 0 \tag{2.36}$$

With the diffusion coefficient D and the source term SdE being the number of neutrons slowing down into dE minus the neutrons slowing down out of dE. To solve this equation one has to introduce the quantity:

$$d\tau = -\frac{D}{\xi \Sigma_s}\frac{dE}{E} \tag{2.37}$$

Introducing this into equation 2.36 with some minor calculations explained in [Ragheb, 2011] one arrives at the "Fermi Age Equation":

$$\nabla^2 q = \frac{\partial q}{\partial \tau} \tag{2.38}$$

With τ which is called the Fermi age. The units of τ are cm^2 but the name is adopted from a parabolic diffusion equation with similar shape to 2.38. To calculate the Fermi age of a specific energy on has to integrate:

$$\tau = -\int_{E_0}^{E_n} \frac{D}{\xi \Sigma_s}\frac{dE}{E} = \frac{\overline{D_F}}{\xi \overline{\Sigma_s}} ln\left(\frac{E_0}{E_n}\right) \tag{2.39}$$

With $\overline{D_F}$ being the averaged diffusion coefficient and $\overline{\Sigma_s}$ the averaged scattering cross section over the energy range of interest [M. Ragheb, 2019]. Solving equation 2.38 leads to:

$$q = \frac{\dot{Q}}{\sqrt{(4\pi\tau)^3}} \cdot e^{\frac{-r^2}{4\tau}} \tag{2.40}$$

Where $\dot{Q}$ is the source strength at the position r = 0 and q is proportional to the flux of neutrons at a certain energy and a given position. Comparing equation 2.27 with equation 2.40 then it becomes obvious that the chance of a neutron to reach a certain distance in a material without scattering is decreasing with e^{-r} while the probability of a neutron reaching the same distance via diffusion decreases with e^{-r^2}. It first requires some distance inside the moderator for fast neutrons to scatter initially therefore, the number of neutrons with E_n first increases for small distances and then decreases as r^2 becomes larger than τ. This implies first that a fraction of fast neutrons will always escape as it would be inefficient to further increase the dimensions to capture these neutrons.

The second implication is, that the distance to the moderator surface has to be matched to the Fermi age of a given energy to maximize q. This strongly influences the moderator design and connects the moderator dimensions to the energy regime it is intended for.

It has to be mentioned that the Fermi Age Theory does require an infinite medium and low absorption cross sections as well as a continuous energy transfer during collisions. These conditions are not met in the experiment but give a sufficient estimate for the moderator dimensions which can be optimized

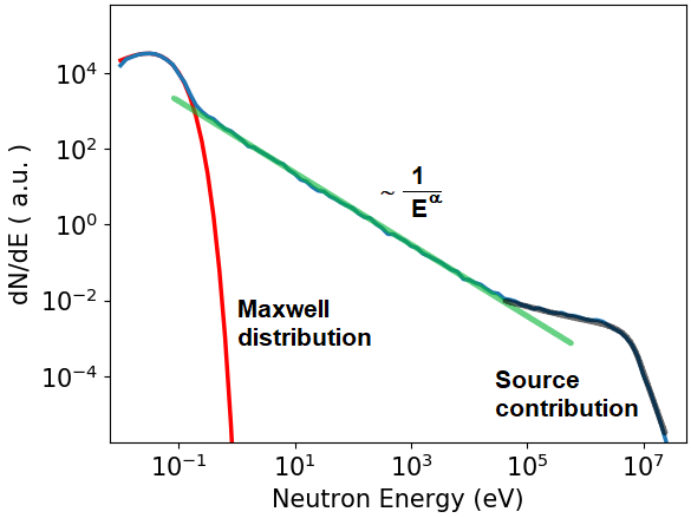

Figure 2.3: Differential representation of the moderated neutron spectrum. The red curve is a Maxwell distribution caused by thermalized neutrons. The green curve is a result of the moderation process. α is the leakage coefficient and has, in this case, a value of 0.94. The black part is caused by neutrons coming from the source and did not undergo any moderation.

using Monte-Carlo simulations. An important difference to the predicted theory comes from the finite size of the moderator, resulting in a change of the neutron energy distribution following:

$$\frac{dN}{dE} \sim \frac{1}{E^\alpha} \tag{2.41}$$

with $\alpha < 1$ being the leakage factor [Lamarsh and Baratta, 2001] caused by neutrons leaving the moderator at the sides or through losses from absorption. This energy distribution is characteristic for a moderated neutron spectrum between energies from 1 eV to 100 keV as it can be seen in figure 2.3 indicated by the green line.

At higher energies, the spectral shape is dominated by the original source distribution. The mean free path for fast neutrons is rapidly increasing above 100 keV and with energy and therefore, the likelihood of leaving the moderator without interaction. This part of the spectrum is marked in black in figure 2.3. At energies below 0.1 eV the neutrons have a similar kinetic energy as the protons they collide with. This enables a transfer of momentum from the protons back to the neutrons and therefore, the neutron distribution becomes Maxwellian (red curve) and is defined by the moderator temperature T:

$$\frac{dN}{dE} = \frac{2\pi N_0}{(\pi k_B T)^{3/2}} \sqrt{E} \cdot e^{-\frac{E}{k_B T}} \tag{2.42}$$

With the total number of neutrons per unit volume N_0 and the Boltzmann constant k_B. For room temperature this distribution peaks at 0.025 eV or 2200 m/s [Keith E., 2014].

2.6 Neutron Detection

Neutrons do not possess an electric charge, which makes them particularly interesting for material probing as they can propagate deeply into materials, without being significantly disturbed on their pathway. This feature, on the other hand, makes them also difficult to detect because they only interact via nuclear forces. Neutrons consequently have to be detected via the creation of secondary particles from nuclear reactions. For neutrons in the region above 100 keV, here called fast neutrons, elastic (n,p) reactions are used to create recoil protons in plastic scintillators. The protons are stopped and excite the scintillator in the process which emits light. The disadvantage of plastic scintillators is, that they are also sensitive to γ-radiation and therefore, measures have to be taken to distinguish γ from neutron radiation, either via time of flight, pulse-shape discrimination or by the use of extensive lead shielding.

For lower neutron energies the efficiency of recoil proton detection drastically decreases. The thermal regime is described by equation 2.42 and consists of energies around 25 meV. Epi-thermal neutrons are classically defined from $\approx$ 1 eV to 100 eV [Stacey, 2018]. Those two types in combination will be called slow neutrons. For slow neutrons, predominantly ^{10}B and ^{6}Li detectors are used as these isotopes have high (n,α) reaction cross section in the low energy regime. Even though ^{3}He has the highest cross section as seen in figure 2.4, it is rather expensive. The increasing scarcity of He and especially ^{3}He has caused the fraction of helium-based detectors to decline.
It can be seen that the cross section for Li and B are changing with the neutron velocity following a $1/v_n$ decrease in σ. This means that detectors that have an efficiency of 90 % in the thermal regime have a reduced sensitivity to 14 % at 1 eV or 1.4 % at 100 eV, making it difficult to detect neutrons in higher energy ranges. Common detectors in this range are borated multi-channel-plates (MCP) or lithium-glass scintillators, that can be used for either imaging or spectroscopy, depending on their readout system.

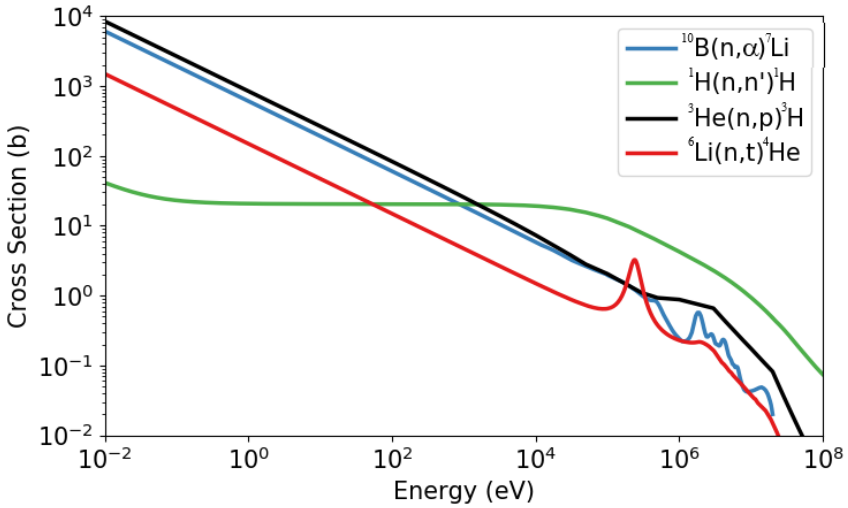

Figure 2.4: Reaction cross sections for isotopes used in neutron detection [Koning and Rochman, 2012]. ^{3}He (black) has the highest detection efficiency followed by ^{10}B in blue and by ^{6}Li. The cross sections are decreasing proportional to $1/v_n$, except for hydrogen. For elastic neutron scattering on hydrogen σ is comparably low until 10^4 eV. At this point, all other cross sections have decreased to a point where they can not be used for detection anymore.

3 Neutron Sources as a Tool for Material Analysis

Many scientific problems require some type of radiation to probe samples in different states. For ions and electrons, the needed species can be inserted into a particle accelerator and brought to their desired speed. For neutrons, this is not possible since they do not have an electric charge. Free neutrons can only be created via nuclear interactions as they can neither be stored nor directly accelerated. therefore, neutron sources have to provide customized neutron beams depending on the desired usage. This section will introduce the most common neutron sources and will discuss their advantages and disadvantages. Afterward, the most promising applications for LDNS are introduced.

3.1 The Most Common Neutron Sources

With the wide field of applications discussed above the human ingenuity has come up with different ways of producing neutron radiation. The most common source types will be introduced with their most important features like size, cost neutron production rate and flux to subsequently compare them to LDNS.

3.1.1 Spallation Sources

Spallation sources are large neutron production facilities with the most prominent examples being the Los Alamos Neutron Science CEnter (LANSCE) [Nelson et al., 2018] and the ESS [Connaster, 2019]. These sources accelerate protons to the GeV regime and direct them onto a high-Z converter material like tungsten. This causes an intra-nuclear cascade from which secondary particles like protons, neutrons and α-particles are emitted. These particles have energies high enough to cause nuclear reactions in neighboring nuclei as well. This second step is called an inter-nuclear cascade and produces neutrons mostly by evaporation of the nucleus. With the combination of these processes between 20 to 30 neutrons per incoming proton are released [Comsan, 2011]. The emitted neutron spectrum from this reaction channel follows a Maxwellian distribution [Goldenbaum, 2004] given by:

$$d\Phi(E_n) \sim \frac{E_n}{T_n^2} \exp\left(\frac{-E_n}{T_n}\right) \tag{3.1}$$

where E_n is the neutron energy and T_n is the nuclear temperature which ranges typically from 2 to 8 MeV. The neutrons produced by the first reaction, on the other hand, are reaching up to 800 MeV [Goldenbaum, 2004]. These neutrons are hard so shield and require an immense amount of material for attenuation. This includes several meters of concrete, high-Z materials for reflection and γ-attenuation as well as large quantities of moderation materials like polyethylene, beryllium or water. As a result, the size and the cost of these sources are drastically increased. With these large moderation structures, a large fraction of the produced neutrons is lost in the slowing down process leading to a low moderation efficiency. For a 800 MeV spallation source $2{\cdot}10^{16}$ n/s are emitted with a reported moderator surface flux of $2{\cdot}10^{13}$ n/(cm^2 s) [Russell et al., 1988]. At LANSCE the thermal flux

at 8.8 m is $2.4{\cdot}10^7$ n/(cm^2 s) [Vogel et al., 2016]. This is equivalent to a 4π-source with a strength of $2.3{\cdot}10^{14}$ n/s. The protons accelerated by LANSCE have a macro pulse length of 625 μs [LANL, 2019b] [Rybarcyk et al., 2012] but for short pulse operation a proton storage ring can be used to compress the bunch to 125 ns [Nowicki et al., 2017].

Spallation sources are the largest type of neutron sources. The total length of the ESS is 623 m [Connaster, 2019] with an estimated cost of $1.5{\cdot}10^9$€. The provided thermal peak neutron flux at the source is expected to be 10^{17} n/(cm^2 s) [Goldenbaum, 2004]. This makes the ESS one of the brightest neutron sources available. The high investment and operation cost limit the number of worldwide operational spallation sources to a small number and only important key experiments can be conducted as the total amount of available beamtime is limited.

3.1.2 Electron Linear Accelerators for (γ,n) Reactions

Besides the production of neutrons based on high energy ion irradiation, it is also possible to utilize (γ,n) reactions to produce neutrons. A prominent example for this technique is the Geel linear electron accelerator facility (GELINA) in Belgium which accelerates an electron beam up to 100 MeV to direct it onto a rotating uranium target. The resulting bremsstrahlung is capable of causing photo-nuclear and photo-fission reactions with neutrons up to 20 MeV [Schillebeeckx et al., 2015] [Anderson et al., 2016]. A post acceleration compression magnet is reducing the electron pulse length down to 1 ns, which is also the pulse width of the resulting neutron emission. A single pulse is able of providing $3{\cdot}10^{10}$ neutrons and the facility is operating at 800 Hz providing a source strength of $2.5{\cdot}10^{13}$ n/s. Neutrons are then moderated by a polyethylene block for neutron resonance and cross section measurements. The closest target station at GELINA is at a distance of 10 m and has a thermal flux of $8{\cdot}10^4$ N/(cm^2 s).

3.1.3 Fission Reactors

An alternative way of producing neutrons is by utilizing nuclear fission. During every fission reaction of ^{235}U + n on average 2.45 neutrons are emitted [World Nuclear Association, 2018] following an evaporation like spectrum proportional to:

$$N(E) \sim E^{\frac{1}{2}} \cdot exp\left(\frac{-E}{T_n}\right) \tag{3.2}$$

with a nuclear temperature of $T_n = 1.29$ MeV [Goldenbaum, 2004]. In this reaction scheme, only one neutron per reaction is available for extraction while the others are needed to sustain the fission reaction. The most common type of reactor-based neutron sources are the Training, Research Isotopes General Atomic (TRIGA) reactors. The TRIGA MARK II reactor LENA in Pavilia operates at 250 kW power and has installation costs of 9.3 Million (inflation adjusted) [Wehring, 1995]. It is capable of producing $1{\cdot}10^{13}$ n/(cm^2 s) inside the reactor core in the thermal regime during steady-state operation. In pulsed mode operation it can generate up to $1.1{\cdot}10^{16}$ n/(cm^2 s) [IAEA, 2009]. Pulsed mode in this context describes reactor pulses on the order of ms [Pungercic and Snoj, 2018] and is therefore much longer than the neutron pulses at an LDNS or a spallation source. TOF experiments involving a reactor require several beam choppers which results in large losses in neutron numbers. An additional downside

of these types of neutron sources is that they produce nuclear waste and their operation is connected to the known risks of nuclear reactors.

3.1.4 Compact Accelerator-Driven Neutron Sources

Compact Accelerator Driven Neutron Sources (CANS) are smaller than spallation sources, typically in the range of 15 to 100 m and operate between 3 and 100 MeV [Brueckel, 2018]. Thereby either protons or deuterons are accelerated in a conventional accelerator and directed on lithium, beryllium or vanadium since these elements have the highest neutron yield in that energy range. When classical accelerator structures are used, they are often limited in their current density by space charge effects. This restricts the operation to a maximum current for most structures to around 100 mA [Ott, 2018] even though some experimental accelerators have surpassed this limit through beam neutralization [Seidl et al., 2017]. To compensate for the limit in current, CANS often use longer beam pulses in the range of 100 μs [Brueckel, 2018] to maximize the neutron output.
There are currently many projects under development to provide small to medium-sized CANS. A prominent example is the Jülich High Brilliance Source (HBS) which is expected to have a source yield up to 10^{16} n/s [Rücker et al., 2016]. While this is one of the larger CANS, smaller projects like the NOVA ERA with $2{\cdot}10^{13}$ n/s source strength or the RIKEN RANS proton linac with 10^{12} n/s are under development. The latter is one of the smallest CANS with 15 m in length. Its successor RANS-II is planned to be even smaller with a length below 5 m to enable it to be transportable.

3.1.5 Sealed Tube Neutron Generators

Compact accelerators that utilize deuterium - deuterium (DD) or deuterium - tritium (DT) fusion to create neutrons are commercially available for neutron production. The reaction D + D $\rightarrow$ ^{3}He + n yields neutrons with 2.45 MeV and D + T $\rightarrow$ ^{4}He + n emits 14.1 MeV neutrons. Small portable neutron generators with a source strength of 10^8 n/s start at costs of around 10^5€ [Thermo Fischer Scientific, 2019]. These fusion reactions have the advantage that their cross sections are high at considerably low energies around 50 to 100 keV eliminating the need for large acceleration structures. This enables them to be rather compact in comparison to other sources but their maximum flux is limited as well as their lifetime [Ludewigt et al., 2007]. An advantage of these sources in comparison to reactors or radioactive isotopes is, that they can be turned on and off, depending on the needs of the user. The neutron emission of these tubes is mono-energetic and they are either run in continuous operation or in pulse bursts with a duration of 5 μs [Thermo Fischer Scientific, 2008b].

3.1.6 Radioactive Isotopes

The smallest type of neutron sources are radioactive isotopes. Neutrons first were discovered by the combination of the α emitter polonium with the element beryllium [Garrett, 1962]. Today for reasons of practicality [NRC, 2010] mostly Americium - Beryllium (AmBe) or ^{252}Cf sources are used for neutron

production via isotopes. While californium is a natural neutron emitter, AmBe is creating neutrons via the reaction

$$^{241}\mathrm{Am} + ^{9}\mathrm{Be} \rightarrow ^{237}\mathrm{Np} + \alpha + ^{9}\mathrm{Be} \rightarrow ^{237}\mathrm{Np} + ^{12}\mathrm{C} + \mathrm{n} \tag{3.3}$$

With an average neutron energy of 4.2 MeV and reaching up to 11 MeV [NRC, 2010]. The neutron yield of these sources can be scaled up simply by increasing the amount of radioactive material but with higher activity, also handling becomes more difficult. A major problem of these sources is that they are constantly emitting neutrons and they cannot be turned off. This limits their usability to small experiments that rely on a constant neutron flux without pulsed emission.

3.1.7 Laser-Driven Neutron Sources

A laser-driven neutron source uses the TNSA or the RITA effect of high power laser-matter interaction to accelerate protons or deuterons from a thin target like a deuterated polymer foil in the μm to nm regime. A converter material, typically lithium or beryllium is then placed in the ion path to convert them via the nuclear reactions into neutrons. The concept of using a spatially separated ion source from the neutron source is called the "pitcher-catcher configuration" and is shown in figure 3.1. This configuration has demonstrated the highest neutron yields so far [Kleinschmidt, 2017]. Previous experiments have delivered $5.3(0.8)\cdot10^{10}$ neutrons per shot. The uncertainty of this number represents the standard deviation of 9 consecutive shots [Kleinschmidt, 2017]. The emission of these sources has two components. One is emitting neutrons isotropic in all directions and has its origin mostly in compound reactions. The other has a strong forward oriented neutron emission created by break-up, stripping and pre-equilibrium reactions. This increased flux has a Gaussian shape with a half opening angle of 50° [Kleinschmidt, 2017]. Peak fluxes in this direction were measured by [Roth et al., 2013] with up to $1.4(0.3)\cdot10^{10}$ n/sr corresponding to $1.9(0.3)\cdot10^{11}$ neutrons in a 4π equivalent. Maximum neutron energies detected so far are close to 100 MeV [Taddeucci and Favalli, 2018] [Roth et al., 2013].
Laser neutron source spot sizes can be brought down to 1 mm [Guler et al., 2016], in comparison to cm spot sizes for spallation sources [Batygin et al., 2018]. This enables a high-resolution imaging with this type of sources. Also, the pulse width of LDNS at the source is only limited by the distance between pitcher and catcher and the ion energy distribution. For a catcher distance of 3 cm and an ion energy spread from 4 to 100 MeV this results in a pulse length of 0.9 ns. These short pulse lengths can be used to investigate fast changing processes on the ns-scale.

Neutron sources driven by lasers are a rather novel concept and there are currently neither commercial sources available nor are there any facilities solely dedicated to laser neutron production. Most experiments are currently carried out at existing high power laser facilities like PHELIX, Trident or Texas PW [Bagnoud et al., 2010] [Moncur et al., 1995] [Martinez et al., 2012] with intensities between 10^{20} to 10^{21} W/cm^2 and repetition rates of 1 shot every 60 to 90 minutes. This low repetition rate is mostly caused due to the thermal heat load in the amplifiers resulting in a distortion of the wavefront [Patrizio, 2020] and the time needed for this heat to be removed by the cooling system. In newer laser systems more efficient laser diode pumping is used and active cooling systems enable a better removal of the heat. This enables these systems to operate at a much higher repetition rate. The Exteme Light Infrastructure (ELI) [Mourou et al., 2011] L3 beamline, which is currently in its final commissioning phase will be able to operate at 1 PW with 30 fs and 30 J in a 10 Hz repetition rate in the near future [Eli Beamlines, 2019]. The Scalable High-power Advanced Radiographic Capability (SHARC) laser system which is currently under development at the Lawrence Livermore National Laboratory (LLNL)

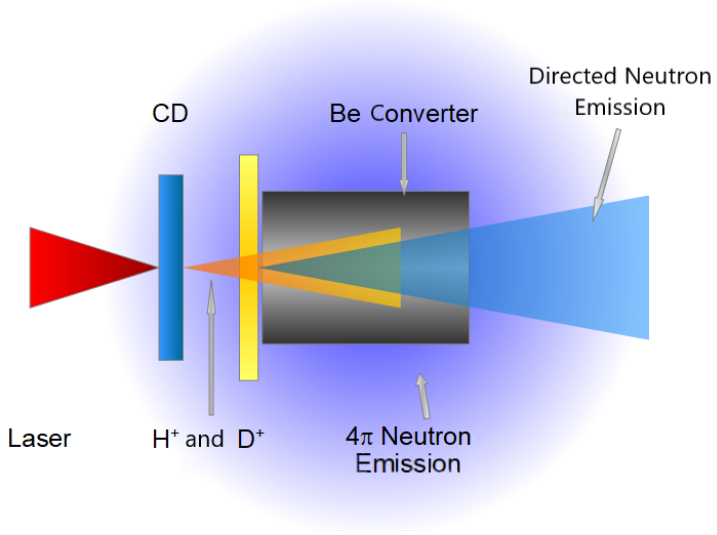

Figure 3.1: Laser-based neutron generation in the pitcher-catcher configuration. Ions from the laser acceleration process are directed onto a converter where they produce neutrons via nuclear processes. Some of these reactions produce an isotropic neutron emission in 4π while others have a strong forward orientation. The converter is protected from the hot plasma through an ablation shield displayed in yellow.

[Siders, 2018] is even more promising as a laser neutron source. It is capable of delivering 150 J in 150 fs at a 10 Hz repetition rate. Even though pulse length and energy are slightly different from the PHELIX system it can be approximated that such a system can produce similar neutron numbers per shot. Therefore a neutron production rate of $5{\cdot}10^{11}$ n/s can be anticipated [Kleinschmidt, 2017]. With these information, it is possible to put laser neutron sources into perspective to other sources.

3.2 Comparison of Neutron Sources

A look at table 3.1 reveals the key attributes for every source type. Spallation sources and pulsed nuclear reactors have the highest neutron production rate in the order of 10^{16} n/s which is three orders of magnitude higher than CANS and photo-fission sources. LDNS have a comparably low production rate in the order of 10^{11} to 10^{12} n/s which is still four orders of magnitude higher than portable neutron generators. If these numbers are compared to the actual thermal flux at the detector position these relations change drastically. Reactors might still have the highest average flux in this category of 10^9 n/(cm^{2}s) but this is measured directly inside the reactor core without any energy resolution and is therefore limited to applications like Neutron Actication Analysis (NAA) that do not rely on energy discrimination. This leaves spallation sources at the highest detector flux rate around 10^7 n/(cm^{2}s) which is only two orders of magnitude higher than for the LDNS as well as for CANS and electron linacs. The value for LDNS is based on the measurements conducted in section 5.1 and scaled with the repetition rate of 10 Hz. The two orders of magnitude difference in detection and moderation efficiency between spallation sources and LDNS comes from two major factors. The neutron energies produced by laser acceleration are much lower and less moderator material is needed. This reduces the absorption of neutrons inside the moderator as well as the overall size of the moderator-reflector structure. With a smaller moderator and a better energy resolution at an LDNS, the detector can be placed much closer to the source.

Table 3.1: Comparison between different neutron sources. Values are exemplary for existing sources taken from [Comsan, 2011] [Brueckel, 2018] [Thermo Fischer Scientific, 2008b] [UM Radiation Facilities, 2019] [Pungercic and Snoj, 2018] [Thermo Fischer Scientific, 2019]. The cost per n/s is calculated according to the ratio of facility installation cost divided by the number of neutrons/(cm^2s). The values for the CANS represent the NOVA-ERA concept.

Source	Neutron/s	$n_{Th}/(s{\cdot}cm^2)$ det.	Min pulse length	Size	Cost [€]	$€/\frac{n}{s\cdot cm^2}$
LDNS	$5\cdot10^{11}$	$2\cdot10^5$	< ns	15 m	$\approx 10^7$	50
Spallation	$10^{15}-10^{16}$	$2\cdot10^7$	125 ns - 625 μs	1 km	$1.5\cdot10^9$	75
Electron Linac	$3{\cdot}10^{13}$	$8{\cdot}10^4$	1 ns	100-200m	N/A	N/A
CANS	10^{13}	10^5	139 μs	10 - 50m	$6\cdot10^6$	60
Reactor	10^{16}	10^9	1-10 ms	10m	$9.3\cdot10^6$	0.01
Neutron Tube	10^8	$<10^2$	5 μs	1m	10^5	1000

A major limiting factor for applications is the pulse length. For all applications that rely on TOF for energy differentiation, it is required that the flight time is large in comparison to the pulse length. With propagation times of thermal neutrons in the order of 500 μs/m this is only a problem for reactors but can be solved via the usage of beam choppers at the cost of large fractions of the beam. For epi-thermal neutrons, these propagation times drastically decrease to 10s of μs/m. This would require flight path lengths for CANS in the range of hundreds of meters, making the detection inefficient. LANSCE is capable of reducing the pulse width of 625 μs down to 125 ns [Nowicki et al., 2017] with the use of pulse compression inside a storage ring.

For electron linacs and LDNS with pulse durations in the low ns regime, the initial time uncertainty is dominated by the moderation time which is between 100 ns and 1 μs for most epi-thermal neutrons. This enables the positioning of a detector much closer to the source. Depending on the desired resolution, distances as close as a meter can be achieved. This makes those two sources the most efficient options for neutron resonance spectroscopy as this technique has the highest requirements on the TOF uncertainty.

A comparison between the sizes shows that the smallest pulsed source is a neutron tube which is also the only option that is portable by a person. Recent developments at RANS-II [Otake, 2019] and at LDNS (section 6.1) indicate that also these sources are approaching a stage of mobile usage, even though these sources would require a truck for transportation. Spallation sources are at the other end of the spectrum with 623 m for the ESS which is also connected to the highest cost of over one billion euros. Electron linacs are smaller but are still considerably large in size as they have to be able to accelerate electrons up to 100 MeV. CANS operate between 3 and 50 MeV [Brueckel, 2018] and can therefore, be build smaller but they are still larger than LDNS is most cases.

A particularly interesting parameter is the cost for usable neutrons at the detector. For this value, the installation cost for each source is divided by the thermal neutron flux at the detector position. The most cost-efficient neutron flux can be gained by using a nuclear reactor but this only holds true if no energy resolution is needed. LDNS are the most cost-efficient source type with the capability of thermal and epi-thermal energy selection. They are slightly more efficient than CANS although there is some margin of error in the price for an LDNS as they have not been build yet. Spallation sources are about 50 % less cost-efficient per usable neutron than LDNS making it a viable option to build multiple laser-driven neutron sources across Europe instead of a large spallation source at a single location. A comparison between neutron tubes and LDNS shows the huge potential of small laser neutron sources as they are

200 times more cost-efficient. For neutron producing electron accelerators, no data about construction cost was publicly available but it is expected that due to the large size and high electron energy, such a source is more comparable to an ion accelerator like the HBS than to the NOVA-ERA and therefore at least one order of magnitude more expensive.

This comparison reveals the different strengths of each source type. Spallation sources have the highest benefits for measurements that require long and intense irradiation. This comes due to the fact that the measurement time has to be long in comparison to the sample preparation time or otherwise the high flux is not used efficiently and a less intense source could be used as well. CANS have large pulse widths and are therefore beneficial for measurements with thermal or cold neutrons like neutron diffraction as those neutrons have a lower velocity and therefore a longer flight time. Electron linacs like GELINA are on the other side of the spectrum and are build for a high resolution and are well equipped for cross section measurements that require a high accuracy. Reactors have the highest benefit for measurements that only need a high average neutron flux without an energy resolution. Neutron tubes can be beneficial for terrain that can not be accessed with vehicles and require a portable neutron source. LDNS have their advantage in their small size and low cost and can be therefore used for measurements that do not require the high average flux of a spallation source or the energy resolution of an electron linac. They could be in principle be used for similar measurements as CANS with similar performance but the highest benefit for an LDNS can be achieved with epi-thermal neutron measurements that rely on isotope identification. This is due to the fact that these measurements can benefit the most from the short pulse length and the close proximity of the detector to the source, making these measurements more efficient and no large acceleration structures like in a spallation source or an electron linac are needed. The next chapter will give an introduction to the potential applications for an LDNS and then focus on those with the highest potential.

3.3 Applications for Laser-Driven Neutron Sources

Neutrons are needed, whenever there is a demand for non-invasive testing and when other analysis methods reach their limitations. This is the case if a low Z-material like hydrogen or carbon is encapsulated inside a high-Z surrounding. In an X-ray image, it would be impossible to see these materials as they do not provide enough contrast. With a neutron radiography, this is possible as seen in figure 3.2 (a) where the fuel inside a diesel injection nozzle was resolved. This ability makes neutron radiography a complementary tool to X-rays diagnostics.

Another field of application in which non-destructive testing is required is archaeology where samples are unique, extremely rare and have an unknown origin. In archaeology, neutrons are used to identify various artifacts due to their unique capability to distinguish between different isotopes.

An example for this is the Buggenum sword from the bronze ages [Postma et al., 2017] displayed in figure 3.2 (b), which was found in the Netherlands and examined at the GELINA facility [Schillebeeckx et al., 2014][Postma et al., 2010]. A measurement of the distribution of the isotopes enabled the researchers to trace back the origin of the sword to the Danube region and a neutron radiography revealed the internal structure inside the handle (c).

Another important application is the probing of used nuclear fuel rods. As these samples are often still highly radioactive, they cannot simply be opened up to check if the fuel was burned as efficiently as

(a) (b) (c)

Figure 3.2: The potential of neutron radiography. (a) shows a radiography of an injection nozzle of a diesel engine demonstrating the ability to resolve the presence of hydrogenous liquids inside metal surroundings. (b) the Buggenum sword from the middle bronze age was examined in a neutron beam with NRCA, Neutron time of flight diffraction and via tomography. These techniques have resolved hidden internal structures and the isotopic composition traced the sword back to the Danube region. Image (b) is a photography corresponding to the radiographic image in (c). Images are extracted from [Lehmann et al., 2015] and provided from the courtesy of the Leiden University [Postma et al., 2017].

expected. With intense neutron irradiation, a tomography can be performed and the presence of ^{235}U or the distribution of fission products can be investigated [Vogel et al., 2016].
A field of application where neutrons and X-rays are needed simultaneously is the security sector. At airports and harbors, containers from all over the world arrive day and night. In Hamburg alone, 8.7 million containers were shipped in 2018 [Marketing, 2019] leaving little to no time for manual inspections. There are solutions for X-ray scanners [Smiths Detection Group, 2019] which are capable of scanning entire freight containers and identify most hazardous or illegal shipped goods. Certain kinds of explosives or fissile material pose a security threat as it can not be properly identified just by the use of X-rays [Smith Detection Group, 2018]. Neutrons could help to identify these materials as they are capable of detecting explosives from their nitrogen to oxygen ratio [Lanza, 2007] and fissile elements like uranium with the use of the differential die away method [Jordan and Gozani, 2007]. Today portable neutron generators [Thermo Fischer Scientific, 2019] are used for this purpose. A source that simultaneously emits X-rays and neutrons could replace both systems with a single source.

For industrial applications, small-sized neutron sources are of particular interest since many products are subjected to high-quality standards and must endure harsh stressful conditions. Therefore defects inside the material often only become visible after long expensive stress testing or in customer operation. Internal defects can be detected via a neutron radiography [Kobayashi et al., 1992] and save testing time as well as reducing the risk of failure of essential components during operation.

For many of the applications mentioned above either no pulsed operation is needed like in the case of radiography or it is sufficient as long as the pulse length is in the regime of ms to μs. While LDNS can still be beneficial in these cases from their smaller size and cost, they are most advantageous for applications that require a short neutron pulse width. TOF based material identification methods have therefore the highest benefit if operated with a laser neutron source. Such techniques are neutron resonance

spectroscopy and neutron resonance imaging. For this reason, they are discussed in further detail in the section below.

3.3.1 Neutron Resonance Spectroscopy

The presence of compound nuclear resonances that drastically increase the neutron cross section enables the identification of materials by using the increased reaction and absorption rate for resonant neutrons. For such a measurement a short neutron pulse with a broad energy spectrum (white pulse) is emitted as the source and the transmission over time behind the sample is measured. Figure 3.3 displays the resonance structure for the tungsten isotopes ^{182}W and ^{186}W as well as for ^{113}Cd to display the variety of resonance structures. These resonances can range from narrow peaks to "giant" resonances as seen in cadmium. Also, their peak absorption can range from a few b to 10^5 b or higher.

Neutron resonance spectroscopy can be divided into two sub-categories [Schillebeeckx et al., 2014]: Neutron Resonance Capture Analysis (NRCA) and Neutron Resonance Transmission Analysis (NRTA) [Postma et al., 2017]. Both methods are non-destructive measurement diagnostics to determine the elemental and isotopic composition of materials by utilizing the highly energy-dependent cross sections of nuclear reactions. With these dependencies, different isotopes have their unique distribution of resonances across a wide range of energies. This distribution can be used, similar to a fingerprint, to identify the presence of isotopes inside a sample. The shape of a nuclear resonance can be described by the Breit-Wigner formula [Fernández et al., 2019]:

$$\sigma_n(E) = \sigma_0 \frac{(\Gamma/2)^2}{(E - E_R)^2 + (\Gamma/2)^2}. \tag{3.4}$$

σ_0 is the cross section at the resonance, Γ is the resonance width and inversely proportional to the lifetime of the excited state of the compound nucleus. E_R is the resonance energy and is defined by the virtual energy state of target and neutron as well as the transferred energy towards the nucleus $E_t = E/(A+1)$ with the atomic mass number A. If the material has a (n,γ) neutron capture resonance, then the emission of prompt-γ-rays increases proportionally to $\sigma_n(E)$. NRCA utilizes this relation by measuring the γ-emission as a function of neutron arrival time at the sample. Knowing the distance from the neutron source to the sample as well as the sample distance to the detector, it is possible to assign every γ-event to a neutron energy. This technique is especially interesting for larger samples or structures that do not allow a measurement in transmission. If this technique is used with an energy sensitive γ-detector, it is called Prompt Gamma Neutron Activation Analysis (PGNAA). This enables to determine a contamination inside a material according to their depth and concentration which has a high demand in civil engineering where the chlorine contamination of concrete can yield information about the corrosion inside buildings and bridges [Maslehuddin et al., 1996][Naqvi et al., 2006][Kirkpatrick et al., 2002].

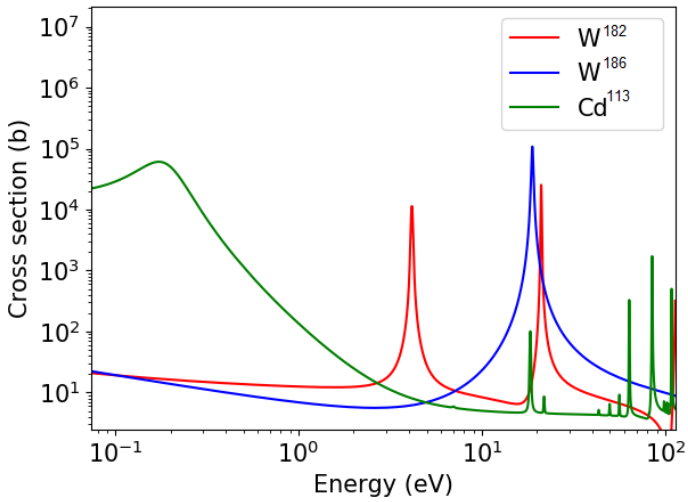

Figure 3.3: Total neutron reaction cross sections for different isotopes of tungsten and cadmium [Brown et al., 2018]. This resonance structure is unique for every isotope and can be used to identify materials.

The second analysis method of NRS works similar to NRCA but is measuring the neutron spectrum in transmission hence NRTA. This method will be of main interest in this work and is therefore discussed here in further detail. If a white neutron beam passes through a sample, the transmission can be calculated by:

$$T(E) = e^{-\sum_k N_k \sigma_{\mathrm{tot}_k}(E)} \tag{3.5}$$

with the total cross section $\sigma_{\mathrm{tot}_k}(E)$ and N_k the number of atoms per unit area of nuclei k [Schillebeeckx et al., 2014]. $\sum_k$ indicates the summation over all cross sections for present isotopes and should not be mistaken with the macroscopic cross section. With $\sigma_{\mathrm{tot}_k}(E)$ known for most elements, it is possible to determine the areal density of isotope k from the transmission at resonant energies. For an accurate n_k determination, the measurement has to be independent of the detector efficiency and the shape of the neutron flux. For this purpose, the experimental transmission is calculated by:

$$T_{exp} = \frac{C_{in} - k_T B_{in}}{C_{out} - k_T B_{out}} \tag{3.6}$$

As a function of counts with the sample in place C_{in}, the counts without a sample C_{out} as well as the background contribution B with the sample in and out of position. The factor k_T accounts for uncertainties from systematic effects in the background contribution [Schillebeeckx et al., 2014]. With this approach, only the changes in counts are compared with each other and detector efficiency variations are canceled out. The background contribution can be determined by the black resonance technique, in which known samples are inserted into the beam with large resonances, capable of fully absorbing the neutron beam, hence called black. Afterward an analytical function connects all black resonances to create a background function.

The resonances described in equation 3.4 are subject to Doppler broadening from the thermal motion of the nuclei inside the material. Therefore the resonant energy condition is fulfilled when

$$E_r = \frac{1}{2} m_n (v_n - V_z)^2 \tag{3.7}$$

with the neutron velocity v_n and the thermal velocity component of the target nucleus in neutron propagation axis V_z. Assuming Maxwell Boltzmann statistics, the velocity distribution is given by [Fernández et al., 2019]:

$$S(E_r)\,\mathrm{d}E_r = \pi^{-1/2} \cdot \frac{\exp\left(-\left(\frac{E_r - E}{\Delta}\right)^2\right)}{\Delta}\mathrm{d}E_r \tag{3.8}$$

Important here is Δ which is the near resonant Doppler width given through [Schillebeeckx et al., 2015]:

$$\Delta = \sqrt{\frac{4Ek_BT}{A}} \approx \sqrt{\frac{4E_rk_BT}{A}} \tag{3.9}$$

With A being the atomic mass number of the target nucleus. Defining the quantity ϵ by the ratio of

$$\epsilon = \frac{\Gamma}{\Delta} \tag{3.10}$$

Then for large ϵ, the pure natural width can be assumed. If ϵ is small, then the resonance is Doppler dominated.

3.3.2 Neutron Resonance Imaging

If the techniques of neutron resonance spectroscopy and neutron radiography are combined, it is called neutron resonance imaging (NRI). The idea behind this concept is to spatially resolve isotope distributions inside a sample. This technique has been successfully demonstrated at accelerators. [Kai et al., 2017] were capable of identifying a tungsten and a tantalum plate by their resonant neutron absorption and also determined their position. [Schillebeeckx et al., 2015] used neutron imaging on overlapping structures of metal wires to resolve each metal individually. The method behind NRI is similar to NRS based on time of flight but instead of integrating over the entire detector surface, they are spatially resolved. Creating several images with the same exposure time but at different energy intervals allows to scan through the neutron energy spectrum. Areas of the sample that contain an isotope with a resonance that matches the exposure time window will appear darker in comparison to neighboring time windows. The relative darkening of each pixel can be used to calculate the number of atoms present of this isotope. While NRS requires an energy resolution high enough to identify changes of the cross section inside a sample, NRI can integrate over the entire resonance, reducing the requirements on the TOF resolution. If several NRI images are taken from different angles it is possible to create a resonance tomography.

4 Optimization of Laser-Driven Neutron Sources for Neutron Resonance Spectroscopy

Laser-driven neutron sources are still in their early development stages. This part of the dissertation will focus on the development of an LDNS setup for neutron resonance spectroscopy. Figure 4.1 shows the different components necessary for such a system. Each of them has to be optimized for an efficient operation as spectroscopy tool. The laser needs to accelerate a maximal number of ions per shot while still being able to operate at a sufficiently high repetition rate. The targetry system has to provide thin targets at the same rate as the laser is firing. This has to be possible with low maintenance requirements and a high reliability. The catcher material and dimensions have to be matched to the incoming ion spectrum and the moderator has to slow down the neutrons to epi-thermal energies with high efficiency. The collimation system must be designed to minimize the background contributions. The detector has to have a high time resolution and detection efficiency while still being able to operate in a high noise environment and to withstand the γ-flash. The following chapter will go through each of these components, discuss the state of the art as well as the dominating parameters and find an optimized solution.

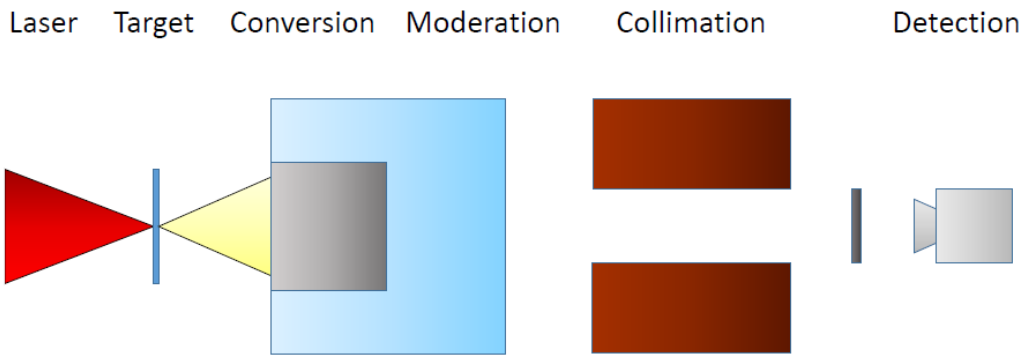

Figure 4.1: Schematic view for neutron resonance spectroscopy. A high power laser is focused on a target and ions are produced. The ion beam is converted into neutrons which are moderated to low energies. Emitted neutrons are collimated and pass through a sample. Afterward, they are detected and the spectrum is investigated. In the actual setup collimation and detection take place under 90 °towards the laser but is modified here for better visibility.

4.1 Influence of the Laser Parameters on Ion Acceleration

The ion acceleration mechanism depends on the complex interplay of laser intensity, laser energy, pulse duration, contrast and target thickness. Depending on the initial parameters the hot electrons generated by the laser can have different distributions, densities and temperatures. To enable an accurate prediction for the ion spectrum, a meta-analysis on laser ion acceleration is conducted in this section. For laser neutron generation it is most important how the initial laser parameters convert into an ion spectrum with specific key attributes that are essential to neutron conversion. These attributes are the maximum ion energy in the spectrum, henceforth called cut off energy E_c, the number of ions N_P, as well as the spectral shape T_P. A typical laser ion spectrum mostly consists out of a superposition of

two ion distributions with different ion temperatures caused by a variation of the electron temperature inside the target. Attempts to predict the influence of the laser on the ion acceleration will be discussed and a new approach will be introduced on how to predict the cut off energy as well as the number of accelerated ions. The spectral shape will be investigated in section 4.3 as it is strongly connected to the catcher material.

Previous works by Mora and Fuchs model the ion acceleration as a free plasma expansion into a vacuum [Mora, 2003][Fuchs et al., 2006]. The fundamental idea behind this model is, that the ion energy scales with the hot electron temperature predicted from eq. 2.15 via

$$E_{max} = 2ek_B T_{hot}\left[ln(\tau_p + \sqrt{\tau_p^2+1})\right]^2 = 2em_e c^2\left(\sqrt{1+a_0^2}-1\right)\cdot\left[ln(\tau_p + \sqrt{\tau_p^2+1})\right]^2 \tag{4.1}$$

With $\tau_p = \omega_{pi}\cdot\tau_{acc}/2.33$, τ_{acc} =1.3 $\cdot\tau_{\text{laser}}$, the elementary charge e and the ion plasma frequency ω_{pi}. As it can be seen in figure 4.2 this model shows agreement with experimental data in the region of 10^{18} W/cm^2 but massively overestimates cut off energies for higher intensities above $\approx 10^{19}$ W/cm^2. Another model proposed by [Jung et al., 2015] expects an energy per nucleon scaling with:

$$E_{max} = \frac{5}{12}\tau_{\text{laser}}^{0.28}\cdot(a_0-1)[MeV] \tag{4.2}$$

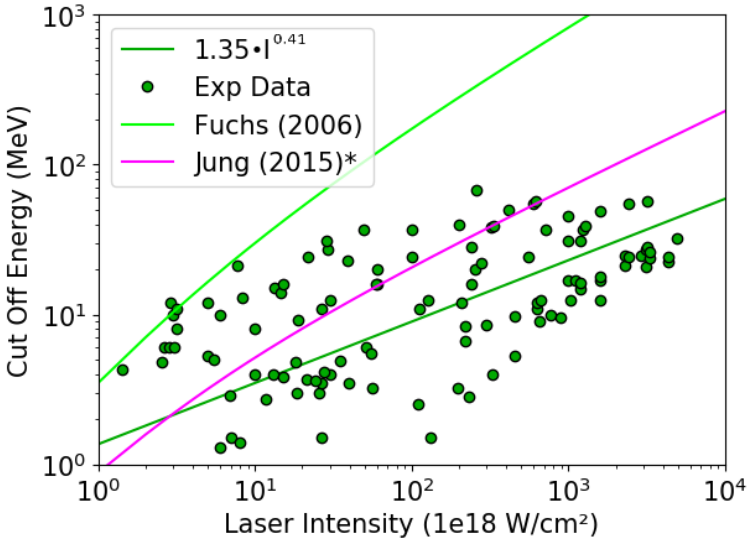

Figure 4.2: A comparison of common TNSA scaling laws with cut off energies found in the literature. Each green dot represents an experimental cut off energy. The data was collected from various sources with different laser parameters. The wide spread of the data points shows that it is not possible to predict a cut off energy from the laser intensity. The only commonality is that the average E_c increases with higher intensities as indicated by the dark green line. The cyan curve resembles the scaling predicted by [Fuchs et al., 2006] and the red is a scaling proposed by [Jung et al., 2015]. Both do not match the data. Sources for the data points are found in the text.

This scaling law underestimates ion energies at lower intensities in the 10^{18} W/cm^2 region and overestimates above 10^{21} W/cm^2. It has to be noted that the Jung law originally described carbon but was modified to predict MeV/nucleon. Both scaling laws have been plotted in figure 4.2 for a 650 fs laser pulse with 1.053 μm wavelength in comparison to 116 experimental data points collected from various publications all across the field [Brenner et al., 2011] [Busold, 2014] [Cianchi et al., 2018] [Ceccotti et al., 2007]

[Clark et al., 2000] [Daido et al., 2012] [Dover, 2017] [Fang et al., 2016] [Fuchs et al., 2006] [Flippo et al., 2008b] [Green et al., 2014] [Kaluza et al., 2004] [Khaghani et al., 2017] [Kraft et al., 2018] [Lundh et al., 2007] [Macchi, 2017] [Morrison et al., 2018] [Poole et al., 2018] [Robson et al., 2007] [Noaman-ul Haq et al., 2018] [Schwind et al., 2019] [Wagner, 2014] [Wagner et al., 2016] [Zeil et al., 2010] [Zepf et al., 2001].

There have been other scaling laws proposed [Schreiber et al., 2006], but a theoretically derived scaling law that applies for all pulse duration and intensity regions has proven to be difficult. This becomes obvious by comparing the green curve in figure 4.2 with fit values of $E_P(I) = 1.35 \cdot I^{0.4}$ with the data. The average deviation of the experimental values from the fit function is 140 % but many values vary up to 400 % from this value. A good example for this are intensities around $2.5{\cdot}10^{20}$ W/cm^2 where cut off energies from 3 MeV to 67 MeV are recorded .

This large discrepancy shows that the ion cut off energy cannot be simply calculated from the laser intensity. A more profound method is taken in the following part by splitting the intensity:

$$I = \frac{E_L}{\tau_{laser} \cdot \pi \cdot r^2} \tag{4.3}$$

into the contributing parameters like energy E_L, laser pulse duration τ_{laser}, and focal spot area, respectively the FWHM radius of the laser spot on target r. Each of these parameters needs to be treated independently for their influence on the ion cut off energy. Previous attempts focused on deducing the dependency of these parameters from theoretical calculations with limited success as seen in figure 4.2. In contrast to that this work will follow an approach used in pattern recognition and machine learning [Bishop, 2006]. By using a vast amount of data variations in the setup can be treated as noise and variations in E_c solely depending on the energy can be isolated.

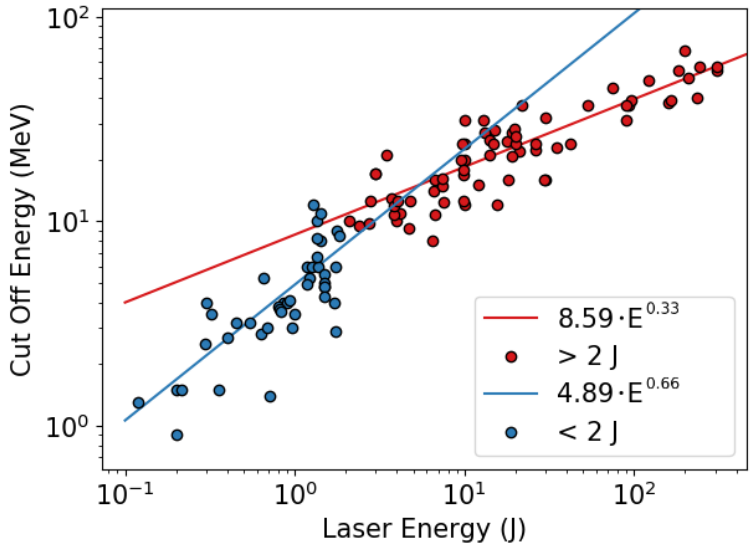

Figure 4.3: Experimental cut off energies as a function of laser energy. Blue data points contain less than 2 J of laser energy and scale with $\sim E^{0.66}$ while laser pulses with higher energies > 2 J, here shown in red, scale with $\sim E^{0.33}$.

Figure 4.3 shows the cut off energy of the same experimental data points from figure 4.2 as a function of the laser pulse energy. It is visible that the spread in cut off energy is clearly reduced to 37% for < 2 J

and to 24% above 2 J. This is on average a 4.7 times smaller spread than seen in figure 4.2 and allows much more accurate predictions about the cut off energies of a laser system. The separation in above and below 2 J is arbitrary and comes from the bend inside the data points. The cause of this behavior is yet not fully understood and requires further investigations. The blue curve with $E_L < 2\,\mathrm{J}$ scales with $E_L^{0.66}$ and is therefore increasing faster than the red curve with $E_L^{0.33}$.

If the energy of a laser is raised from E_0 to E_1 then the cut off energy of the ions increases by a factor $(E_1/E_0)^{0.33}$. This only applies if the intensity for both beams is the same, e.g. by increasing the focal spot area at the same time. If the focal spot remains the same as it is the case for most intensity scans, then the increase in intensity additionally changes the laser electron interaction and therefore the scaling. To see the influence purely caused by changes from variations in I_L, the focal spot radius has to be varied at constant E_L and τ_{laser}.

The intensity depends on the laser spot radius proportional to $1/r^2$. For an accurate scan of the dependency of this parameter, many different focusing parabolas with the same laser would have to be used to create uniform Gaussian spots with different radii. Since most facilities are limited in their parabola variety, it is more practical to conduct a focal scan. In this scan, the target is moved to different distances from the focal point to increase the spot radius. This procedure is more vulnerable to aberrations in the beam quality leading to not perfectly round focal spots. Nonetheless, this is a good enough approximation to investigate the influence of varying the intensity while keeping E_L and τ_{laser} constant.

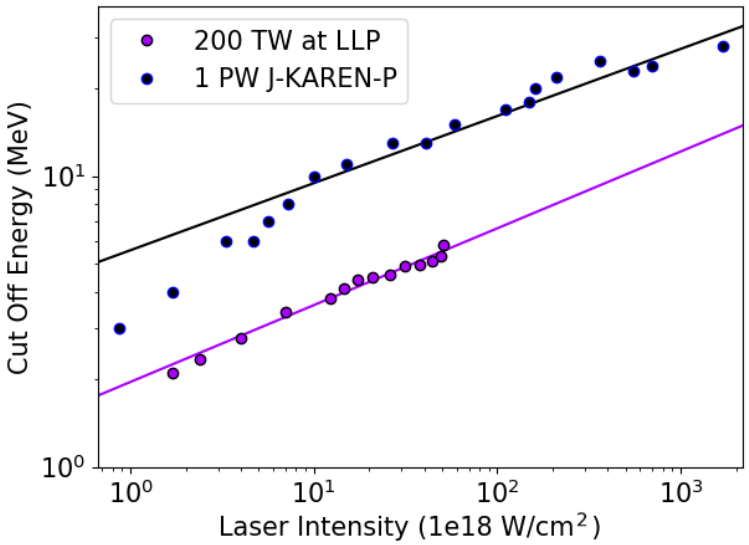

Figure 4.4: Comparison of cut off energies for a focus scan with a 200 TW laser and a 1 PW laser. Both laser follow a similar decrease in E_c with the drop in intensity. The black fit scales with $I^{0.23}$ and the purple fit with $I^{0.26}$. Below 10^{19} W/cm^2 the data deviates from the fit, most likely caused by an in-homogeneous focal spot. Data extracted from [Dover, 2017] and [Noaman-ul Haq et al., 2018].

At the Laboratory for Laser Plasmas (LLP) in the Shanghai Jiao Tong University, a focal spot scan was conducted with a 200 TW laser system on a video home system (VHS) tape target with a thickness of 15 μm [Noaman-ul Haq et al., 2018]. A similar scan was conducted at the J-KAREN-P 1 PW (30 J, 30 fs) laser [Dover, 2017]. The results are displayed in figure 4.4. For J-KAREN-P $E_C(I_r) = 5.6 \cdot I^{0.23}$ and the LLP data can be fitted with $E_c(I_r) = 2.0 \cdot I^{0.26}$. These data sets agree with each other with only very small

deviations. The change in E_c caused by intensity variations is therefore proportional to $I^{0.25(1)}$. If this is compared to the scaling with the energy one arrives at:

$$E_c(I,E) = I^{0.25} \cdot I^{0.33} = I^{0.58} \approx \sqrt{I} \tag{4.4}$$

Which is close to the $\sqrt{I}$ scaling often described when intensity and energy are simultaneously increased. The third parameter that has to be investigated is the pulse length. For J-KAREN-P and at LLP pulse duration scans were conducted as well from 30 to 280 fs for the former and from 24 to 930 for the latter. The results can be seen in figure 4.5.

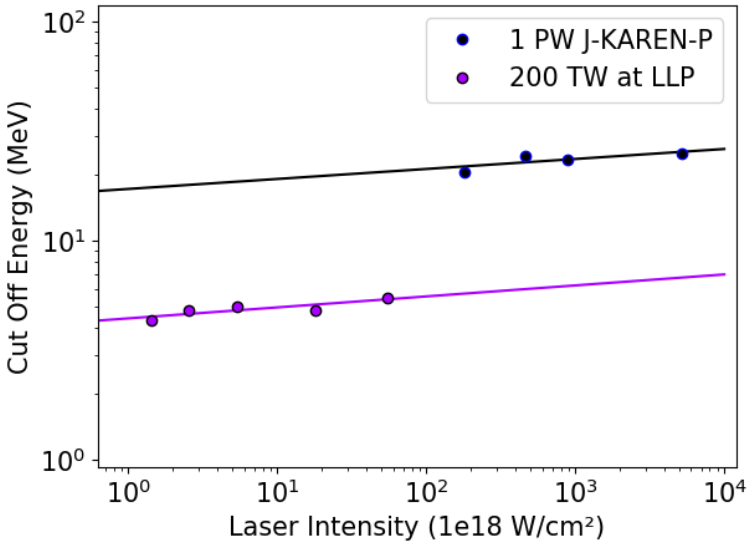

Figure 4.5: Scans in intensity via a variation of the laser pulse length τ_{laser} with a 200 TW and a 1 PW laser [Dover, 2017][Noaman-ul Haq et al., 2018]. The black fit function is $17 \cdot I^{0.046}$ and the purple function is described by $4.4 \cdot I^{0.050}$. Both lasers systems show a lower dependency on τ_{laser} than to the other parameters.

Both laser systems show a similar behavior for an increase in pulse length and therefore respectively decreasing the intensity. The J-KAREN-P cut off energies scale with $17 \cdot I^{0.046}$ and the LLP data follows a $4.4 \cdot I^{0.050}$ dependency. The difference in cut off energy is caused by the larger energy contained in the 30 J pulse. Those two experiments agree well with each other and the variations are in the uncertainty of the fit and from averaging multiple data points. From a comparison of the scaling caused by the pulse duration following a dependency of $\tau^{-1/20}$ with the influence of the energy $E_c(E_L)$ following $E^{1/3}$ it becomes apparent that the laser energy has a much higher influence on the ion acceleration than the pulse length.

The scans above were conducted between 30 fs and up to 1 ps. For longer pulse duration between 1 and 8 ps [Robson et al., 2007] has investigated how an increase in pulse length by constant intensity influences the cut off energy. This was done by proportionally increasing the laser energy up to 400 J. In this regime, no significant dependence can be seen from an energy increase and the cut off energies remain mostly constant.
The lower influence of the pulse length can be explained by the presence of competing processes inside the target. A decrease in intensity causes a lower laser ponderomotive potential [Fuchs et al., 2006][Mora, 2003] and therefore a drop in the electron temperature. On the other hand, longer laser pulses have shown to reduce the reflectivity on the target surface [Fourmaux et al., 2013] which increases the conversion efficiency. In addition, electrons can recirculate more often inside the

target for longer pulses, increasing the electron temperature. For short pulses, the acceleration time is limited through the shorter pulse duration causing lower cut off energies.
For these two laser systems mentioned above, positive and negative influencing processes mostly cancel out each other leaving only a weak dependence on the pulse duration. The influence of these effects has been discussed by [Daido et al., 2012] and [Flacco et al., 2010] and optimum pulse lengths between 100 and 200 fs have been proposed for most efficient acceleration [Fuchs et al., 2006]. It has to be noted that [Flacco et al., 2010] did see a larger increase in cut off energy with shorter pulse lengths and thin targets for a 250 mJ laser operating between 10^{18} W/cm^2 and $4{\cdot}10^{19}$ W/cm^2. This indicates that these parameters do have a degree of freedom for different systems.

The cut off energy is one important aspect but the total number of protons N_P is of equal importance. This number depends on the conversion efficiency η_L of the laser energy into the kinetic energy of the protons. With a higher η_L more protons can be accelerated. This also applies to the laser energy as the product $E_{\text{kin}} = \eta_L \cdot E_L$ defines the total kinetic energy of the protons. An increase in laser energy will simultaneously increase the electron and ion temperature. This causes that some of the increase in kinetic energy will be spend to shift the ion distribution to higher average energies. To estimate the impact of this effect the results of figure 4.3 can be used. It is known [Roth and Schollmeier, 2017] that the maximal electric field in the sheath and therefore E_c is proportional to the temperature. With

$$k_B T \sim E_c \sim E_L^{1/3} \tag{4.5}$$

one can estimate that at least two thirds of the laser energy are responsible for enhancing the number of accelerated ions rather than their energy. [Robson et al., 2007] investigated the conversion efficiency of laser energy to protons above 4 MeV for increasing E_L. The results are displayed in figure 4.6 (a) and a fit is applied. This indicates that $\eta_L(E_L) = 0.01 \cdot E_L^{1.1} + 1$ in between 30 J and 300 J. This would suggest a scaling of N_P in the range of $E_L^{1.8}$ to $E_L^{2.1}$ in this regime. To compare this result to data in the literature various experimental ion spectra were collected and the proton numbers above 4 MeV were integrated [Green et al., 2014] [Almomani,] [McGuffey1 et al., 2017] [Cianchi et al., 2018] [Gaillard et al., 2011] [Zepf et al., 2001] [Flippo et al., 2008a] [Flippo et al., 2008b] [McKenna et al., 2008]. The result is displayed in figure 4.6 (b).

For the laser systems with more than 50 J the red fit indicates a scaling with $E_L^{2.4(3)}$ which matches in the margin of error the theoretical expectations as well as the scaling found by [Brenner, 2012] with $N_P \sim E_L^{2.1(3)}$. As it is not known which prediction is the most accurate, further considerations will use the mean value between the theoretical prediction, the experimental scaling and the results of [Brenner, 2012] which is:

$$N_P \sim E_L^{2.1(3)} \tag{4.6}$$

For the data points in blue, these findings do not match and show only a linear scaling with $E_L^{1.2(3)}$. This is likely to be connected to the usage of smaller focal spots and therefore higher relative intensities at laser facilities that have only a small pulse energy. Also, these lasers often have a smaller pulse width to additionally increase the intensity. For an adequate result of laser ion scaling such a measurement would have to be performed at a single laser system. Besides that, it is expected that the conversion efficiency drastically drops for lower energies and intensities as a_0 approaches 1 [Fuchs et al., 2006].

Table 4.1 displays all scaling parameters that have been found in this chapter. For maximizing E_c and N_P the laser energy hast to be chosen as high as possible with a minimum focal spot size. This can be done

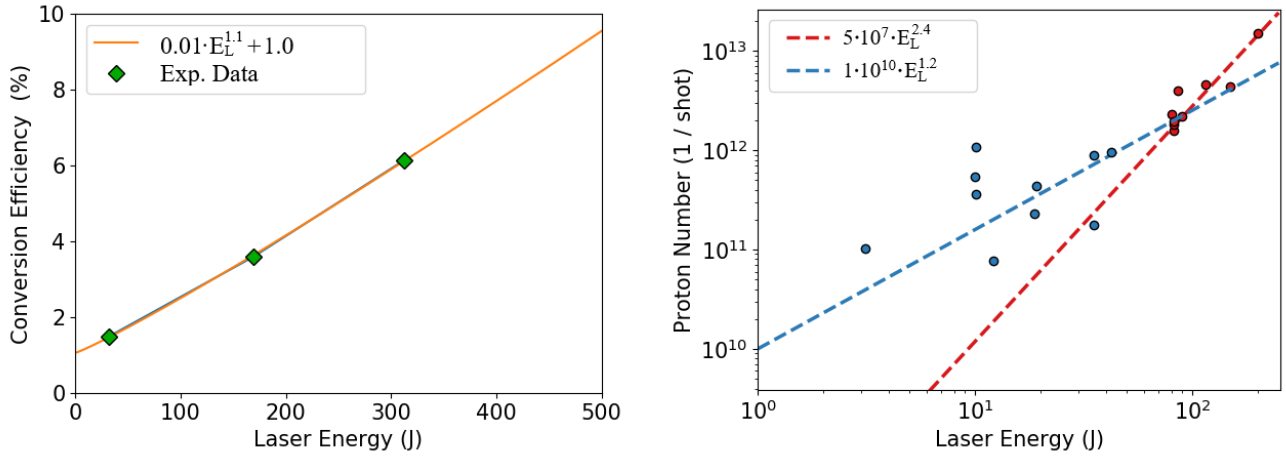

(a) (b)

Figure 4.6: (a): The laser conversion efficiency into protons with energies above 4 MeV measured by [Robson et al., 2007]. This shows that an increase in laser energy causes higher conversion efficiency into protons proportional to $E_L^{1.1}$. (b) The variation of the number of accelerated protons with different laser energies. The blue dots are experiments with a laser energy below 50 J and they exhibit an almost linear scaling with $E_L^{1.2(2)}$. The red dots above 50 J show a stronger increase with $E_L^{2.4(3)}$.

Table 4.1: Summary of the scalings determined in this section. The first column indicates what part of the ion spectrum is affected by which laser parameter. The third column shows the exponent the ion parameter is scaling with in the form of A^b.

Ion parameter	Laser parameter	Dependency
E_c	E_L	1/3
E_c	τ	-1/20
E_c	r	-1/2
N_P	E_L	2.1

at the cost of the pulse length as this parameter has the lowest influence on the ion parameters as long as the intensity is above 10^{18} W/cm^2. An optimal pulse length for ion acceleration has been found by various sources to be around 100 to 200 fs [Fuchs et al., 2006] [Flacco et al., 2010]. For further research in this topic, the dependency of the pulse length and the radius have also to be determined for N_P.

4.2 Evaluation on Potential Target Systems

The choice of an adequate targetry system has a large impact on the performance of an LDNS. The target has to be thin enough to benefit from the effects of relativistic induced transparency, stable, possible to produce in large quantities and it has to be possible to be operated at a high repetition rate. Besides that, it needs to be large enough to be reliably hit by the laser and the target system has to survive the laser impact. For high repetition rates, it is also important that the target is mostly debris free. Additionally an operation with protons as well as with deuterons should be possible. With this amount of limitations, finding a suitable system is not an easy task and therefore the most commonly used target systems are

introduced and evaluated on these conditions as well as on their technical readiness to find a suitable candidate.

4.2.1 Deuterated Polymer Foils

The state of the art target technology for current LDNS are deuterated polymer foils in the sub-μm regime. With these targets the PHELIX laser system was capable of producing $5{\cdot}10^{10}$ neutrons with a single shot reliably [Kleinschmidt et al., 2018]. These targets are produced by dissolving deuterated polystyrene in butanol and applying it via spinn-coating to a flat silicon wafer. With a variation in rotation frequency and polymer concentration in the solution the thickness can be tuned. The polymer is separated from the substrate in a water bath and afterwards the polymer sheet is attached to the final target mount [Tebartz et al., 2016]. These steps are done manually and are time intensive. In addition to that, they have to be characterized via white light interferometry to determine their thickness.

These typically between 200 to 800 nm thin targets are very efficient in ion acceleration [Wagner et al., 2016] but require a high contrast of the laser system [Wagner, 2014]. For most experiments, these targets are exchanged by hand and are replaced after each shot. This procedure requires opening the vacuum chamber and typically takes between 30 minutes to an hour.

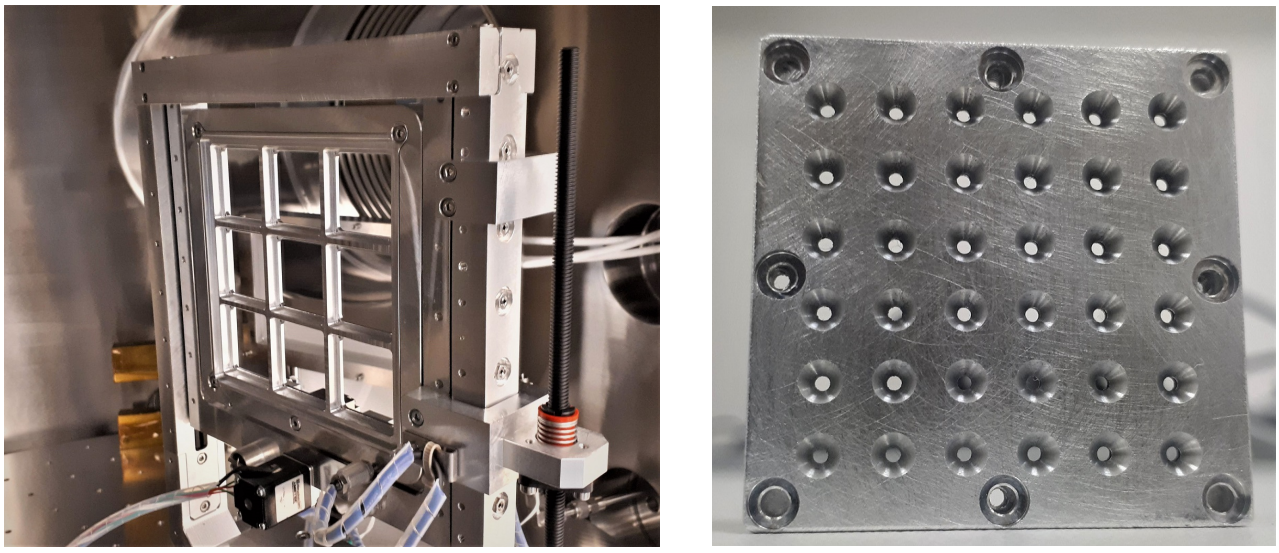

(a) (b)

Figure 4.7: (a): Target array holder at the ELI Beamlines facility. In every free spot, an array (b) with 36 targets can be placed. The array holder is designed in a way that the expanding plasma after a shot can not damage neighboring targets. The holder is motorized and can place every target into the laser focus position between shots. The focal positions have to be recorded prior to the laser operation. In this manner, up to 324 consecutive targets can be shot without opening the vacuum chamber.

A more elegant solution is attaching the target foil not to a single target holder but to a target matrix. This matrix is a holder with many recesses as seen in figure 4.7 (b) where each hole is functioning as a single target. A prerequisite of this method is the protection of neighboring targets from debris and shock waves during a shot which could disturb the integrity of the thin foils. A solution to this problem is covering the front and the back of the target with a mask that only allows debris to move forward and backwards leaving neighboring targets unharmed. Another advantage of this method is that the polymer

foil can be floated on the entire matrix at once, eliminating the need to repeat this process for every target individually.

The target alignment to the laser focus spot has to be done automatically to be able to operate at high repetition rates. Therefore a fast movable final focusing diagnostic is required that can record the position of every target relative to the laser focus in advance via image recognition software. With this information and multiple precise motorized stages, it is possible to move a new target into the focus without human intervention.

The temporal separation of target production and experiment makes foil and array targets optimal for experimental campaigns at other facilities that are not solely dedicated for neutron production as these targets work reliably. Another advantage of these targets is the possibility of fabricating them with relatively low effort down to 100 nm with a very small surface roughness [Tebartz et al., 2016]. This enables to operate ion acceleration at the onset of the relativistic transparency to gain higher ion energies. On the other hand, targets with such a small thickness require a very high contrast of the laser, otherwise, shock waves and pre-expansion from the pre-pulse could mitigate the acceleration and lead to lower cut off energies and lower ion numbers [Kaluza et al., 2004].

Installing and positioning a foil array has a rather low degree of complexity. This is the result of two traits of the foil targets. First, the laser focal spot diameter ($< 10\,\mu$m) is much smaller than the target surface (> 1 mm) and therefore small fluctuations or misalignment in the x-y plane are negligible. The second trait is high stability in laser forward direction due to the absence of freely moving parts inside the metal matrix. The position of the target is controlled by high precision stages leaving only a small degree of freedom in this direction that is typically smaller than the Rayleigh length of the laser. Another benefit of this type of targets is, that they are solid and therefore vacuum compatible and do not drastically impair the chamber vacuum before or during a shot.

Although there are many advantages for this type of target, there are also downsides to this technology. First of all, solid plastic targets produce more debris than liquid targets and the debris is often in the form of molten polystyrene which coats nearby optics and parts of the final focusing parabola. This reduces the performance over time. The debris can be removed by submerging the optics in an acetone solution but this requires frequent maintenance. Another disadvantage of these targets is the inevitable contamination with water vapor and hydrocarbon residues on the rear target surface which will act as a proton source during acceleration. If the main goal is the acceleration of deuterons, these protons are reducing the electric field experienced by the deuterons and therefore reducing their cut off energy as well as total deuteron numbers.
Although the use of arrays instead of single targets increases the number of shots that can be taken in a row, this number is still limited. In figure 4.7 an array holder is displayed that has space for up to nine arrays with 36 targets each. With a repetition rate of 1 Hz the entire target holder has to be replaced after 5 minutes. This would drastically improve the statistics of current laser neutron experiments, but for continuous operation this repetition rate is still to low. Venting the target chamber, replacing the array holder and restoring the vacuum takes approximately an hour, with 12 hours of operation per day, this target type could produce up to $4{\cdot}10^{13}$ neutrons per day if a yield of $5{\cdot}10^{10}$ neutrons per shot is assumed. The current state of the art of production for these target types is manual fabrication and the time for fabrication and characterization can be estimated to be between 10 minutes to 1 hour, depending on the available infrastructure. This would result in between 18 to 108 working hours for target preparation for every day of operation. With this information, it is possible to say that arrays might be a viable solution for experimental campaigns through their easy implementation in existing infrastructures but are impractical for commercial applications.

4.2.2 Tape Target

Overcoming the limit of matrix targets, it is possible to utilize VHS tape for a TNSA target as proposed by [Noaman-ul Haq et al., 2017]. These tapes consist of 15 μm thick Mylar with embedded iron oxide particles and are placed on two spools as seen in figure 4.8. In between the spools, the tape is unwrapped and fixated in position by four highly polished stainless steel bolts and can be targeted by the laser.

The fluctuations in position in laser forward direction reported by Noaman-ul-Haq are $\sigma = 14\,\mu$m. Comparing this with the results from the focal scan in figure 4.4, it is possible to say that these fluctuations in position are acceptable for most lasers. Similar to foil targets, the pointing stability in transverse directions is negligible since the tape is many orders of magnitude larger than the laser focus. The surface roughness of these targets is rather small with 168 nm peak to valley variations, minimizing shot to shot variations. [Noaman-ul Haq et al., 2018] conducted their experiment at 0.2 Hz. With 1.4(0.3) J in 25 fs on a 6 μm FWHM spot, they achieved cut off energies of 5.9(0.3) MeV which is in good agreement with figure 4.3. Similar experiments were conducted at BELLA [Bulanov et al., 2019] using aluminum foil as a target. The advantages of using Mylar instead of aluminum are the higher tear resistivity of Mylar and a smaller Electro Magnetic Impulse (EMP) is created by the use of non-metal targets [Noaman-ul Haq et al., 2017].

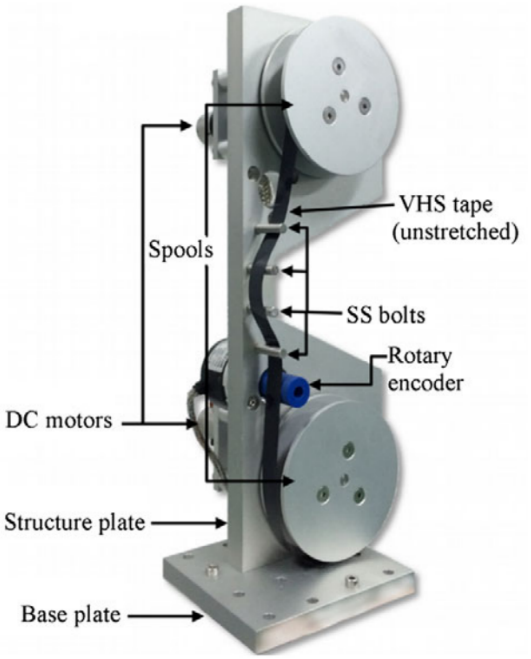

Figure 4.8: Tape target setup from [Noaman-ul Haq et al., 2017] for ion acceleration. A VHS tape is uncoiled from one roll, and recoiled to another, serving as a TNSA target in between.

The main advantage of this system is its simplicity. VHS tape can be cheaply bought up to 400 m in length. Estimating a minimum shot distance on the tape of 2 to 5 cm, a single VHS tape could last in between 8000 and 20000 shots. This would be an equivalent of 2 to 5 hours of operation time at 1 Hz. For larger high repetition rate neutron sources the tape could be bought directly from the manufacturer at any given size. A 40 cm diameter roll, which easily still fits into the target chamber, can hold up to 9 km of target tape and would last between 50 to 125 hours at 1 Hz. The speed required for the target to move is similar to the speed of VHS tape inside a video recorder on the order of cm/s. Higher repetition rates would increase the stress on the tape but this could be counteracted by using wider tape or increasing the distance between shots on the tape to avoid an accumulation of damage at nearby areas.

The limits of this target are estimated to be on the order of several 10s of Hz when the mechanical stress from the high velocity between the steel bolts and the tape is getting to high and leads to deformations of the target [George et al., 2019]. This limit is yet not found and has to be investigated experimentally.

The downsides of this type of targets are linked to the thickness and composition of the material. With 14 μm the target is too thick for benefiting from effects of relativistic transparency and therefore lower ion energies are expected. A possible solution could be switching to a more durable material that can be produced in thinner layers. an LDNS based on this target thickness would need less restrictions on the contrast as discussed in section 4.12 opening financial resources that could be invested in a higher laser

energy to compensate for the increased thickness.

Since the tape is not deuterated, mostly protons and carbon ions are accelerated with these targets. Fabricating the entire film out of deuterated Mylar would drastically increase the price of this target and would also limit the range of manufacturers capable of producing this film. Since most of the film is not used as target but as structural support material, this would also be a very inefficient use of deuterated material.

To overcome this problem, it would be possible to evaporate heavy water on the rear side of the tape directly before a shot, to create a deuterated contamination layer. This could be done by a combination of short synchronized spray pulses and differential pumping installations directly after the first spool.

The increased target thickness will contribute to the production of debris. Similar to foil targets, the liquified Mylar will coat surrounding optics and the target chamber so that regular maintenance is required.

4.2.3 Cryogenic Jets

A possible option to minimize the debris is to use a laminar jet of cryogenic hydrogen as a target material. The benefit of these jets is that they can theoretically operate without interruption as long as they have a sufficient supply of hydrogen and liquid helium as coolant. Using a deuterium jet provides a pure D^+ beam without the contamination protons that reduce the acceleration efficiency in solid deuterated foil targets. The low electron density of liquid hydrogen with $5{\cdot}10^{22}\,\mathrm{cm}^{-3}$ is closer to the critical density of modern lasers around $10^{21}\,\mathrm{cm}^{-3}$ and therefore the absorption of the laser energy is enhanced. Also the onset of relativistic transparency is reached with lower laser intensities [Kim et al., 2016]. This can lead to a more efficient acceleration of protons and deuterons with higher energies. In the curse of this thesis, a participation at an experimental campaign at the Texas Petawatt laser was performed to evaluate the applicability of this source type at an LDNS. The gained insights are included into the following assessment of publicly available information.

The cryogenic hydrogen jet works by cooling H_2 or D_2 down to temperatures between 17 and 24 K [Gauthier et al., 2016] [Kim et al., 2016] inside a cryostat by the usage of liquid helium to regulate the temperature. Once the hydrogen is liquefied it is forced through a nozzle aperture that defines the jet shape. An image of the jet and a laser shadowgraphy can be seen in figure 4.9 to illustrate the working principle. Experiments with cylindrical jets from 5 to 10 μm as well as rectangular jets with up to 2x40 μm have been conducted [Gauthier et al., 2016]. To prevent the aperture and the source from damage, the laser is focused between 1 and 2 cm below the nozzle of the jet. At this distance the spatial jitter is around 4 to 10 μm depending on the nozzle and other jet parameters. The cylindrical jet of [Gauthier et al., 2016] has accelerated ions with a 140 J and 700 fs laser pulse to slightly below 2 MeV which is comparably low to other experiments. The most likely reason for this is, that a cylindrical geometry accelerates TNSA ions in 360 degrees instead of the $\pm 30°$ common for flat targets and therefore reducing the fast ion numbers below the threshold of detection. Besides that, with a 10 μm target and a 13 μm FWHM focal spot, a significant amount of laser energy is missing the target.

To prevent this, planar jet targets are preferred since the flat rear surface provides an increased forward ion emission. The downside of these small 2-4 μm thick slits is that they are prone for clogging from small particles inside the system as well as from debris produced during the laser plasma interaction.

Additionally, impurities inside the hydrogen gas like microscopic water crystals or other elements can block the slit. This blockage can also be caused by freezing hydrogen as it enters the vacuum and experiences evaporative cooling, which reduces the hydrogen temperature below its freezing point. Warming up and exchanging the nozzle and cooling down again takes in between 3-4 h and therefore the entire system has high purity and cleanliness standards.
Another point that has to be noticed is that laser ion acceleration requires high vacuum conditions and with a liquid hydrogen jet firing into a vacuum, evaporation will take place. This effect will be especially large with the planar jets that have a larger surface area than cylindrical jets of a comparable size. [Goede, 2019] measured the gas flow and the vacuum pressure for different jet diameters. At their target chamber a 2 μm jet required a gas flow rate of 12 SCCM and was operated at $5{\cdot}10^{-5}$ mbar. In contrast to that, the 20 μm jet had a drastically increased gas flow rate of 1200 SCCM at a vacuum pressure of $5{\cdot}10^{-3}$ mbar. This additional gas has to be removed from the vacuum chamber to maintain a vacuum sufficient enough to operate the jet at stable conditions and not to contaminate the laser compressor with hydrogen. This requires high pumping power and differential pumping between the target chamber and the compressor.

With the decreased density a hydrogen jet becomes more susceptible to pre-pulses and requires the usage of a plasma mirror [Kim et al., 2016]. This will decrease the laser energy reaching the target and counteract the benefits of the lower density to a certain degree. Also, plasma mirrors have to be replaced frequently since every shot requires an undisturbed area on the mirror. Since this requires direct access to the target chamber, additional warming up and cooling down time of the nozzle is required.

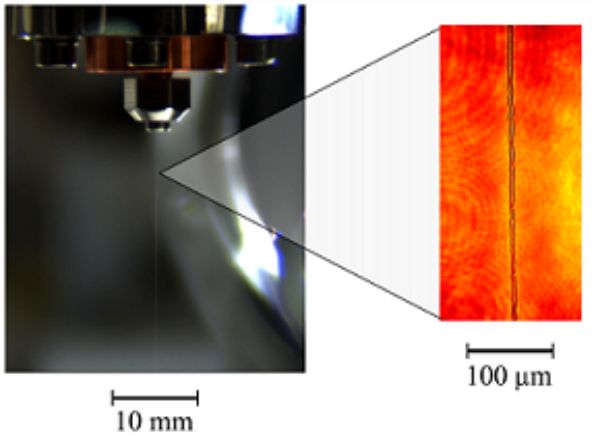

Figure 4.9: Image (left) and laser shadowgraphy of the cryo jet developed by [Kim et al., 2016] at SLAC. With different nozzles a variety of jet widths ranging from 5 to 40 μm can be produced with thicknesses down to 2 μm

Cryogenic hydrogen jets require, depending on the aperture, a specific combination of chamber pressure, hydrogen temperature and hydrogen pressure which has to be maintained to prevent the jet from moving, becoming unstable or breaking up into a spray. Poor thermal conductivity or insufficient insulation can cause parts of the system to change their temperature over time, moving this stable operation point in the phase space. Therefore it is beneficial to monitor the temperature of the jet source at several positions as well as probing the position of the jet at all times. For solid targets, the position in relation to the focal spot of the parabola can be determined from the forward direction by a single focal spot diagnostic which is replaced by the catcher during shot operation. For jets with their ability to move around during operation, the position and orientation have to be monitored from several directions simultaneously. This can be done with simultaneous laser back-lighting from ±45°and 90°degrees to the laser direction. While this technique is proven [Obst et al., 2017] it adds additional complexity to the system and reduces space inside the target chamber.

The comparable size of the focal spot to the target diameter imposes high requirements on the laser pointing stability. For a 2x20 μm jet and a 12 μm FWHM diameter spot, the fluctuations in the direction transversal to the jet should be below 7 μm RMS to maintain in the flat part of the jet. Larger fluctuations lead to a decreased ion acceleration or a complete miss of the jet. A solution to this problem was

developed by [Kraft et al., 2018] who have constructed a solid hydrogen ribbon with 1 mm width and a thickness down to 50 μm. This was done by cooling the hydrogen down to its triple point at 14 K inside a reservoir and heating the upper part, causing the pressure to rise over 100 bar inside the reservoir. This pressure was then used to force the solid hydrogen in the lower part through a nozzle which is giving the ribbon its dimensions. They managed to accelerate protons up to 14 MeV with a 350 fs and 8 J laser pulse. The same system was able to accelerate 18 MeV protons from a 10 μm gold target. It can be expected that future iterations with an even thinner ribbon will get to higher energies as they approach the regime of relativistic transparency acceleration.

A major problem with cryogenic jets is maintaining the integrity of the nozzle during the shot. During the beamtime at the Texas Petawatt laser with laser energies around 120 J the nozzle that defines the jet shape was damaged after every shot. This requires a manual replacement after each shot and defeats the purpose of a high repetition target. The working hypothesis is, that the nozzle is either destroyed by high electron currents flowing towards the laser plasma or from the shock wave propagating inside the jet towards the nozzle. A combination of both effects is also likely. This problem has not been solved yet for high power lasers with energies above 100 J but [Obst et al., 2017] reported in an experiment at the DRACO laser efficient proton acceleration up to 20 MeV with a repetition rate of 1 Hz. This experiment was conducted with 2.6 J in 30 fs shooting at 1.5 cm below the nozzle. This is approximately two times higher in ion energy than other experiments with similar laser energies as seen in figure 4.3. Operating this target at low laser energies solves two problems simultaneously. First, less energy is contained inside the pre-pulse and therefore no plasma mirror is necessary [Obst et al., 2017] but cut off energies are reduced on average in this case. Second, the low energy reduces shock waves as well as the current formations to a level that can be tolerated by the nozzle. Future experiments require a laser energy scan to determine the threshold for the durability of these target systems.

For higher laser energies several approaches have been proposed to prevent the nozzle from damage. The most common two are either cutting the jet shortly before the shot with a chopper fan or with a comparably low power laser [Rehwald, 2019]. The idea behind these approaches is to interrupt the direct connection between laser plasma interaction and the nozzle by physically cutting the jet. The chopper in addition blocks the direct line of sight and preventing debris from damaging the nozzle. With this method [Rehwald, 2019] successfully shot a cryo-jet with 23 J in 30 fs with ion energies consistently above 25 MeV and with selected shots reaching up to 50-60 MeV. The usage of the chopper enabled them also to shoot at 10 mm from the nozzle instead of 20, increasing their hit probability from 30 % to 90 %.

With these latest results the usage of a cryogenic jet might be promising for low energy, high-intensity laser systems like DRACO or GEMINI. Such systems could be increased in repetition rate in the 10 Hz to 10 kHz range to compensate for the low energy [Siders, 2018]. Up to date, these sources still have to prove their applicability for high energy laser systems. Further development is currently done by several groups around the globe to solve this problem [Gauthier et al., 2016] [Schnürer et al., 2005] [Rehwald, 2019]. The main arguments against this target type for an LDNS is the high degree of complexity and the early development stage. The cryogenic temperatures, the narrow target width, the nozzle damage, the susceptibility to pre-pulses and to nozzle clogging are all vulnerabilities to a continual operation. Each of these problems can be solved individually but a favorable approach would be the usage of a target system with a lower complexity and a higher technological readiness.

To overcome the main difficulties of cyo-jets, the low temperature and the small target diameter, it is possible to operate liquid jets or synchronized droplets with water or ethylene glycol at room temperatures as it has been demonstrated by [Vinokhodov et al., 2016] and [Hah et al., 2016]. This part will focus on the colliding leaf target system as it is used by [Morrison et al., 2018]. In this setup, two ethylene glycol jets collide at an angle forming a liquid leaf. This leaf is $\approx 0.5\,\text{mm}$ wide and its thickens reaches from $2\,\mu\text{m}$ down to 500 nm depending on the position at the leaf. This very thin but comparably wide target has a high stability of $2\,\mu\text{m}$ in focal direction. This enables a significantly higher hit rate as well as an increased shot to shot reproducibility due to less influence of the laser pointing stability.

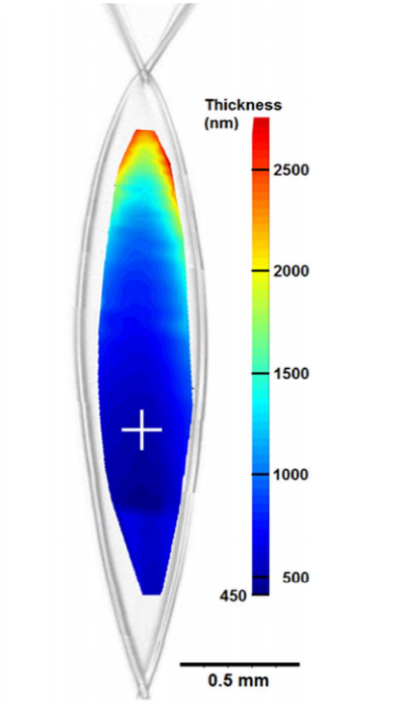

Figure 4.10: Shadowgraphy and thickness of the liquid leaf target. Two colliding $30\,\mu\text{m}$ thick ethylene glycol jets form a 0.5 mm wide liquid leaf that can be used as a target. Figure adopted from [Morrison et al., 2018].

The experiment conducted by [Morrison et al., 2018] used a high repetition kHz laser system with $5{\cdot}10^{18}\,\text{W/cm}^2$ via 5 mJ on target in 40 fs with a $1.8\,\mu\text{m}$ FWHM focal spot and were capable of producing up to 2 MeV protons with a reported conversion efficiency of 0.5 %. The usage of ethylene glycol allowed continuous operation of the jet at $2.7{\cdot}10^{-2}\,\text{mBar}$ inside the vacuum chamber and at $5.3{\cdot}10^{-2}\,\text{mBar}$ during kHz shot operation. This was possible through the 320 times lower vapor pressure of ethylene glycol in comparison to water and through the usage of a drainage system that collects the liquid from the jet and transports it into a separate collection tank.

Investigations for a maximum repetition rate were conducted by [George et al., 2019] under the same laser conditions as mentioned earlier and estimated an upper repetition rate of 10 kHz could be reasonable. For higher energies that are capable of damaging the nozzle, the usage of a chopper or a disruptive laser pulse has to be considered. Disrupting the leaf at its formation point with a leaf flow velocity of 16 m/s [Morrison et al., 2018] it would take 1.5 ms to fully recover the entire leaf with a length of 2.5 cm. This enables an upper repetition rate of around 650 Hz for this system if a chopper is necessary. An interruption in the middle of the leaf, aiming at higher positions or using a smaller leaf could increase this repetition rate to at least 1 kHz.

According to these results, ethylene glycol liquid leaf jets represent a debris free, sub μm, self-renewing target system for operation up to 1 kHz respectively 10 kHz depending on the laser parameters. The usage of ethylene glycol instead of pure hydrogen will quite likely reduce possible cut off energies [Kim et al., 2018] but the lower target thickness can compensate for that. The main benefit is the drastic reduction in complexity of the setup by not using cryogenic components and therefore removing potential vulnerabilities and delays related to that. The nozzles for the liquid leaf jet have a diameter of $30\,\mu\text{m}$ in comparison to the $2\,\mu\text{m}$ reported by [Goede, 2019] and are much less likely to be clogged by small particles.

4.2.5 Influence of Target Thickness and Pre-Pulses

As different target systems were discussed earlier the impact of target thickness was pointed out. This parameter can significantly affect the acceleration process but the manner of its interaction demands further explanation. During the TNSA process, electrons are heated at the critical density and accelerated to the rear surface where the electron sheath is produced. Partly hot electrons are reflected at the Debye-sheath formed at the rear side and propagate back to the front surface. Back at the front, the electrons can be heated again by the laser and further increase the hot electron temperature [Mackinnon et al., 2002] [Neely et al., 2006]. The time for this re-circulation is depending on the target thickness and thinner targets allow more re-circulations during the laser pulse.

In figure 4.11 the left plot shows thickness scans from different experiments collected by [Poole et al., 2018]. For this plot, cut off energies were compared to the target thickness in the regime free from pre-pulse triggered degradation of the ion beam. Every data set was fitted with the function $E_{max}(d) = A/d^b$. For experiments 1 - 3 [Neely et al., 2006] [Ceccotti et al., 2007] [Dollar et al., 2013] with laser energies ranging from 0.3 J to 1.3 J the dependence scales with $d^{-0.21(2)}$ and for 4-6 [Zeil et al., 2010] [Mackinnon et al., 2002] [Green et al., 2014] with $E_L = 10(3)$ J with $d^{-0.43(5)}$. A similar difference in scaling effects in these energy regions has been observed in figure 4.3 and has to be further investigated at a laser with a high repetition rate to complement this parameter scan. A possible connection could be the higher absorption efficiency for increasing laser energy changing the dynamics of the hot electrons inside the target. The increase in cut off energy with decreasing target thickness is accompanied with an increase in conversion efficiency observed by [Neely et al., 2006] as it can be seen in figure 4.11 (b) (green). For this 0.3 J, 33 fs laser system with 10^{19} W/cm^2 the conversion efficiency increased approximately one order of magnitude by reducing the thickness from 10 μm to 100 nm. This increase in conversion efficiency followed a proportionality of $d^{-2/5}$. It is clearly visible that the increase in conversion efficiency η is strongly correlated to the ion temperature with $\eta \sim T_p^2$.

Reducing the target further in thickness, the ion temperature and conversion efficiency as well as cut off energy decrease again. This is the result of shock waves, caused by laser pre-pulses or the ASE pedestal, propagating through the target and causing perturbations at the rear surface. This creates a plasma on the rear side with a large plasma scale length reducing the acceleration effect from the hot electrons [Batani et al., 2010]. To avoid this effect, the target thickness d has to fulfill:

$$d > \tau_p \cdot \sqrt{\frac{\gamma+1}{1}\frac{P_S}{\rho_0}} \tag{4.7}$$

with the adiabatic constant of the material γ, the time gap between pre-pulse and main pulse arrival τ_p, the initial density ρ_0 and the shock pressure

$$P_S(Mbar) = 8.6\left(\frac{I}{10^{14}}\right)^{2/3}\lambda^{-2/3}\left(\frac{A}{2Z}\right)^{1/3} \tag{4.8}$$

with the intensity I in W/cm^2, the laser wavelength in μm and the atomic weight A as well as the atomic number Z of the shocked material [Batani et al., 2010]. Considering this equation, the minimum thickness is only weakly depending on the intensity with $I^{1/3}$ but is directly proportional to the time delay between the arrival of the pre-pulse and the main pulse. Consequently neither pre-pulses nor the rising edge of the laser pulse can exceed the threshold of 10^{10} W/cm^2 [Flacco et al., 2010][Batani et al., 2010] for generating a shock wave at grater times than τ from equation 4.7. It is reasonable to assume that

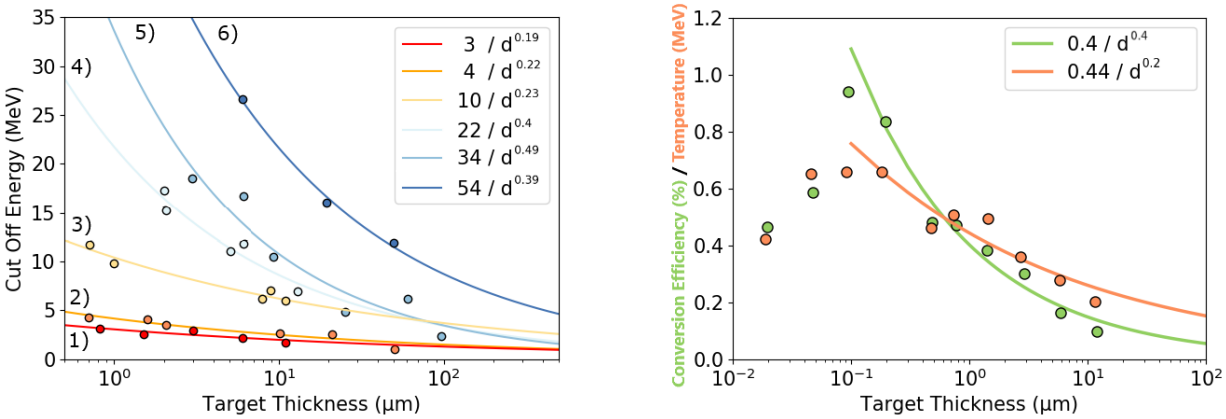

(a) Cut off energies without prepulse

(b) Cut off energies with prepulse

Figure 4.11: Left: Experimental cut off energies taken from [Poole et al., 2018] are plotted as a function of target thicknesses above 1 μm. Data points 1-3 are experiments ranging from 0.3 J to 1.3 J laser energy. Each data set is fitted and the cut off energy decreases $\sim d^{-0.21(2)}$ with the target thickness. Data sets 4-6 are from experiments with 10±3 J and the cut off energy decreases $\sim d^{-0.43(5)}$. Right: Conversion efficiency (green) and ion temperature (orange) as a function of target thickness. Both increase with thinner targets until an optimum is reached. For targets < 100 nm the laser pre-pulse is causing a decrease in both temperature end conversion efficiency.

ASE contrast and pre-pulse contrast have different limitations as the later ones contain much less energy than the ASE pedestal. For lasers that have small focal spot sizes and therefore reach high intensities, this limitation is strongest as pre-pulses increase proportional to the peak intensity. A laser system with 10^{22} W/cm^2 requires a contrast better than 10^{-12} to be able to shoot thin targets without disturbance from the shock wave.

A parametric study has been conducted by [Kaluza et al., 2004] while varying the ASE pedestal duration from 0.5 to 2.5 ns and scanning the cut off energies at different thicknesses as seen in figure 4.12 (a). Decreasing the thickness similar as seen in figure 4.11 (a) the ion energy increases with smaller thickness until an optimum is reached. For thinner targets equation 4.7 is no longer fulfilled and the shock wave is capable of propagating to the rear surface causing perturbations and an increase in the plasma scale length. With an expansion of τ this optimum is already reached at thicker targets. This limits the acceleration to lower ion temperatures and therefore smaller cut off energies as well as a decreased conversion efficiency. Since both factors have a negative influence on the neutron yield, a high contrast is crucial for laser neutron generation. The results of a 3 ps long pre-pulse with a peak intensity in the range of 10^{13} W/cm^2 arriving 1.4 ns before the main pulse at the PHELIX laser can be seen in figure 4.12 by comparing (b) and (c). Image (b) displays the proton imprint on a RCF from a beamtime at PHELIX in 2017. This shot was taken with a two orders of magnitude higher pre-pulse contrast on a 650 nm thick deuterated polystyrene target using 226 J of laser energy. The ion distribution is smooth across the film. For image (c), taken in 2018 also at PHELIX with similar target and laser parameters. The lower pre-pulse contrast of 10^{-7} damaged the target to a degree that the ion emission in the center was almost fully suppressed and a ring-shaped structure was formed. This drastic reduction in accelerated ions directly affects neutron production. Also since the fastest TNSA ions are usually in the center, the cut off energies were drastically reduced to 32 MeV instead of 68 MeV [Wagner et al., 2016] typical for these targets.

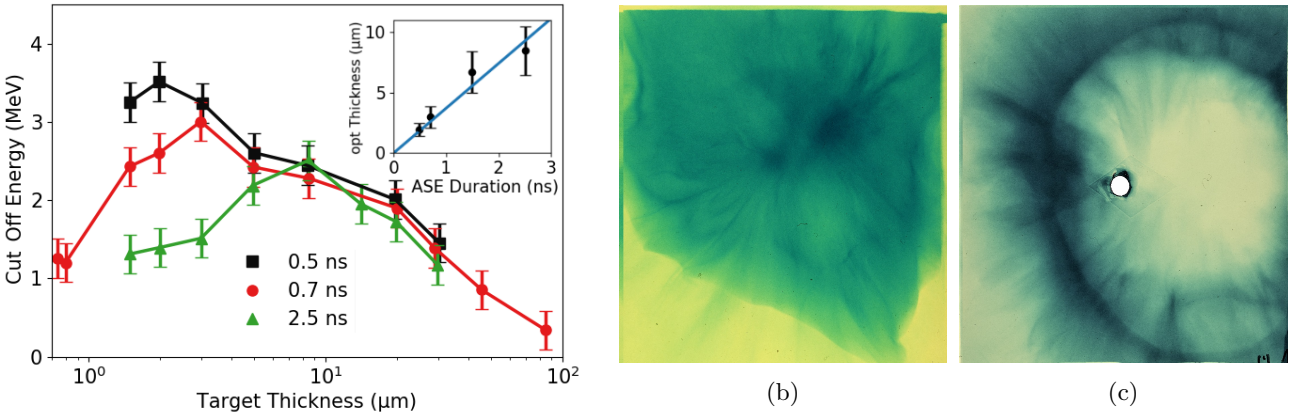

(a) (b) (c)

Figure 4.12: (a): Cut off energies as a function of target thickness for 0.5, 0.7 and 2.5 ns ASE pre-pulse duration. With increasing duration, the optimum thickness is reduced and therefor, the cut off energy as well. Data adapted from [Kaluza et al., 2004]. (b): TNSA ion imprint on Radio Chromatic Film (RCF) without a pre-pulse. This shot was taken at PHELIX on a 650 nm deuterated polystyrol target at a beamtime in 2017. (c): RCF film from a beamtime in 2018. A single 3 ps long pre-pulse with 10^{13} W/cm^2 at 1.4 ns before the main pulse was present at that time. The hollow ring indicates a strong perturbation in the center of the acceleration field at the rear surface.

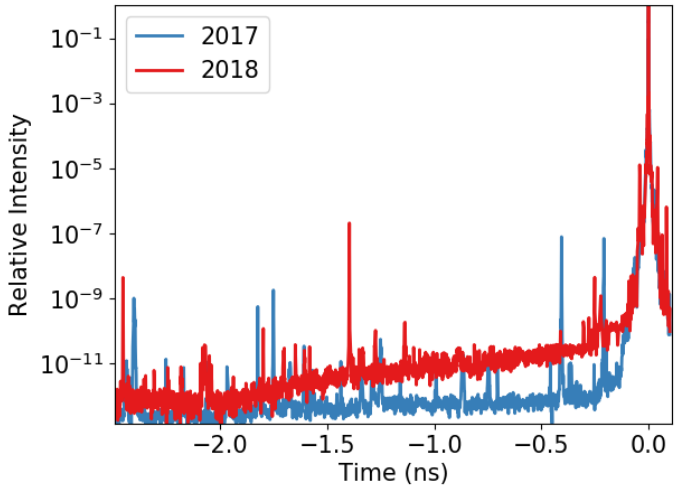

Figure 4.13: Contrast measurements at the PHELIX laser system using a third order cross-correlator [Schanz et al., 2017] for a neutron beamtime in 2017 and in 2018. In the latter experiment at 1.4 ns before the main pulse arrival a pre-pulse with a peak intensity on the order of 10^{13} W/cm^2 was detected which caused damage to the thin polymer targets and required switching to thicker silicon targets in the range of 25 to 50 μm.

In consideration of these results, it is recommended to use a sub-μm target with the lowest thickness possible that still satisfies equation 4.7 to have the highest neutron yield from the increase in cut off energy and conversion efficiency. For single-shot targets, this option will most likely be a thin foil array because of the low complexity and adjustable thickness. For high repetition rate targets, the referred target is a liquid leaf jet since it has a variable thickness on the leaf depending on the focal spot position and can be increased or decreased in thickness by changing the collision dynamics of the streams.

4.3 Catcher

The catcher is the central part of an LDNS and responsible for the neutron generation. It has to simultaneously guarantee a high neutron conversion rate while being able to withstand the irradiation from the hot laser plasma for extended periods of time without experiencing strong degradation. This section will discuss these requirements in detail in relation to the incoming ion spectrum.

4.3.1 Neutron Yield

The choice of the converter material is essential for an effective neutron generation. On the one hand, a high cross section for neutron producing reactions is required to increase the interaction probability, on the other hand, a low stopping power enables the incoming ion to interact with more nuclei on its beam-path. Besides the stripping and the break-up reactions discussed in section 2.4.1 there are a variety of other nuclear reactions contributing to the neutron yield. In figure 4.14 (a) the most contributing cross sections of deuteron impinging on beryllium are displayed.

It is visible that different energy regions have dominant contributing reactions. Below 10 MeV the stripping reactions are dominating the neutron production. For higher energies from 10 and 20 MeV the (d,n+α) reaction has the highest impact while above 20 MeV, the deuteron break-up prevails. The black curve is the sum of all neutron producing reactions weighted with the number of neutron produced in each reaction. These cross sections are taken from the TENDL2017 [Koning and Rochman, 2012] database and are not based on actual measurements as there is not a sufficient amount of deuteron data available, therefore they have to be treated with caution. A comparison between the ^{7}Li(p,n)^{7}Be cross sections from the TENDL2014 database with the ENDF/B-VII.0 database show a discrepancy of almost a factor of two. The large discrepancies for the different cross section libraries in combination with the low availability of experimental data concerning the neutron cross sections of Be and Li under deuterium irradiation caused a restriction of further investigations in this section to the effect of (p,n) reactions only.

Figure 4.14 (b) shows the scaled (p,xn) reaction cross sections for lithium, beryllium and vanadium. These three elements are all possible candidates for an effective neutron converter material. Lithium has the highest cross section with around 300 mb for low energies below 6 MeV and also the lowest reaction threshold energy of 1.88 MeV[Chichester, 2012]. For higher energies above 6 MeV the reaction cross section rapidly decreases to low 10s of mb. Beryllium has a higher threshold energy of 2.06 MeV and has only cross sections of 100 to 200 mb but for a much wider energy range up to 40 MeV. This enables ions with a much wider energy spectrum to contribute to the neutron production. Vanadium has only small neutron production cross sections below 100 mb until 15 MeV. After that, the cross sections are rapidly increasing mostly caused by the ^{51}V(p,6n)^{46}Cr reaction with up to 410 mb. The six neutrons produced by this reaction drastically boost the scaled (p,xn) cross section up to 2.46 b. According to their cross sections, the hypothesis can be made that lithium would be a good converter material for low energy protons while vanadium would be beneficial for highly energetic protons.

To investigate this further, the reaction cross sections have to be compared with the mean free path of the ions inside the material. As it is known from equation 2.27, the reaction probability depends on the product of the macroscopic cross section $\Sigma_{n_{tot}}(E)$ with the distance travelled inside the material L_{stop}. The distance an incoming ion can travel inside the catcher depends on the energy loss inside the material

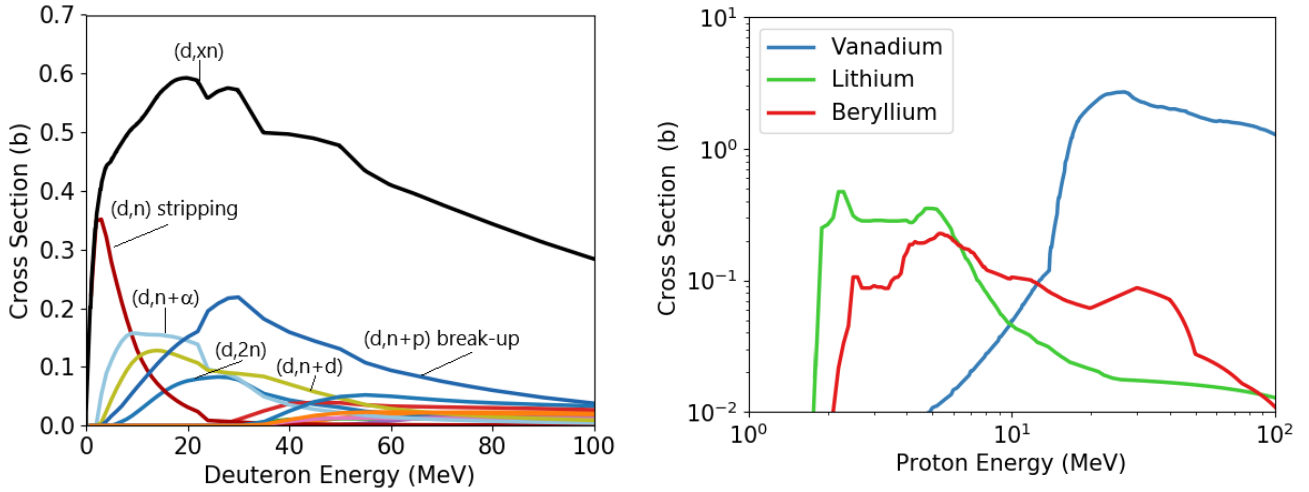

(a) (b)

Figure 4.14: (a) Neutron producing cross sections for different reactions of deuterons on beryllium. For different energies certain reactions are dominant. Below 10 MeV the stripping reaction dominates while above 20 MeV the break-up has the most significant impact. The black curve is the summation of all relevant cross sections scaled with the number of neutrons each reaction is producing. (b): The (p,xn) reaction cross sections for lithium beryllium and vanadium. These cross sections are also scaled for xn-reactions. Lithium has the highest cross section for energies below 6 MeV and has a lower threshold energy but for higher energies the cross section decreases rapidly. Beryllium has intermediate neutron production cross sections but for a wider range from 2.5 to 40 MeV. Vanadium has small cross sections below 15 MeV but has rapidly increasing cross sections mostly owed to a large ^{51}V(p,6n)^{46}Cr cross section of 0.41 (b).

$\frac{dE}{dx}$ which is described by the Bethe-Bloch formula. For intermediate energies in the range of 10s of MeV it can be written in the first order Born-Bethe approximation [Sugiyama, 1981]:

$$-\frac{dE}{dx} = \frac{4\pi Z_P^2 Z_T N e^4}{m_e v^2} \ln\left(\frac{2m_e v^2}{I}\right) \tag{4.9}$$

with the atomic number Z_P of the projectile and Z_T for the target material, the mean excitation energy I, the electron mass m_e, the particle velocity v as well as the atomic number density $N = A_v \cdot \frac{\rho}{M}$. ρ is the material density, M the nucleon number of the target and A_v the Avogadro number. Lithium with the lowest number density and Z = 3 has consequently the highest stopping range and vanadium with Z = 23 the lowest. The stopping ranges as a function of energy for all three elements can be seen in figure 4.15 (a). With the impact of the electronic stopping inside the converter, the ion energy constantly changes with its position. Therefore, for an accurate calculation of the neutron production, the neutron production probability has to be integrated over the entire track length L_{stop} until the ion reaches the threshold energy E_t. L_{stop} is calculated in the continuous slowing down approximation [Swift and McNaney, 2009] through:

$$L_{stop} = \int_{E_0}^{E_t} \frac{1}{\frac{dE}{dx}} dE \tag{4.10}$$

Where E_0 represents the initial ion energy and E_t is the threshold energy for neutron production. The probability of a (p,n) reaction at the energy E in the range from x to dx [Wilson et al., 2005] is given via:

$$N\sigma_n(E)dx = \frac{N\sigma_n dE}{\frac{dE}{dx}} \tag{4.11}$$

The probability over the entire energy range can be calculated:

$$p(E_0) = \int_{E_0}^{E_t} \frac{N\sigma_n}{\frac{dE}{dx}} dE = \int_{E_t}^{E_0} \frac{N\sigma_n}{\frac{-dE}{dx}} dE = \int_{E_t}^{E_0} \frac{N\sigma_n}{\frac{4\pi Z_p^2 Z_T N e^4}{m_e v^2} \ln\left(\frac{2m_e v^2}{I}\right)} dE \tag{4.12}$$

From this equation can be seen that the neutron production probability is independent of the number density N as it is present in the numerator and the denominator and therefore as well independent from ρ. This integral is not trivial to solve and therefore the Monte Carlo code PHITS [Tsai et al., 2018][Boudard et al., 2013][Iida et al., 2007] was used to calculate the neutron yield for different proton energies for all three elements. Through the unavailability of the corresponding lithium cross sections in the JENDL library commonly used by PHITS, the TENDL2017 [Koning and Rochman, 2012] database was used for all calculations to be consistent. As expected lithium has the highest yield at low proton energies until 15 MeV where the yield for all elements overlaps. At larger energies vanadium has the highest production of neutrons per incoming proton. The lithium yield above 15 MeV is the lowest which is likely caused by the decrease in cross sections for higher energies as seen in figure 4.15. The dashed lines are fits in the form of

$$N(E) = a \cdot E^b \cdot exp\left(-\frac{c}{E}\right) \tag{4.13}$$

The corresponding fit values can be found in table 4.2. For higher energies, the yield follows a proportionality of E^b but for lower energies, the shape of the cross sections and the threshold energy have a strong influence, which is corrected by the exponential term which converges towards 1 for multiple of

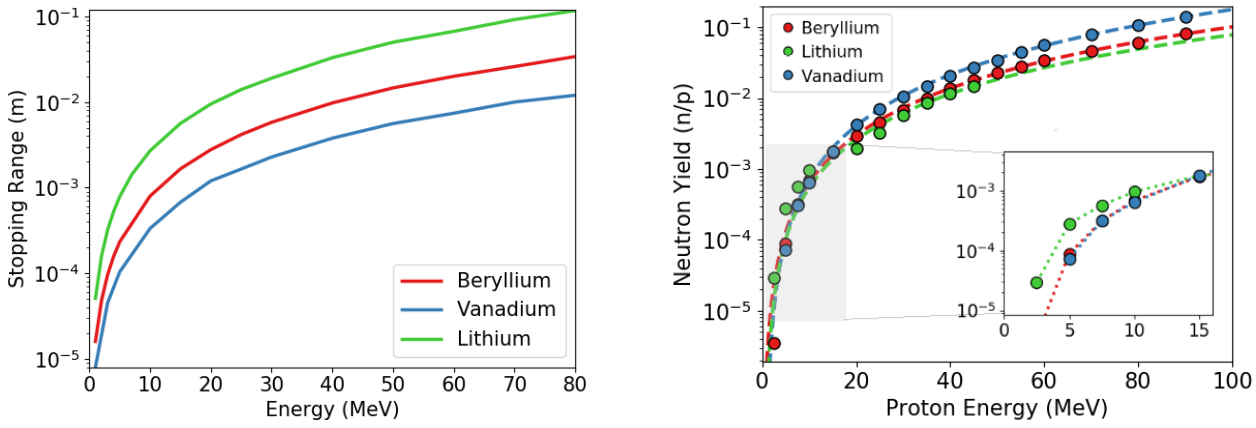

(a) (b)

Figure 4.15: (a) Stopping range of protons in lithium, beryllium and vanadium. With growing proton energy the stopping range drastically increases. Ranges were calculated with SRIM [Ziegler et al., 2010]. (b): PHITS simulation for the thick target neutron yield of mono-energetic protons using the TENDL2017 database. Dashed lines are fits to the data. They show good agreement for V and Be but do not match to Li below 20 MeV. Dotted lines in the zoomed area are interpolations to guide the eye.

c. A clear correspondence between the stopping range in figure 4.15 (a) and the neutron yield in (b) is visible. Vanadium compensates for its lower stopping range with the increased neutron cross sections at high energies. Higher energetic ions lose less energy per unit length than slower ones and therefore travel larger distances within a certain ΔE. High neutron production cross sections in this energy regime consequently have a larger effect than cross sections at lower energies.

Table 4.2: Fit values for the neutron yield from figure 4.15 (b). They describe the neutron yield as a function of particle energy in the form of equation 4.13. Lithium shows the lowest scaling with b =2.05 while vanadium scales with the highest value of b =2.25.

	a	b	c
Lithium	6.3e-6	2.05	2.7
Beryllium	4.8e-6	2.17	1
Vanadium	5.6e-6	2.25	3.7

4.3.2 Influence of the Ion Distribution on Neutron Generation

Protons with high energies have the largest neutron yield. If this is compared to the shape of a TNSA ion spectrum it is apparent that the ions with the highest energy have the lowest quantity. To study the impact of the incoming ions on the neutron production the influence of the spectral distribution has to be integrated into this calculation. This means that the number of ions/MeV has to be convoluted with the neutron yield for each energy over the entire spectrum to get a prediction on how much neutrons are produced.

In figure 4.16 a proton spectrum from PHELIX [Wagner, 2014] is displayed by the red triangles. Ions produced by laser ion acceleration follow a Maxwellian distribution caused by the hot electrons in the sheath. For many laser ion acceleration experiments it is possible to observe two different temperature distributions inside the spectrum, caused by hot electrons in the beam center and colder electrons at outer regions [Brauckmann, 2018]. The colder distribution contains on average one order of magnitude more ions than the hotter distribution. In figure 4.16 (a) the temperature fits can be described by:

$$P(E) = A \cdot \sqrt{\frac{8m}{\pi}} \cdot \left(\frac{1}{E_T}\right)^{3/2} E \cdot \exp\left(-\frac{E}{E_T}\right) \tag{4.14}$$

With a scaling factor A and the ion temperature E_T. For the orange curve the fit parameters are $A = 1.3{\cdot}10^{19}$ and $E_T = 1.33\,\text{MeV}$. The blue curve is described by $A = 1.15{\cdot}10^{18}$ and $E_T = 8.8\,\text{MeV}$. The yield function from figure 4.15 (b) for beryllium is used to convert the ion distributions from (a) to a neutron yield for each energy in (b). It is clearly visible that the impact on the neutron yield from the ions with the lower temperature distribution is much smaller even though their particle numbers are one order of magnitude higher than for the distribution with a temperature of 8.8 MeV. The highest impact for this ions spectrum is from protons between 20 and 40 MeV. This maximum depends on the spectral shape and is a direct consequence of the ion temperature. A comparison between the temperature and the particle numbers in the spectrum shows that the temperature has a by far grater impact on the produced neutrons than the absolute numbers.
For maximizing the neutron gain the preferable option is to increase the ion temperature. To measure this quantity is not always simple as often more than one temperature is present or no continuous spectrum is available to fit the temperature. This problem can be evaded by linking

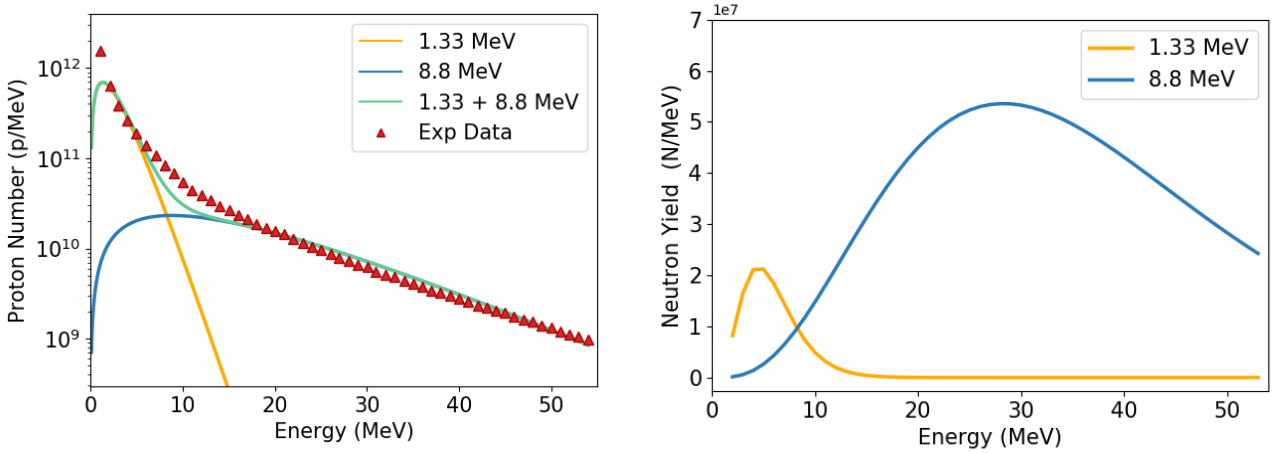

(a) (b)

Figure 4.16: (a) Ion spectrum from a shot at PHELIX [Wagner, 2014] in red. Most of the time TNSA spectra consist of ions with two different Maxwellian temperature distributions. This spectrum is a combination of an ion distribution with a temperature of 1.33 MeV (orange) and 8.8 MeV (blue). The sum of both distributions (green) is in good agreement of the experimental spectrum. (b): The total neutron yield for every proton energy of both ion distributions from (a). The conversion is done by using the yield function determined in figure 4.15 (b). It can be seen that even though the orange curve contains way more protons, the overall neutron production is much smaller. Most of the neutrons are produced from ions with energies between 20 and 40 MeV for this spectrum.

the spectral shape directly to the cut off energy. E_c has been intensively discussed in section 4.1 and it is possible to predict from the laser parameters. For this purpose, 20 ion spectra from various publications [Brenner et al., 2011] [Cianchi et al., 2018] [Macchi, 2017][Kraft et al., 2018] [Kaluza et al., 2004] [Morrison et al., 2018] [Zepf et al., 2001] [Busold, 2014] [Schwind et al., 2019] [Higginson et al., 2018] [Wagner, 2014] [Khaghani et al., 2017] [Fang et al., 2016] were taken and fitted with temperature distributions similar to figure 4.16 (a). From figure 4.16 (b) it is visible that the distribution with the higher E_T is dominant for neutron production, therefore the colder E_T impact is neglected. In the next step, the ion temperature is plotted against the cut off energy and fitted by a linear function. The result is displayed in figure 4.17 (a).

The ion temperature and the cut off energy do show a clear linear dependency following the relation $E_c = 7.9 \cdot E_T$. This result can be used to predict a neutron gain from a given cut off energy. Following this path further, the neutron yield for a subset of ten ion spectra from figure 4.17 (a) with different laser parameters and cut off energies was calculated by convoluting the yield function of beryllium from figure 4.15 (b) with the ion spectra. This procedure allows a prediction of the neutron conversion efficiency based on the cut off energy and respectively from the ion temperature. The red fit in figure 4.17 (b) extrapolates the dependency of the neutron conversion efficiency, from here called η_c, as a function of the cut off energy. It is described by

$$\eta_c = 1.14 \cdot 10^{-6} \cdot E_c^{3/2} \tag{4.15}$$

η is only dependent on the cut off energy and therefore respectively the spectral shape and not on the number of ions accelerated by the laser. The dependency of the laser energy on the ion numbers has been discussed in section 4.1 with the result that $N_P \sim E_L^{2.1}$. The number of protons is directly proportional to the number of neutrons produced, hence the total neutron yield per shot is given by

$$N = \eta_c \cdot N_P \sim \eta_c \cdot E_L^{2.1} \tag{4.16}$$

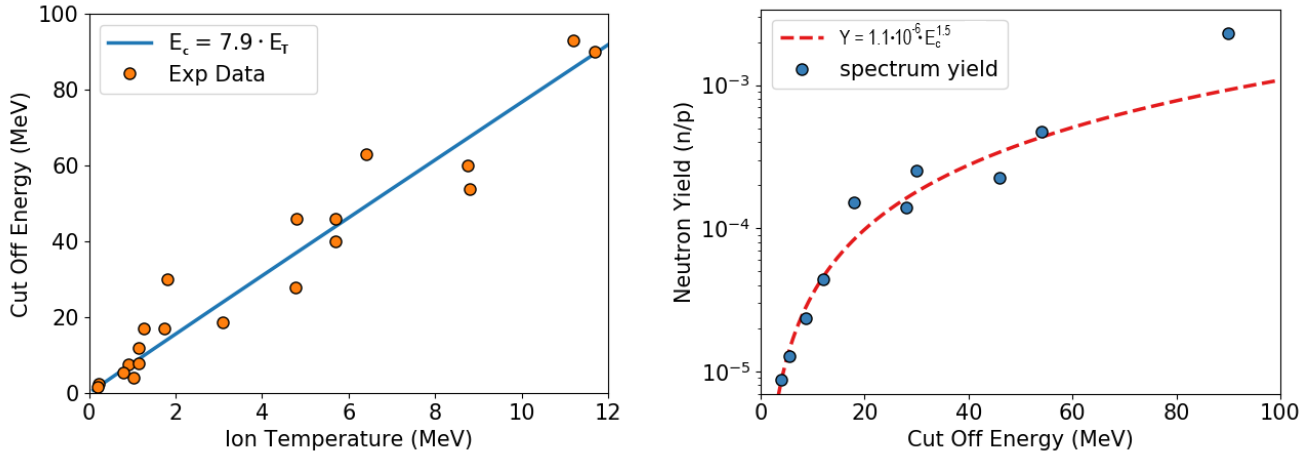

(a) (b)

Figure 4.17: (a) The Ion temperature plotted against cut off energies. The data is taken from 20 different ion spectra extracted from literature. Sources can be found in the text. Cut off energies range from 4 to 93 MeV. There is a clear linear relation between those two values displayed by the blue fit. (b): Calculated relative neutron yield per ion for a subset of the experimental laser ion spectra from (a) as a function of their cut off energy. The catcher material was beryllium. The red curve is a fit function with the parameters $Y(E_c) = 1.1 \cdot 10^{-6} E_c^{1.5}$. The last data point is from a spectrum with missing information below 4 MeV and therefore overestimates the abundance of higher ion energies.

η is a function of E_c and the most accurate prediction for E_c found so far is from figure 4.3 with $E_c = 8.59 \cdot E_L^{1/3}$. Inserting this correlation into equation 4.16 then the total neutron yield is proportional to

$$N \sim E_c^{3/2} \cdot E_L^{2.1} \sim \left(E_L^{1/3}\right)^{3/2} \cdot E_L^{2.1} = E_L^{2.6}. \tag{4.17}$$

It has to be noted that this approach neglects the influence of other parameters like the focal spot radius, target thickness and pulse length which can vary the results of figure 4.3 and therefore on E_c. Also this estimation was done for laser energies above 2 J. For lower energies the scaling increases to $N \sim E_L^{3.1}$.

It is important to know how the laser parameters and the ion distribution impact the neutron production rate. For NRS not only the fast neutrons are of interest but also those that have been moderated to the epi-thermal region. To illustrate the dependence of thermal and epi-thermal neutrons on the cut off energies, figure 4.18 displays the neutron spectra emitted from the moderator side surface. Similar to figure 4.17 only the ion distribution is varied in this PHITS simulation to focus on the effects caused by the spectral shape. It is noticeable that the fast neutron peak above 1 MeV is increasing the strongest with the cut off energy while the ratio of thermal and epi-thermal neutrons remains similar.

For simplicity epi-thermal refers to neutrons between 1 and 10 eV in the following sections since they are most relevant for the spectroscopy of tungsten conducted in section 5.1 even though this expression typically refers to a wider energy range.

Even though more neutrons leave the moderator at high energies, this does not have a significant effect on the moderation efficiency. The ratio of epi-thermal to produced neutrons in total remains rather constant ranging from 0.6 to 1.6 % for all cut off energies.

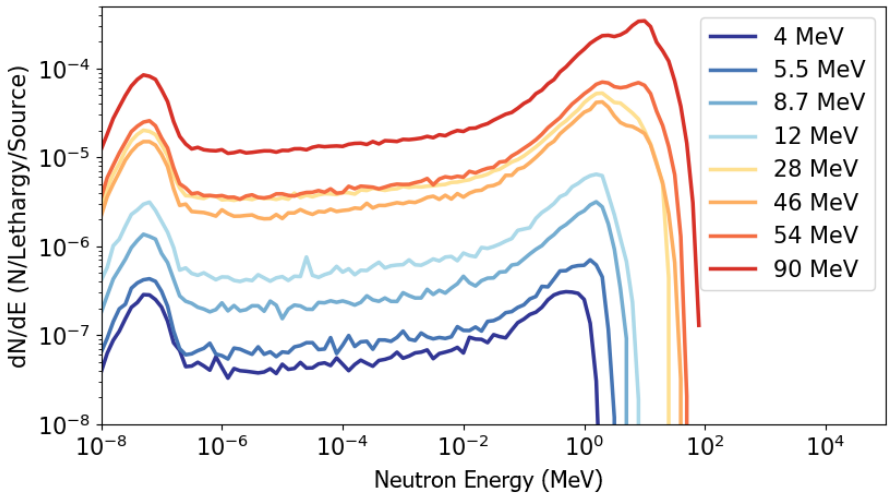

Figure 4.18: Various neutron spectra emitted from the moderator surface. Each graph is the result of a different ion spectrum impinging on the catcher. Only the cut off energy and the corresponding spectral shape is varied, not the particle numbers. Increasing E_c from 4 to 90 MeV results in a more than two orders of magnitude higher epi-thermal neutron flux.

4.3.3 Catcher Material Choice

The insight was gained from figure 4.15 (b) that lithium has the highest neutron gain for low proton energies while vanadium is optimal for high energetic ions. It was shown in section 4.3.2 that not only the ion energy is important for the neutron gain but also the distribution. This brings up the question, what kind of catcher material is suitable for which ion spectrum. For low energetic ion distributions below 15 MeV this question is easy to answer since lithium has the highest gain in this energy range.

For ion spectra with cut off energies higher than that, this question becomes non-trivial because the yield strongly depends on the spectral shape. If the cut off energy is higher than 15 MeV but the majority of the produced neutrons are created by ions in the spectrum below 15 MeV then lithium would still be beneficial. Figure 4.19 shows the emitted neutron spectrum from a PHITS simulation for a E_c =32 MeV ion spectrum [Green et al., 2014] impinging of different catcher materials. Figure 4.19 (a) shows the corresponding neutron conversion efficiency for each catcher with a comparison to an ion beam with E_c =54 MeV [Wagner, 2014]. Even though the first spectrum reaches up to 32 MeV, the benefits from ions below 15 MeV in lithium still outweigh the gain from energies between 15 and 32 MeV in beryllium or vanadium. As it can be seen for the spectrum with 52 MeV this has shifted for higher cut off energies and beryllium is most efficient for a single material catcher.

To gain an advantage from both materials it is possible to create a stacked catcher with lithium in the front and vanadium or beryllium in the back. To ensure all protons below 15 MeV are stopped in the lithium, the minimum thickness has to be equal to the stopping range which is slightly below 6 mm for 15 MeV. Protons with higher energies will exit the lithium at the rear surface but due to the energy loss inside the first layer, their energy will be reduced. If their energy at the point of exit is lower than 15 MeV then the neutron gain in the second material will be less than it would be if they would have continued propagating inside lithium. Therefore this technique can only be efficient if the cut off energies are above 23 MeV because those ions still have more then 15 MeV when they enter the second catcher layer.

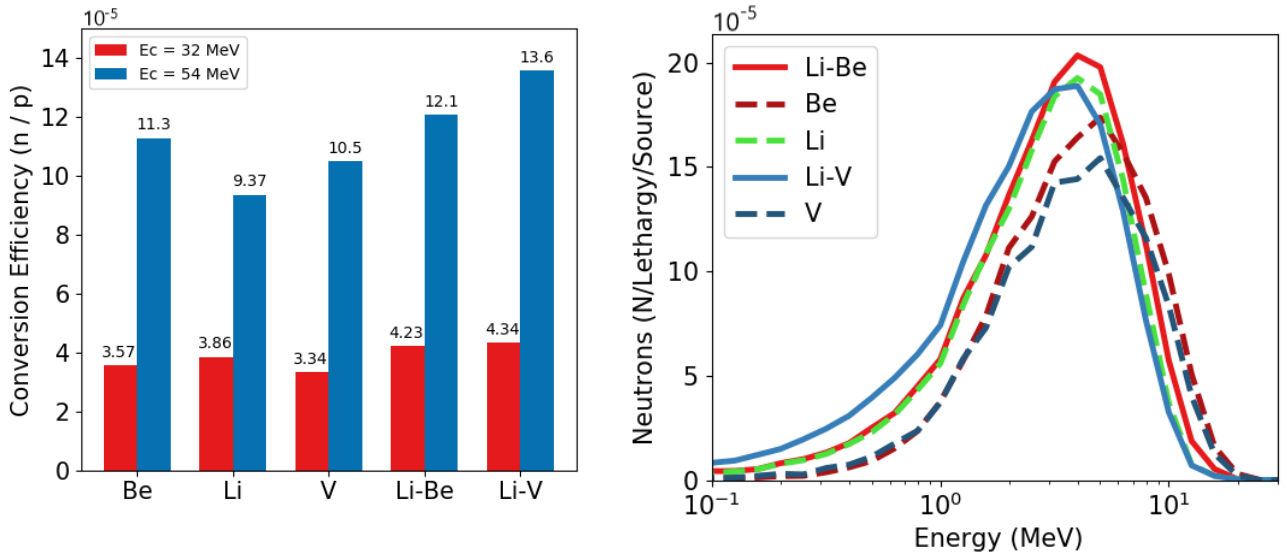

(a) (b)

Figure 4.19: (a) Emitted neutrons per proton for different converter materials and cut off energies. For a catcher made out of a single material, lithium is preferable for the 32 MeV [Green et al., 2014] spectrum and beryllium for 54 MeV [Wagner, 2014]. If materials are combined then a layer of 6 mm of lithium followed by vanadium has the highest gain. This configuration shows an increase of 20(1) % in comparison to a beryllium catcher in both cases. (b) Simulated neutron spectrum produced by TNSA ions impinging on different catcher materials. The spectra correspond to the red bars in (a). The combination of 6 mm of lithium with vanadium has the highest neutron production and neutrons are shifted towards lower energies and can be moderated more efficiently.

The dashed lines in figure 4.19 are from a single material catcher while the solid lines are from combinations with 6 mm lithium in the front followed by a 3x3 cm cylinder out of beryllium or vanadium. It is visible that the stacked catchers produce more neutrons which are also shifted to lower energies. This is beneficial since lower energetic neutrons can be moderated more efficiently. In figure 4.19 (a) it is clearly visible that the combination of lithium with vanadium is for 32 and for 54 MeV beneficial with an increase by 12% in the first case and by 20% more neutrons in the second case. Therefore this would be the favorable catcher material combination.

4.3.4 Catcher Geometry

Besides the catcher material, its geometry can also play an important role for maximizing the neutron yield. For neutrons to be available for spectroscopy they first have to enter from the catcher into the moderator. This can only happen if they leave the catcher into the forward direction or through the side surfaces indicated by the blue lines in figure 4.20. If they exit into the backward direction, they cannot be moderated and are therefore lost. If neutrons are produced close to the surface, then their chance to be lost in this way is higher than if they are produced deeper inside the catcher. The production depth of the neutrons is limited by the stopping range of the ions in the material which is for most energies close to the surface. To move the neutron production further into the catcher a recess in the shape of a cone can be drilled into the surface. Such a structure is known to reduce the backwards flux for fast neutrons [Dabruck, 2018] but has not been investigated for its impact on the epi-thermal neutron flux of an LDNS.

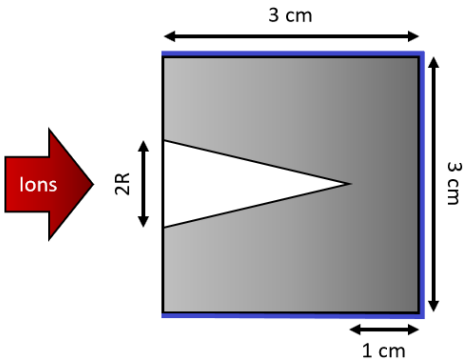

Figure 4.20: Design of the catcher. Ions enter from the left side and produce neutrons in the converter material. Ideally, neutrons would leave trough the surfaces marked in blue and enter the moderator to be slowed down. The fraction of neutrons that are exiting into the backwards direction do not reach the moderator and cannot be used. The introduction of a cone at the front surface can reduce this fraction. Table 4.3 compares the impact of the cone radius R on the flux through both surfaces.

The catcher and the moderator were modeled in PHITS similar to figure 4.1 and the neutron flux was observed for various surfaces for different cone radii. The simulation was conducted under ion irradiation of a spectrum from the GEMINI laser [Green et al., 2014] with $E_c = 32\,\text{MeV}$ as this most closely resembled the cut off energies present in the experimental campaign in section 5.1.
In table 4.3 the results are displayed for a beryllium and vanadium catcher. The units displayed are surface crossing neutrons per proton. Lithium was neglected as it has a much lower macroscopic scattering cross section and higher stopping ranges than the other materials making this effect negligible. For beryllium, an increase in the cone radius reduces the number of back-scattered neutrons. For a 10 mm cone radius 32 % fewer neutrons leave the catcher into the backwards direction than for a flat surface. The ions counted crossing into the moderator increase only by 13 %. This discrepancy is most likely caused by diffusion effects when neutrons are scattered from the moderator back into the catcher slightly distorting these values but the tendency towards a higher flux is still visible. While it can be seen that the cone does affect the fast neutrons, its impact on the epi-thermal neutrons on the moderator surface is less prominent. An increase of 6 % is visible between the absence of a cone and for R = 5 mm. This is not significantly larger than the margin of error of this simulation.

For vanadium, without a cone, it is visible that the number of neutrons leaving in the backward direction is 2.7 times larger than for those entering the moderator. Also the number of epi-thermal neutrons, in this case, is 1.3 times lower than for beryllium under similar conditions. This effect is most likely caused by the shorter stopping range of vanadium as seen in figure 4.15 (a) which leads to a neutron production closer to the surface making it much more likely for the neutron to diffuse out into the vacuum. While a cone does show a benefit, the better solution in this case is to reduce the thickness of the catcher to match it to the stopping range of the ions. This case is labeled in the last row of table 4.3 with ”flat 2.5“ where 2.5 stands for the thickness in mm. The number of neutrons transported into the moderator is in this case increased by 49 % and the epi-thermal neutron yield is comparable to the best beryllium results. With this configuration, the neutrons have to travel a much smaller distance through the catcher and the probability of scattering is reduced.

Table 4.3: Table of neutrons crossing various surfaces. Neutrons that are reflected inside the catcher can be scattered into the backwards direction towards the laser. These neutrons are lost for moderation. Different catcher geometries can reduce this. The first column specifies the catcher material, the second one the radius of a 2 cm long cone in the catcher center. The third column are neutrons per proton leaving the catcher in laser backwards direction. The fourth column are neutrons crossing the catcher surface towards the moderator. The last column represents neutrons leaving the moderator at the side surface with energies between 1 and 10 eV.

Material	Radius / mm	Backwards / 10^{-4}	Into Moderator /10^{-4}	Epi-thermal / 10^{-6}
Be	0.0	1.11	1.28	1.12 ± 0.06
Be	5.0	1.01	1.32	1.19 ± 0.06
Be	7.5	0.90	1.36	1.17 ± 0.06
Be	10.0	0.76	1.44	1.11 ± 0.08
V	0	1.20	0.45	0.87 ± 0.04
V	5.0	1.09	0.49	0.96 ± 0.06
V	Flat 2.5	1.13	0.67	1.17 ± 0.07

These results show that the catcher geometry has an impact on the direction of the fast neutrons but the effect on the moderated neutrons is rather small for beryllium. The best results were obtained with a 5 mm cone radius with a 6 % increase in flux. For vanadium, the effect on epi-thermal neutrons is higher but in this case, a thin disc is more efficient than a cone.

4.3.5 Limitations and Material Related Obstacles

The materials mentioned above have been discussed on their applicability for neutron generation. Although this is the main prerequisite for their usage in an LDNS, other factors can limit the overall applicability. Beryllium is toxic and can cause cancer [Sanderson et al., 2001] if inhaled in the form of dust. As laser ion irradiation causes ablation at the catcher surface from the high velocity impact of the expanding plasma this would cause pulverization of the beryllium surface and cause health hazards for operators. For this reason, a beryllium catcher is usually protected by a thin, robust and exchangeable ablation shield. As these shields stop a large fraction of the ions below 20 MeV this reduces the total efficiency of a beryllium converter. Additionally, beryllium is known to suffer from blistering [Quirós et al., 2017], the formation of small hydrogen bubbles inside the material that leads to tensions and to material failure over time. For accelerators, this problem is usually circumvented by reducing the Be thickness slightly below the stopping range so that the protons are stopped inside a material behind the converter where the resulting hydrogen can be transported away. This is not possible with LDNS as the spectrum has a wide range of energies, all with different stopping ranges.

The high reactivity requires lithium to be shielded from air and moisture or it is subject to rapid oxidation and material degradation. Even though in a vacuum chamber this does not cause any problems it prevents the simultaneous operation of a water-based liquid jet in combination with a lithium catcher as lithium reacts violently with H_2O. This is still the case if the lithium is initially coated due to the plasma ablation of the coating that will expose the lithium after time. Also, the low melting temperature of lithium at 181°C can cause a problem at high repetition rates.

Table 4.4: The maximum repetition rate possible for continuous operation with different laser systems and catcher materials. A lithium catcher does require active cooling for all laser systems for efficient operation. In the column with Li_{cooled} the catcher thickness increases with larger cut off energies and stopping ranges. The second option refers to a stacked Li-V catcher.

Laser \Catcher	Li	Be	V	Li_{cooled}
1 J	0.1 Hz	5 kHz	150 kHz	160 kHz
30 J	2 mHz	110 Hz	3.3 kHz	700 Hz / 3.5 kHz
150 J	0.2 mHz	11 Hz	330 Hz	53 Hz / 350 Hz

The energy of the laser that is converted into fast ions will be deposited inside the catcher with every shot. While the heat transfer inside such a system is rather complex and would require a numerical simulation software [Bianco et al., 2008] it is still possible to give an approximation by comparing the thermal energy entering the system with the dominant mechanism of energy transfer out of the system. With no air present in the vacuum chamber the main contribution of a non-cooled system is via radiative cooling of the front surface. Therefore the equation :

$$E_L \eta \, f = A \epsilon \sigma \Delta T^4 \tag{4.18}$$

Has to be fulfilled with the laser energy E_L, the conversion efficiency η the repetition rate f, the front surface area A, the emissivity ϵ, the Stefan-Boltzmann constant σ and the temperature difference between the surface and the vacuum chamber ΔT [Stefan, 1879]. A steady-state is reached when the amount of energy entering the system is equal to the amount that is irradiated away. The maximum surface temperature the catcher can have is equal to its melting temperature. For a lithium catcher with 1.5 cm radius and the target chamber at 20°C this energy is only 1 mW due to the low emissivity and melting temperature [Prishvitsyn, 2019][Gray, 2019]. η depends on the laser energy and the target thickness as reported by [Neely et al., 2006] and is for laser systems with around 1 J in the regime of 1 %. Therefore such laser systems with a repetition rate above 0.1 Hz are capable of reaching the melting point of lithium and require active cooling. Without cooling, a lithium catcher with dimensions as described in figure 4.3.4 requires 6.5 kJ of implanted energy to reach the melting temperature. This is equivalent with 11 minutes of operation at a 1 kHz system.

Beryllium has a higher melting point at 1287°C [Gray, 2019] and therefore a drastically increased radiative energy loss of 51 W. Under similar conditions, the maximum repetition rate it could be operated without melting would be 5.1 kHz. For higher laser energies in the regime of 150 J the conversion efficiency can reach values around 3 % as seen in figure 4.6 [Robson et al., 2007]. On such a system the maximum repetition rate the neutron source can be operated without cooling would be 11 Hz. For vanadium with an even higher melting temperature of 1910°C this repetition rate is further increased to 330 Hz [Wenner et al., 1915].

If an active cooling system is present, the right side of equation 4.18 changes as the heat transport now is dominated by the thermal conductivity of the system. Assuming the ideal case that the rear side of the catcher can be actively cooled to room temperature, then the thermal energy transported from the front surface to the rear surface is proportional to the thermal conductivity k, the cross-section area A and the difference in temperature of the front surface to the rear surface ΔT and inversely proportional to the distance between both surfaces d. Equation 4.18 can in this case be rewritten as:

$$E_L \eta \, f = \frac{k \cdot A \cdot \Delta T}{d} \tag{4.19}$$

This increases the maximum deposited power for a 3 cm long lithium cylinder to 320 W. This can be drastically increased by reducing the lithium thickness to 6 mm as discussed for a stacked catcher to increase the maximum acceptable power without melting to 1.6 kW. Similar calculations can be done for beryllium and vanadium with a maximum heat flow of 6 kW and 17 kW respectively. This heat flow is more than sufficient enough for not limiting the repetition rate since above the kHz region the target is becoming the limiting factor for the repetition rate. For this reason, only for lithium, the active cooling option is listed in table 4.4. With these results, it is possible to say that the usage of lithium as catcher material for a continuous operation does require an active cooling system. Short burst operation for a limited time is still possible. The burst operation limits are 11 minutes for a 1 kHz rep rate system at 1 J or for 2 minutes with a laser delivering 150 J at 10 Hz. The limits of a beryllium catcher are less likely determined by the heat load than through problems from ablation and blistering in the surface layer. For a more accurate prediction, the implantation of heat from the expanding plasma, the hot electron irradiation and the nuclear processes have to be simulated. Within this simple model vanadium and a combination of a thin stacked lithium-vanadium catcher with active cooling shows the most promising results as a catcher for a high repetition neutron source.

4.4 Moderator

Neutrons produced from the ions impinging on the converter material leave the catcher with energies in the MeV region. This is many orders of magnitude higher than the energy regime with resonances of interest for NRS which are on the order of a few eV to keV, therefore the neutrons have to be slowed down. As discussed in section 2.5 this is done most efficiently for an LDNS via elastic collisions with hydrogen in a polyethylene moderator. From equation 2.31 it is known that the average amount of collisions to reduce the neutron energy from E_0 to E_n is proportional to $ln(E_0/E_n)$. To reduce the energy from 1 MeV to 1 eV on average 16 collisions are required. The decreasing of the scattering cross section of hydrogen above 100 keV causes fast neutrons to have a larger mean free path between collisions and therefore enables them to travel much further through the moderator. The highest neutron energies are emitted into the forward direction [Roth et al., 2013] hence in this direction the largest amount of moderation material is necessary to slow them down. For a moderator design, it is important into which direction the slow neutron flux has to be optimized. For an experiment, a sample could either be placed into the forward direction or under 90°. For this approach, the 90°option is chosen because it enables to moderate a higher fraction of fast neutrons due to its increased length in forward direction. This additionally avoids interference from the γ-flash at the detector position, which is strongest into the forward direction.

An optimal moderator would be designed in a way that the average distance neutrons travel from the catcher to the surface match the moderation length and the corresponding Fermi age for the desired energy as discussed in equation 2.40. With neutrons being emitted at a wide energy range and at many different positions an analytical solution cannot be found and a parameter scan using a PHITS simulation is preferred. For the optimization the same ion spectrum as in section 4.3.3 with cut off energies of 32 MeV was chosen to maintain consistency with the previous simulations.

To find the optimal parameters, the catcher is surrounded by a cuboid of polyethylene and the length, height and width are varied while the epi-thermal neutron flux into the direction of the detector is mea-

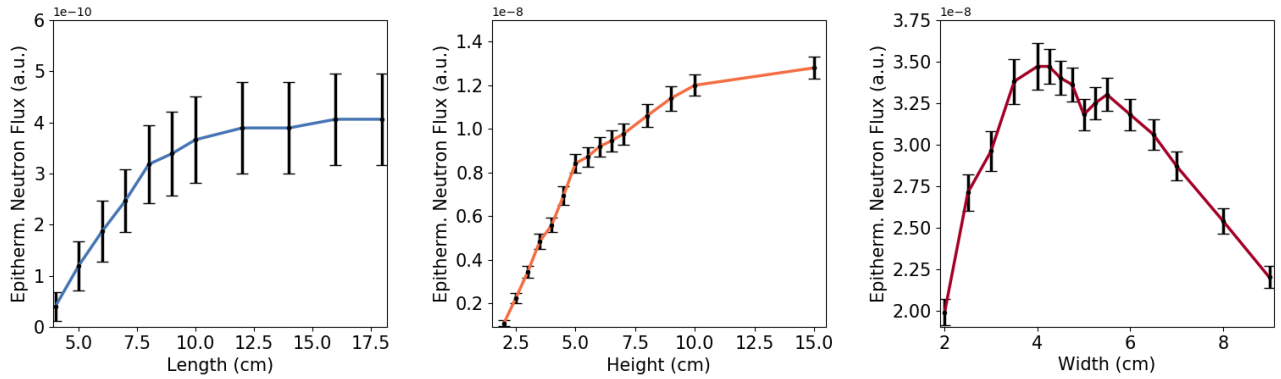

(a) (b) (c)

Figure 4.21: Simulated epi-thermal neutron flux for different moderator dimensions. The initial neutron distribution is produced by a TNSA spectrum with $E_c = 32$ MeV protons inpinging on beryllium. The length is measured from the catcher surface while width and height are measured from the catcher center and are increased in both directions. (a) : Effect of increasing the length of the moderator while remaining the other parameters at h = 1.5 cm, w = 1.5 cm. (b) Change in neutron flux with increased height while maintaining l = 18 cm and w = 1.5 cm. (c) : Epi-thermal flux as a function of moderator width with dimensions h = 10 cm and l = 18 cm. a) and b) show a saturation with increasing size. With increasing moderator width in c) a maximum is reached after which the flux droppes again due to the limited drift length of epi-thermal neutrons.

sured at a distance of 50 cm. Figure 4.21 shows the dependency of the flux as a function of the cuboid parameters. The length is measured from the beginning of the catcher surface as seen in figure 4.22 (b). The width and height are measured from the center of the catcher and are increased in the ± direction equally. For the length scan in (a), the other parameters are held constant at 1.5 cm. It can be seen that the flux increases rapidly until a length of 10 cm after which it begins to saturate. After 18 cm no significant increase in the flux can be seen.

For figure 4.21 (b) the length is set to 18 cm and the height is increased. Until a height of 5 cm the flux is strongly increasing followed by a lower gradient until 10 cm. From 10 to 15 cm the increase in flux is minimal. For 4.21 (c) a height of 10 cm was chosen and the length was remained at 18 cm. Increasing the width from 2 to 3.5 cm is accompanied by a strong increase in flux with a maximum at 4 cm. For further increasing the width, the flux is reduced until 5 cm followed by a second maximum at 5.5 cm after which the flux is decreasing again.

Below 4 cm, the increase in PE width allows more fast neutrons to scatter and to contribute to the moderation process. For a further increase in width, the average diffusion drift length of the neutrons becomes smaller than the distance to the surface and it is less probable that the neutrons are leaving the surface at the right energy. The second peak at 5.5 cm is most likely caused by neutrons that were emitted in a different initial direction and with other energies. Neutrons that have an initial emission direction oriented towards the surface travel through less moderator material than those emitted under a larger angle. Therefore it is likely that the neutrons from the second peak are emitted close to the catcher.

In section 4.3.4 the catcher was optimized to reduce the number of neutrons scattered into the backwards direction so they are not lost for moderation. It is consequently a logical step to modify the shape of the moderator to capture more of these backwards moving neutrons. For this purpose, two wings

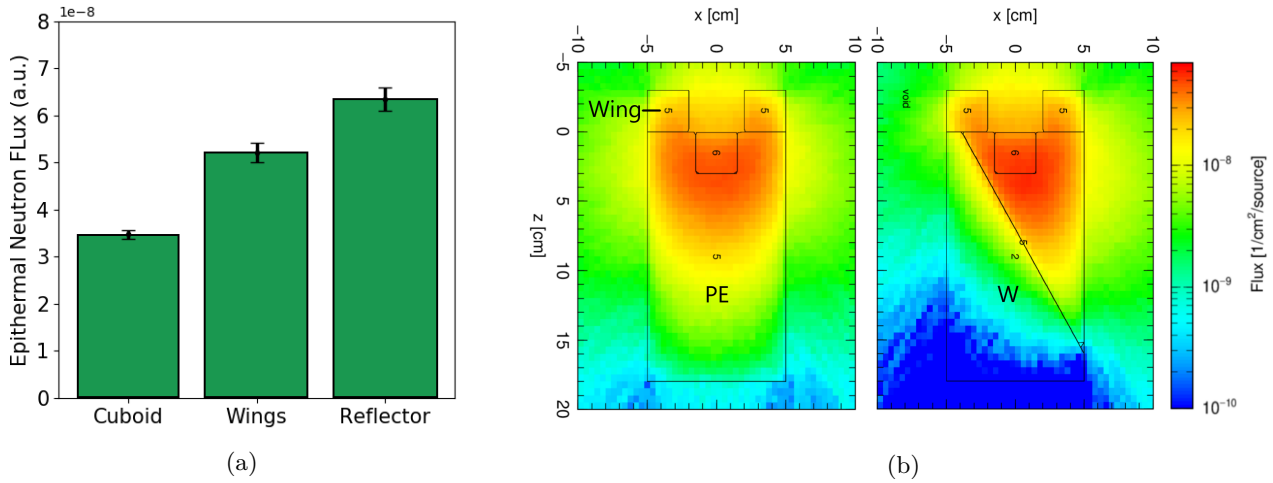

(a) (b)

Figure 4.22: (a) : Epi-thermal neutron flux improvements for different moderator modifications. Cuboid stands for the result of the dimension optimization from figure 4.21. Adding two wings in front of the moderator as seen in the (b) increases the epi-thermal flux by 50 % and shifts the optimal width of the moderator from 4 to 5 cm. By replacing parts of the moderator with a tungsten reflector as seen in the right image the flux can be increased by additional 21 %.

were added at the front surface of the moderator as seen in figure 4.22 (b) on the left side and in figure 4.24 (a) on the right side. Simulations show that these wings increased the epi-thermal flux by 50 %. Their presence required an increase in the total moderator width from 4 to 5 cm to be most efficient. This strengthens the argument that the second peak seen in figure 4.21 (c) is caused by neutrons emitted close to the catcher since the wings are also in close proximity to the catcher.

In other neutron production sites like spallation sources or CANS, neutron reflectors are used to direct fast neutrons that would otherwise leave the moderator back into the moderating material to give them again a chance to be slowed down [Brueckel, 2018]. This is a well-established technique for thermal or cold neutrons as they can diffuse over large distances inside the moderator before they are absorbed. For epi-thermal sources this is more difficult since these neutrons have much smaller diffusion length. Additionally, the increase from reflectors on the time uncertainty has to be kept at a minimum. For this purpose, heavy and dense elements like tungsten are good candidates since they do not contribute to the moderation. Tungsten has additionally high (n,xn) cross sections [Koning and Rochman, 2012] to increase the available neutron numbers further. This makes it the preferred reflector choice. An approach on how to utilize reflectors in LDNS is shown in figure 4.22 (b) on the right side. The parts of the moderator which are averted from the detector are replaced by tungsten. This approach redirects fast neutrons from the left to the right side and simultaneously increases the propagation length of those neutrons in the PE which increases their chance to be moderated. This reflector could increase the epi-thermal flux by additional 21 % as seen in figure 4.22 (a). Through the high weight of the tungsten, this type of reflector cannot be used in the current setup because it exceeds the maximum weight of the motorized stages used to move the moderator inside the target chamber. It nonetheless shows that for dedicated laser-driven neutron sources where the setup is allowed to have a higher degree of complexity, reflectors can be used to further increase the moderation efficiency.

For optimization of an LDNS it is important to know how neutrons interact with the moderator and how the interaction varies with different energies. For a better understanding of these processes figure 4.23 shows the neutron flux as a function of position in a horizontal transverse section through the moder-

ator center as well as on its detector facing surface for different energies. The moderator design with wings was chosen as the reflector system is currently not viable at experiments. All plots have different color scales to highlight the important features for each energy region. (a) and (d) show the thermal neutron distribution and illustrate the higher diffusion length of thermal neutrons as they are spread more homogeneously across the moderator than it is the case for all other energies. As these neutrons have scattered on average more than 18 times, all of their initial directionality from their production is lost. The drop in flux on the side surfaces in comparison to the forward direction is caused by neutron leakage into the vacuum. (b) and (e) show the epi-thermal flux which has its maximum closer to the catcher in a more radial symmetric distribution until the radius reaches the surface. This is expected as the moderator is designed to match the Fermi age for this energy. From (a - c) it is visible that the neutrons emitted from the moderator have the highest flux perpendicular to its surface. This is the result of the neutrons not having their last scattering event at the surface but at a certain depth inside the PE. Neutrons with a propagation direction after the last scattering event perpendicular to the surface have the smallest amount of material to pass through and therefore a lower probability to undergo additional scattering. As the distance to the surface increases with $1/\cos(\alpha)$ with α being the angle to the surface normal vector, this causes the emission to follow a similar distribution convoluted with the surface flux.

For higher neutron energies as displayed from (g to l) the behavior undergoes significant changes. (g) shows a strong increase in flux at the front surface of the catcher. This indicates that the majority of neutrons from 0.1 to 1 MeV have already been emitted from the catcher with this energy and did not undergo any previous scattering to be moderated. The same is true for higher energies. In (i) and (k) it is possible to see an increase in the flux at the position of the wings from -3 to 0 cm. As there is less material in the pathway from the catcher to the wing surface fewer scattering processes take place. This decreases the likelihood that neutrons are moderated down to lower energies. An important feature becomes evident in (i) and (l) which contains neutrons with energies above 10 MeV. The neutron distribution in (i) shows a strong deviation from the $1/\cos(\alpha)$ dependency and the trajectory lines visible at the outer regions show a clear origin in the catcher. In general, it can be seen that the neutron flux is only weakly affected by the presence of the moderator. This indicates that the neutrons did not undergo any scattering on their pathway through the moderator and therefore it is possible to say that neutrons produced in the catcher with initial energies above 10 MeV play a subordinate role in the contribution to the supply of (epi-)thermal neutrons in the simulated setup.

This also explains why there is no significant dependency on the moderation efficiency for different ion cut off energies for the investigated moderator. Although higher cut off energies are capable of producing higher neutron energies, it does not make a difference since the fast part of the spectrum does not contribute to the moderation in either case. In (i) and (l) additionally, the directionality from the pre-equilibrium emission becomes evident as the flux has a strong increase in the forward direction. [Kleinschmidt, 2017] has investigated this effect and found that the neutron beam has a Gaussian shaped increase in the forward direction with a half opening angle of 50° with an increase of flux at the center with a factor of 4 compared to the 4π emission.

As the moderator and the catcher have been optimized, it is of interest how these changes compare to previous experiments. For a direct comparison, the experiments of Kleinschmidt at the Trident laser facility and at PHELIX are chosen [Kleinschmidt, 2017][Kleinschmidt et al., 2018] due to the fact that they have the closest resemblance to the experiments in this work. The catcher used at PHELIX in that experiment consisted of beryllium discs with a 5 cm diameter of variable thickness with 50 μm copper plates in between. In the front a 2 mm aluminum ablation shield protected the beryllium from the hot plasma and the discs were encapsulated by a hollow tungsten cylinder with a wall thickness of 1 cm.

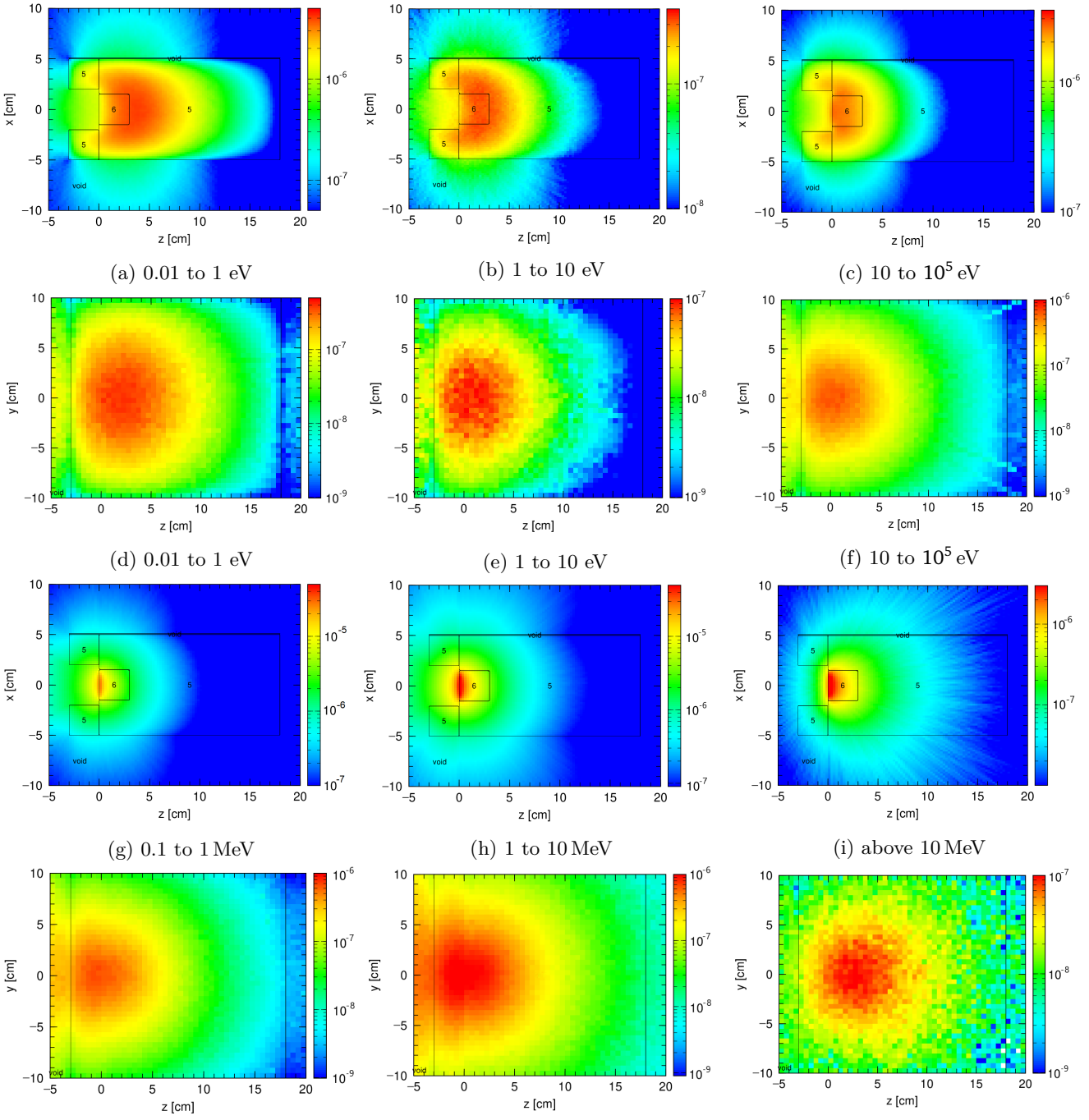

(a) 0.01 to 1 eV (b) 1 to 10 eV (c) 10 to 10^5 eV

(d) 0.01 to 1 eV (e) 1 to 10 eV (f) 10 to 10^5 eV

(g) 0.1 to 1 MeV (h) 1 to 10 MeV (i) above 10 MeV

(j) 0.1 to 1 MeV (k) 1 to 10 MeV (l) above 10 MeV

Figure 4.23: Neutron flux distribution in 1/cm^2/proton for different energy regimes across the moderator. Row one and three are horizontal cross sections through the moderator center and two and four are the corresponding neutron flux across the moderator surface. All plots have a different color scaling to highlight their unique features.

In the Trident experiment a 3x3 cm beryllium cylinder was used with a 1.5x1.5 cm cylindrical recess in the center. This catcher was surrounded by a High Density PolyEhtlylene (HDPE) moderator as seen in figure 4.24 (a) on the left side.

To compare the changes in the epi-thermal neutron yield a series of PHITS simulations were conducted in which different aspects were improved. As a point of reference, the first catcher design used at PHE-

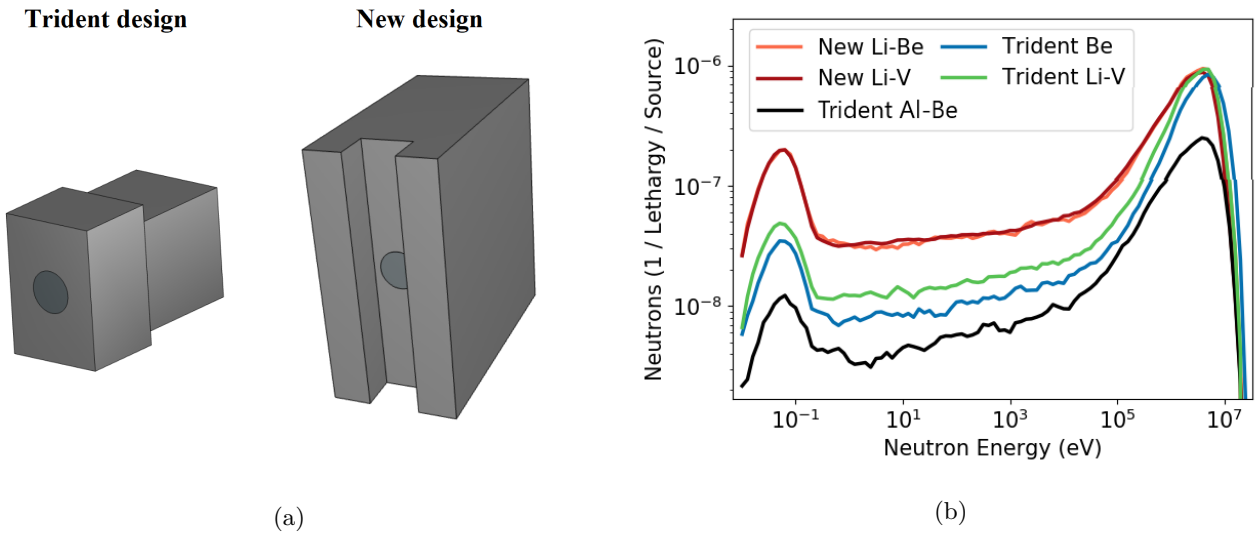

Figure 4.24: (a) left: moderator design used at the Trident laser facility for NRS [Kleinschmidt, 2017]. Right: new optimized moderator design with wings. (b) : Moderated neutron spectrum simulated by PHITS with 32 MeV cut off proton irradiation on different designs. The black curve is a combination of the Trident moderator seen in (a) and the catcher used at PHELIX by [Kleinschmidt et al., 2018][Kleinschmidt, 2017] composed of a stacked beryllium disc catcher with 2 mm aluminum in the front encapsulated by a 1 cm thick tungsten reflector. For the blue curve the catcher was exchanged with a pure beryllium cylinder with the dimensions used at trident. For the green curve a stacked Li-V catcher was used. The orange and red curves are simulations with Li-Be and Li-V stacked catchers in combination with the new optimized moderator design from (a).

LIX and the first moderator design from Trident [Kleinschmidt, 2017] are combined in the black graph. The catcher design changes for the Trident experiment resulted in an epi-thermal neutron increase by a factor of 2.3, shown in the blue curve. This is mostly caused by removing the aluminum shielding plate as it is stopping most incoming low energy ions without creating a significant number of neutrons. Switching from the beryllium catcher to a stacked lithium-vanadium catcher could increase the yield by an additional factor of 1.5 as it is displayed via the green graph. The influence of the new moderator design becomes evident in the orange and red curve with Li-Be and Li-V catchers. From green to red an epi-thermal neutron flux increase is achieved by a factor of 2.7. This makes a total improvement in epi-thermal flux to the Trident design of a factor of 4.1 The corresponding thermal flux is showing an even larger increase of a factor of 6.

While the neutrons have been slowed down in the moderator, a certain time t_s has passed until they reach the surface. Δt_s defines the moderation uncertainty and is the main contribution to the energy uncertainty in this setup. It, therefore, limits the minimum detector distance for a given energy resolution. This makes Δt_s a substantial parameter that has to be investigated. A PHITS simulation is used to determine the time delay of neutrons crossing the moderator surface after their creation for different energies. Figure 4.25 shows the distribution of t_s for various energies from 1 eV to 1 keV. For each graph, the energy uncertainty is ±1 %. The time needed for surface crossing varies with energies from around 30 ns for 1 keV to 2 μs for 1 eV since slower neutrons require on average more collisions and take more time to reach the surface. Besides the decrease in neutron numbers for lower energies caused by the leakage it can be seen that the ratio $\Delta t_s/t$ remains constant for all energies. This figure illustrates a major benefit of LDNS against conventional sources. The minimal pulse width a spallation source like LANSCE can operate at is 125 ns [LANL, 2019b] and therefore the time uncertainty has to be greater than this value. If this is compared to figure 4.25 then it becomes evident that an LDNS has a lower time

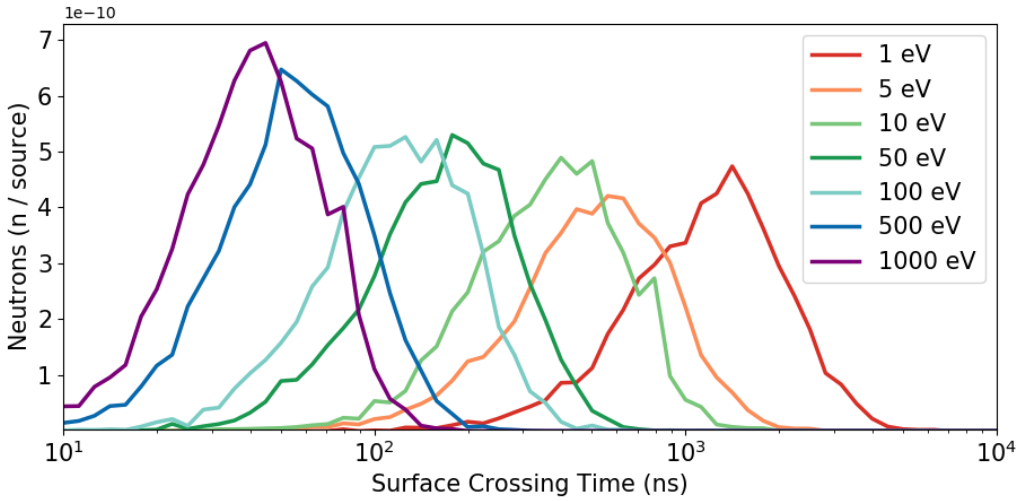

Figure 4.25: The time of neutrons with a certain energy crossing the moderator surface after the laser simulated via PHITS. The energy uncertainty for each graph is ±1 %. Higher energies have a lower Δt_s but the ratio $\Delta t_s/t$ remains constant. This defines the minimal time and therefore energy resolution for each neutron energy.

uncertainty for all energies above 100 eV.

Neutrons that have been slowed down in the moderator need to be transported to the detector. During this process, it is necessary that all detected neutrons have propagated on a straight pathway from the moderator through the sample to the detector. To ensure this is the case, an efficient collimation system has to be installed.

4.5 Collimator

The collimation system serves two main purposes. The first one is to block slow neutrons from entering the detector that are not coming directly from the moderator. The second function is to block fast neutrons to get into close proximity to the detector as they can be moderated in the B-HDPE shielding surrounding the detector and cause background noise. The shape of the collimator is strongly connected to the dimensions of the moderator, the sample and the detector. If the sample is smaller than the detector, then the collimator is required to focus neutrons at the sample to ensure no neutrons are detected that have bypassed the sample. This can be done by having the collimation aperture shaped like two truncated cones mirrored at the surface of the sample. For smaller samples, the number of accessible neutrons is reduced as fewer neutrons pass through the sample.

For a proof of principle experiment, it is beneficial to have a sample size larger than the detector. In this configuration the collimator aperture can have the shape of a single truncated cone with its top being the surface of the detector and its bottom is the moderator surface. This configuration can be seen in figure 4.26 and the diverging cone structure in the collimator is indicated by the black lines in the center. The collimator itself consists of several B-HDPE sheets with 5 % boron content by weight and a thickness of 5 cm each. The distance between the sheets is maximally spaced to increase the likelihood of fast neutrons that have scattered once to be directed away from the detector and not to scatter again

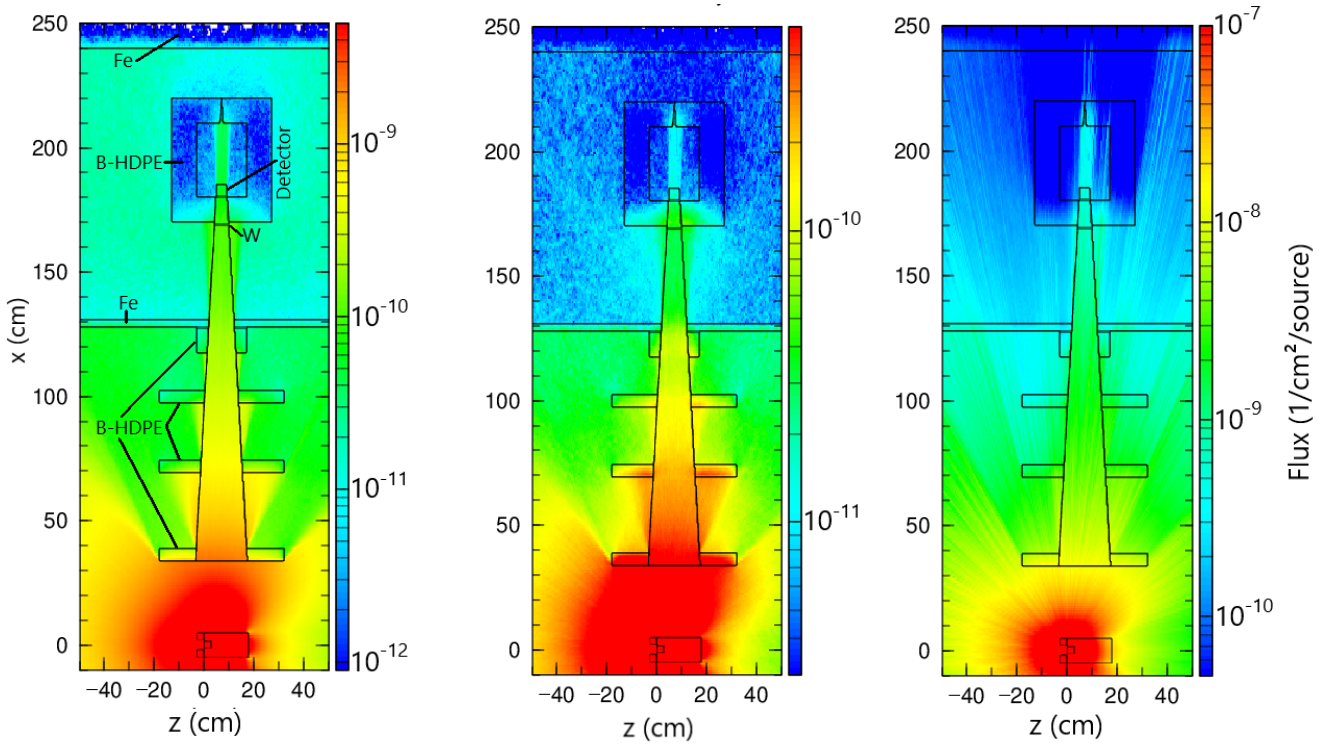

(a) Thermal (b) Epi-thermal (c) Above 1 MeV

Figure 4.26: The simulated neutron flux in the collimation system developed for NRS. Neutrons emerge from the moderator and hit four borated HDPE sheets inside the target chamber. Those with the matching trajectory can propagate through recesses towards the detector which is placed outside the chamber surrounded by 10 cm of HDPE. This setup aims to reduce the background contribution of neutrons at the detector position. (a - c) show the flux of neutrons in the thermal (a) and epi-thermal (b) regime as well as for neutrons above 1 MeV (c). The collimated neutron beam has an one order of magnitude higher flux than the surrounding background. Thermal and epi-thermal neutrons are fully stopped in the B-HDPE. Fast neutrons experience only a small attenuation and require more shielding.

in another collimator layer. The detector itself is placed inside a B-HDPE box with 10 cm wall strength and one collimation entrance.

Figure 4.26 and 4.27 are the result of a PHITS simulation in which the experiment from section 5.1 was reconstructed. Figure 4.26 shows the thermal, epi-thermal and fast neutron flux in the horizontal plane while figure 4.27 displays the vertical neutron flux. In 4.26 (a) it can be seen that the thermal neutrons are directly stopped in the B-HDPE layers close to the surface of each of the first four collimator layers. At the detector shielding, the thermal neutrons do not penetrate deep into the polyethylene from the sides and the back. In contrast to that, the front side of the shielding box shows a high flux of thermal neutrons until shortly before the detector. These thermal neutrons are the result of fast neutrons that penetrate deep into the shielding before they scatter and get moderated. This effect is visible in (c) where the fast neutron flux is only reduced close to the inner surface of the shielding and some neutrons are capable of passing through this shielding. Nonetheless, a distinct collimated neutron beam with a flux one order of magnitude higher than the background is visible inside the detector shielding. The exact signal to background ratio is 15(4):1.

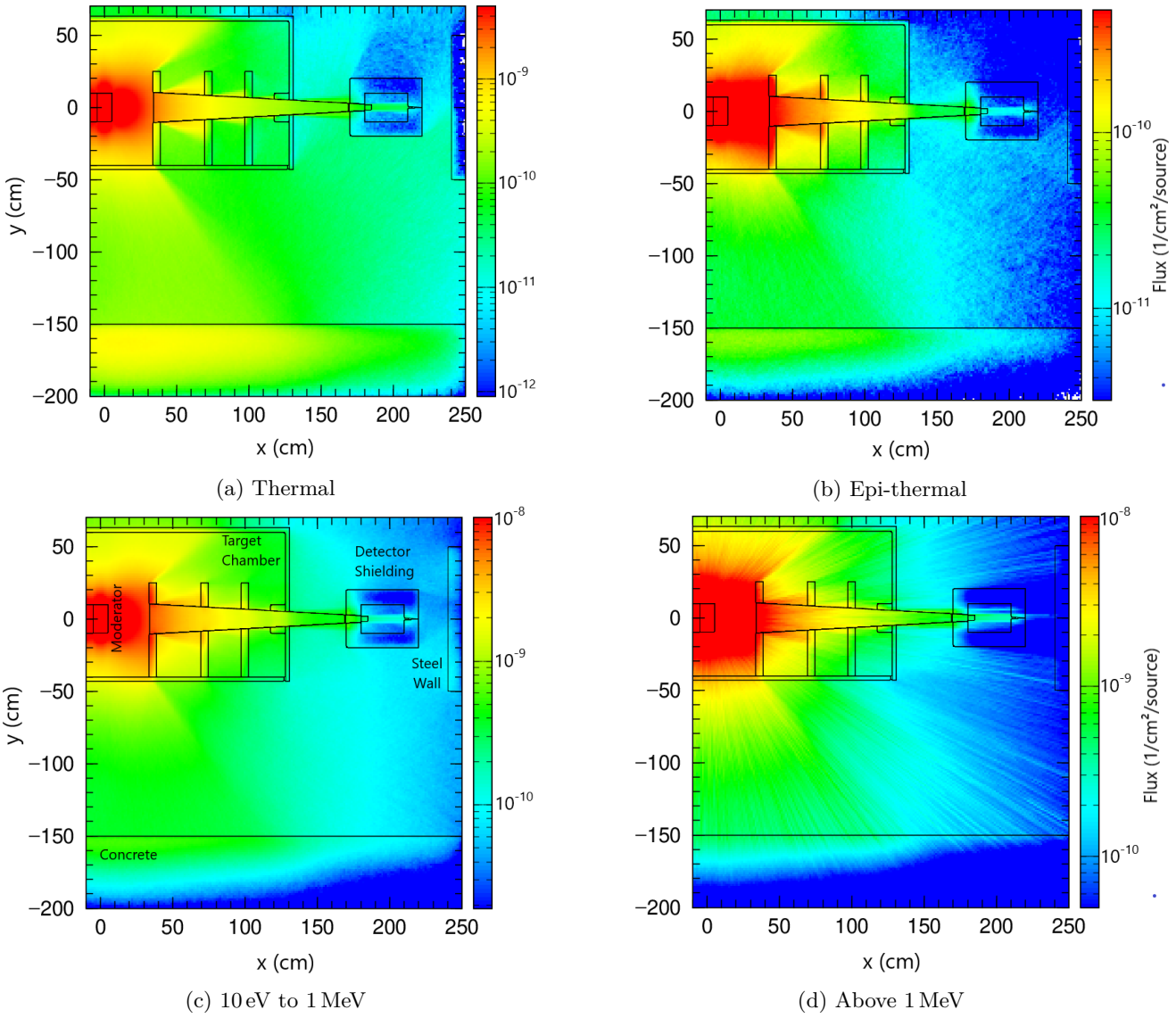

(a) Thermal

(b) Epi-thermal

(c) 10 eV to 1 MeV

(d) Above 1 MeV

Figure 4.27: Side view of the setup shown in figure 4.26 which resembles a reconstruction of the PHELIX target area. This illustrates the origin of background contributions of neutrons in the experiment. While the collimator blocks almost all thermal and epi-thermal neutrons, many other neutrons are moderated in the concrete in the floor and cause a large background in the entire target area.

One thing that is noticeable, is that the remaining thermal background outside the detector box does not show any correspondence to the geometry of the collimator. The reason for this behavior becomes evident in figure 4.27 (a). These thermal neutrons do not have their origin in the moderator but are the result of fast neutrons being moderated in the concrete in the floor which are then scattered upwards. The neutrons diffuse up to 50 cm deep into the concrete before their flux rapidly decreases. The hypothesis that most thermal neutrons outside the detector box have their origin in the floor is strengthened by the clear edges above and behind the detector box of which a prolongation reveals their source in the concrete.

A comparison to (b) shows a significant difference in the epi-thermal distribution. There the influence of the collimator is more prominent and distinct shadows can be seen in the flux which is in total less homogeneous. Another observation from (b) is that the 3 cm thick steel wall of the target chamber acts as a strong barrier for the epi-thermal neutrons, while the flux in (d) has a much lower attenuation.

This simulation has shown that the developed collimation system significantly reduces the neutron flux in the area surrounding the detector and increases the ratio between neutrons that are coming directly from the moderator and those that have scattered in the target area and therefore contribute to the background. The spatial background contribution inside the detector shielding box is one order of magnitude lower than the collimated neutron beam. The high thermal flux in the front of the detector shielding does pose a problem as these neutrons are capable of diffusing into the center of the box. This can cause background contributions via direct absorption in the detector as well as via the formation of absorption γ-radiation inside the B-HDPE.

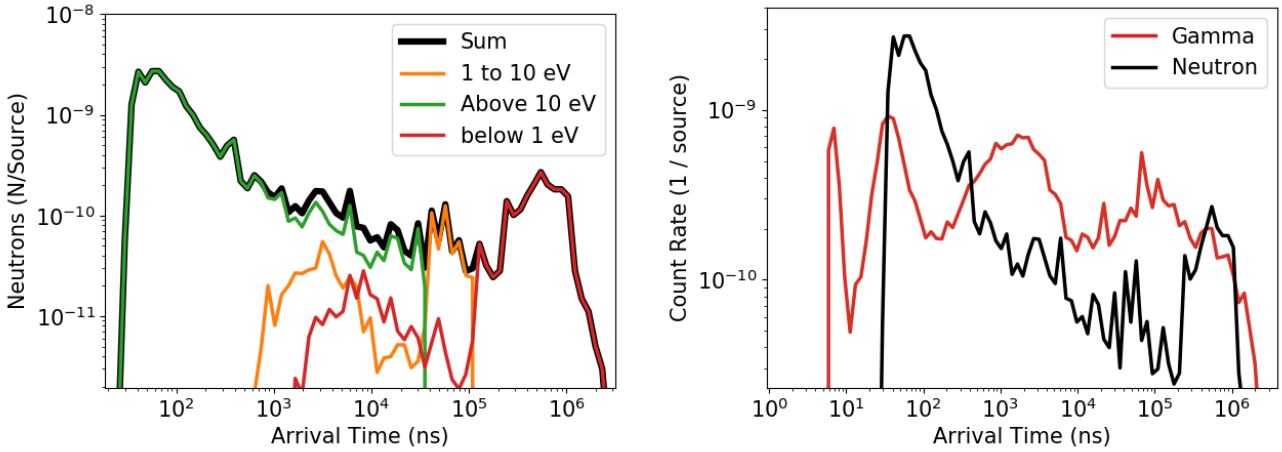

(a) (b)

Figure 4.28: (a) : The arrival time of neutrons with different energies at the detector position in the simulation setup seen in figure 4.27. Neutrons with more than 10 eV are marked in green, those between 1 and 10 eV in orange and slower neutrons in red. The sum is displayed in black. Thermal and epi-thermal neutrons arrive earlier than their velocity and the distance would allow. This means that these neutrons do not have their origin in the moderator and cause a distortion of the measurement. (b) : The arrival of γ-radiation is correlated to the arrival of neutrons with different energies. Especially at arrival times later that 10 μs the γ-contribution becomes an important background contribution.

To investigate these contributions further, figure 4.28 shows the arrival times of neutrons with different energies at the detector (a) as well as for the γ-radiation (b). (a) shows the arrival time of neutrons below 1 eV in red, between 1 and 10 eV in orange and neutrons above 10 eV are displayed in green. The sum of all neutrons arriving over time at the detector is visible in black. The beginning of the green curve at 27 ns corresponds to neutrons with an energy of 25 MeV. This matches the maximum of emitted neutron energies displayed in figure 4.19. The abrupt cut of the green curve and the strong rise of the orange curve corresponds to the arrival time of the 10 eV at 42 μs. Even though the fastest epi-thermal neutrons are expected to arrive at that time, neutron events from this energy regime are registered as early as 650 ns after the shot. If it is assumed that the fastest neutrons in this energy group are the ones detected first, then with a given arrival time and a maximum energy of 10 eV their origin is about 2.9 cm away. A similar approach can be done by assuming the slowest end of this early peak corresponds to 1 eV neutrons. Arriving after 10 μs limits the maximum distance traveled to 14 cm. A similar approach can be taken with the red curve resulting in a maximum distance of 9 cm and a minimum distance of 3.2 cm. These findings support the hypothesis that the main contribution of the neutron background stems from

the moderation of fast neutrons in the last layers of borated polyethylene.

This problem has to be solved for future experiments to further reduce the background. A promising approach would be inserting a steel reflector directly in front of the last B-HDPE shielding layers. The thickness has to be thicker than the mean free path of the fast neutrons in steel which is between 4 to 5 cm [Koning and Rochman, 2012] depending on the energy.

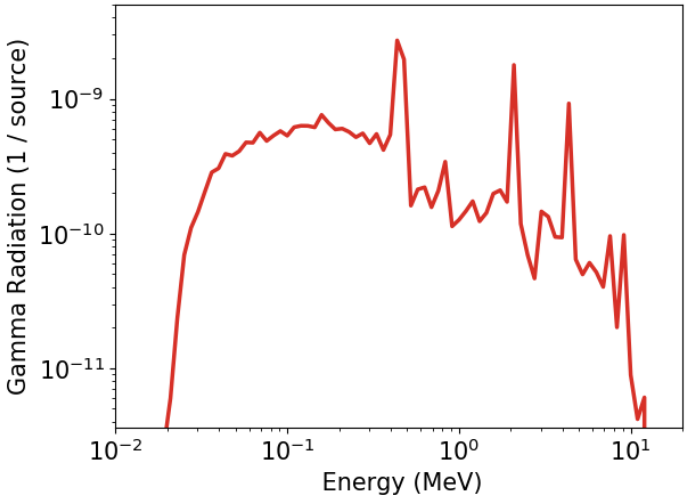

Figure 4.29: The γ-spectrum detected in the simulation at the position of the detector. The 511 keV annihilation peak and the neutron absorption peak of hydrogen at 2.2 MeV is clearly visible. The lower end of the spectrum can be shielded with a thin lead plate to reduce the background.

The influence of the γ-background over time is visible in figure 4.28 (b). The first photons arrive between 6 to 7 ns which corresponds to the time it takes light to travel from the catcher to the detector. After this first peak, the γ-background drastically drops and then increases again shortly before the first fast neutrons arrive. This behavior indicates that this γ-peak is caused by the absorption of these fast neutrons as there is not enough time for them to be moderated. Around 1 μs a third wider increase in γ-activity is observed which coincides with the orange and red neutron peaks and therefore likely to be caused by the absorption of slow neutrons in the B-HDPE. It is also visible that for timings greater than 1 μs the γ-background is larger than the neutron flux at the detector. With a γ-sensitivity of 1 % [ProxiVision, 2019] and an increasing efficiency proportional to t this is less of a problem for thermal neutron detection. In contrast to that, for neutron energies above 1 eV for which the detection efficiency for neutrons is reduced below 10% the γ-contribution becomes significant.

The γ-contribution can be mitigated by adding lead shielding around the detector. With the strong decreasing mass attenuation coefficient of lead with higher energies and the limited space, only the low energy γ-radiation can be shielded. As it is visible in figure 4.29 most of the emitted energies are below 600 keV and therefore 5 mm of lead are required to have a significant reduction in the γ-background [McAlister, 2012].

4.6 Borated Multi Channel Plate Detector

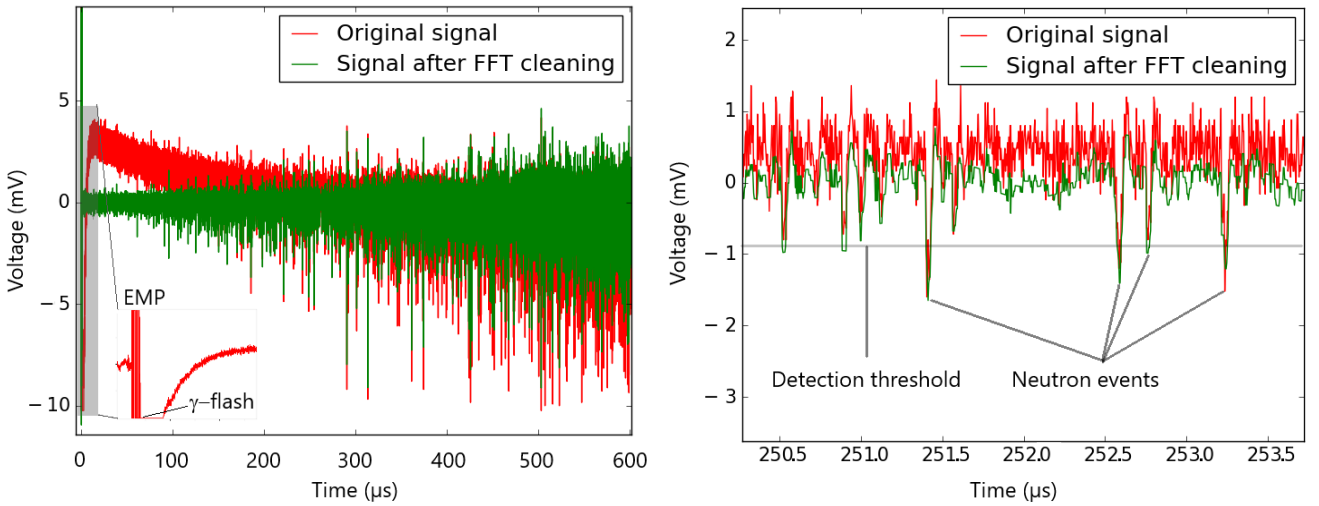

(a) (b)

Figure 4.30: (a) : Raw MCP signal in red. The curve shows a strong overshoot after the γ-flash. For accurate peak detection, the signal is processed and low frequencies, as well as the offset, are removed by a Fourier filter and high-frequency oscillations and noise is suppressed via a median filter. The green curve is the result of the processing. (b) : A magnification of (a). The position and the shape of the neutron peaks did not change and therefore the energy resolution is not affected by this method. A threshold for peak discrimination is visualized by the grey line. The peak detection is improved as the offset is reduced.

A borated Multi Channel Plate (MCP) [Scientific, 2019] in chevron configuration [Wüest et al., 2007] was used for the neutron spectroscopy. The neutron detection efficiency of this detector was 50 % at 25 meV [ProxiVision, 2019][Kleinschmidt, 2017][Knoll, 2000]. The active area of the detector is 40 mm in diameter and is placed inside a EMP shielding to reduce noise during the shot. The detector is a prototype in which the anodes of all channels inside the MCP are connected to create a single output channel with a fast response time at the cost of the spatial resolution. When a neutron is absorbed by the boron inside the channel wall, an α particle is emitted which creates an electron avalanche inside the channel due to the electric field. This electron current then can be detected at the anode. A single neutron event produces a signal with a FWHM from 10 to 25 ns and a peak voltage between 1 and 10 mV, depending at which depth the neutron was absorbed. Higher peaks have a larger FWHM and are caused when an alpha particle is emitted closer to the surface, then the electrons have a longer path inside the channel for multiplication and they experience a higher potential difference from the electric field. Taking the 10 ns as a minimum condition to clearly identify single events, a maximum detection rate of 100 n/μs is possible for this detector. To calculate the maximum acceptable neutron fluence, the detection efficiency has to be taken into account. The main reaction for neutrons inside the MCP is ^{10}B(n,α)^{7}Li which has a cross section that decreases with $\sim 1/\sqrt{E}$ as seen in figure 2.4 and therefore the detection efficiency decreases as well. For 1 eV the efficiency is theoretically reduced to 8 %, to 4 % at 4 eV and to 1.7 % at 21 eV. Therefore a fluence of 200 n/(μs·cm^2) or a peak flux of at the detector of 2·10^8 n/(s·cm^2) is tolerable at 4 eV.

In an LDNS experiment at PHELIX the output of the detector was measured as a function of time after a shot. The red curve in figure 4.30 (a) is the raw signal. For better visibility, a zoom into the first 10 μs is shown in the lower-left part to display the fast oscillations from the EMP followed by an oversaturation caused by the γ-flash. The EMP signal starts 700 ns before the γ–flash. The latter causes

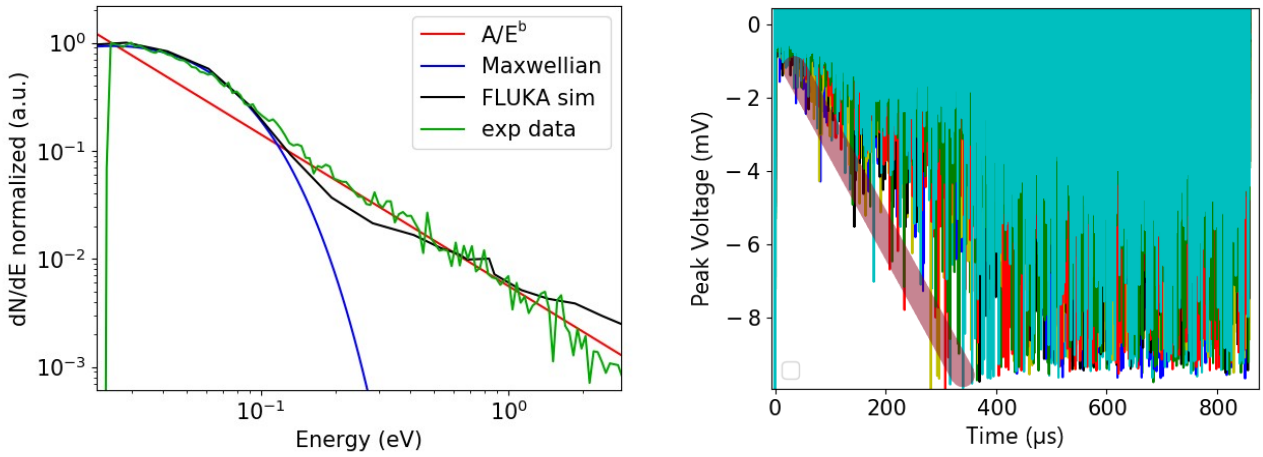

(a) (b)

Figure 4.31: Left: A comparison of the normalized neutron spectrum detected by the MCP (green) and a FLUKA simulation (black). A Maxwellian distribution was fitted to the data with $T_{fit} = 291(15)$ K. In the thermal regime experiment and simulation show a good agreement but for E > 0.11 eV they deviate and the neutron numbers decrease with $E^{-1.4}$ (red graph) for the measured data and with $E^{-0.92}$ for the simulation. Right: MCP neutron event peak heights as a function of time for multiple shots. The maximum peak height increases with 27(3) μV/μs until in reaches a maximum of 9.5(2) mV at 350(50) μs, as indicated by the red bar. This behavior indicates a change in acceleration voltage over time inside the MCP connected to a lower sensitivity for energies > 110 meV.

a strong overexcitation inside the MCP. The MCP remains in saturation for 1.8 μs followed by a swing back that causes an overshoot up to +3 mV of the baseline signal. This overshoot decays over $\approx$ 350 μs back to a mean value of 0 mV. Before neutron events can be properly identified, the large background from the overshoot has to be removed as well as electrical noise. The first part of the signal processing was done by removing low frequencies and periodic oscillations via a fast Fourier transformation (FFT) filter [Nunez-Iglesias et al., 2017]. To remove high-frequency aperiodic noise, a median filter was applied. The result is the green curve in figure 4.30 (b) which shows an exemplary zoom into the signal to compare the position and the shape of the neutron peaks, before and after the signal processing. The position and therefore the energy of the peaks has not changed but the offset is removed as well as a large fraction of the noise. In the next step, a peak detection algorithm is recording the position of every neutron event with a threshold voltage > 0.94 mV. This number was chosen to keep the rate of false positive peak detection low by risking to have a higher number of false negatives. This is beneficial as lower detected neutron numbers can be compensated by more shots, but a higher background distorts the spectroscopy, especially at the resonances. The voltage was derived from comparisons between background shots that did not produce any neutrons and normal shots.

The accumulated data of 9 shots can be seen in figure 4.31. The neutron numbers per energy bin were corrected with the expected reduction in detection efficiency from the decreasing boron cross section (green graph). To compare the response function with a FLUKA [Battistoni et al., 2007] simulation (black graph), the curves were normalized to their maximum. Both graphs show a strong agreement in the thermal region around 25 meV. A Maxwellian fit to the experimental data reveals a moderator temperature of 291(15) K = 18(15)°C. Applying the same fit to the simulation data, a temperature of 289 K is the result. This shows that the correction of the detector response with $1/\sqrt{E}$ applies to the thermal neutron data as the Maxwell distribution was not distorted for the scaled signal.

For neutron energies larger than 110 meV, the FLUKA simulation and the detected signal show large deviations. As discussed in equation 2.41, the neutron spectrum in the epi-thermal regime follows a $1/E^b$ dependency. The simulation of this setup would predict b = 0.92(2) but a fit to the experimental data (red) reveals b = 1.4(1). This violates the condition b < 1 as discussed earlier and hints towards a discrepancy between the actual detector efficiency and the assumed $1/\sqrt{E}$ dependency for higher energies or earlier detection times. To investigate this phenomenon, the peak heights of all neutron events for different shots are plotted over time in figure 4.31 (b). Between 0 and 350(50) μs there is a clear trend in peak height increase indicated by the dark red bar. Afterwards, the maximum peak height remains constant, slightly below 10 mV. This timing coincides with the relaxation time of the MCP output voltage seen in figure 4.30. The corresponding energy to neutrons arriving at 350 μs is 140(40) meV which is within the margin of error fitting to the 110 meV at which point the experimental data and the simulation start do deviate.

The working hypothesis is that the γ-flash is over-saturating the MCP and the high electron current inside the detector is temporally reducing the electric field inside the MCP. The argument could be made that the increasing amplitude is related to slower neutrons being absorbed closer to the surface because of the higher absorption probability and therefore leading to a higher electron gain. At a closer look, this argument is decrepit since neutrons are absorbed randomly inside the MCP if their mean free path is larger than the MCP thickness leading to a stochastic distribution of peak heights. Therefore at least 10 % of the neutrons would be absorbed in the upper 10 % of the MCP and thus leading to corresponding peak heights. In contrast to that, out of 2923 counted events between 0 and 350 μs none of these maximum peak heights show a significant deviation from the red marking in figure 4.31.

To avoid this effect for future experiments, the direct line of sight from the MCP to target and catcher has to be blocked with high-Z materials to avoid a high γ-exposure. If this is not possible through geometric constrains, a decoupling of the MCP from the high voltage during the first few μs after the laser target interaction could also solve this issue. If non of these options is successful, the MCP could be exchanged with a ^6Li-glass scintillator coupled to a Photo Multiplier Tube (PMT). This has the benefit that the scintillator can be placed in the direct line of sight of the catcher while the PMT can be placed behind a lead shielding and the photons can be transported via a light guide. The downside of this approach is the longer decay time of ^6Li-glass scintillators which is around of 100 ns [Scintacor, 2019] and therefore reducing the accuracy.

The discussion of the detector completes the process of the optimization and theoretical characterization of a laser-driven neutron source setup for a neutron resonance transmission analysis. The gained insights were used to experimentally validate the predictions and to demonstrate the applicability of an LDNS for NRS.

5 Experimental Results for a Laser-Driven Neutron Material Analysis

In this chapter the results from an experimental campaign at the PHELIX laser are presented. This campaign aimed to conduct a NRTA measurement on a tungsten sample as proposed in section 4 to demonstrate that it is possible to identify materials by using an LDNS. Besides this main goal several other detectors were operated in a parasitic mode to characterize the neutron spectrum and to perform thermal neutron radiographies. The setup can be seen in figure 5.1.

For this chapter first an overview of the experimental conditions and the setup is given and the source is characterized. Afterwards the experimental results are discussed in detail. In addition, the results are used to predict their applicability for material research at more advanced laser neutron facilities.

5.1 Experimental Conditions

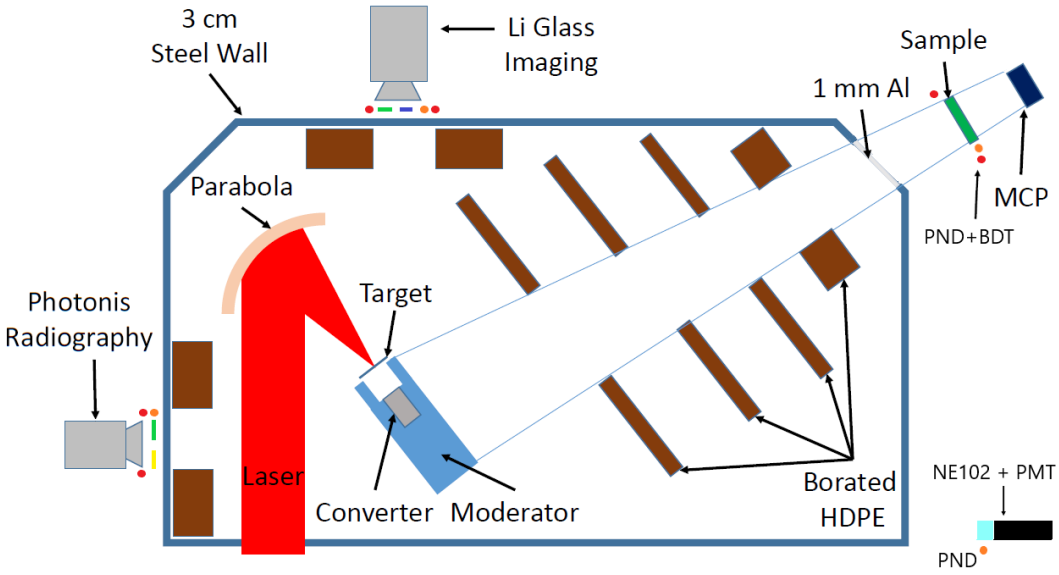

Figure 5.1: setup at the Phelix laser facility to conduct neutron resonance spectroscopy. In parasitic operation mode two thermal neutron radiography detectors were operational and a PMT coupled to a NE102 plastic scintillator for fast neutron detection. Red circles are thermal bubble detectors and orange circles are fast bubble detectors.

5.1.1 Methodes

In this setup the MCP for a NRTA measurement, two gatable neutron radiography detectors as well as a fast neutron detector were present. The latter was consistent of a NE102 plastic scintillator coupled with a PMT (E2979-500 MOD) [Photonics, 1998]. The orange circles are Personal Neutron Dosimeters (PND) and red circles are Bubble Detector Thermal (BDT) from Bubble Technology Industries [Harrison et al., 2017] [Vanhavere et al., 2002][Ing et al., 1997]. As a converter material a 3 cm long beryllium cylinder is used with a 1.5 cm radius. In the front of the catcher a conical recess was present with a radius of 0.75 mm. The catcher was protected by a 1 mm thick Kapton layer from the plasma ablation. The B-HDPE is used at several positions for neutron collimation. A 1 mm thick aluminum flange is used in the NRS beam path to reduce scattering. The laser parameters in this experiment were 180(12) J in 600(100) fs on a 4(1) μm spot diameter (FWHM) . This allowed intensities between 10^{20} and 10^{21} W/cm^2. The ns-contrast was at 10^{-7} and the 100 ps-ASE pedestal contrast at 10^{10} as seen in figure 4.13. The low ns-contrast was caused by a 3 ps long pre-pulse at 1.4 ns before the main pulse. This limited the acceleration efficiency of the protons as well as the cut off energy as discussed in section 4.2.5. RCF stacks [Wagner, 2014] and a Thomson parabola [Ding, 2018] were used to characterize the ion beam. Mean cut off energies were at 33(10) MeV. Deuterated polystyrol targets with 600-900 nm thickness were used as well as 10, 25 and 50 μm thick silicon targets. Through the low contrast, 50 μm as well as 25 μm showed the highest performance. At PHELIX under similar conditions but with high contrast, average cut off energies of 70 MeV were observed at target thicknesses of up to 1 μm [Wagner et al., 2016]. The thickness scaling from section 4.2.5 with $d^{-0.21}$ from 1 to 25 μm would predict a reduction in cut off energies down to 36 MeV which is close to the observed 33 MeV. The scaling with $d^{-0.43}$ would predict 18 MeV cut off energies which is underestimating the proton energies for this laser system.

5.1.2 Neutron Source Characterization

The low contrast in this beamtime reduced the neutron production. This makes the measurements not representative for lasers like PHELIX. To compensate this effect for the predictions on other lasers, the neutron production is compared to a similar experiment at PHELIX in 2017 to estimate how many neutrons would be available for the measurements under normal operation conditions. The neutron dose was measured with PND and BDT detectors at $\approx$ 45 degrees towards laser forward direction behind the moderator. Figure 5.2 (a) shows the measured neutron flux for the operation with and without a pre-pulse. With the pre-pulse the thermal as well as the fast neutron flux are reduced by a factor of 25. This means that all experiments in this section are performed with 25 times less neutrons than it would be possible under normal conditions at PHELIX.

The validity of the neutron flux measurements done with the BDT and PND detector needs to be checked to verify this claim. To do this one can calculate the thermal moderation ratio:

$$R_{mod} = \frac{N_{thermal}}{N_{fast}} \tag{5.1}$$

This value is rather similar for both experiments with $R_{mod} = 2.51(1.7)$ for this beamtime and $R_{mod} = 2.47(0.5)$ for the previous beamtime. This is either the result of the usage of similar moderator geometries or it is connected to the sensitivity of the BDT detectors for fast neutrons. Every BDT reportedly [Ing et al., 1997] has a 10(2) times lower sensitivity to dose detection from fast neutrons than for thermal neutrons. During these campaigns the measured dose for every PND was routinely 10 times higher

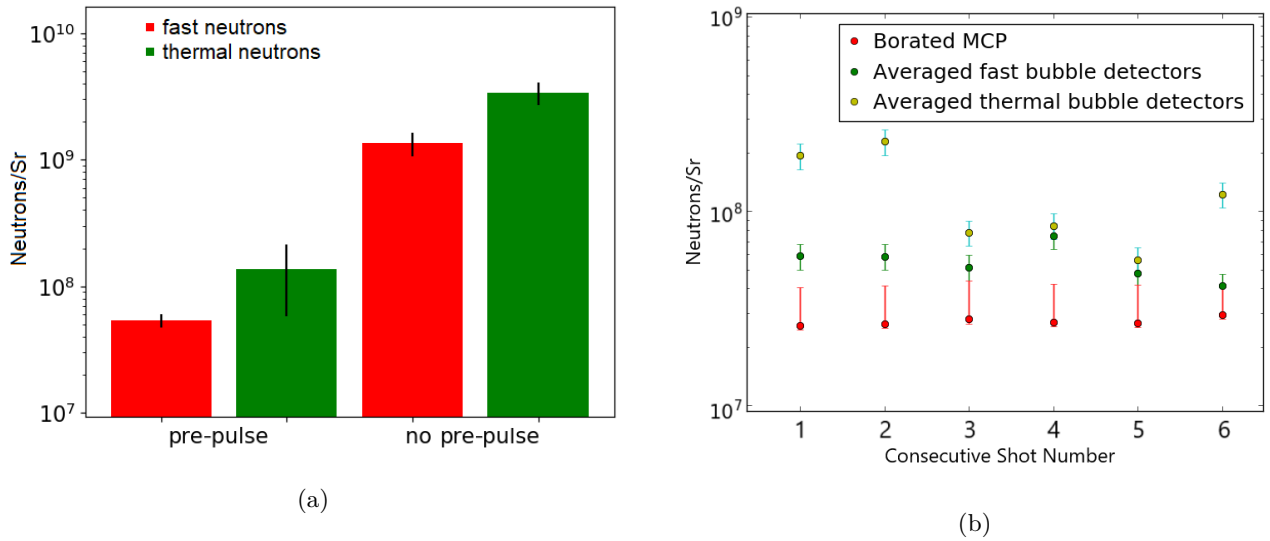

(a) (b)

Figure 5.2: (a) : Neutron numbers per steradiant for thermal and fast neutrons measured with PND and BDT detectors in this and the previous beamtime in december 2017 at PHELIX without the presence of a pre-pulse as see in figure 4.13. The lower contrast resulted in a reduction in measured neutron flux by a factor of 25 in thermal and fast neutrons. (b) : Neutron flux for consecutive shot numbers detected with PND, BDT and with the MCP. The fast neutron flux and the MCP measurements show a high stability while the BDT measurements have large fluctuations caused by statistical uncertainties.

than for the corresponding BDT. The BDT dose was therefore corrected by the expected dose from fast neutrons. Since there was no absolute calibration of the bubble detectors it cannot be ruled out that fast neutrons had a larger contribution to the BDT dose than anticipated. Slight variations in the received BDT dose have a much larger effect on the neutron numbers since the thermal conversion coefficient from mrem to N/cm^2 is 36 times higher than for neutrons with 1 MeV [US NRC, 2014]. In addition, the low number of bubbles in the BDT in the range from 1 to 10 bubbles per shot lead to statistical fluctuations.

It is therefore possible that the thermal neutron count measured by the BDT is overestimated. The measurements done with the PND detectors are not affected by this effect. As these detectors also see a factor of 25 less neutrons, this can be seen as still valid. With this conclusion, from now on only results from the experiment with the pre-pulse are discussed. The measurements done with the MCP represent a more reliable source for the thermal flux as this detector is capable of single neutron detection, although it is quite likely to underestimate the neutron flux as discussed in section 4.6. This underestimation is indicated by the large error-bars to higher neutron numbers in figure 5.2 (b). In this plot 6 consecutive shots are displayed with calculated neutron numbers from PND and BDT detectors as well as measured with the MCP. For this plot the flux of all PND and BDT displayed in figure 5.1 were averaged to reduce statistical fluctuations. Shot 1-5 were taken on 50 μm silicon targets, while shot 6 is a 25 μm target. It is noticeable that the MCP indicates much lower shot to shot fluctuations with $\overline{N}_{\mathrm{MCP}}$=2.7(1)$\cdot 10^7$ n/sr than the bubble detectors with $\overline{N}_{\mathrm{PND}}$=5.4(1)$\cdot 10^7$ n/sr and $\overline{N}_{\mathrm{BDT}}$=1.3(6)$\cdot 10^8$ n/sr. The ratio $\overline{N}_{MCP}/\overline{N}_{PND}$ is 0.5(1) and is therefore much smaller than $\overline{N}_{BDT}/\overline{N}_{PND}$=2.4(1) . From a comparison to a PHITS simulation in figure 4.22 it is possible to see that the theoretical ratio of N_{therm}/N_{fast} is 0.18(1) and therefore even smaller than suggested by the MCP measurements. This discrepancy has to be further investigated in future beamtimes to guarantee sufficiently accurate measurement results.

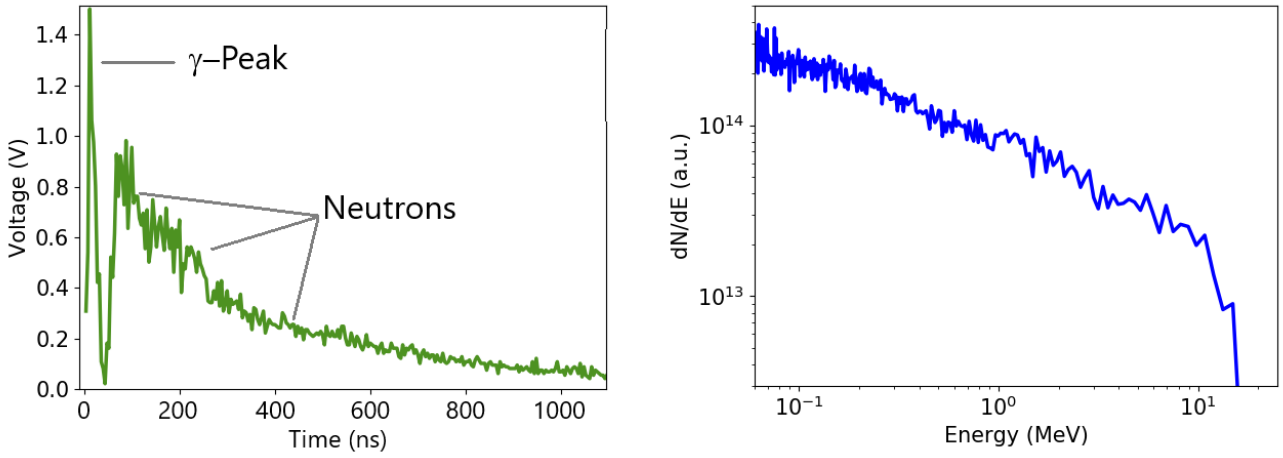

(a) (b)

Figure 5.3: (a) : Voltage output from a PMT coupled to a plastic scintillator. On the left side the excitation from the γ-flash is visible which almost decays to base level before the excitation from fast neutrons is beginnig. (b) : Conversion of the neutron signal into an energy spectrum while considering the differences in σ_{scat} for hydrogen collisions inside the scintillator. Neutron cut off energies are at 16(2) MeV.

The raw data from the fast neutron detector is shown in figure 5.3 (a). The arrival of the γ-flash causes a sharp spike at the beginning which decays quickly before the first neutrons arrive. An exponential decay was fitted to the decaying slope of the γ-flash and is then subtracted from the neutron signal to exclude non-neutron contributions. The TOF method was used to convert the neutron signal into the energy domain. In addition to that, the signal was convoluted with the decreasing scattering cross section of hydrogen. This has to be done as the interaction probability inside the scintillator is changing with the neutron energy and this has to be compensated. The result is displayed in figure 5.3 (b). It can be seen that the neutron spectrum has cut off energies of 16(2) MeV. This value is very close to 50 % of the cut off energy of the ion beam. This result is consistent to the simulations in figure 4.19 which predicted neutron cut off energies around 18 MeV. With a characterized neutron source it is now necessary to determine the experimental background contributions and to compare them to the predicted values from section 4.5.

5.1.3 Determination of Uncertainties and Background Contributions

For a successful NRTA, three prerequisites are necessary. First, it has to be ensured that all neutrons, that are counted at the detector have passed through the sample. The second is, that neutrons that have scattered inside the sample or at the collimator are removed from the beamline. The third prerequisite is that the TOF uncertainty at the MCP is smaller than the detector bin with used for resolving the resonance. The first condition is met by the usage of the collimator, discussed in section 4.5 in combination with a sample size, larger than the detector. The second prerequisite is mostly met but 7(2) % background contribution from fast neutrons scattered in the collimation layer is predicted. This has to be verified experimentally.

The third requirement is determining the distance between moderator and detector d. If neutrons of a certain energy E_n are detected with a time spread Δt_n the assigned energy will be $E_n + \Delta E_n$ which

is proportional to $\left(\frac{d}{t+\Delta t}\right)^2$. For a fixed Δt_n in an experiment its impact on the energy uncertainty can be reduced by increasing d. This method is discussed in detail in section 6.3. The contributions to the energy uncertainty in this measurement come from four components:

- the beam pulse duration t_b
- the point of absorption in the detector L_d
- the moderation time t_m
- the uncertainty of origin inside the moderator L_m

The beam pulse duration describes the duration of the incoming ion pulse that is creating the neutrons. In the case for LDNS, the ion pulse is generated in the regime of fs to ps by the laser interaction. The catcher is 3 cm away from the target giving a t_b TOF difference of 1.2 ns between 2 MeV and 33 MeV for protons and 1.6 ns for deuterons. This time uncertainty if therefore negligible for LDNS.

The position of absorption in the detector is limited to the thickness of the micro-channel plate and is small in comparison to the beam length and only plays a minor role. The largest contributions to the uncertainty are the last two points. First the moderation time t_m, i.e. the time the neutron moves inside the moderator before it reaches its final energy through collisions and second the L_m which is the distance from the last scattering event towards the moderator surface. As both of these processes depend on the moderator configuration it is difficult to find an analytical solution to these problems, therefore L_m and t_m are composed into t_s which describes the time delay between neutron generation and crossing the moderator surface.

This time was simulated with PHITS and predicted a 1 μs FWHM pulse width for 4 eV. The median crossing time $\overline{t_s} = 0.75\,\mu s$ can be treated as an offset in time and the FWHM Δt_s is treated as an uncertainty.

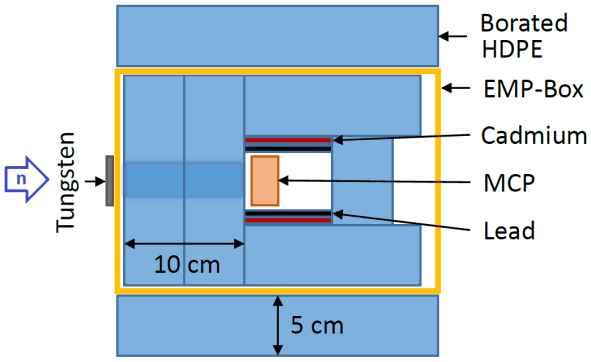

Figure 5.4: The MCP is shielded by 10 cm of B-HDPE in all directions except the back direction where shielding was reduced to 5 cm. The tungsten sample is placed outside the Faraday cage. In direct proximity to the MCP a layer of 1 mm thick cadmium is installed to absorb scattered thermal neutrons.

The detector was placed at 1.804(5) m distance surrounded by 10 cm of 5 % B-HDPE with a collimator opening into the direction of the moderator as seen in figure 5.4. A 1 mm thick copper casing was acting as a Faraday cage for EMP protection. 1 mm of cadmium around the detector prevented scattered thermal neutrons from entering the detector from the sides. Additionally, a lead layer is reducing the background contribution of absorption-γ-radiation. The tungsten sample is placed in front of the collimation entrance at the outer side of the Faraday cage. Placing the sample at this distance and not directly in front of the detector has two benefits. With the larger distance, the MCP covers a smaller solid angle and therefore neutrons that are scattered inside the sample have a higher likelihood of missing the detector. Since the ^{182}W resonance is comprised of an elastic scattering and an absorption resonance, this increases the resonance contrast as more neutrons are removed at resonant energies. Also, scattered neutrons have a longer beam path than non-scattered neutrons and therefore the TOF resolution would be decreased.

The second benefit comes from a reduction in γ-background. Neutrons that are absorbed via a (n,γ) reaction release radiation that could be detected by the MCP and be falsely identified as a neutron. This is especially important at the resonance. If the sample is directly in front of the MCP, then the increase in absorption at the resonance leads to a higher γ-presence. In this case, this increase would overlap with the expected decrease of events during the resonance, mitigating the resonance depth.

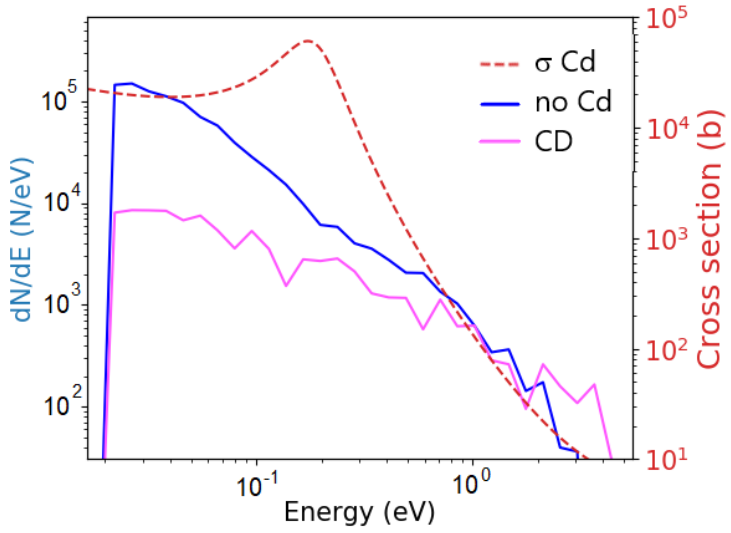

Figure 5.5: Blue: single-shot neutron spectrum with a free beam path between moderator and MCP. The thermal peak at 25 meV is visible. Red dotted: The cross section for the ^{113}Cd(n,γ)^{114}Cd reaction. Pink: The neutron beam path was blocked with 1 mm thick cadmium. The high cross section acts as a black resonance filter and events detected inside the resonance are contributions from the background. The signal to noise ratio at 25 meV is 17(1):1.

To determine the signal to noise ratio, a 1 mm thick cadmium sample was placed inside the beam path. Cadmium, especially the isotope ^{113}Cd has a high cross section for a neutron capture reaction on the order of $>10^4$ b as it can be seen in figure 5.5. This Cd sheet functions as a black resonance filter and effectively no thermal neutrons should be detected. The blue graph in figure 5.5 is a single-shot without Cd between MCP and moderator. The Maxwellian peak from thermalized neutrons below 200 meV is clearly visible from the change in the slope gradient.

The pink graph is a single shot with the cadmium sheet between detector and moderator. The count rate for energies above 1 eV is for both shots rather similar. As the Cd cross section increases towards lower energies, both slopes are diverging. On the pink signal there is no indication of thermalization and the count rate at 25 meV is 17 times smaller than for the free propagating beam. Therefore it is possible to say, that this setup managed to achieve a signal to noise ratio of 17(1):1 in the thermal regime (at 25 meV). This is in rather good agreement with the simulations conducted in section 4.5 which predicted a ratio of 15(4):1.

Events detected at this black resonance can have multiple origins. One option is that fast neutrons have scattered somewhere in the target area and are directed towards the detector from a transversal direction. Since they have a high energy, they can penetrate deeply into the borated HDPE surrounding the detector. There they are moderated by the hydrogen and have a chance to reach the MCP causing an event. This type of background could be reduced by an increase in borated HDPE shielding around the detector.

The option of neutrons scattering further upstream in the collimator also exists. If a neutron travels through a distance with a certain energy and undergoes a scattering event during which it loses energy, then the arrival time at the detector will not represent its energy as the total time will be the sum $t_n = v_1 \cdot s_1 + v_2 \cdot s_2$. The collimator design was made to reduce these events and the simulation in figure 4.28 (a) predicts no significant share from these neutrons.

The largest contribution as it has been simulated in section 4.5 is from fast neutrons impinging directly from the catcher on to the last layer of the collimator where they are moderated down to the (epi)-thermal regime and cause background contributions.

5.1.4 Neutron Resonance Transmission Analysis on a Tungsten Sample

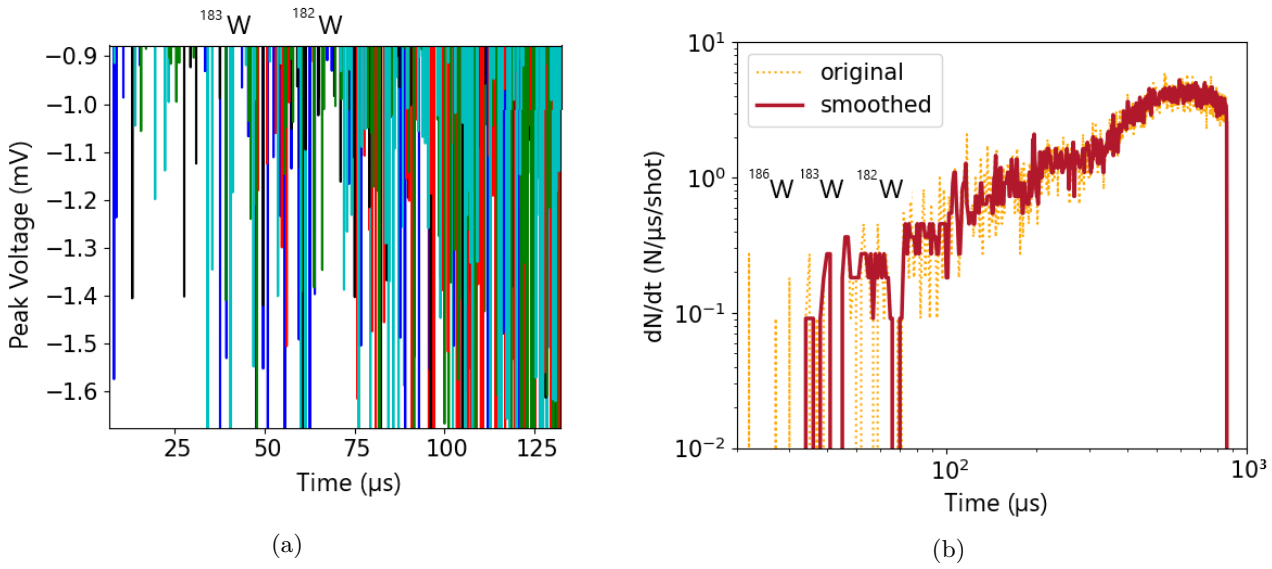

Figure 5.6: (a): MCP peak height distribution as a function of time for several shots, indicated by different colors. The isotope names indicate at what time neutrons would be affected by the resonances. In close proximity to the resonances the peak density as well as peak height is decreased. (b): Detected neutrons/μs from (a) as a function of time normalized to one shot. The ^{182}W resonance is clearly visible, while the ^{183}W resonance is close to the start of the discontinuous part of the spectrum. For the ^{186}W resonance the spectrum is discontinuous and cannot be resolved anymore.

In the next step, the cadmium sample was replaced by a 50x50x2.7 mm tungsten plate. 11 neutron spectra were recorded in this configuration to gain sufficient statistical data. First, the event pulse height over time will be investigated to search for indications of the presence of a resonance. The result can be seen in figure 5.6. Every color represents a different shot to facilitate the recognition of patterns inside the data. The sample was composed of natural tungsten which consists of the isotopes ^{182}W (27 %), ^{183}W (14 %), ^{184}W (31 %) and ^{186}W (28 %) [NIST, 2019]. ^{182}W has the resonance with the lowest energy from these isotopes at 4.15 eV followed by ^{183}W with a resonance energy of 7.6 eV. The time of arrival for these energies has been indicated in figure 5.6 by the corresponding isotope symbol. The center of

the ^{182}W resonance is expected to occur at 64 μs and neutrons that are predicted to be resonant with ^{183}W will arrive at 47 μs. At these arrival times, a clear reduction in peak height as well as in detected peak density is observable. Around 65 μs a 4(1) μs long period occurs with no detected neutrons in a region of the spectrum where the average event density is 3.1(7)N/μs.

This is clearly visible in figure 5.6 (b) where the detected event density is displayed in neutrons/μs over time, normalized by the number of shots. The orange dotted line represents the original data, while the red line is smoothed with a three-point median filter to remove fluctuations from poor statistics. The second gap starts at 41.7 μs and has a width of 4(0.5) μs with a surrounding peak density of 2.2(3) N/μs. This lower neutron density is the result of the decreasing sensitivity from the boron cross section with higher energies as well as the decreased sensitivity caused by the γ-flash for earlier arrival times. The tungsten isotope ^{186}W has a wide resonance at 18 eV which reduces the transmissivity between 35 and 25 μs by more than 50 % and therefore worsening the signal to noise ratio in this regime even further. In this regime in figure 5.6 (b) the spectrum is discontinuous and no resonances can be resolved anymore. For this reason, only the resonances for isotope 182 and 183 will be further discussed.

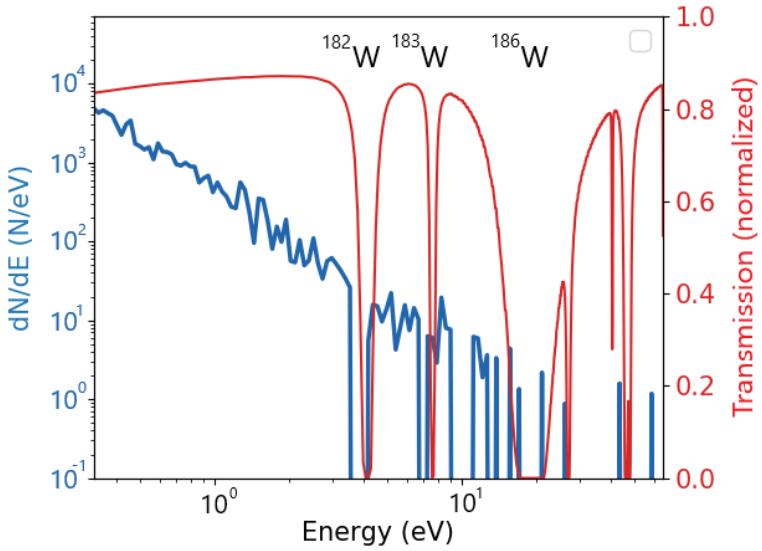

Figure 5.7: Neutron resonance capture analysis of a 2.7 mm thick tungsten sample. The blue graph is the data from figure 5.6 transferred into the energy domain. The red graph displays the theoretical transmission of the neutron flux through the sample, normalized to 1 for every energy. Resonances in the experimental data are slightly shifted towards lower energies as where they would be expected.

Figure 5.7 displays the data from figure 5.6 transferred into the energy domain in blue. The calculated transmissivity for a 2.7 mm thick tungsten sample of natural composition is plotted in red. The resonance of ^{182}W is 0.61(5) eV wide and has its center at 3.88(2) eV. This is a shift of 0.27 eV or 6.5(5) % towards lower energies and an increase in width by 20 % in comparison to the theoretical curve. The ^{183}W resonance is shifted by 0.64(20) eV or 8.4(2.6) % towards lower energies and has its center at 7.0(2) eV. The width is increased by 51(60) % from 0.35 eV to 0.61(20) eV. The uncertainty is calculated by varying the energy bin width in the algorithm. The increase in width is most likely caused by the small number of neutrons available and will be discussed later as well as the energy shift. First, it has to be determined if the drop in count rate is caused by a resonance or if it is the result of statistical fluctuations that coincide with the resonances.

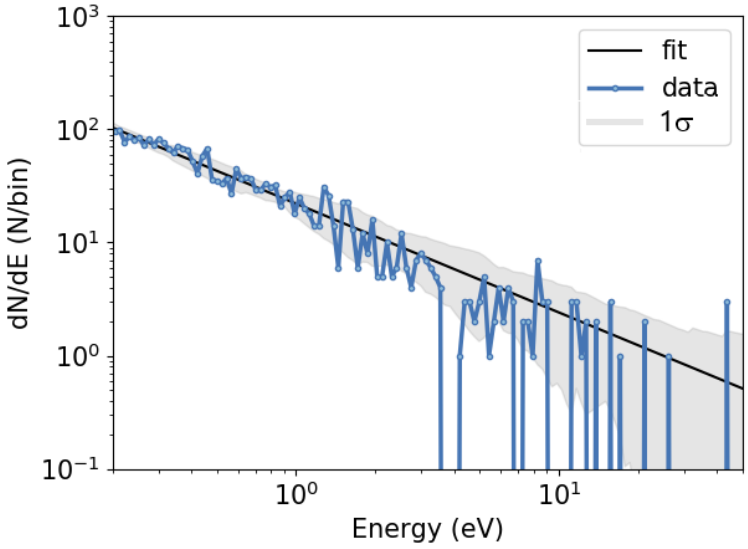

Figure 5.8: Experimental data in blue and the $1 \cdot \sigma$-range for each data point calculated by statistical deviations from the fit function displayed in black. At the first resonance four points are outside the $1 \cdot \sigma$ environment while it is only one point for the second resonance.

For a sufficient assessment of the resonances, an evaluation of the fluctuations of the signal has to be conducted. In figure 5.8 the resonance data is plotted in the form of detected neutrons per energy bin. For this data, a function was fitted in the form of

$$\overline{N}(E) = 22.04 \cdot E^{-0.96} \tag{5.2}$$

represented by the black line. This function shows a good agreement with the measured data and can be used as a reference for fluctuations. It is also visible that the fluctuations increase with neutron energy which has to be taken into account. To estimate the average fluctuations in a given region the standard deviation from the fit function in equation 5.2 is calculated by

$$\sigma(E_n) = \sqrt{\frac{1}{15} \sum_{k=n-7}^{n+7} (\overline{N}(E_k) - N(E_k))^2} \tag{5.3}$$

where $N(E_n)$ is the experimental data at the given energy bin. In figure 5.8 the grey area symbolises regions $< 1 \cdot \sigma$ deviation from the fit function. In the next step, all points at the resonance that are outside the $1 \cdot \sigma$ regime are assigned to a likleyhood that this fluctuation occurred by chance. For ^{182}W four consecutive energy bins are outside the $1 \cdot \sigma$ environment.

The necessary calculation can be done by expressing the deviation $\Delta_{E_n} = \frac{\overline{N}(E_n) - N(E_n))}{\sigma(E_n)}$ in terms of multiples of σ:

- $\Delta_{E_1} = 1.80 \cdot \sigma \hat{=} 3.6\%$
- $\Delta_{E_2} = 1.82 \cdot \sigma \hat{=} 3.4\%$
- $\Delta_{E_3} = 1.70 \cdot \sigma \hat{=} 4.5\%$
- $\Delta_{E_4} = 1.32 \cdot \sigma \hat{=} 9.3\%$

To calculate the likelihood for each bin to undergo a statistical fluctuation that large just by chance one has to integrate the Gaussian-shaped probability density function from $-\infty$ to Δ_{E_n} and determine the complement:

$$F(\Delta_{E_n}) = 1 - \int_{-\infty}^{\Delta_{E_n}} -\frac{1}{2\pi} e^{-\frac{x^2}{2}} \tag{5.4}$$

This probability is indicated above for every energy bin. The total probability that all four data points at the resonance are at these low levels per chance can be calculated by the product of all individual likelihoods:

$$\prod_{n=1}^{4} F(\Delta_{E_n}) = 5 \cdot 10^{-4}\ \% \tag{5.5}$$

This likelihood is essentially zero and it can be claimed with high confidentiality that this resonance is not the result of statistical fluctuations but caused by the presence of tungsten in the beam path.

For the resonance of ^{183}W only one energy bin is outside the $1 \cdot \sigma$ range with a Δ_{E_n} of $1.67 \cdot \sigma$. This determines according to equation 5.4 and 5.5 the likelihood of being a statistical fluctuation to 4.7 %. The threshold of statistical significance is 5 % [Abdi and Salkind, 2007] for which the result falls slightly below but changing the averaging range in equation 5.3 by ±30 % can increase the likelihood to 5.4 %. Varying the energy bin width in the algorithm to a higher resolution decreases the likelihood down to 1 %. Since these parameters can be chosen arbitrarily in this phase space, the upper bound of the likelihood is set to 5.4 % and the lower bound to 1 %.

The resonances observed in this experiment are shifted towards lower energies in comparison to literature values [Brown et al., 2018]. The origin of this shift has to be inspected to uphold the authenticity of the resonances. Both resonances show a shift in the same direction, suggesting either a systematic error in the detector distance or in the determination of the neutron propagation time. In the evaluation algorithm, the time is determined by:

$$t = t_a - t_0 - t_c - t_s \tag{5.6}$$

where t_a is the detection time of the neutron. t_0 is the arrival time of the γ-flash in the detector signal. $t_c = 6$ ns is the time delay for light to propagate from the catcher to the detector and t_s is the average scattering time it takes for neutrons to be moderated to a certain energy and to cross the moderator surface. t_c was estimated by PHITS simulations for this setup to be around 1 μs for 4 eV as seen in figure 6.7. For the theoretical values and the experimental data to be in agreement, an additional offset t_{err} is required. For ^{182}W this offset can be calculated to be $t_{\text{err}} = 2.2(2)$ μs and for ^{183}W $t_{\text{err}} = 2.1(7)$ μs these values are in agreement in consideration of their uncertainty. The origin of the 2.1 μs delay could be caused by the electrical high noise environment in the target area in combination with the over-saturation of the first

2-3 μs, aggravating an accurate determination of t_0. To reduce this uncertainty for future measurements an improved Faraday cage has been designed and tested to increase the EMP resilience.

There is also the possibility that the length from the moderator to the detector has been underestimated. The measured distance from the center of the moderator surface towards the detector is 1.80(1) m and for a sufficient compliance of the resonances a total distance of 1.87(1) m and 1.88(3) m for ^{182}W and ^{183}W would be required. There is a certain variance for neutron origins inside the moderator as well as the uncertainty of the distance measurement, but these values are $\approx$ 1 cm and therefore a 8 cm shift is not possible. Also, the average time neutrons need to cross the surface is already included in t_s making this contribution even smaller. A combination of several systematic errors affecting the position and the width can be assumed since the experimental setup was rather complex. A list of contributing uncertainties is displayed in table 5.1. It has to be noted that [Kleinschmidt, 2017] also observed a shift of an indium resonance by 0.16 eV in her experimental data even though this shift was in the positive direction.

Table 5.1: A listing of dominant contributing uncertainties. Effects that contribute to the position are systematic errors that can be adjusted for by changes in the setup. Uncertainties in the width are the result of random processes, inherent to the setup.

origin	^{182}W	^{183}W	position / width	uncertainty value
distance	0.04 eV	0.08 eV	position	1 cm
Δt_0	0.12 eV	0.13 eV	position	1 μs
data processing	0.02 / 0.05 eV	0.2 / 0.2 eV	position / width	bin width
Δt_s	0.12 eV	0.13 eV	position / width	1 / 0.5 μs
Doppler broadening	0.05 eV	0.06	width	20°C
total	3.88(0.18) eV	7.0(0.29) eV	position	-

5.2 Spatially Resolved Material Analysis

The neutron beams provided by an LDNS are also of large interest for conduction neutron radiographies and especially NRI. This section will discuss the results of the two radiography detectors present in that beam-time.

5.2.1 Thermal Neutron Radiography

The neutron attenuation inside a sample depends on the nucleus configuration of present isotopes and the material number density. With a detector capable of spatially resolving neutrons, a radiographic image of a sample can be made. The attenuation of the neutron signal on each pixel is proportional to $\exp(-\Sigma_{tot} \cdot d)$ as stated in 2.27. Therefore, for a known material the thickness d be calculated by the attenuation. It is also possible for a given thickness to determine the macroscopic cross section Σ_{tot} and thereby identify the material.

To prove that this method is possible with an LDNS, a thermal neutron radiography of 1 mm thick sheets of indium and cadmium in front of a 2 mm thick lead shield was conducted at the PHELIX facility. The

experiment was operated in parallel to the NRS as seen in figure 5.1 on the left side. The detector was placed in front of a 1 mm thick Al flange in the target chamber wall and with a direct line of sight to the moderator. The angle between detector and the moderator side surface was 52°. This slightly distorted the time of arrival of neutrons but since image integration times were much larger than the distortions, this can be neglected.

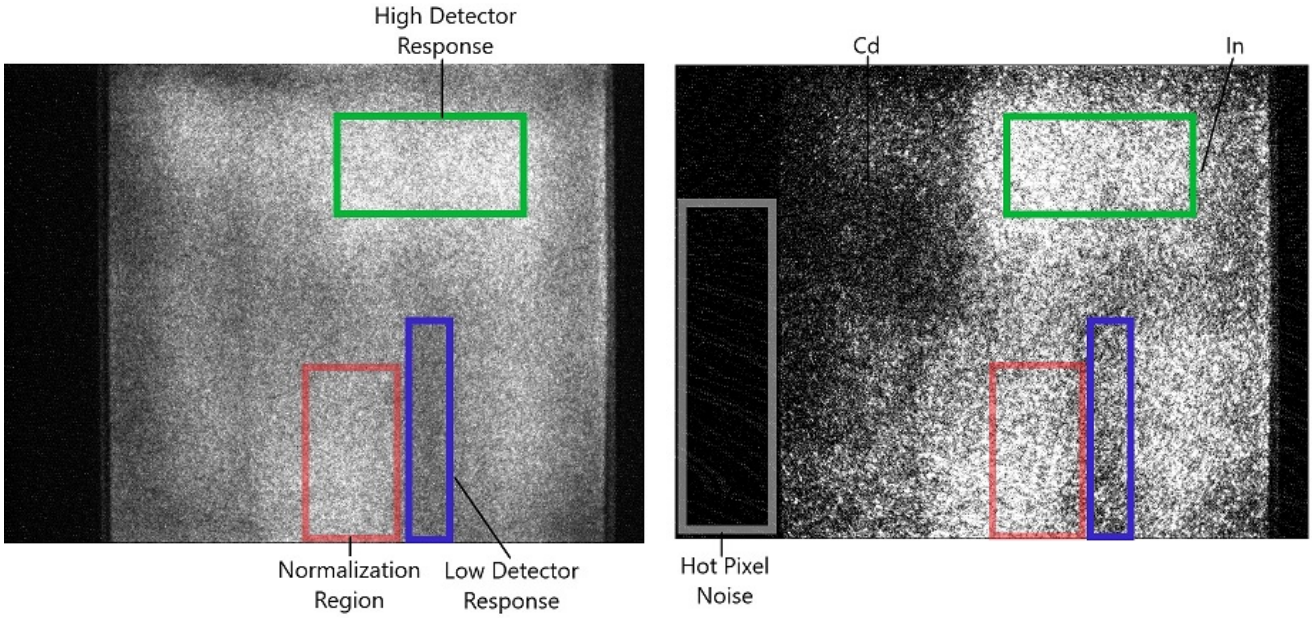

(a) Background Image

(b) Raw Neutron Radiography

Figure 5.9: (a): Background signal of the Photonis detector without samples and blocked neutron beam. The illumination is a result of the γ-flash and not from neutrons. (b): Raw output signal of a neutron radiography shot. It is noticeable that the background signal has bright and dark areas, attributed to low and high response regions of the detector. The same response behavior is visible in the radiography, indicated by blue and green rectangles. Also, the total intensity is different for both shots, therefore a reference area for normalization was chosen in red which did not contain any samples. The gray box indicates the presence of hot pixel noise from the ProxiKit on image areas that are not part of the phosphor screen.

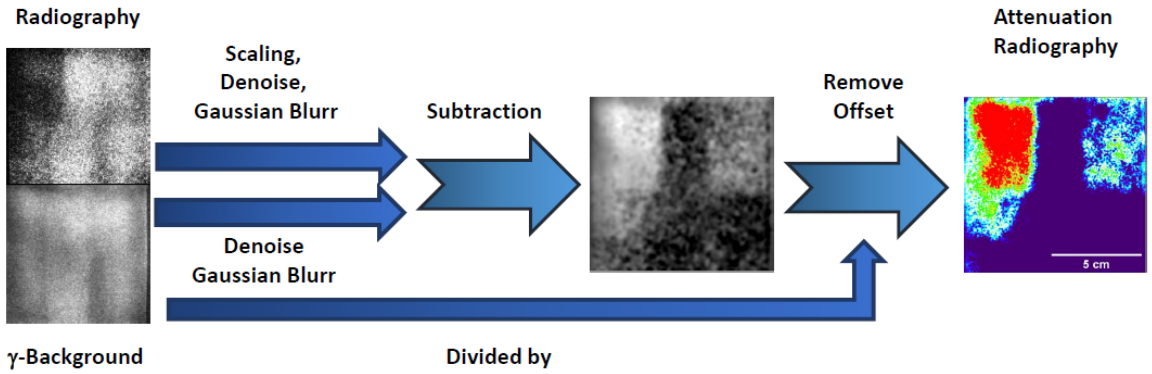

Figure 5.10: A schematic visualization of the construction of the attenuation radiography. The raw image and the background are scaled by intensity, noise is reduced and a Gaussian-blur filter is smoothing the pixel distribution. The radiography is subtracted from the background and the resulting image is normalized by dividing through the background image pixel by pixel. Afterwards, the mean pixel value in a blank area is calculated and removed from the image as an offset.

The detector used is a combination of the Neutronic [i] system [Photonis, 2019] in combination with a ProxiKit gated camera from ProxiVision [ProxiVision GmbH , 2019]. Neutronic [i] is a 10x10 cm large borated MCP coupled to a fast phosphor screen inside a vacuum housing. The phosphor screen was observed from the rear side through a window by the ProxiKit camera. The entire setup was light thigh enclosed and shielded from stray neutrons by 10 cm of borated HDPE.

The raw radiography image data of a single shot with 170 J and $5(2)\cdot10^7$ n/sr can be seen in figure 5.9 on the left side. The image was taken at 59 μs after the laser impact with an exposure time of 757 μs. With a given detector distance of 1.14 m this corresponds to neutron energies from 2 eV to 10 meV. According to PHITS simulations, this energy interval contains approximately 80(5) % of all neutrons below 100 eV.

A comparison to the background image on the left side illustrates several problems. Although the detector was exposed to a homogeneous radiation field from the γ-flash, a strong variation in brightness for different areas can be seen. This was caused by a spatially dependent response function of the phosphor screen coupled to the MCP. These areas of high and low response can also be seen in the radiography and would distort the results if left uncompensated. A direct background subtraction was not possible in this case since the background image had much higher pixel values through the large intensity of the γ-flash. Therefore, the red marked area which did not contain any samples was chosen for a comparison. An integration of all pixel values in this area for both images generated a scaling factor for normalization. In the next step, the remove outlier [Meijering, 2019] algorithm of Image-J was used to eliminate hot pixels and electric noise in the image caused by the high electromagnetic background

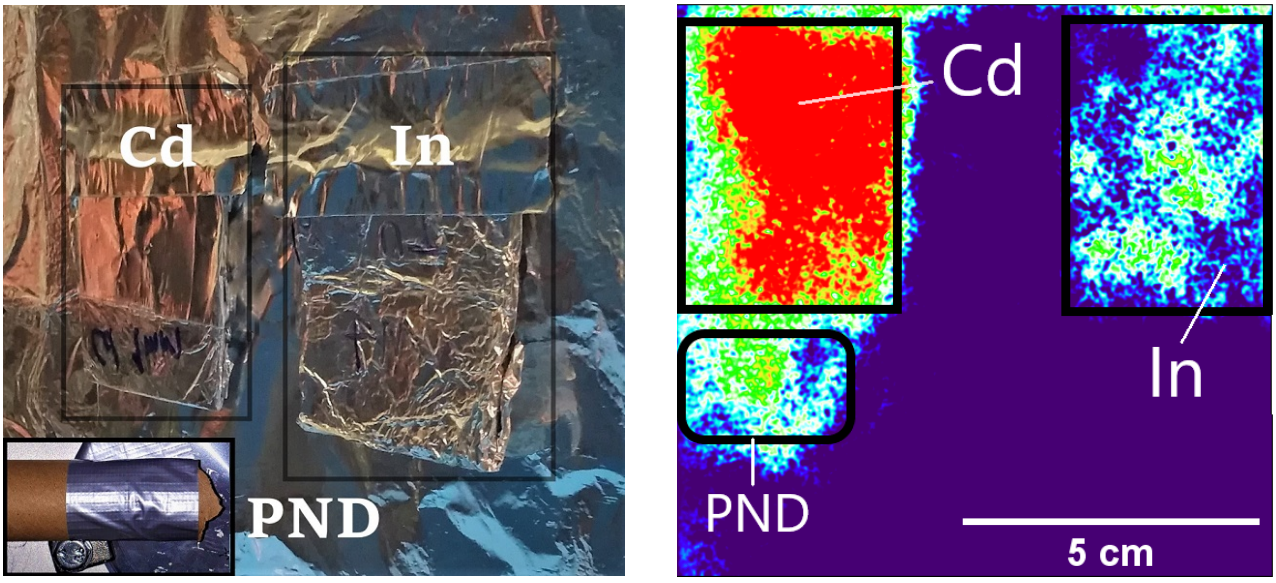

(a) (b)

Figure 5.11: (a): Samples in front of a thermal neutron radiography detector from [Photonis, 2019]. The left sample is a 1 mm thick cadmium sheet with a homogeneous thickness. The right sample is a self-made indium sheet with an in-homogeneous thickness varying from 0.6 mm to 1.5 mm. On the lower left side, a bubble detector is indicated which was placed at this position in line of sight between detector and moderator. (b): A single-shot neutron radiography of the samples seen in (a). A false color thermal spectrum is representing the neutron attenuation. Red represents high and purple low absorption. The inhomogeneous sample thickness of the indium is well represented in the radiography. Black rectangles indicate the sample position.

in the target area. The size and the intensity of this noise were determined by a comparison of pixels outside the phosphor screen on the left image side. This area is indicated by the grey box.

The different nature of excitation by photons and neutrons and the higher statistics in the left image did cause an unequal detector response for both images. While the background image was excited rather homogeneously and had only pixel to pixel variations, the neutron image did show single neutron events as spots out of ≈ 20 pixels surrounded by background noise. To avoid localized alterations by these discrete neutron events, a Gaussian-blurr filter [Robert Fisher, 2019] with a radius of 10 pixel was applied to smooth the intensity distributions for neighboring pixels.

With these preparations it is possible to create an attenuation plot, displaying the relative attenuation as a function of position. This is done in several steps. First, the radio-graphic image is subtracted from the background. The resulting image is divided by the background image pixel by pixel to compensate for background intensity variations. Afterwards, an area is chosen which is known to withhold no samples. This area is used to determine the mean offset value of the image-background. An offset subtraction yields an image for which each pixel value (32 bit) represents the normalized attenuation of the neutron beam at this position. A schematic visualization of the process can be seen in figure 5.10 and the resulting radiography is displayed in figure 5.11 (b) together with an image of the samples (a). It has to be noted that a bubble detector was placed slightly below the cadmium sample in direct line of sight between detector and moderator. The attenuation caused by this PND detector can be clearly seen.

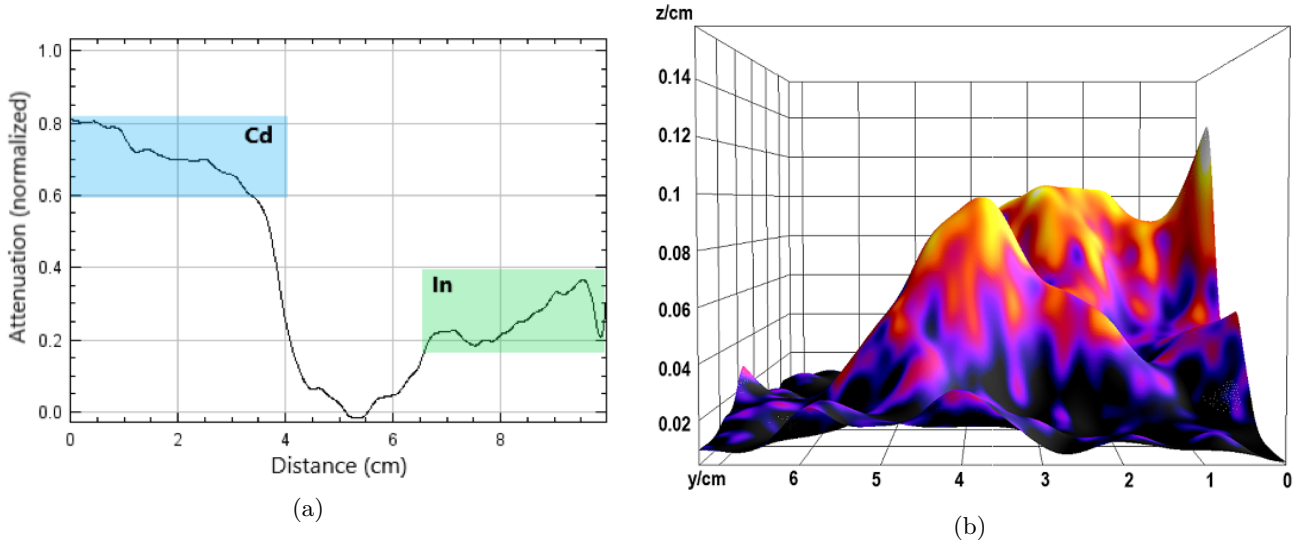

(a) (b)

Figure 5.12: (a): A profile plot through the radiographic image from figure 5.11 (b) through the cadmium and the indium sample. The average attenuation by Cd is 70(10) %. The attenuation by Indium is at 30(8) %. Approximating the indium cross section as constant for many neutron energies in this regime with $\sigma_{tot} \approx 100$ b, then the average thickness can be calculated to be 0.94(32) which is close to the actual thickness of 1.0(5) mm. (b) is a 3D representation of the calculated indium sample thickness.

The benefit of this type of image is the direct relation between the attenuation and the sample thickness if the material is known. This was utilized in figure 5.12. In the left image, the horizontal line profile through the samples in figure 5.11 (b) is drawn to invest the attenuation as a function of position. On the left side, the cadmium plate causes an attenuation of 70(10) %. The central valley without any samples has almost zero attenuation with 3(2) %. The indium sample on the right has an average attenuation

of 30 % with a 22 % on the left side and up to 36 % on the right side. For the observed energy interval during this shot the total neutron cross section is rather constant except for the resonance at 1.45 eV and for very slow neutrons as seen in figure 5.13 (b). For simplification, the cross section is assumed to be at a constant value of $\sigma_{\text{tot}} = 100$ b for the given energies. It has to be noted that for a more accurate thickness determination the neutron spectrum has to be convoluted with the cross section but this is part of future work when more data is available to improve the statistics. The uncertainty caused by the absence of a neutron-induced background image is most likely higher than the uncertainty of the assumption of a constant cross-section. With equation 2.27, 2.23 and 2.24 it is possible to calculate the sample thickness with:

$$d = \frac{-ln(1-a)}{\Sigma_{tot}} \tag{5.7}$$

with the attenuation value a and the total macroscopic cross section Σ_{tot}. This estimates a thickness between 0.65 and 1.26 mm for the indium sample. This corresponds very well with the measured thickness ranging from 0.6 to 1.5 mm. This thickness calculation is not limited to the line-out and can be applied to the image directly for every pixel. Figure 5.12 (b) shows the smoothed 3D thickness distribution of the indium sample ranging from 0.4 to 1.3 mm. These variations in the thickness are also present in the indium sample and are caused by the manual fabrication process as this indium plate was forged out of indium wire under the influence of pressure and heat.

This result shows that it is possible to create a two dimensional thickness measurement of a thin sample through a lead shielding by using a single shot of a laser-driven neutron source with cut off energies around 30 MeV. It has to be added that this is the first thermal neutron radiography image utilizing this kind of source.

Ion spectra with this cut off energies have already been produced at the Astra Gemini laser system by [Green et al., 2014] with 10 J in 45 fs. Similar laser facilities are capable of operating at 10 Hz [Eli Beamlines, 2019] and can be used to drastically improve the statistical uncertainty. This becomes especially promising as a single shot already measured the thickness with an error of less than 50 %.

5.2.2 Neutron Resonance Imaging

The next step after a spectroscopy and a radiography would be combining both techniques to neutron resonance imaging. While the neutron numbers in this beam-time were to low to perform such a measurement, a gatable neutron imaging system was used to determine the required flux for conducting NRI at an LDNS.
The detector used for this NRI is a combination of a ^6Li-glass scintillator with a highly-sensitive gated camera. The camera used was a PCO Digicam Pro, enhanced with an MCP image intensifier. The CCD-chip has a diagonal width of 11 mm and contained 1280x1034 pixels. The minimum time resolution was 3 ns which is more than sufficient for resonance imaging. The scintillator used was a GS-20 from Scintacor with a 98 ns decay time from 90 to 10 %, a light yield of 20-30% of anthracene and an emission wavelength of 395 nm [Scintacor, 2019]. The decay time of the GS-20 is relatively large in contrast to plastic scintillators or the time resolution of a MCP but compared with the moderation uncertainty in the regime of μs and to the resonance linewidth of the proposed samples, this uncertainty is acceptable. This detector system can be operated in two configurations visible in figure 5.13 (a). In the upper system,

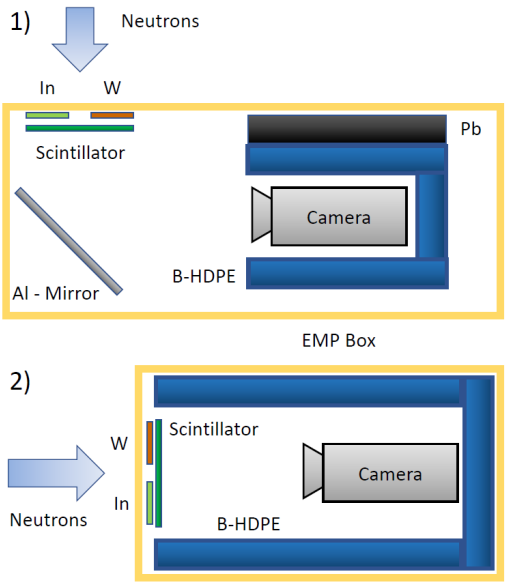

(a)

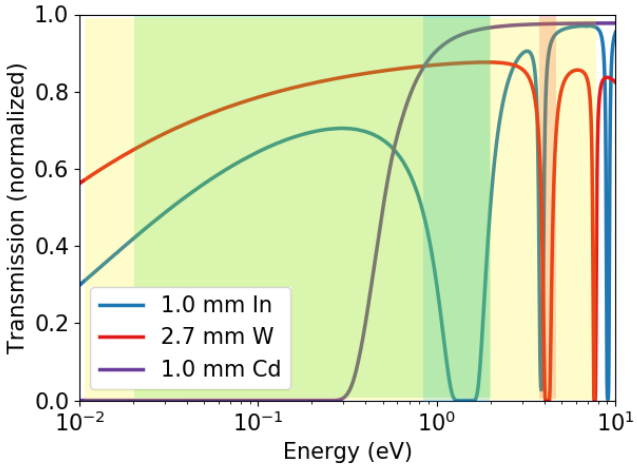

(b)

Figure 5.13: (a 1): Two setup possibilities for a neutron resonance imaging detector. In the upper setup, the camera is shielded from neutrons and X-rays coming from the source for a reduction of the image noise. The neutrons pass through the light-tight EMP box and the samples and reach a ^6Li-glass scintillator. The emitted light is reflected via an aluminum mirror towards the camera. (a 2): A similar setup but with the camera in direct line of sight towards the neutron source. This smaller setup had to be chosen because of spatial limitations in the experimental area. (b) A transmission plot for indium tungsten and cadmium. The green area indicates the energy window for the Photonis-detector radiography while the yellow area is the neutron exposure for the ^6Li-glass radiography. Blue and red areas are the FWHM of the indium and tungsten resonances.

neutrons enter through the wall of a light-tight Faraday cage here called EMP box and pass through the samples and reach the scintillator. The emitted light is reflected via an aluminum mirror towards the camera. This setup has the benefit that the camera is not directly in the line of sight of the incoming neutrons and the γ-flash. Therefore additional lead and borated HDPE shielding can be installed to reduce the background noise produced inside the camera. Aluminum is chosen as a mirror material because it does not contain (n,γ) resonances, in contrast to silver, in the low energy range. This could additionally increase the background noise and is not preferable. For an effective NRI measurement this would be the optimal configuration. Through limitations in the available space in the target chamber area it was not possible to operate in this configuration and setup number 2) in figure5.13 (a) was chosen. This option requires less space but the camera is directly exposed to the neutron irradiation and the γ-flash.

In front of the scintillator a 2.5x2.5 cm tungsten sample with a thickness of 2.7 mm was placed together with a 5x5 cm indium sample with a thickness of 1 mm separated by 1.5 cm of free space. Both samples are mounted on a 1 mm thick aluminum plate for structural support. A radiography was taken with a duration of 2 ms, containing all neutron energies from 7.2 eV to 2 meV. The image processing was done similarly to figure 5.10 but due to large variations in the background from shot to shot no normalization could be done and therefore no absolute attenuation values could be calculated. The result is visible in figure 5.14. Figure (a) shows the relative intensity attenuation as a function of position. Tungsten shows the highest reduction in pixel intensity with a factor 1.8(1) in comparison to the background in the free space between the samples as seen in the line out plot in figure 5.14 (b). Indium shows a lower reduction ratio of 1.35(5).

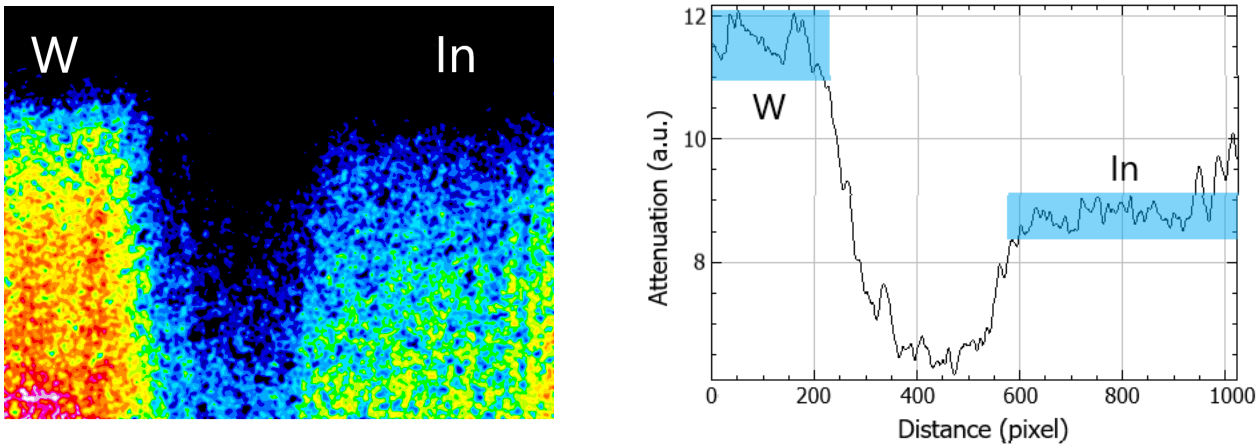

(a) (b)

Figure 5.14: (a): Neutron attenuation at the ^6Li-glass detector radiography. Red colors indicate increased neutron attenuation. The position of the indium and the tungsten sample are clearly visible. (b): A lineout through both samples and the 1.5 cm between. The attenuation from tungsten is 1.4 times higher than for indium even though it should be lower according to simulations. A possible cause could be a non-negligible X-ray background interfering with the neutron signal.

It has to be noted at this point, that these values stand in conflict with PHITS simulations which predict a neutron attenuation for indium by 56% but only an attenuation through the tungsten sample by 34 %. The cause of this discrepancy is not fully understood yet but a possible explanation could be that a large part of the background is caused by X-rays interacting with the scintillator for which the tungsten sample would cause a higher attenuation than the indium through its higher-Z number and density. The indium radiography in comparison is rather close to the predicted value and can be considered as a reference value for a successful radiography.

In the next step, the question has to be answered how many neutrons are needed to create a radiography with a similar quality but with a smaller energy window that fits the indium resonance. This can be done by integrating the neutron spectrum produced by the moderator over the energy window size of the image from 2 meV to 7.2 eV. This is then compared to the number of resonant neutrons in the spectrum:

$$N_{In} = \frac{\int_{2\,meV}^{7.2\,eV} \frac{dN}{dE} dE}{\int_{0.82\,eV}^{1.94\,eV} \frac{dN}{dE} dE} = 27 \tag{5.8}$$

The width of those images is indicated in figure 5.13 by the blue and yellow areas. This result means that the threshold number of produced neutrons needs to be N_{In} times higher than in this shot to perform neutron resonance imaging with this setup with a single shot on an indium sample. For this estimate the indium resonance at 1.45 eV was chosen with the FWHM width from 0.82 to 1.94 eV. To resolve the ^{182}W resonance at 4.15 eV this number would increase to $N_W = 112$. The average fast neutron number for this shot was $6{\cdot}10^8$ N so the total number of neutrons required for the indium resonance is $2{\cdot}10^{10}$. For a tungsten resonance imaging a minimum of $7{\cdot}10^{10}$ neutrons are required. A comparison to figure 5.2 shows that this is possible with 1-2 shots of PHELIX in the high contrast configuration.

As this chapter demonstrated the capabilities of LDNS of an existing laser facility dedicated for conducting experiments for different research groups at a low repetition rate, the next chapter will focus on the capabilities of a dedicated laser neutron systems with state of the art technology.

6 Design of Laser-Driven Neutron Sources for Material Analysis

With a laser solely dedicated to neutron production, many design limitations are lifted. As there is not one single system that could satisfy all needs for every purpose, it is more efficient to design such a system for a specific goal. Therefore this chapter will introduce three different LDNS concepts to satisfy the main demand for neutron sources. The first system will focus on small transportable neutron sources for applications in the security sector as well for on-site material inspection. The second design will introduce a stationary LDNS system for material analysis methods that require a high number of neutrons per second like spectroscopy, neutron tomography or resonance imaging. The third concept investigates the requirements for LDNS to be used as a high peak flux source for temperature measurements of warm dense matter via NRS.

6.1 Combined Mobile Neutron and X-ray Source

The first system is developed to satisfy the need for small mobile sources for an on-site demand for neutrons and X-rays. Such systems are of high interest for the security sector [Lanza, 2007]. Current techniques for cargo screening rely on X-ray radiography to determine hidden illegal goods or security threats. These techniques have their limits and cannot detect certain kinds of explosives as well as fissile material [Smith Detection Group, 2018][Megahid et al., 2009]. Those materials can be identified through neutron irradiation either by PGNAA, NAA or by the usage of a differential die away analysis [Jordan and Gozani, 2007]. For these detection methods often small neutron generators are used with a limited source strength in the range of 10^8 n/s [Thermo Fischer Scientific, 2008a].

The benefit of an LDNS is that such a device produces simultaneously intense neutron and X-ray pulses from a single source as the hot electrons in the target irradiate high amounts of bremsstrahlung. This effect is amplified if a high-Z catcher material is used to rapidly stop the hot electrons in the forward direction. To maximize the neutron and X-ray output this section will discuss the optimal laser parameters, the specific design of the catcher-reflector configuration followed by the characterization of the radiation output based on a PHITS simulation. This information will then be used to discuss the applications of such a device.

For a mobile source, a compromise between size, laser energy and repetition rate has to be found. While a strong neutron scaling with E_L has been found in this work, an increase in energy often comes at a cost in repetition rate as more heat has to be removed out of the system [Patrizio, 2020] and it is generally required to be larger in size. Therefore in this section, the other pathway is chosen by utilizing the high repetition rate to compensate for the loss in neutrons per shot. The limitations for the repetition rate of an LDNS were investigated in section 4 and the conclusion was made that the target system is the limiting factor. The highest repetition rate is possible with liquid droplet targets but their proton emission is not directed enough, therefore liquid leaf targets are chosen with a maximum repetition rate of around 1 kHz.

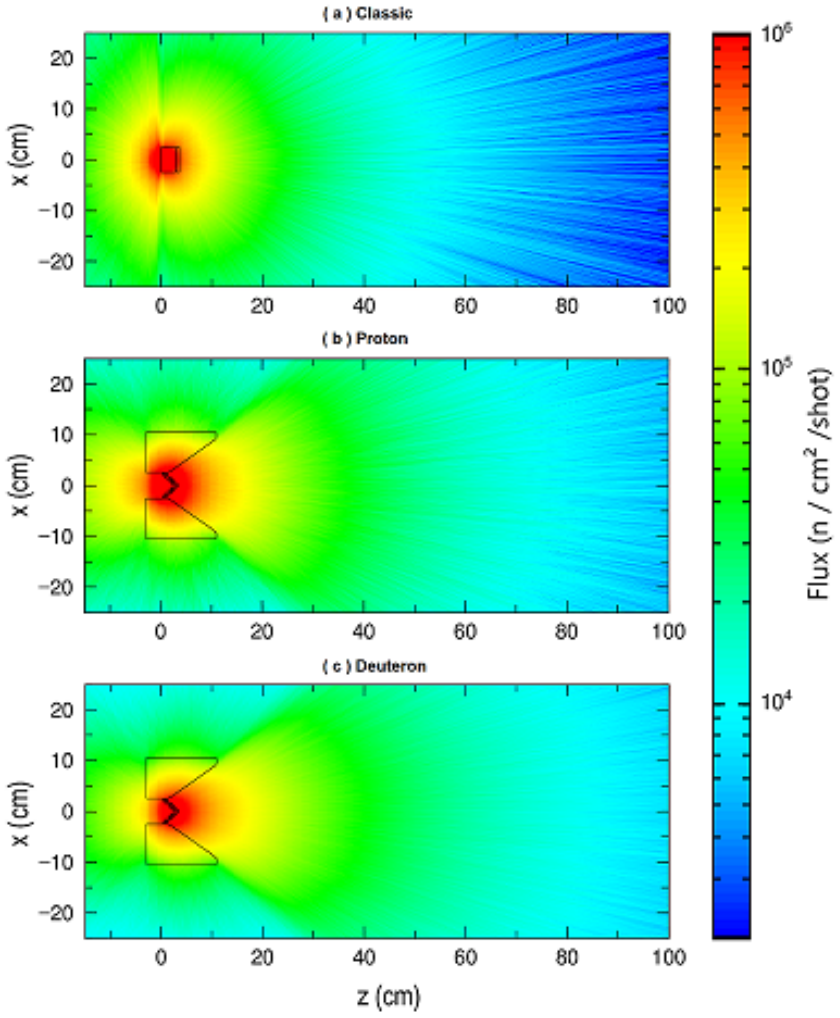

Figure 6.1: Simulated neutron flux of a single shot for three different configurations. (a) is the measured proton spectrum of [Zulick et al., 2013] from a 1 J laser extrapolated to a 25 °half opening angle and directed on to a cylindrical lithium catcher. (b) shows the resulting neutron flux of the same proton spectrum impinging on a catcher and reflector combination designed for a combined X-ray and neutron source. The catcher is a conical combination of lithium followed by a tungsten layer. A tungsten reflector redirects neutrons into the forward direction. (c) is the same setup irradiated with the corresponding deuteron spectrum from [Zulick et al., 2013].

In the next step, a laser system has to be found that is capable of accelerating a sufficient number of ions to adequate energies to be able to produce neutrons. Laser ion acceleration has been demonstrated with laser energies of 5 mJ at $5{\cdot}10^{18}$ W/cm^2 up to 2 MeV. The total proton yield at this point was rather small at $1{\cdot}10^{10}$ p/sr [Morrison et al., 2018]. Brenner demonstrated an increase in proton flux to $1{\cdot}10^{11}$ p/sr with a laser system utilizing 353 mJ at similar intensities and cut off energies of 2.5 MeV. This is still not high enough for efficient neutron generation, although the cut off energy could be increased with a smaller focal spot. To enter a regime viable for applications it is advantageous to further increase the laser energy up to 1 J to benefit from the observed quadratic increase in ion numbers from section 4.1. Potential candidates are lasers from the Dira series fabricated by [Trumpf Scientific, 2019]. They are currently developed to operate at 1 J, 1 kHz with pulse lengths between 50 and 500 fs [Metzger, 2018]. They have already demonstrated a system that can operate at the 600 mJ level and further improvements

are expected in the near future [Herkommer et al., 2019].

As this laser system is still under development, no ion acceleration data is available but at similar systems like the HERCULES laser [Yanovsky et al., 2008] experiments have been conducted by [Zulick et al., 2013] at the University of Michigan. A laser pulse with 1 J in 40 fs has accelerated protons up to 10 MeV as well as deuterons to 5 MeV. This was done by utilizing an F/1 off axis parabola with a 1.3 μm FWHM focal spot with peak intensities of up to $2{\cdot}10^{21}$ W/cm^2. These ions were directed on different catcher materials to invest the neutron yield. The maximum flux measured was $1(0.5){\cdot}10^7$ n/sr from protons impinging on lithium-fluoride followed by $3(1.4){\cdot}10^6$ n/sr for deuterons directed on LiF as well. The maximum flux is three orders of magnitude lower than the results reported by [Roth et al., 2013] at the TRIDENT laser at similar intensities of 10^{21} W/cm^2 but with 70 times less laser energy. This scaling agrees with the results of the blue curve from figure 4.6 and equation 4.17.

The recorded proton and deuteron spectrum can be used to recreate these conditions in a PHITS simulation to optimize the catcher and reflector system for this laser with the purpose of maximizing the fast neutron and X-ray generation in the forward direction. The simulation assumed a 25° half opening angle characteristic for TNSA [Schollmeier, 2009] and the insights gained from section 4 were used to construct the setup seen in figure 6.1.

The upper plot is functioning as a reference and shows the neutron flux created by the proton beam hitting a lithium cylinder. This created a flux of $2.7{\cdot}10^3$ n/cm^2 at 1 m distance or $2.7{\cdot}10^7$ n/sr which is about a factor of three larger than the reported flux by [Zulick et al., 2013]. Considering that in this case pure lithium was used and that the TNSA divergence angle was estimated this can be seen as a good agreement with the experiment and enables to evaluate the influence of the design changes.

Figure (b) shows the neutron flux caused by the same proton spectrum for a design that could be used as a combined neutron and X-ray source. This setup consists of a first 6 mm thick layer of lithium followed by 4 mm of tungsten in a hollow cone structure. The first layer is dedicated to converting ions into neutrons while the second layer is a high-Z material to efficiently stop electrons that are emitted in the TNSA process to create bremsstrahlung as an X-ray source. The surrounding structure is a tungsten reflector to redirect neutrons via scattering. With this setup, the neutron flux in the forward direction was additionally increased by a factor of two with $5.6{\cdot}10^7$ n/sr/shot at 1 m distance.

Although deuterons have a much higher neutron yield per particle [Rücker et al., 2016] they are less efficiently accelerated due to their lower charge to mass ratio resulting in lower cut off energies as well as total numbers [Zulick et al., 2013]. As a result of this, 70% fewer neutrons are produced with the deuterated source than with protons. Nonetheless, the neutron emission created by deuterons has a higher directionality which compensated for this effect leading to a total flux in the forward direction of $6.9{\cdot}10^7$ n/sr. This is 23 % higher than for the proton acceleration.

This increase in flux is rather small compared to the higher cost of deuterated material. The main benefit of using deuterated targets in this system comes from the higher neutron energies caused by the reaction:

$$^2d + ^7Li \rightarrow ^8Be + n + 15.03\,\text{MeV} \tag{6.1}$$

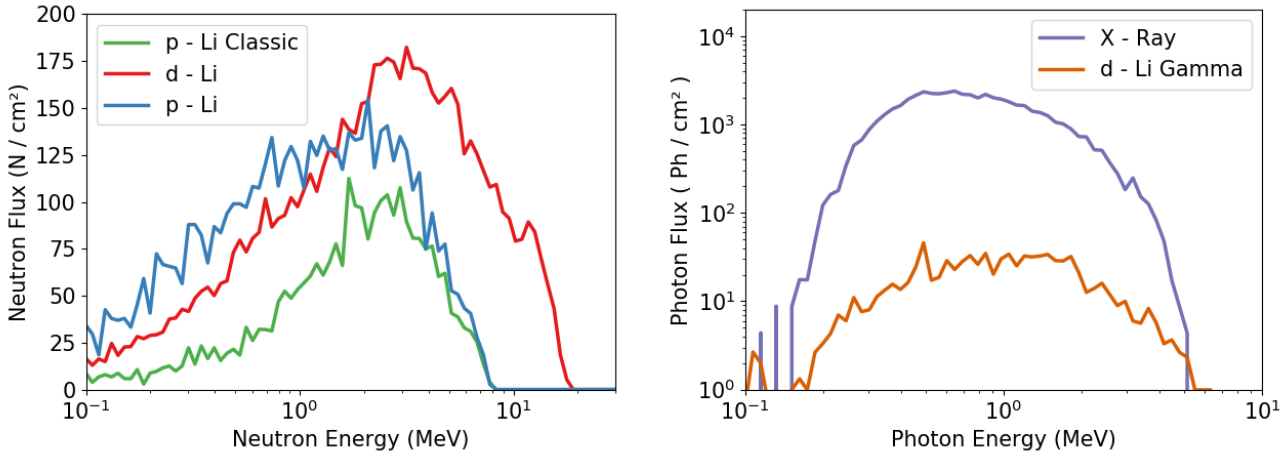

(a) (b)

Figure 6.2: (a): The simulated neutron flux at 1 m distance for the proton and deuteron spectrum reported by [Zulick et al., 2013]. The green curve serves as a reference for protons on a lithium cylinder. The blue curve shows the improvements from the reflector and catcher design seen in figure 6.1. In the red graph the deuteron spectrum is used. The higher energy comes from the large Q-value of the d-^{7}Li reaction.

which has a large positive Q-value of 15.03 MeV for deuterons. In contrast to that, the reaction

$$^1p +^7 Li \rightarrow^7 Be + n - 1.64\,\text{MeV} \tag{6.2}$$

has a negative Q-value and will produce neutrons with less energy. This enables a deuteron based neutron source to produce high energetic neutrons up to 20 MeV with a relatively low laser energy of 1 J. The neutron spectra of a single shot at 1 m distance can be seen in figure 6.2 (a) for each of the three different configurations. The d-Li reaction in red is showing a strong shift towards higher energies in comparison to the p-Li reaction in blue. Comparing the green and the blue curve it can be seen that the setup changes did not affect the highest energies but strongly increased the flux of neutrons between 100 keV and 3 MeV into the forward direction.

The flux caused by a single shot of around $3{\cdot}10^3$ N/cm^2 is rather low compared to other neutron sources (Table 3.1), this drastically increases when the repetition rate of 1 kHz is taken into account. Then the maximum neutron flux will be between $1{\cdot}10^{10}$ n/(sr·s) based on the experiment conducted by [Zulick et al., 2013] and $7{\cdot}10^{10}$ n/(sr·s) predicted by the simulations. This is similar to the neutron production of a laser like trident [Roth et al., 2013] or PHELIX [Kleinschmidt et al., 2018] if it is operated at 1 Hz.

In the next step, the production of X-rays has to be investigated. The production of highly energetic electromagnetic radiation can have three different origins in such a setup. The first source is from the hot electrons inside the target that emit radiation as a result of their high temperature in the MeV region. The size of this source is typically in the regime of the laser spot diameter [Armstrong et al., 2019] and slightly increased for targets where the thickness is larger than the focal spot size [Schollmeier, 2009] but still in the low μm-regime. The emission spectra produced by this effect have been investigated by [Günther, 2011] for laser systems with energies between 15 and 96 J resulting in photon cut off energies similar to the expected proton cut off energies of such a system. For laser systems in the 1 J regime no such experimental data was available.

The second source of X-rays is created when the hot electrons emitted from the target impinge on the tungsten layer where they are rapidly decelerated and create bremsstrahlung. Such an electron spectrum was observed by [Brauckmann, 2018] at the ARCTURUS laser while it was operated at 1 J in 27 fs focused with an f/2 parabola down to a 3 μm FWHM spot reaching intensities of up to 10^{20} W/cm^2. This is more than one order of magnitude lower in intensity than at the HERCULES laser but is sufficient enough to invest the produced X-ray spectrum. It has to be kept in mind that the maximum photon energies can be increased by the usage of a parabola with a lower f-number. If the electron scaling with focal spot size has a similar behavior than the ion cut off energy scaling, then an increase in maximum photon energy by a factor of $(I_{\mathrm{HER}}/I_{\mathrm{ARC}})^{0.25} = 20^{0.25} \approx 2$ is possible. Similarly, a reduction in maximum energy can be achieved by increasing the focal spot size or defocusing.

For the ARCTURUS experiment corresponding particle in cell (PIC) simulations are available [Brauckmann, 2018] predicting the electron divergence angle to around ± 5°. This electron distribution is again modeled with PHITS and directed on the same catcher as seen in figure 6.1. The photon flux of a single shot is seen in figure 6.3 with a forward orientated flux of 5.3·10^8 Ph/sr. The matching photon spectrum is displayed in figure 6.2 (b). In addition, the third source of EM radiation is displayed in the same figure which is caused by nuclear reactions of the ions interacting with the catcher nuclei resulting in the emission of γ-radiation. It can be seen that this contribution is two orders of magnitude lower than the bremsstrahlung and can be neglected.

The 5.3·10^8 Ph/sr are equivalent to a source strength of 6.7·10^9 photons for a single shot. Including the repetition rate, this X-ray source would deliver around 250 μSv/s or 1 Sv/h at 1 m distance. This is a similar dose rate as it is produced by mobile X-ray screening platforms which range from 0.1 to 2 Sv/h [J. Clayton, 2019]. It has to be noted that this calculation does not include the bremsstrahlung produced inside the target which will most likely increase the delivered dose rate by a large fraction. This value therefore represents a lower boundary for the X-ray production.

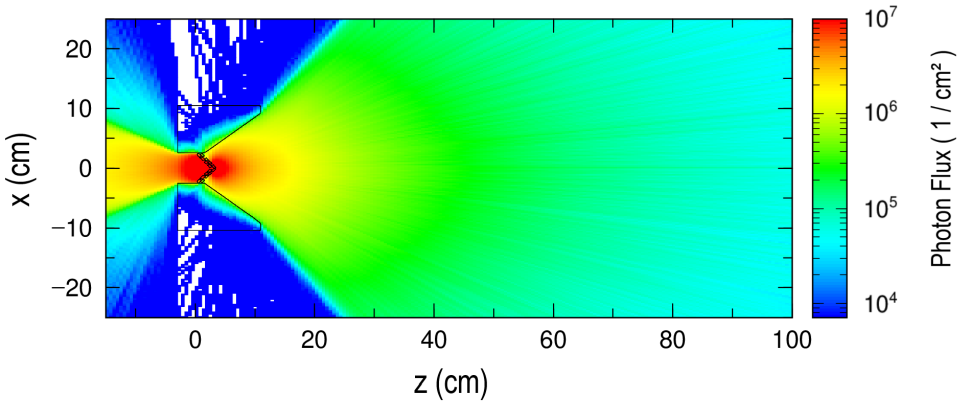

Figure 6.3: PHITS simulation for the generation of x-rays at an LDNS. The same setup as in figure 6.1 is irradiated with an electron spectrum recorded at the ARCTURUS laser with 1 J in 27 fs by [Brauckmann, 2018]. The Photon flux is in forward direction 5.3·10^8 Ph/sr per shot.

With a neutron flux of 10^{10} n/(sr·s) and an X-ray flux on the order 10^{11} Ph/(sr·s) or higher a large range of applications become possible. Besides the applicability for security systems that were already mentioned such a mobile system could be used to determine the degree of corrosion inside bridges. [Naqvi et al., 2006] were capable of determining the chlorine content of a concrete sample via PGNAA with the use of an MP320 neutron generator [Thermo Fischer Scientific, 2008a] within 120 minutes up to a minimum concentration of 0.03 weight percentage. Scaling this measurement with the source strength of such an LDNS system, this measurements could be done in a time frame of 1 to 6 s. This makes it applicable for real-time measurements on the street.

Another promising application for such a system is the identification of trace elements in archaeological artifacts on-site or the measurement of the precious-metal content in raw ores via neutron activation analysis. [El-Taher et al., 2003] were capable to identify the gold content in ore samples down to the low ppm regime. Such a measurement with a laser source would require an equivalent measurement time of 6 days per sample but irradiating a large number of samples simultaneously would increase the efficiency. Additionally decreasing the accuracy reduces the measurement time allowing a drastic improvement in the gold mining efficiency.

These are the capabilities of a small mobile laser-driven neutron source. This source type is mostly limited by the compactness of the laser system. For applications that do not require mobility, larger laser system can be build, capable of providing orders of magnitude more energy per shot and therefore a much higher neutron production rate. Such a system can aim to provide neutrons to users that are in need of a high average neutron flux but have no access to spallation sources.

6.2 High Performance Neutron Sources Driven by Laser Acceleration

Without the size restrictions, an LDNS is only limited by the current laser technology which is on the one hand rapidly evolving but on the other hand still constraint by a trade off between repetition rate and laser energy as discussed earlier. It is either possible to try to compensate an intermediate repetition rate in the Hz regime with a higher energy to benefit from the strong scaling of the neutron numbers with E_L or one sacrifices energy for a kHz repetition rate. An example for a high energy, intermediate rep-rate would be the SHARC laser with 150 J in 150 fs operating at 10 Hz which is currently under development at the LLNL [Siders, 2018]. In parallel to that LLNL is developing the Big Aperture Thulium (BAT) system. This laser is capable of operating up to 10 kHz with 30 J and a pulse length of 100 fs. These two systems can be compared to each other to evaluate which approach can produce a higher neutron flux and serve as a reference to place LDNS into perspective to conventional sources.

Both of these systems are not operational yet. A comparison can still be made if ion spectra from lasers with similar single-shot parameters are chosen as a representative. For a shot with 30 J the results of [Busold, 2014] with 30(5) J and cut off energies at 28 MeV was chosen. For an ion spectrum that can resemble a SHARC shot the decision was made to use a spectrum from [Wagner, 2014] at the PHELIX laser with $E_c = 64$ MeV and energies around 160 J. These spectra were implemented into a PHITS simulation with the optimized catcher-moderator design from section 4. The simulation was normalized to the reported ion numbers from [Busold, 2014] and [Wagner, 2014] and the moderated neutron flux was

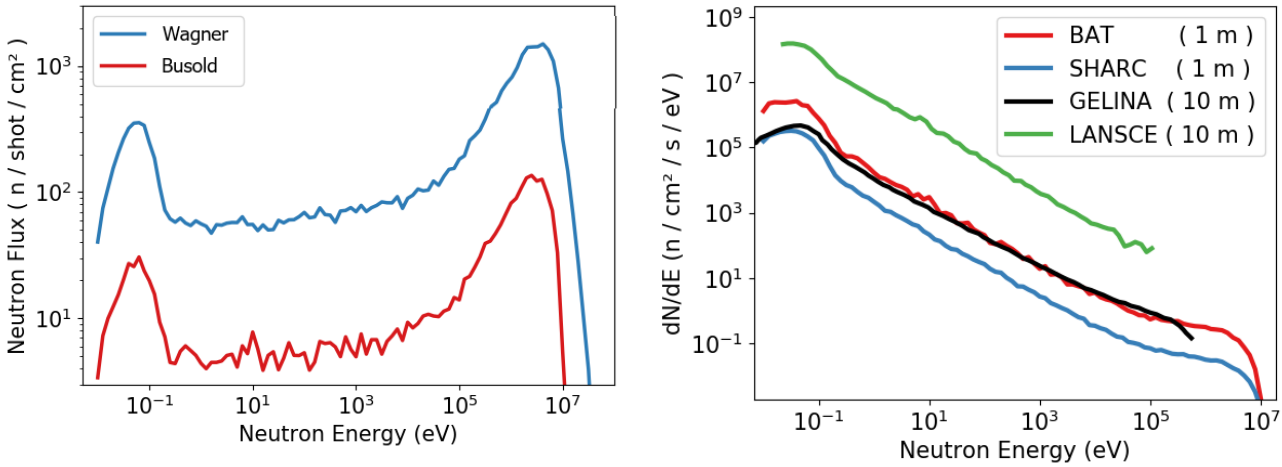

(a) (b)

Figure 6.4: (a): Simulated moderated neutron flux at 1 m distance for two ion spectra produced by PHELIX. The first spectrum is based on the results of [Busold, 2014] with 30(5) J (red) and the second one is modeled after a spectrum from [Wagner, 2014] with a laser output of 160(40) J (blue). As catcher, the Li-V combination was used and the moderator design from section 5.1. The thermal and epi-thermal flux of the blue curve is 12 times higher. (b) : Scaled neutron spectra when the laser systems from (a) are operated at the repetition rate of the BAT (30 J, 1 kHz) and the SHARC (150 J, 10 Hz) system.

recorded at 1 m distance for both cases, which is the closest detector position for NRI. The result can be seen in figure 6.4 (a). The spectrum from Wagner that resembles a SHARC shot has with $2.3{\cdot}10^4$ n/cm^2 a 12 times higher thermal neutron flux per shot than the spectrum simulating the BAT system. If this result is scaled with the expected repetition rate of each system then this ratio drastically changes. Even though BAT is indicated with 10 kHz [Siders, 2018] only a 1 kHz repetition rate is assumed as this is the limit predicted in section 4.2 for the target for such a system. The result of this scaling can be seen in figure 6.4 (b) in the form of neutrons/(cm^2·s·eV). To make a comparison to other existing pulsed neutron sources possible, the corresponding flux values of GELINA [Schillebeeckx et al., 2015] and LANSCE [LANL, 2019a] at 10 m are displayed as well.

In this simulation, the BAT system shows an epi-thermal flux at the detector similar to the closest GELINA detector and 1.5 orders of magnitude below the flux of LANSCE. The exact values can be seen in table 6.1. The close proximity of a detector at 1 m would greatly reduce the energy resolution but NRI and tomography measurements could be still conducted as they have fewer restrictions on the energy resolution than NRS. The SHARC system shows a thermal flux of $3{\cdot}10^8$ n/(sr·s) which is low in comparison to a scaling from the experimental data in figure 5.2 which would predict a thermal flux of $8{\cdot}10^9$ n/(sr·s). Reasons for this discrepancy can be that the simulation only used protons while the experiment also accelerated deuterons. Another reason can be that the laser performance in the experiment of [Wagner, 2014] was not optimal as the average performance in his experiments was at cut off energies around 40 MeV which is 30 MeV lower than energies reported at later times at PHELIX [Wagner et al., 2016]. [Higginson et al., 2018] were able to use similar laser energies to accelerate protons up to 93 MeV with 2.3 times more ions in the beam. According to the scaling for E_c this would lead to a 6 times higher neutron yield.

With these results, it can be said that an increase in repetition rate by a factor of 100 out-weights an energy increase by a factor of 5 under the assumption that the target system can handle the repetition

Table 6.1: Neutron flux for various sources. N_{epi} is the integrated flux from 1 to 10 eV in figure 6.4 (b) while N_{Th} corresponds to the flux below 1 eV. the last column compares the thermal flux per steradiant as the flux is measured at different positions.

Source	N_{epi} / n/(cm^{2}s)	N_{Th} / n/(cm^{2}s)	N_{Th} / n/(sr · s)
SHARC	$5 \cdot 10^3$	$3 \cdot 10^4$	$3 \cdot 10^8$
BAT	$4 \cdot 10^4$	$3 \cdot 10^5$	$3 \cdot 10^9$
GELINA	$3 \cdot 10^4$	$8 \cdot 10^4$	$8 \cdot 10^{10}$
LANSCE	$1 \cdot 10^6$	$2 \cdot 10^7$	$2 \cdot 10^{13}$

rate at that energy level. Such a laser system can deliver neutron flux rates similar to GELINA and with a reduced energy resolution. The LANSCE detector flux is still more than one order of magnitude higher but for TOF based imaging techniques like NRI the shorter pulse spread Δt can be used as an advantage. At repetition rates in the kHz regime, the arrival time of thermal neutrons from a previous pulse can overlap with the arrival time of epi-thermal neutrons from the next pulse. This requires the installation of a cadmium filter in the beam path to create a pure epi-thermal neutron beam.

6.3 Laser Neutron Sources for Temperature Measurements on Warm Dense Matter

Equation Of State (EOS) measurements are of fundamental importance for understanding and describing materials in extreme conditions like Warm Dense Matter (WDM). Such states exist in the interior of massive planets like Jupiter or in laser shock experiments. These conditions are yet not fully known and an experimental verification of different EOS theories could help to obtain a better understanding of the formation of our solar system and therefore also for the hunt for exo-planets [Yuan et al., 2005][Nettelmann, 2011]. The largest challenge in these short-lived states is an accurate determination of the bulk temperature. Currently existing techniques for temperature measurements in this regime like pyrometry are limited to the surface temperature. Other approaches based on X-rays such as Thomson scattering are limited to thin samples and to low-Z numbers [Fernández et al., 2019]. This section will invest the possibility of a temperature measurement of such states based on NRS Doppler broadening with a laser-driven neutron source. To do this the requirements and limitations are discussed and possible solutions are introduced.

Experiments already have shown [P. H. Fowler, 1977][Kai et al., 2017] that bulk temperature measurements of static samples via neutron transmission analysis are possible and [Yuan et al., 2005] proved that this technique can be extended to dynamic compression experiments. For this measurement, an explosively launched flyer plate collided with a molybdenum plate doped with ^{182}W to create up to 63 GPa of pressure. The temperature was determined by the Doppler broadening of the 21.1 eV resonance of the tungsten isotope.

The difficulty for such dynamic measurements is that the neutron pulse width is required to be short in comparison of the lifetime of the rarefaction-free shocked state. Yuan realized this by placing the sample at < 1 m next to the moderator at target station 2 at LANSCE. They reported a pulse duration of resonant energies at the sample of less than 200 ns. While this proof of principle experiment was done at a spallation facility, these sources are not available at laser shock experiments. A compact neutron

source like an LDNS is preferable as shock and neutron generation both require a laser. In addition, the lower detector distance, as well as the short pulse duration only limited by the moderation time, allow better utilization of the produced neutrons. [Fernández et al., 2019] have investigated the feasibility of this source for NRS thermometry and compared it to the experiment from Yuan. They aimed for a temperature accuracy of 2 % and defined parameters such a source has to fulfill to be in this accuracy. This section discusses these parameters in respect of the setup used in section 3.3.1 and investigate if it is applicable for a NRS thermometry measurement.

First, it has to be investigated if the resonance of ^{182}W is Doppler dominated or linewidth dominated. The resonance at 4.15 eV has a linewidth of $\Gamma = 0.107$ eV. For the temperature measured by Yuan of 875 K the Doppler width is $\Delta = 0.088$ eV and therefore from equation 3.10 it follows that $\epsilon = 1.3$. The resonance is consequently neither Doppler nor linewidth dominated but in an intermediate regime. This hampers the analytical calculation of the resonance width and therefore the results of [Kai et al., 2017] are consolidated. They used the REFIT code developed by [Moxon et al., 2010] to estimate the changes in transmission for this resonance with increasing temperature. Their results can be seen in figure 6.5. According to this approach, the transmission at the resonance center shows the largest changes from temperature variation. For experimental conditions, this is rather impractical as the transmission at the center for thicker samples around 1 mm reaches values of below 0.1% which is orders of magnitude lower than the background noise estimated from figure 5.5. Therefore changes below a transmission of 10 % can not be detected with this setup. A more promising approach would be a comparison of the flanks of the resonance.

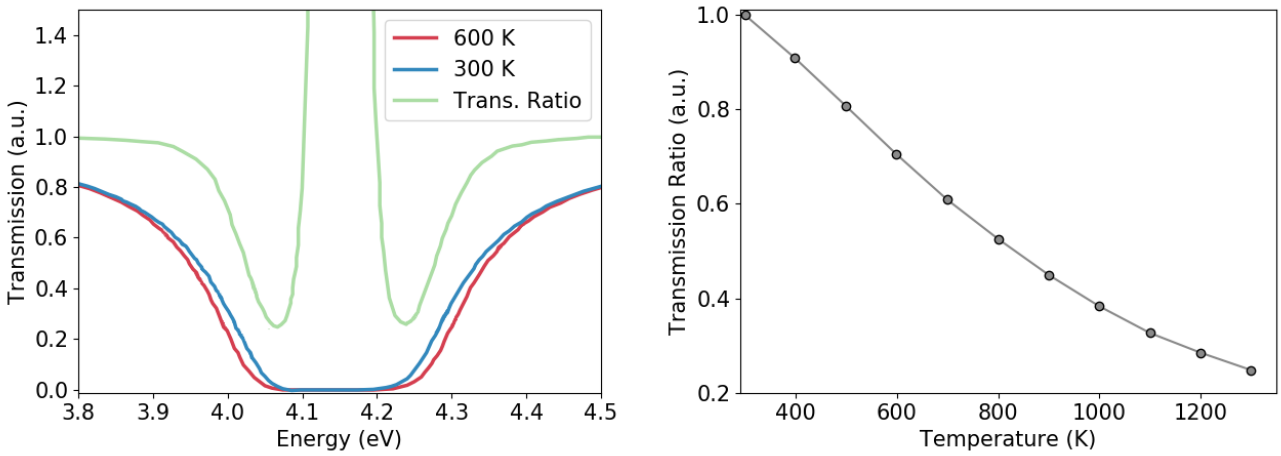

(a) (b)

Figure 6.5: (a): The blue graph displays the neutron transmission through a 1 mm thick tungsten sample at 300 K. For the red graph, the sample temperature was statically increased to 600 K and shows signs of Doppler broadening. The green graph is the ratio of the transmission between both graphs and enables a temperature assignment. (b): The transmission ratio as a function of temperature at 4 eV is a steady decreasing function in this regime. Simulation data was adopted from [Kai et al., 2017].

Figure 6.5 (a) shows the simulated transmission of a 1 mm thick tungsten sample at 300 K in blue and a to 600 K heated sample in red [Kai et al., 2017]. The heated sample is clearly Doppler broadened, which can be illustrated by the transmission ratio of both curves, displayed in green. The flanks of the resonance between 3.9 eV and 4.05 eV as well as from 4.25 eV to 4.4 eV show a strong dependence on the sample temperature. The transmission ratio at 4 eV was calculated by [Kai et al., 2017] for different

sample temperatures and the result is displayed in figure 6.5 (b). The resulting curve is a steady decreasing function with the temperature. Using a single energy bin that integrates over each flank region would enable a direct comparison for different temperatures. This would make it possible to determine the temperature slightly before and after the beginning of the shock.

For an adequate depiction of the sample temperature, all resonant neutrons have to pass the sample within a time frame of similar temperature conditions. [Yuan et al., 2005] proposed for this time $\tau_{rsl} = 200\,\text{ns}$ to probe the sample as during this time frame the rarefaction wave has not formed which would otherwise change the sample temperature conditions. The spread in arrival time of neutrons with two different energies is related to the distance L_W from the sample to the moderator. The largest distance allowed for a maximum time spread can be calculated by:

$$L_W < \frac{\tau_{rsl} \cdot \sqrt{\frac{2}{m}}}{\sqrt{\frac{1}{E_{min}}} - \sqrt{\frac{1}{E_{max}}}} = 9.3\,cm \tag{6.3}$$

The sample has to be placed at 9.3 cm behind the moderator to capture all resonant neutrons within this time frame. Moving the sample close to the moderator also reduces the visible surface area of the moderator to the detector. This reduces the number of available neutrons and therefore the statistical accuracy. The results of figure 4.23 can be used to place the field of view to the area of the moderator with the highest brightness to partly counteract this effect.
By comparing single bins for the temperature calculation, only the upper and the lower end of each bin have to fulfill these conditions. In this case E_{min}=3.9 eV and E_{max}=4.05 eV have to be inserted into equation 6.3. This allows an increase of the minimum distance to 26 cm to the moderator. A larger sample distance increases the visible moderator surface from the detector as indicated in figure 6.6.
So far in this approach neutrons were treated as they are emitted simultaneously from the moderator. As it has been pointed out in figure 4.28, the neutrons are emitted with a time uncertainty of $\Delta t_s = 1\,\mu s$ from this moderator at 4.15 eV. This sets a limit to the minimum distance of the detector L so that the time difference in an energy bin is larger than the emission uncertainty. This can be done by replacing τ_{rsl} in equation 6.3 with Δt_s. This sets the minimum distance of the detector to 1.29 m. which is much closer than the 4 m proposed by [Fernández et al., 2019] and would increase the neutron flux by a factor of 10 in comparison.

Comparing τ_{rsl} with Δt_s reveals a fundamental problem with this approach. If the initial time spread of the neutrons is larger than the duration of a stable temperature in the sample, then the measurement will be distorted.

There are four possible options to approach this issue. The first option would be to go to a resonance with a higher energy and therefore profiting from the shorter Δt_s for higher neutron energies. [Fernández et al., 2019] proposed the usage of the ^{182}W resonance at 21 eV. Switching to the 21 eV resonance does come at a cost of reduced detector efficiency by 56 % from the reduction in boron cross sections for higher energies. In addition, the number of neutrons/eV decreases with $E^{-0.92}$ and therefore the number of neutrons inside this resonance is decreased by 61 % in comparison to the 4.15 eV resonance. These factors lead to a combined reduction in available resonant neutrons to 17 % of the number of neutrons that can be used at 4.15 eV

[Fernández et al., 2019] estimated Δt_s by assuming all neutrons have their origin within one mean free path from the surface and used their propagation time for that distance as uncertainty. While it is true

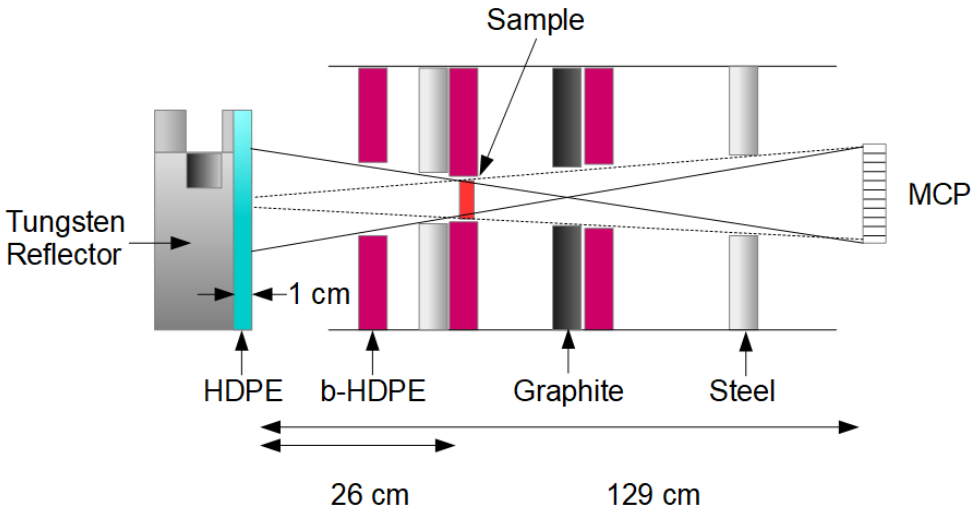

Figure 6.6: Possible setup for NRS thermometry. The sample is placed in between moderator and detector and a combination of borated HDPE, steel and graphite layers are collimating the neutron beam to ensure all neutrons have passed through the sample. Parts of the moderator have been replaced by tungsten as described in the text to reduce Δt_s.

that most neutrons have their origin within this depth, the time-spread neutrons need to be moderated to this energy is neglected. This contribution to Δt_s is significant and increases the 80 ns spread from this analytical approach to 500 ns calculated by PHITS and displayed in figure 6.7. 500 ns is a reduction in Δt_s by 50 % but still not sufficient for a time resolution of 200 ns. As previously discussed in figure 4.25, Δt_s drops below 200 ns for neutron energies above 100 eV. Therefore the ^{182}W resonance at 115 eV could be used. If the reduced neutron numbers and the decrease in efficiency at these energies are considered, the number of detectable resonant neutrons decreases to 5 % in comparison to the 4.15 eV resonance.

The second approach would be the use of a chopper made out of a highly neutron absorbing material like boron-carbide to reduce the neutron time spread. The maximum neutron emission for 4 eV neutrons appears according to figure 6.7 between 550 and 750 ns. If it is possible to isolate this time interval, it would still contain 22 % of all neutrons with resonant energies. With time scales in the ns regime, it has to be verified if this is technically feasible. Most neutrons are emitted from an area around 7 cm in diameter at the moderator surface. If a chopper would have to travel this distance in 200 ns it would require a speed of 350 km/s. This is close to the galactic escape velocity of 500 km/s [Carney et al., 1988] and can be seen as technical not feasible.

The third option that can be investigated to reduce the pulse width is a reduction of the thickness of the moderating material. If the thickness of the moderator approaches similar dimensions as the scattering length of the neutrons in this material, the likelihood increases that neutrons leave the moderator after a scattering process. This decreases the likelihood of neutrons reaching lower energies as this requires on average a higher number of scattering events. This approach favors neutrons that have undergone a lower number of scattering events to reach a certain energy. Therefore they have traveled a smaller distance in the moderator before they are emitted and a respectively smaller time spread. Simply reducing the size of the moderator would drastically reduce the epi-thermal neutron flux as seen in figure 4.21 which is not desirable. A more sophisticated solution is to replace large parts of the moderator with a material that still retains the diffusion of neutrons towards the surface but does not contribute to moderation. If this is combined with a thin moderation layer at the surface, then the time resolution is

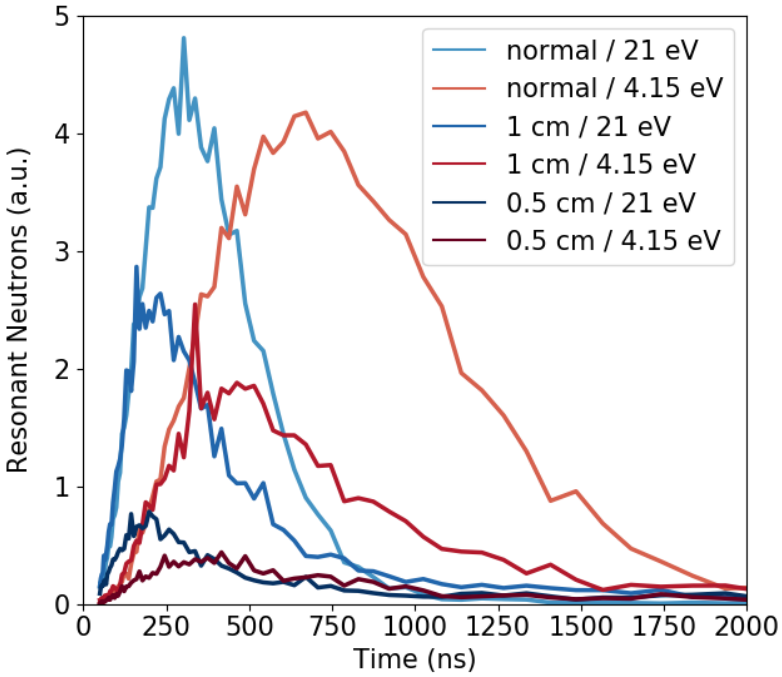

Figure 6.7: The time delay for resonant neutrons crossing the moderator surface. The bright colors are corresponding to the normal moderator design discussed in section 4.4. For the darker colors, the moderator body was replaced by a tungsten reflector and only the last 1 respectively 0.5 cm facing the detector was made out of HDPE for moderation as indicated in figure 6.6. The smaller moderation thickness decreased the peak width but the height as well. Thinner moderators have a smaller FWHM but also less resonant neutrons.

increased with only intermediate losses in the neutron flux. The details of such a moderator-reflector combination can be seen in figure 6.6. The results can be seen for a moderation layer thickness of 1 cm and 0.5 cm in figure 6.7 and in comparison to the normal moderator consistent fully out of polyethylene.

With a 1 cm thick HDPE layer Δt_s was reduced from 1 μs to 740(50) ns for the 4.15 eV resonance. Losses in moderation efficiency reduced the number of available neutrons to 37 % in comparison to the original setup. For 21 eV Δt_s is decreased from 520(40) to 400(40) ns with 61 % neutrons left. Further shrinking the moderator width to 0.5 cm decreased Δt_s down to 630(50) ns but also reduced neutrons in this energy range to 8 %. For 21 eV these values are 350(40) ns with a reduction to 19 % of resonant neutrons. The results can be seen in figure 6.7

Comparing these first three approaches to reduce Δt_s below 200 ns then it is possible to say that the only way to do this is via switching to the ^{182}W resonance at 115 eV. The other approaches are either not technically feasible or do not accomplish the desired pulse width reduction. A fourth approach would be changing the experimental parameters in such a way, that the temperature remains constant for a longer time period. This would require more laser energy at the shocked sample, but as well would increasing the neutron production rate by a factor of 20 to be able to operate at 115 eV. Another option could be switching from laser heating to heavy ion heating. Such an option would be possible at the FAIR facility [Mintsev et al., 2016] [Sharkov and Varentsov, 2013] if it is equipped with a high power laser in the kJ regime.

If the approach is chosen to increase τ_{rsl} to 1 μs then it is possible to use the experimental results from section 5.1 to predict a minimum source strength for a desired 2 % temperature accuracy. If the approach is chosen to switch to the 115 eV resonance, then the neutron numbers predicted here have to be scaled by a factor of 20. According to Poisson statistics [Hartung et al., 2012] the uncertainty for each bin scales with:

$$\frac{\delta N}{N} = \frac{1}{\sqrt{N_{bin}}} \tag{6.4}$$

Inserting the 2 % accuracy provides a minimum of 2500 N/bin. From figure 5.6 the average detected neutron numbers per μs next to the resonance are given with 0.33(8) N/μs per shot. The first energy bin at the resonance from 3.9 to 4.05 eV has a time width of 0.88 μs and therefore the reference value for this experiment is 0.29 N/bin. This shows that to reach the required accuracy with this setup, an increase in the neutron source strength by a factor of 8600 is required.

From figure 5.2 (a) the 4π equivalent of each shot is $7(1)\cdot10^8$ N. Scaling this number by a factor of 8600 would give a total neutron count of $6.0\cdot10^{12}$. With the proposed decrease in detector distance of 1.29 m this can be reduced to a 4π equivalent of $3.1(1.7)\cdot10^{12}$ N.

This is a factor of 62 times higher in neutron numbers than the current record held by [Kleinschmidt et al., 2018] with the PHELIX laser, with $5\cdot10^{10}$ neutrons. The most straight forward way to increase the neutron numbers would be by increasing the laser energy as this has the highest impact on the neutron numbers. From section 4.1 it is known that the neutron numbers in this energy region are proportional to $E_L^{2.6}$. This can be used to predict the energy requirement of the needed laser system. If PHELIX is approximated with 200 J laser energy then one can calculate:

$$E_L = 200\,J \cdot 62^{1/2.6} = 978\,J \approx 1\,kJ. \tag{6.5}$$

This estimation of 1 kJ required laser energy only holds true if the contrast remains sufficiently high and no pre-pulses exceed 10^{10} W/cm^2. For changing to the 115 eV resonance the minimal required energy can be estimated with this method to be around 3 kJ corresponding to a source strength of $6\cdot10^{13}$ N.

7 Summary and Outlook

In the course of this thesis, a setup for non-destructive material analysis based on laser-driven neutron sources was developed and tested at the PHELIX laser facility. For an adequate evaluation of the potential of such a setup to serve as an alternative to existing neutron sources, it was divided into its individual components. For each part, the requirements have been defined and the influence on the neutron production has been investigated. In this context, various scaling laws have been identified and the individual components were optimized to maximize the neutron yield. This was completed with an evaluation of the limitations of each part to maintain realistic conditions. This knowledge was then used to predict the capabilities of three different neutron sources based on low, intermediate and high energy laser systems to asses their applicability to existing material analysis techniques.

A comparison of the attributes of existing neutron sources revealed that LDNS have the highest potential as an epi-thermal neutron source as measurements have the highest benefits of the short pulse length in this regime. For this reason, a setup was developed to maximize the neutron flux in this regime. As the first step to this goal, the influence of the laser parameters on the ion production was determined. It was shown that the cut off energy does not simply scale with the intensity as commonly assumed but has individual dependencies on the laser energy ($E_L^{1/3}$), pulse length ($\tau^{-1/20}$) and focal spot size ($r^{-1/2}$). This was followed by a conceptual study of existing targetry solutions which lead to the conclusion that a liquid leaf target is the best solution for a high repetition rate LDNS as it can operate at the highest repetition rates for the longest time without interruption while being at a high technological readiness level. With the usage of the Monte Carlo code PHITS it was possible to make predictions which part of the ion spectrum has the highest influence on the neutron yield and how the yield depends on the cut off energy. With this information it was possible to design a new catcher out of 6 mm thick lithium followed by a vanadium cylinder with a thickness matched to the stopping range of the cut off energy of the ion spectrum. Simulations for this configuration predict a 20(1) % higher number of fast neutrons compared to a beryllium catcher and a 50 % increase in epi-thermal flux due to a higher moderation efficiency. A systematic design approach for the moderator enabled an additional increase in epi-thermal flux by 270 % in comparison to the design used by [Kleinschmidt, 2017] for moderation. Within this optimization process, a new collimator was developed to reduce the background while maximizing the moderated neutron flux on the detector. With this approach a signal to noise ratio of 15(4):1 is predicted by the simulations and the measured ratio was 17(1):1 at the detector. The borated MCP used for detection was calibrated and an algorithm was developed to filter the output signal to remove the background caused by the high noise environment.

In the second part of this thesis, an experiment at the PHELIX laser facility was conducted to demonstrate the applicability of the proposed setup under real conditions. In this experiment, it was possible to fully characterize the source by simultaneously measuring the fast and slow neutron spectrum. The moderated neutron beam was used to successfully identify the isotopes ^{182}W and ^{183}W inside a tungsten sample via NRTA. This was the first neutron resonance spectroscopy measurement with a laser-driven neutron source that was capable to identify multiple isotopes. It was also shown that it is possible at this system to use the black resonance filter technique to determine the signal to background ratio. Parallel to the spectroscopy, it was possible to determine the thickness of a 1 mm indium plate behind a 2 mm thick

lead shield from a single-shot through a thermal neutron radiography. The accuracy of this measurement was better than 50 %. A second thermal neutron radiography detector was used to successfully resolve an indium and a tungsten sample.

In the third part, PHITS simulations were used to predict the performance of LDNS based on state of the art laser systems. The first source was based on a 1 J laser system developed by TRUMPF-Scientific [Metzger, 2018] that operates at 1 kHz. This LDNS demonstrates the potential of a mobile combined source of neutrons and X-rays for applications in the security sector. Simulations and scaled numbers from an experiment predict a neutron flux between 1 and $7{\cdot}10^{10}$ n/(sr·s) with a simultaneous hard X-ray flux of 10^{11} Ph/(sr·s). The second LDNS that was introduced in this context was a stationary epi-thermal neutron source based on the setup from section 4 in combination with the SHARC and BAT laser system. With simulations based on experiments, it was shown that these systems can deliver epi-thermal neutron fluxes at the detector with up to $4{\cdot}10^{4}$ n/(cm^{2}s) which is in similar dimensions as it is possible for conventional neutron sources. Lastly, the potential of a high energy laser system was evaluated on the applicability of NRS based warm dense matter temperature measurements. The required laser parameters have been calculated to be between 1 and 3 kJ depending on the shock conditions. In this process, fundamental problems with the proposed design of [Fernández et al., 2019] have been pointed out and potential solutions have been discussed.

For future work, it is important that the scalings developed in this thesis have to be verified with experiments. This requires more parameter scans with independent variations in the pulse length, the laser energy and the focal spot size on a single laser system while measuring the cut off energy and the number of accelerated ions simultaneously. The maximal repetition rate a liquid leaf target can operate at is not known for lasers with a higher E_L and has to be identified as a function of energy. Also, a systematic study has to be performed on how the use of deuterated materials impacts the neutron yield for different laser energies. The process of neutron producing reactions from protons and deuterons is so far not sufficiently examined in the regime of 1 MeV to 100 MeV from an experimental point of view. Cross sections have to be measured and included in the Monte Carlo codes. These codes also have to be cross calibrated against each other and compared to a laser neutron experiment. The proposed Li-V and Li-W catcher designs have to be evaluated experimentally. For a continuous operation, the ablation of the catcher material over time has to be investigated as well as the nuclear activation. Also, simulations for the activation of the target area from neutron absorption are required and a determination of the shielding requirements of a laser-driven neutron facility.

Glossary

γ-flash - γ and hard X-ray emission caused by the laser target interaction. 35, 63, 73, 79, 80, 84, 86, 87, 89, 91

B-HDPE - 5 % borated high density polyethylene. 69, 70, 72, 73, 77, 81

black resonance - A resonance with a strong absorption that filters out all neutrons with matching energies. 32, 82, 109

catcher - Converter material for neutron production. 5, 14, 26, 35, 46, 51, 52, 56, 57, 58, 59

epi-thermal neutrons - neutrons with energies between 1 and several 100s of eV. In most parts of the thesis this term referes to the energy range of 1 to 10 eV out of experimental relevance. 57, 60, 63, 69, 70, 72

fast neutrons - neutrons with energies above 0.1 MeV. 18, 19, 20, 57, 59, 60, 109

hot electrons - Electrons heated by the laser into the MeV regime. 8, 11, 12, 35, 49, 55, 95, 98, 99

slow neutrons - neutrons in the thermal and epi-thermal regime. 18, 21, 69, 73, 90

thermal neutrons - neutrons with energies below 1 eV that follow a Maxwellian energy distribution with the moderator temperature. 27, 65, 70, 101

white - Neutron beam with a broad energy spectrum. 31

Acronyms

AmBe Americium - Beryllium. 25

ASE Amplified Spontaneous Emission. 9, 49, 50

BAT Big Aperture Thulium. 100, 101, 110

BDT Bubble Detector Thermal. 77, 78, 79

CANS Compact Accelerator Driven Neutron Sources. 25, 27, 29

ELI Exteme Light Infrastructure. 26

EMP Electro Magnetic Impulse. 44, 74, 81, 86, 91

EOS Equation Of State. 102

ESS European Spallation Source. 5, 23, 24, 28

HBS High Brilliance Source. 25

HDPE High Density PolyEhtlylene. 66, 69, 82, 89, 91, 104, 105, 106

LANSCE Los Alamos Neutron Science CEnter. 23, 27

LDNS Laser-Driven Neutron Sources. 2, 5, 6, 23, 29, 87, 99

LLNL Lawrence Livermore National Laboratory. 26, 100

MC Monte Carlo. 2

MCP Multi Channel Plate. 74, 91

NAA Neutron Actication Analysis. 27, 95

NRCA Neutron Resonance Capture Analysis. 31

NRI Neutron Resonance Imaging. 5, 33, 87, 91, 100, 101

NRS Neutron Resonance Spectroscopy. 2, 5, 16, 17, 32, 33, 57, 63, 66, 69, 76, 77, 87, 95, 101, 102, 104, 110

NRTA Neutron Resonance Transmission Analysis. 31, 32, 77, 80, 109

PGNAA Prompt Gamma Neutron Activation Analysis. 31, 95, 99

PMT Photo Multiplier Tube. 76, 77, 79

PND Personal Neutron Dosimeters. 77, 78, 79, 90

RCF Radio Chromatic Film. 50, 77

RITA Relativistic Induced Transparency Acceleration. 12, 13, 26

SHARC Scalable High-power Advanced Radiographic Capability. 26, 100, 101, 110

TOF Time-Of-FLight. 17, 24, 27, 28, 30, 33, 80, 81, 101

TRIGA Training, Research Isotopes General Atomic. 24

WDM Warm Dense Matter. 102

8 Acknowledgements

Als allererstes möchte ich mich bei Prof. Dr. Markus Roth für die Möglichkeit bedanken, ein derart spannendes Thema zu bearbeiten, sowie für das Vertrauen, mich innerhalb des Themengebietes frei bewegen zu können. Ich habe in den letzten drei Jahren so viel gelernt wie selten zuvor. Markus hatte immer für mich ein offenes Ohr wenn ich Probleme oder neue Ideen hatte wie man das Thema weiterführen könnte. Er hat immer für eine gute Atmosphäre in der Arbeitsgruppe gesorgt und ich danke ihm, dass er uns ermöglicht dahin zu gehen, wo noch niemand zuvor gegangen ist.

Mein besonderer Dank gilt auch Annika Kleinschmidt, welche mich in das Thema eingeführt und mir mit ihrer Erfahrung beiseite gestanden hat. Auch dafür dass sie bei unseren Experimenten immer mit von der Partie gewesen ist, selbst als sie schon nicht mehr in der Arbeitsgruppe gewesen ist.

Desweiteren gilt mein Dank Stefan Scheuren, welcher mir während seiner Master Thesis einiges an Arbeit abgenommen hat, sowie zu jeder Zeit motiviert und mit vielen Ideen am geholfen hat das Projekt vorranzubringen.

Auch bedanken möchte ich mich bei Dennis Schumacher, den ich häufig mit technischen Fragen gequält habe, bei denen ich nicht weiter wusste. Genauso möchte ich mich bei Vincent Bagnoud für das regelmäßige Motivieren zum Laufen bedanken, sowie bei Simon Röder für den Kaffee und das Biotop. Genauso danke ich der gesamten Plasmaphysik an der GSI und dem Phelix Laser Team.

Mein Dank gilt auch Alexandra Tebartz, für das Herstellen unserer Targets, sowie Gabriel Schaumann für die Hilfe und Unterstützung im organisatorischen Bereich.

Bei meiner Familie möchte ich mich bedanken, da sie es mir erst ermöglicht hat diesen Weg einzuschlagen und immer hinter dem gestanden hat was ich tue. Ein besonderer Dank geht raus an David Held, Andy Manteuffel und vor allem an Lea-Alicia Auth die mir während meiner Thesis seelischen und moralischen Beistand geliefert haben, wenn ich ihn am nötigsten gebraucht habe. Danke Dafür.

Mein Dank gilt natürlich auch den Leuten die sich aufopferungsvoll dem Lesen meiner Thesis angenommen haben, darunter Isabella Fath, Benedikt Schmitz und Franziska Treffert, die mir damit einige schlaflose Nächte beschert haben.

Bibliography

[Abdi and Salkind, 2007] Abdi, H. and Salkind, N. J. (2007). Encyclopedia of measurement and statistics. *Thousand Oaks, CA: Sage. Agresti, A.(1990) Categorical data analysis., New York: Wiley. Agresti, A.(1992) A survey of exact inference for contingency tables. Statist Sci*, 7:131–153.

[Alfven, 1986] Alfven, H. (1986). Model of the plasma universe. *IEEE transactions on plasma science*, 14(6):629–638.

[Almomani,] Almomani, A. Tnsa a new particle source for conventional accelerators. `http://nnp.physik.uni-frankfurt.de/activities/FrSem/almomani_2012.pdf`, year = 2012, note = Accessed: 2020.02.04.

[Anderson et al., 2016] Anderson, I., Andreani, C., Carpenter, J., Festa, G., Gorini, G., Loong, C.-K., and Senesi, R. (2016). Research opportunities with compact accelerator-driven neutron sources. *Physics Reports*, 654:1–58.

[Armstrong et al., 2019] Armstrong, C., Brenner, C., Jones, C., Rusby, D., Davidson, Z., Zhang, Y., Wragg, J., Richards, S., Spindloe, C., Oliveira, P., et al. (2019). Bremsstrahlung emission from high power laser interactions with constrained targets for industrial radiography. *High Power Laser Science and Engineering*, 7.

[Bagnoud et al., 2010] Bagnoud, V., Aurand, B., Blazevic, A., Borneis, S., Bruske, C., Ecker, B., Eisenbarth, U., Fils, J., Frank, A., Gaul, E., et al. (2010). Commissioning and early experiments of the phelix facility. *Applied Physics B*, 100(1):137–150.

[Batani et al., 2010] Batani, D., Jafer, R., Veltcheva, M., Dezulian, R., Lundh, O., Lindau, F., Persson, A., Osvay, K., Wahlström, C., Carroll, D., et al. (2010). Effects of laser prepulses on laser-induced proton generation. *New Journal of Physics*, 12(4):045018.

[Battistoni et al., 2007] Battistoni, G., Cerutti, F., Fasso, A., Ferrari, A., Muraro, S., Ranft, J., Roesler, S., and Sala, P. (2007). The fluka code: Description and benchmarking. In *AIP Conference proceedings*, volume 896, pages 31–49. AIP.

[Batygin et al., 2018] Batygin, Y., Garnett, R., Rybarcyk, L., et al. (2018). Emittance growth and beam losses in lansce linear accelerator. In *ICFA ABDW on High-Intensity and High-Brightness Hadron Beams (HB'18), Daejeon, Korea, 17-22 June 2018*, pages 70–74. JACOW Publishing, Geneva, Switzerland.

[Bauer et al., 1995] Bauer, D., Mulser, P., and Steeb, W.-H. (1995). Relativistic ponderomotive force, uphill acceleration, and transition to chaos. *Physical review letters*, 75(25):4622.

[Bertsch et al., 1996] Bertsch, G., Reinhard, P.-G., and Suraud, E. (1996). Particle evaporation from semiclassical dynamics. *Physical Review C*, 53(3):1440.

[Bianco et al., 2008] Bianco, N., Manca, O., Nardini, S., and Tamburrino, S. (2008). A numerical model for transient heat conduction in semi-infinite solids irradiated by a moving heat source. In *Proceedings of the COMSOL Conference*, pages 1–7.

[Bishop, 2006] Bishop, C. M. (2006). *Pattern recognition and machine learning*. springer.

[Borghesi et al., 2006] Borghesi, M., Fuchs, J., Bulanov, S., Mackinnon, A., Patel, P., and Roth, M. (2006). Fast ion generation by high-intensity laser irradiation of solid targets and applications. *Fusion Science and Technology*, 49(3):412–439.

[Boudard et al., 2013] Boudard, A., Cugnon, J., David, J.-C., Leray, S., and Mancusi, D. (2013). New potentialities of the liège intranuclear cascade model for reactions induced by nucleons and light charged particles. *Physical Review C*, 87(1):014606.

[Brauckmann, 2018] Brauckmann, S. (2018). *Erzeugung von Röntgenstrahlung durch intensive Laserpulse*. PhD thesis.

[Brenner et al., 2011] Brenner, C., Green, J., Robinson, A., Carroll, D., Dromey, B., Foster, P., Kar, S., Li, Y., Markey, K., Spindloe, C., et al. (2011). Dependence of laser accelerated protons on laser energy following the interaction of defocused, intense laser pulses with ultra-thin targets. *Laser and Particle Beams*, 29(3):345–351.

[Brenner, 2012] Brenner, C. M. (2012). *Laser-Driven Proton Beams: Mechanisms for spectral control and efficiency enhancement*. PhD thesis, University of Strathclyde.

[Brown et al., 2018] Brown, D. A., Chadwick, M., Capote, R., Kahler, A., Trkov, A., Herman, M., Sonzogni, A., Danon, Y., Carlson, A., Dunn, M., et al. (2018). Endf/b-viii. 0: the 8th major release of the nuclear reaction data library with cielo-project cross sections, new standards and thermal scattering data. *Nuclear Data Sheets*, 148:1–142.

[Brueckel, 2018] Brueckel, T. (2018). The hbs project from a high brilliance source to compact sources for universities. `http://2fdn.neel.cnrs.fr/IMG/pdf/Worshop_Cans/Bruckel_HBS_2FDN_2018.pdf`. Accessed: 2019-08-23.

[Bulanov et al., 2019] Bulanov, S. S., Park, J., Bin, J., Ji, Q., Steinke, S., Schroeder, C. B., Vay, J.-L., Esarey, E., Schenkel, T., and Leemans, W. P. (2019). Laser ion acceleration studies at bella center (conference presentation). In *Laser Acceleration of Electrons, Protons, and Ions V*, volume 11037, page 1103702. International Society for Optics and Photonics.

[Busold, 2014] Busold, S. (2014). *Construction and characterization of a laser-driven proton beamline at GSI*. PhD thesis, Technische Universität.

[Carney et al., 1988] Carney, B. W., Latham, D. W., and Laird, J. B. (1988). A survey of proper-motion stars. v-extreme-velocity stars and the local galactic escape velocity. *The Astronomical Journal*, 96:560–566.

[Ceccotti et al., 2007] Ceccotti, T., Levy, A., Popescu, H., Reau, F., d'Oliveira, P., Monot, P., Geindre, J., Lefebvre, E., and Martin, P. (2007). Proton acceleration with high-intensity ultrahigh contrast laser pulses. *Physical review letters*, 99(18):185002.

[Chichester, 2012] Chichester, D. L. (2012). Production and applications of neutrons using particle accelerators. In *Industrial Accelerators and Their Applications*, pages 243–305. World Scientific.

[Cianchi et al., 2018] Cianchi, A., Andreani, C., Bedogni, R., Festa, G., Planell, O. S., and Senesi, R. (2018). Towards a compact laser based neutron source. In *Journal of Physics: Conference Series*, volume 1021, page 012011. IOP Publishing.

[Clark et al., 2000] Clark, E., Krushelnick, K., Davies, J., Zepf, M., Tatarakis, M., Beg, F., Machacek, A., Norreys, P., Santala, M., Watts, I., et al. (2000). Measurements of energetic proton transport through magnetized plasma from intense laser interactions with solids. *Physical Review Letters*, 84(4):670.

[Comsan, 2011] Comsan, M. (2011). spallation neutron sources for science and technology.

[Connaster, 2019] Connaster, R. (2019). Overview presentation - connaster r (ess) , ess fundamentals. https://www.isis.stfc.ac.uk/Pages/overview-presentation-connaster-r-ess.pdf#search=ess. Accessed: 2019.04.03.

[Dabruck, 2018] Dabruck, J. P. (2018). *Target Station Optimization for the High-Brilliance Neutron Source HBS: Simulation Studies Based on the Monte Carlo Method*. Springer.

[Daido et al., 2012] Daido, H., Nishiuchi, M., and Pirozhkov, A. S. (2012). Review of laser-driven ion sources and their applications. *Reports on progress in physics*, 75(5):056401.

[Ding, 2018] Ding, J. (2018). *Generation, Handling and Transport of Laser-Driven Heavy Ion Beams*. PhD thesis, Technische Universität.

[Dollar et al., 2013] Dollar, F., Zulick, C., Matsuoka, T., McGuffey, C., Bulanov, S., Chvykov, V., Davis, J., Kalinchenko, G., Petrov, G., Willingale, L., et al. (2013). High contrast ion acceleration at intensities exceeding 10 21 w cm- 2. *Physics of Plasmas*, 20(5):056703.

[Dover, 2017] Dover, N. (2017). Sheath acceleration up to $5x10^{21}w/cm^2$ at kansai photon science institute. https://agenda.infn.it/event/12611/contributions/15387/attachments/11296/12698/WG2_summary.pdf. Accessed: 2019.09.25.

[Einstein, 1905] Einstein, A. (1905). Über einen die erzeugung und verwandlung des lichtes betreffenden heuristischen gesichtspunkt. *Annalen der physik*, 322(6):132–148.

[El-Taher et al., 2003] El-Taher, A., Kratz, K.-L., Nossair, A., and Azzam, A. (2003). Determination of gold in two egyptian gold ores using instrumental neutron activation analysis. *Radiation physics and chemistry*, 68(5):751–755.

[Eli Beamlines, 2019] Eli Beamlines (2019). Eli beamlines laser 3 hapls 1 pw, 30 j, 10 hz. https://www.eli-beams.eu/facility/lasers/laser-3-hapls-1-pw-30-j-10-hz/. Accessed: 2020-01-04.

[Elizer, 2002] Elizer, S. (2002). *The Interaction of High-Power Lasers with Plasmas*. CRC press.

[Fang et al., 2016] Fang, Y., Ge, X., Yang, S., Wei, W., Yu, T., Liu, F., Chen, M., Liu, J., Yuan, X., Sheng, Z., et al. (2016). Different effects of laser contrast on proton emission from normal large foils and transverse-size-reduced targets. *Plasma Physics and Controlled Fusion*, 58(7):075010.

[Fernández et al., 2019] Fernández, J. C., Barnes, C. W., Mocko, M. J., and Zavorka, L. (2019). Requirements and sensitivity analysis for temporally-and spatially-resolved thermometry using neutron resonance spectroscopy. *Review of Scientific Instruments*, 90(9):094901.

[Flacco et al., 2010] Flacco, A., Sylla, F., Veltcheva, M., Carrié, M., Nuter, R., Lefebvre, E., Batani, D., and Malka, V. (2010). Dependence on pulse duration and foil thickness in high-contrast-laser proton acceleration. *Physical Review E*, 81(3):036405.

[Flippo et al., 2008a] Flippo, K., Humieres, E., Gaillard, S., Rassuchine, J., Gautier, D., Schollmeier, M., Nuernberg, F., Kline, J., Adams, J., Albright, B., et al. (2008a). Increased efficiency of short-pulse laser-generated proton beams from novel flat-top cone targets. *Physics of Plasmas*, 15(5):056709.

[Flippo et al., 2008b] Flippo, K., Workman, J., Gautier, D., Letzring, S., Johnson, R., and Shimada, T. (2008b). Scaling laws for energetic ions from the commissioning of the new los alamos national laboratory 200 tw trident laser. *Review of Scientific Instruments*, 79(10):10E534.

[Forget, 2013] Forget, B. (2013). Neutron interactions and applications.

[Fourmaux et al., 2013] Fourmaux, S., Buffechoux, S., Albertazzi, B., Capelli, D., Lévy, A., Gnedyuk, S., Lecherbourg, L., Lassonde, P., Payeur, S., Antici, P., et al. (2013). Investigation of laser-driven proton acceleration using ultra-short, ultra-intense laser pulses. *Physics of Plasmas*, 20(1):013110.

[Fuchs et al., 1998] Fuchs, J., Adam, J., Amiranoff, F., Baton, S., Gallant, P., Gremillet, L., Héron, A., Kieffer, J., Laval, G., Malka, G., et al. (1998). Transmission through highly overdense plasma slabs with a subpicosecond relativistic laser pulse. *Physical review letters*, 80(11):2326.

[Fuchs et al., 2006] Fuchs, J., Antici, P., dHumières, E., Lefebvre, E., Borghesi, M., Brambrink, E., Cecchetti, C., Kaluza, M., Malka, V., Manclossi, M., et al. (2006). Laser-driven proton scaling laws and new paths towards energy increase. *Nature physics*, 2(1):48.

[Gaillard et al., 2011] Gaillard, S., Kluge, T., Flippo, K., Bussmann, M., Gall, B., Lockard, T., Geissel, M., Offermann, D., Schollmeier, M., Sentoku, Y., et al. (2011). Increased laser-accelerated proton energies via direct laser-light-pressure acceleration of electrons in microcone targets. *Physics of Plasmas*, 18(5):056710.

[Gallagher and Bloomfield, 2013] Gallagher, P. and Bloomfield, D. (2013). Py5012 introduction to plasma physics, lecture 1: multiple-fluid theory of plasmas. *Astrophysics Research Group, Trinity College Dublin*.

[Garrett, 1962] Garrett, A. B. (1962). The neutron identified: Sir james chadwick. *Journal of Chemical Education*, 39(12):638.

[Gauthier et al., 2016] Gauthier, M., Kim, J., Curry, C., Aurand, B., Gamboa, E., Göde, S., Goyon, C., Hazi, A., Kerr, S., Pak, A., et al. (2016). High-intensity laser-accelerated ion beam produced from cryogenic micro-jet target. *Review of Scientific Instruments*, 87(11):11D827.

[George et al., 2019] George, K., Morrison, J., Feister, S., Ngirmang, G., Smith, J., Klim, A., Snyder, J., Austin, D., Erbsen, W., Frische, K., et al. (2019). High repetition rate (>= khz) targets and optics from liquid microjets for the study and application of high intensity laser-plasma interactions. *arXiv preprint arXiv:1902.04656*.

[Gerthsen, 2013] Gerthsen, C. (2013). *Gerthsen Physik*. Springer-Verlag.

[Ghoshal, 1950] Ghoshal, S. N. (1950). An experimental verification of the theory of compound nucleus. *Physical Review*, 80(6):939.

[Gibbon, 2004] Gibbon, P. (2004). *Short pulse laser interactions with matter*. World Scientific Publishing Company Singapore.

[Goede, 2019] Goede, S. (2019). Cryogenic jet targets for high repetition rate experiments at fel and high power laser facilities. `https://www.cnbc.com/2019/06/21/helium-shortage-why-the-worlds-supply-is-drying-up.html`. Accessed: 2019.10.11.

[Gold and Wong, 1963] Gold, R. and Wong, C. (1963). Disintegration of the deuteron in a coulomb field. *Physical Review*, 132(6):2586.

[Goldenbaum, 2004] Goldenbaum, F. (2004). The physics of spallation processes-theory, experiments and applications.

[Gray, 2019] Gray, T. (2019). periodictable.com. `https://periodictable.com/`. Accessed: 2020.01.01.

[Green et al., 2014] Green, J., Robinson, A., Booth, N., Carroll, D., Dance, R., Gray, R., MacLellan, D., McKenna, P., Murphy, C., Rusby, D., et al. (2014). High efficiency proton beam generation through target thickness control in femtosecond laser-plasma interactions. *Applied Physics Letters*, 104(21):214101.

[Griffin, 1966] Griffin, J. J. (1966). Statistical model of intermediate structure. *Physical review letters*, 17(9):478.

[Guler et al., 2016] Guler, N., Volegov, P., Favalli, A., Merrill, F. E., Falk, K., Jung, D., Tybo, J. L., Wilde, C. H., Croft, S., Danly, C., et al. (2016). Neutron imaging with the short-pulse laser driven neutron source at the trident laser facility. *Journal of Applied Physics*, 120(15):154901.

[Günther, 2011] Günther, M. M. (2011). *Untersuchung relativistischer Laserplasmen mittels nukleardiagnostischer Verfahren*. PhD thesis, Technische Universität.

[Hah et al., 2016] Hah, J., Petrov, G., Nees, J., He, Z.-H., Hammig, M., Krushelnick, K., and Thomas, A. (2016). High repetition-rate neutron generation by several-mj, 35 fs pulses interacting with free-flowing d2o. *Applied Physics Letters*, 109(14):144102.

[Harrison et al., 2017] Harrison, R., Di Fulvio, A., Bordy, J., Miljanić, S., Stolarczyk, L., and Knežević, Ž. (2017). Dosimetry for second cancer risk estimation in radiotherapy: measurements in water phantoms. *EURADOS Report*, 1.

[Hartung et al., 2012] Hartung, J., Elpelt, B., and Klösener, K.-H. (2012). *Statistik: Lehr-und Handbuch der angewandten Statistik*. Walter de Gruyter.

[Hegelich et al., 2013] Hegelich, B., Pomerantz, I., Yin, L., Wu, H., Jung, D., Albright, B., Gautier, D., Letzring, S., Palaniyappan, S., Shah, R., et al. (2013). Laser-driven ion acceleration from relativistically transparent nanotargets. *New Journal of Physics*, 15(8):085015.

[Herkommer et al., 2019] Herkommer, C., Krötz, P., Klingebiel, S., Wandt, C., Bauer, D., Michel, K., Kienberger, R., and Metzger, T. (2019). Towards a joule-class ultrafast thin-disk based amplifier at kilohertz repetition rate. In *CLEO: Science and Innovations*, pages SM4E–3. Optical Society of America.

[Higginson et al., 2018] Higginson, A., Gray, R., King, M., Dance, R., Williamson, S., Butler, N., Wilson, R., Capdessus, R., Armstrong, C., Green, J., et al. (2018). Near-100 mev protons via a laser-driven transparency-enhanced hybrid acceleration scheme. *Nature communications*, 9(1):724.

[Hoffmeister, 2014] Hoffmeister, G. (2014). *Influencing laser-accelerated ions by femtosecond-laser desorption*. PhD thesis, Technische Universität.

[IAEA, 2009] IAEA (2009). Physics of uranium and nuclear energy. `http://www-naweb.iaea.org/napc/physics/research_reactors/database/RR%20Data%20Base/datasets/report/Italy%20(Italian%20Republic)%20%20Research%20Reactor%20Details%20-%20LENA,%20TRIGA%20II%20PAVIA.htm`. Accessed: 2019-08-22.

[IAEA-TECDOC, 2008] IAEA-TECDOC (2008). Non-destructive tool for materials testing. Technical report, IAEA-TECDOC-1604, Report of a coordinated research project, 2008, ISBN 978.

[Iida et al., 2007] Iida, K., Kohama, A., and Oyamatsu, K. (2007). Nuclear physics-formula for proton-nucleus reaction cross section at intermediate energies and its application. *Journal of the Physical Society of Japan*, 76(4):44201–44300.

[Ing et al., 1997] Ing, H., Noulty, R., and McLean, T. (1997). Bubble detectors a maturing technology. *Radiation Measurements*, 27(1):1–11.

[J. Clayton, 2019] J. Clayton, J. Van Heteren, J. J. E. S. P. S. S. l. (2019). Radiation effects in linear accelerator operations for non accelerator operations for non destructive testing, security, industrial and medical applications industrial and medical applications. `http://www.indiana.edu/~lens/UCANS/Meetings/UCANSII/PDF_presentations/UCANS_II_Clayton_Thurs_9_45.pdf`. Accessed: 2020.01.01.

[Jordan and Gozani, 2007] Jordan, K. A. and Gozani, T. (2007). Pulsed neutron differential die away analysis for detection of nuclear materials. *Nuclear Instruments and Methods in Physics Research Section B: Beam Interactions with Materials and Atoms*, 261(1-2):365–368.

[Jung et al., 2015] Jung, D., Albright, B., Yin, L., Gautier, D., Dromey, B., Shah, R., Palaniyappan, S., Letzring, S., Wu, H.-C., Shimada, T., et al. (2015). Scaling of ion energies in the relativistic-induced transparency regime. *Laser and Particle Beams*, 33(4):695–703.

[Kai et al., 2017] Kai, T., Hiroi, K., Su, Y., Shinohara, T., Parker, J. D., Matsumoto, Y., Hayashida, H., Segawa, M., Nakatani, T., Oikawa, K., et al. (2017). Reliability estimation of neutron resonance thermometry using tantalum and tungsten. *Physics Procedia*, 88:306–313.

[Kaluza et al., 2004] Kaluza, M., Schreiber, J., Santala, M. I., Tsakiris, G. D., Eidmann, K., Meyer-ter Vehn, J., and Witte, K. J. (2004). Influence of the laser prepulse on proton acceleration in thin-foil experiments. *Physical review letters*, 93(4):045003.

[Keith E., 2014] Keith E., H. (2014). Eee 562 nuclear reactor theory and design. University Lecture.

[Khaghani et al., 2017] Khaghani, D., Lobet, M., Borm, B., Burr, L., Gärtner, F., Gremillet, L., Movsesyan, L., Rosmej, O., Toimil-Molares, M. E., Wagner, F., et al. (2017). Enhancing laser-driven proton acceleration by using micro-pillar arrays at high drive energy. *Scientific reports*, 7(1):11366.

[Kim et al., 2016] Kim, J., Göde, S., and Glenzer, S. (2016). Development of a cryogenic hydrogen microjet for high-intensity, high-repetition rate experiments. *Review of Scientific Instruments*, 87(11):11E328.

[Kim et al., 2018] Kim, J. B., Schoenwaelder, C., and Glenzer, S. H. (2018). Development and characterization of liquid argon and methane microjets for high-rep-rate laser-plasma experiments. *Review of Scientific Instruments*, 89(10):10K105.

[Kirkpatrick et al., 2002] Kirkpatrick, T. J., Weyers, R. E., Anderson-Cook, C. M., and Sprinkel, M. M. (2002). Probabilistic model for the chloride-induced corrosion service life of bridge decks. *Cement and concrete research*, 32(12):1943–1960.

[Kleinschmidt, 2017] Kleinschmidt, A. (2017). *Investigation of a laser-driven neutron source with respect to different fields of application*. PhD thesis, Technische Universität.

[Kleinschmidt et al., 2018] Kleinschmidt, A., Bagnoud, V., Deppert, O., Favalli, A., Frydrych, S., Hornung, J., Jahn, D., Schaumann, G., Tebartz, A., Wagner, F., et al. (2018). Intense, directed neutron beams from a laser-driven neutron source at phelix. *Physics of Plasmas*, 25(5):053101.

[Knoll, 2000] Knoll, G. F. (2000). Radiation detection and measurement, john wiley & sons. *Inc., New York*, 2000.

[Kobayashi et al., 1992] Kobayashi, H., Wakao, H., Ikeda, Y., Ohokubo, K., and Tsuruno, A. (1992). Macroscopic cross section measurements and defect detection in materials using neutron radiography technique. *Journal of Nuclear Science and Technology*, 29(11):1045–1053.

[Koning et al., 2009] Koning, A., Rochman, D., et al. (2009). Talys-based evaluated nuclear data library. *Nuclear Research and Consultancy Group*.

[Koning and Rochman, 2012] Koning, A. J. and Rochman, D. (2012). Modern nuclear data evaluation with the talys code system. *Nuclear data sheets*, 113(12):2841–2934.

[Kraft et al., 2018] Kraft, S. D., Obst, L., Metzkes-Ng, J., Schlenvoigt, H.-P., Zeil, K., Michaux, S., Chatain, D., Perin, J.-P., Chen, S. N., Fuchs, J., et al. (2018). First demonstration of multi-mev proton acceleration from a cryogenic hydrogen ribbon target. *Plasma Physics and Controlled Fusion*, 60(4):044010.

[Lamarsh and Baratta, 2001] Lamarsh, J. R. and Baratta, A. J. (2001). *Introduction to nuclear engineering*, volume 3. Prentice hall Upper Saddle River, NJ.

[LANL, 2019a] LANL (2019a). Lansce fp5 neutron spectrum. `https://lansce.lanl.gov/facilities/lujan/instruments/fp-5/index.php`. Accessed: 2020-01-13.

[LANL, 2019b] LANL (2019b). Lansce time structure. `https://lansce.lanl.gov/facilities/time-structure.php`. Accessed: 2020-01-09.

[Lanza, 2007] Lanza, R. C. (2007). Neutron techniques for detection of explosives. In *Counterterrorist detection techniques of explosives*, pages 131–155. Elsevier.

[Lehmann et al., 2015] Lehmann, E., Grünzweig, C., Jollet, S., Kaiser, M., Hansen, H., and Dinkelacker, F. (2015). Visualisation of diesel injector with neutron imaging. In *Journal of Physics: Conference Series*, volume 656, page 012089. IOP Publishing.

[Ludewigt et al., 2007] Ludewigt, B., Wells, R., and Reijonen, J. (2007). High-yield d–t neutron generator. *Nuclear Instruments and Methods in Physics Research Section B: Beam Interactions with Materials and Atoms*, 261(1-2):830–834.

[Lundh et al., 2007] Lundh, O., Lindau, F., Persson, A., Wahlström, C.-G., McKenna, P., and Batani, D. (2007). Influence of shock waves on laser-driven proton acceleration. *Physical Review E*, 76(2):026404.

[M. Ragheb, 2019] M. Ragheb (2019). Nuclear power engineering - fermi age theory. University Lecture.

[Macchi, 2017] Macchi, A. (2017). A review of laser-plasma ion acceleration. *arXiv preprint arXiv:1712.06443*.

[Mackinnon et al., 2002] Mackinnon, A., Sentoku, Y., Patel, P., Price, D., Hatchett, S., Key, M., Andersen, C., Snavely, R., and Freeman, R. (2002). Enhancement of proton acceleration by hot-electron recirculation in thin foils irradiated by ultraintense laser pulses. *Physical review letters*, 88(21):215006.

[Marketing, 2019] Marketing, H. H. (2019). Containerumschlag im hamburger hafen von 2009 bis 2018. `https://de.statista.com/statistik/daten/studie/29789/umfrage/containerumschlag-im-hamburger-hafen/`. Accessed: 2019-08-22.

[Martinez et al., 2012] Martinez, M., Bang, W., Dyer, G., Wang, X., Gaul, E., Borger, T., Ringuette, M., Spinks, M., Quevedo, H., Bernstein, A., et al. (2012). The texas petawatt laser and current experiments. In *AIP Conference Proceedings*, volume 1507, pages 874–878. AIP.

[Maslehuddin et al., 1996] Maslehuddin, M., Page, C., and Rasheeduzzafar (1996). Effect of temperature and salt contamination on carbonation of cements. *Journal of materials in civil engineering*, 8(2):63–69.

[McAlister, 2012] McAlister, D. R. (2012). Gamma ray attenuation properties of common shielding materials. *University Lane Lisle, USA*.

[McGuffey1 et al., 2017] McGuffey1, C., Brabetz, C., Dozieres, M., Kim, J., Bailly-Grandvaux, M., P.Forestier-Colleoni, Beg, F. N., Roth, M., and Bagnoud, V. (2017). A pump-probe technique for laser-driven proton beam heating to warm, dense states with the phelix laser. *GSI-FAIR SCIENTIFIC REPORT*, page 226.

[McKenna et al., 2008] McKenna, P., Carroll, D., Lundh, O., Nürnberg, F., Markey, K., Bandyopadhyay, S., Batani, D., Evans, R., Jafer, R., Kar, S., et al. (2008). Effects of front surface plasma expansion on proton acceleration in ultraintense laser irradiation of foil targets. *Laser and Particle Beams*, 26(4):591–596.

[Megahid et al., 2009] Megahid, R., Osman, A., and Kansouh, W. (2009). Neutron based techniques for the detection of illicit materials and explosives. In *Satellite Meeting held within the framework of the IAEA International Topical Meeting on Nuclear Research Applications and Utilization of Accelerators*, pages 4–8.

[Meijering, 2019] Meijering, E. (2019). Randomj: An imagej plugin suite for image randomization. `https://imagejdocu.tudor.lu/gui/process/noise`. Accessed: 2019.11.13.

[Metzger, 2018] Metzger, T. (2018). Conference presentation at source workshop on ultrafast thin disk amplifiers. `https://www.euvlitho.com/2018/S35.pdf`. Accessed: 2019.12.31.

[Mintsev et al., 2016] Mintsev, V., Kim, V., Lomonosov, I., Nikolaev, D., Ostrik, A., Shilkin, N., Shutov, A., Ternovoi, V., Yuriev, D., Fortov, V., et al. (2016). Non-ideal plasma and early experiments at fair: Hihex-heavy ion heating and expansion. *Contributions to Plasma Physics*, 56(3-4):281–285.

[Moncur et al., 1995] Moncur, N., Johnson, R., Watt, R., and Gibson, R. (1995). Trident: a versatile high-power nd: glass laser facility for inertial confinement fusion experiments. *Applied optics*, 34(21):4274–4283.

[Mora, 2003] Mora, P. (2003). Plasma expansion into a vacuum. *Physical Review Letters*, 90(18):185002.

[Morrison et al., 2018] Morrison, J. T., Feister, S., Frische, K. D., Austin, D. R., Ngirmang, G. K., Murphy, N. R., Orban, C., Chowdhury, E. A., and Roquemore, W. (2018). Mev proton acceleration at khz repetition rate from ultra-intense laser liquid interaction. *New Journal of Physics*, 20(2):022001.

[Mourou et al., 2011] Mourou, G., Korn, G., Sandner, W., and Collier, J. (2011). Whitebook eli-extreme light infrastructure, science and technology with ultra-intense lasers.

[Moxon et al., 2010] Moxon, M., Ware, T., and Dean, C. (2010). Refit-2009 a least-square fitting program for resonance analysis of neutron transmission. *Capture, Fission and Scattering Data Users' Guide for REFIT-2009-10 (UKNSFP243, 2010)*.

[Mulser and Bauer, 2010] Mulser, P. and Bauer, D. (2010). *High power laser-matter interaction*, volume 238. Springer.

[Naqvi et al., 2006] Naqvi, A., Nagadi, M., and Al-Amoudi, O. B. (2006). Prompt gamma analysis of chlorine in concrete for corrosion study. *Applied radiation and isotopes*, 64(2):283–289.

[Narita and Narita, 1989] Narita, M. and Narita, K. (1989). Average number of collisions necessary for slowing down of neutrons. *Journal of Nuclear Science and Technology*, 26(9):819–825.

[Nature Editorial Comment, 2019] Nature Editorial Comment (2019). Nuclear research and industry today. *Nature Reviews Physics*, 1:171.

[Neely et al., 2006] Neely, D., Foster, P., Robinson, A., Lindau, F., Lundh, O., Persson, A., Wahlström, C.-G., and McKenna, P. (2006). Enhanced proton beams from ultrathin targets driven by high contrast laser pulses. *Applied Physics Letters*, 89(2):021502.

[Nelson et al., 2018] Nelson, R., Vogel, S., Hunter, J., Watkins, E., Losko, A., Tremsin, A., Borges, N., Cutler, T., Dickman, L., Espy, M., et al. (2018). Neutron imaging at lanscefrom cold to ultrafast. *Journal of Imaging*, 4(2):45.

[Nettelmann, 2011] Nettelmann, N. (2011). Predictions on the core mass of jupiter and of giant planets in general. *Astrophysics and Space Science*, 336(1):47–51.

[NIST, 2019] NIST (2019). Atomic weights and isotopic compositions for tungsten. `https://physics.nist.gov/cgi-bin/Compositions/stand_alone.pl?ele=W`. Accessed: 2019.10.23.

[Noaman-ul Haq et al., 2018] Noaman-ul Haq, M., Ahmed, H., Sokollik, T., Fang, Y., Ge, X., Yuan, X., and Chen, L. (2018). Parametric scalings of laser driven protons using a high repetition rate tape drive target system. *Nuclear Instruments and Methods in Physics Research Section A: Accelerators, Spectrometers, Detectors and Associated Equipment*, 909:164–167.

[Noaman-ul Haq et al., 2017] Noaman-ul Haq, M., Ahmed, H., Sokollik, T., Yu, L., Liu, Z., Yuan, X., Yuan, F., Mirzaie, M., Ge, X., Chen, L., et al. (2017). Statistical analysis of laser driven protons using a high-repetition-rate tape drive target system. *Physical Review Accelerators and Beams*, 20(4):041301.

[Nowicki et al., 2017] Nowicki, S. F., Wender, S. A., and Mocko, M. (2017). The los alamos neutron science center spallation neutron sources. *Physics Procedia*, 90:374–380.

[NRC, 2010] NRC, U. (2010). Neutron sources. `https://www.nrc.gov/docs/ML1122/ML11229A704.pdf`. Accessed: 2019-08-23.

[Nunez-Iglesias et al., 2017] Nunez-Iglesias, J., Van Der Walt, S., Walt, S., and Dashnow, H. (2017). *Elegant SciPy: The Art of Scientific Python*. " O'Reilly Media, Inc.".

[Obst et al., 2017] Obst, L., Göde, S., Rehwald, M., Brack, F.-E., Branco, J., Bock, S., Bussmann, M., Cowan, T. E., Curry, C. B., Fiuza, F., et al. (2017). Efficient laser-driven proton acceleration from cylindrical and planar cryogenic hydrogen jets. *Scientific reports*, 7(1):10248.

[Otake, 2019] Otake, Y. (2019). Riken accelerator-driven compact neutron systems rans, rans-ii, rans-iii. `http://www-llb.cea.fr/UCANS8-2019/Otake_Yoshie_oral.pdf`. Accessed: 2020.01.22.

[Ott, 2018] Ott, F. (2018). Compact neutron sources for neutron scattering.

[P. H. Fowler, 1977] P. H. Fowler, A. D. T. (1977). Temperature imaging using epithermal neutrons. *Report proceedings RAL*, 87(056).

[Patrizio, 2020] Patrizio, M. (2020). *Development of an Actively Cooled Large Aperture Laser Amplifier at the GSI Helmholtzzentrum*. PhD thesis, Technische Universität.

[Photonics, 1998] Photonics, H. (1998). Photomultiplier tubes and assemblies. for scintillation counting and high energ physics.

[Photonis, 2019] Photonis (2019). Neutronic [i] neutron imager product description. `https://www.photonis.com/products/neutronic-i`. Accessed: 2019.11.12.

[Poole et al., 2018] Poole, P., Obst, L., Cochran, G., Metzkes, J., Schlenvoigt, H., Prencipe, I., Kluge, T., Cowan, T., Schramm, U., Schumacher, D., et al. (2018). Laser-driven ion acceleration via target normal sheath acceleration in the relativistic transparency regime. *New Journal of Physics*, 20(1):013019.

[Postma et al., 2010] Postma, H., Amkreutz, L., Borella, A., Clarijs, M., Kamermans, H., Kockelmann, W., Paradowska, A., Schillebeeckx, P., and Visser, D. (2010). Non-destructive bulk analysis of the buggenum sword by neutron resonance capture analysis and neutron diffraction. *Journal of radioanalytical and nuclear chemistry*, 283(3):641–652.

[Postma et al., 2017] Postma, H., Amkreutz, L., Fontijn, D., Kamermans, H., Kockelmann, W. A., Schillebeeckx, P., Visser, D., et al. (2017). Neutron-based analyses of three bronze age metal objects: a closer look at the buggenum, jutphaas and escharen artefacts. *Analecta*.

[Prishvitsyn, 2019] Prishvitsyn, AC und Krat, C. u. H. A. u. P. A. (2019). Dependency of the black lithium of the sample temperature. *Questions of atomic science and technology. Series: Thermonuclear Fusion*, 42(2):89–95.

[ProxiVision, 2019] ProxiVision (2019). Mcp neutron detector data sheet. `https://www.proxivision.de/wp-content/uploads/PV_Neutron-Detector_201611.pdf`. Accessed: 2019.10.22.

[ProxiVision GmbH , 2019] ProxiVision GmbH (2019). Proxikit the modular intensified and gated camera. `https://www.proxivision.de/wp-content/uploads/PV_ProxiKit_201705.pdf`. Accessed: 2019.11.12.

[Pungercic and Snoj, 2018] Pungercic, A. and Snoj, L. (2018). Analysis of the jsi triga pulse experiments.

[Quirós et al., 2017] Quirós, C., Mougenot, J., Lombardi, G., Redolfi, M., Brinza, O., Charles, Y., Michau, A., and Hassouni, K. (2017). Blister formation and hydrogen retention in aluminium and beryllium: A modeling and experimental approach. *Nuclear Materials and Energy*, 12:1178–1183.

[Ragheb, 2011] Ragheb, M. (2011). Neutron cross sections. *University of Illinois*.

[Rehwald, 2019] Rehwald, M. (2019). Laser-proton acceleration from a cryogenic hydrogen jet at the draco pw laser. `https://indico.physik.uni-muenchen.de/event/5/contributions/168/attachments/63/85/LPAW_2019_rehwald.pdf`. Accessed: 2019.10.09.

[Robert Fisher, 2019] Robert Fisher, Simon Perkins, A. W. E. W. (2019). Gaussianblur class of imagej. `https://imagej.nih.gov/ij/developer/api/ij/plugin/filter/GaussianBlur.html`. Accessed: 2019.11.13.

[Robson et al., 2007] Robson, L., Simpson, P., Clarke, R. J., Ledingham, K. W., Lindau, F., Lundh, O., McCanny, T., Mora, P., Neely, D., Wahlström, C.-G., et al. (2007). Scaling of proton acceleration driven by petawatt-laser–plasma interactions. *Nature physics*, 3(1):58.

[Roth et al., 2013] Roth, M., Jung, D., Falk, K., Guler, N., Deppert, O., Devlin, M., Favalli, A., Fernandez, J., Gautier, D., Geissel, M., et al. (2013). Bright laser-driven neutron source based on the relativistic transparency of solids. *Physical review letters*, 110(4):044802.

[Roth and Schollmeier, 2017] Roth, M. and Schollmeier, M. (2017). Ion acceleration-target normal sheath acceleration. *arXiv preprint arXiv:1705.10569*.

[Rücker et al., 2016] Rücker, U., Cronert, T., Voigt, J., Dabruck, J., Doege, P.-E., Ulrich, J., Nabbi, R., Beßler, Y., Butzek, M., Büscher, M., et al. (2016). The jülich high-brilliance neutron source project. *The European Physical Journal Plus*, 131(1):19.

[Russell et al., 1988] Russell, G., Gilmore, J., Robinson, H., Legate, G., Bridge, A., Sanchez, R., Brewton, R., Woods, R., and Hughes III, H. (1988). Lansce target system performance. *Advanced Neutron Sources*.

[Rybarcyk et al., 2012] Rybarcyk, L. J. et al. (2012). Characterizing and controlling beam losses at the lansce facility. In *Proceedings of the 52nd ICFA Advanced Beam Dynamics Workshop on High-Intensity and High-Brightness Hadron Beams (HB 2012)*.

[Sahai et al., 2014] Sahai, A. A., Tsung, F. S., Tableman, A. R., Mori, W. B., and Katsouleas, T. C. (2014). Relativistically induced transparency acceleration (rita) of protons and light-ions with ultrashort laser interaction with heavy-ion plasma density gradient. *arXiv preprint arXiv:1402.5370*.

[Sanderson et al., 2001] Sanderson, W. T., Ward, E. M., Steenland, K., and Petersen, M. R. (2001). Lung cancer case–control study of beryllium workers. *American journal of industrial medicine*, 39(2):133–144.

[Sanyal et al., 1996] Sanyal, M., Basu, J., Datta, A., and Banerjee, S. (1996). Determination of small fluctuations in electron density profiles of thin films: Layer formation in a polystyrene film. *EPL (Europhysics Letters)*, 36(4):265.

[Schanz et al., 2017] Schanz, V., Wagner, F., Roth, M., and Bagnoud, V. (2017). Noise reduction in third order cross-correlation by angle optimization of the interacting beams. *Optics express*, 25(8):9252–9261.

[Schillebeeckx et al., 2014] Schillebeeckx, P., Becker, B., Harada, H., and Kopecky, S. (2014). *Neutron resonance Spectroscopy for the characterisation of materials and objects*. Joint Research Centre, European Commission.

[Schillebeeckx et al., 2015] Schillebeeckx, P., Becker, B., Harada, H., and Kopecky, S. (2015). Neutron resonance spectroscopy for the characterization of materials and objects. In *Supplement to Volume I/24*, pages 10–66. Springer.

[Schnürer et al., 2005] Schnürer, M., Ter-Avetisyan, S., Busch, S., Risse, E., Kalachnikov, M., Sandner, W., and Nickles, P. (2005). Ion acceleration with ultrafast laser driven water droplets. *Laser and Particle Beams*, 23(3):337–343.

[Schollmeier, 2009] Schollmeier, M. S. (2009). *Optimization and control of laser-accelerated proton beams*. PhD thesis, Technische Universität.

[Schreiber et al., 2006] Schreiber, J., Bell, F., Grüner, F., Schramm, U., Geissler, M., Schnürer, M., Ter-Avetisyan, S., Hegelich, B. M., Cobble, J., Brambrink, E., et al. (2006). Analytical model for ion acceleration by high-intensity laser pulses. *Physical review letters*, 97(4):045005.

[Schwind et al., 2019] Schwind, K., Aktan, E., Cerchez, M., Prasad, R., Willi, O., and Aurand, B. (2019). A high-repetition rate droplet-source for plasma physics applications. *Nuclear Instruments and Methods in Physics Research Section A: Accelerators, Spectrometers, Detectors and Associated Equipment*, 928:65–69.

[Scientific, 2019] Scientific, N. (2019). Imaging neutron detection with time resolution. `http://www.novascientific.com/demountable_detectors.pdf`. Accessed: 2020.01.27.

[Scintacor, 2019] Scintacor (2019). Lithium glass scintillator data sheet - gs2, gs20 and kg2. `https://www.crystals.saint-gobain.com/sites/imdf.crystals.com/files/documents/glass-scintillator-material-data-sheet_69772.pdf`. Accessed: 2019.11.15.

[Seidl et al., 2017] Seidl, P., Barnard, J., Feinberg, E., Friedman, A., Gilson, E., Grote, D., Ji, Q., Kaganovich, I., Ludewigt, B., Persaud, A., Zimmer, M., et al. (2017). Irradiation of materials with short, intense ion pulses at ndcx-ii. *Laser and Particle Beams*, 35(2):373–378.

[Sharkov and Varentsov, 2013] Sharkov, B. and Varentsov, D. (2013). Experiments on extreme states of matter towards hif at fair. In *EPJ Web of Conferences*, volume 59, page 01011. EDP Sciences.

[Siders, 2018] Siders, C. (2018). New architectures for pw-scale high peak power lasers scalable to near-mw average powers. Technical report, Lawrence Livermore National Lab.(LLNL), Livermore, CA (United States).

[Smith Detection Group, 2018] Smith Detection Group (2018). Private conversation.

[Smiths Detection Group, 2019] Smiths Detection Group (2019). Mobile high-energy inspection system. `https://www.smithsdetection.com/products/hcvm-mobile-x-ray-systems-smiths-detection/`. Accessed: 2019-08-22.

[Snavely et al., 2000] Snavely, R., Key, M., Hatchett, S., Cowan, T., Roth, M., Phillips, T., Stoyer, M., Henry, E., Sangster, T., Singh, M., et al. (2000). Intense high-energy proton beams from petawatt-laser irradiation of solids. *Physical review letters*, 85(14):2945.

[Stacey, 2018] Stacey, W. M. (2018). *Nuclear reactor physics*. John Wiley & Sons.

[Stefan, 1879] Stefan, J. (1879). Uber die beziehung zwischen der warmestrahlung und der temperatur, sitzungsberichte der mathematisch-naturwissenschaftlichen classe der kaiserlichen. *Akademie der Wissenschaften*, 79:S–391.

[Sugiyama, 1981] Sugiyama, H. (1981). Electronic stopping power formula for intermediate energies. *Radiation Effects*, 56(3-4):205–211.

[Swift and McNaney, 2009] Swift, D. C. and McNaney, J. M. (2009). Approximate, analytic solutions of the bethe equation for charged particle range. *arXiv preprint arXiv:0901.4145*.

[Taddeucci and Favalli, 2018] Taddeucci, T. N. and Favalli, A. (2018). Deconvolution of a laser-induced neutron time-of-flight spectrum. Technical report, Los Alamos National Lab.(LANL), Los Alamos, NM (United States).

[Tebartz et al., 2016] Tebartz, A., Bedacht, S., Schaumann, G., and Roth, M. (2016). Fabrication and characterization of thin polymer targets for laser-driven ion acceleration. In *Journal of Physics: Conference Series*, volume 713, page 012005. IOP Publishing.

[Thermo Fischer Scientific, 2008a] Thermo Fischer Scientific (2008a). Thermo scientific p 320 neutron generator manual. `https://assets.thermofisher.com/TFS-Assets/CAD/Specification-Sheets/D10497~.pdf`. Accessed: 2019-12-31.

[Thermo Fischer Scientific, 2008b] Thermo Fischer Scientific (2008b). Thermo scientific p 385 neutron generator manual. `https://assets.thermofisher.com/TFS-Assets/CAD/Specification-Sheets/D10499~.pdf`. Accessed: 2019-12-31.

[Thermo Fischer Scientific, 2019] Thermo Fischer Scientific (2019). P 385 neutron generator quote. Quote. Issued: 2019-08-26.

[Tipler and Mosca, 2004] Tipler, P. and Mosca, G. (2004). Physik für wissenschaftler und ingenieure, 2. dt. auflage.

[Trumpf Scientific, 2019] Trumpf Scientific (2019). Disk regenerative amplifiers. `https://www.trumpf-scientific-lasers.com/en_INT/products/dira-series/`. Accessed: 2019.12.31.

[Tsai et al., 2018] Tsai, P.-E., Lai, B.-L., Heilbronn, L. H., and Sheu, R.-J. (2018). Benchmark of neutron production cross sections with monte carlo codes. *Nuclear Instruments and Methods in Physics Research Section B: Beam Interactions with Materials and Atoms*, 416:16–29.

[UM Radiation Facilities, 2019] UM Radiation Facilities (2019). 250 kw triga reactor. http://radiation.umd.edu/facilities/reactor. Accessed: 2019-08-24.

[US NRC, 2014] US NRC (2014). Nrc: 10 cfr 20.1004 units of radiation dose.

[Vanhavere et al., 2002] Vanhavere, F., Coeck, M., and Noulty, R. (2002). The bdt bubble neutron detector for personal dosimetry.

[Vinokhodov et al., 2016] Vinokhodov, A., Krivokorytov, M., Sidelnikov, Y., Krivtsun, V., Medvedev, V., Bushuev, V., Koshelev, K., Glushkov, D., and Ellwi, S. (2016). Stable droplet generator for a high brightness laser produced plasma extreme ultraviolet source. *Review of Scientific Instruments*, 87(10):103304.

[Vogel et al., 2016] Vogel, S. C., Losko, A. S., Pokharel, R., Ickes, T. L., Hunter, J. F., Brown, D. W., Voit, S. L., Tremsin, A. S., Bourke, M. A., and McClellan, K. J. (2016). Non-destructive preirradiation assessment of un/u-si lanl1 atf formulation. Technical report, Los Alamos National Lab.(LANL), Los Alamos, NM (United States).

[Wagner, 2014] Wagner, F. (2014). *Kontrolle des zeitlichen Kontrastes am Lasersystem PHELIX*. PhD thesis, Technische Universität.

[Wagner et al., 2016] Wagner, F., Deppert, O., Brabetz, C., Fiala, P., Kleinschmidt, A., Poth, P., Schanz, V., Tebartz, A., Zielbauer, B., Roth, M., et al. (2016). Maximum proton energy above 85 mev from the relativistic interaction of laser pulses with micrometer thick ch 2 targets. *Physical review letters*, 116(20):205002.

[Wehring, 1995] Wehring, B. (1995). University reactor sharing program. final report, september 30, 1992–september 29, 1994.

[Wenner et al., 1915] Wenner, F., Weibel, E., Burgess, G., Foote, P., Austin, L., Coblentz, W., Burrows, C., Dickinson, H., Jackson, R., Agnew, P., et al. (1915). Bulletin of the bureau of standards. *V*, 12:469–478.

[Wilks et al., 1992] Wilks, S., Kruer, W., Tabak, M., and Langdon, A. (1992). Absorption of ultra-intense laser pulses. *Physical review letters*, 69(9):1383.

[Wilks et al., 2001] Wilks, S., Langdon, A., Cowan, T., Roth, M., Singh, M., Hatchett, S., Key, M., Pennington, D., MacKinnon, A., and Snavely, R. (2001). Energetic proton generation in ultra-intense laser–solid interactions. *Physics of plasmas*, 8(2):542–549.

[Wilson et al., 2005] Wilson, W. B., Perry, R. T., Charlton, W., Parish, T., and Shores, E. (2005). Sources: a code for calculating (α, n), spontaneous fission, and delayed neutron sources and spectra. *Radiation protection dosimetry*, 115(1-4):117–121.

[World Nuclear Association, 2018] World Nuclear Association (2018). Physics of uranium and nuclear energy. https://www.world-nuclear.org/information-library/nuclear-fuel-cycle/introduction/physics-of-nuclear-energy.aspx. Accessed: 2019-08-22.

[Wüest et al., 2007] Wüest, M., Evans, D. S., and von Steiger, R. (2007). *Calibration of particle instruments in space physics*. InternationaI Space Science Institute.

[Yandow et al., 2019] Yandow, A., Toncian, T., and Ditmire, T. (2019). Direct laser ion acceleration and above-threshold ionization at intensities from 10 21 w/cm 2 to 3× 10 23 w/cm 2. *Physical Review A*, 100(5):053406.

[Yanovsky et al., 2008] Yanovsky, V., Chvykov, V., Kalinchenko, G., Rousseau, P., Planchon, T., Matsuoka, T., Maksimchuk, A., Nees, J., Cheriaux, G., Mourou, G., et al. (2008). Ultra-high intensity-300-tw laser at 0.1 hz repetition rate. *Optics Express*, 16(3):2109–2114.

[Yin et al., 2006] Yin, L., Albright, B., Hegelich, B., and Fernández, J. (2006). Gev laser ion acceleration from ultrathin targets: The laser break-out afterburner. *Laser and Particle Beams*, 24(2):291–298.

[Yoon et al., 2019] Yoon, J. W., Jeon, C., Shin, J., Lee, S. K., Lee, H. W., Choi, I. W., Kim, H. T., Sung, J. H., and Nam, C. H. (2019). Achieving the laser intensity of 5.5× 10 22 w/cm 2 with a wavefront-corrected multi-pw laser. *Optics express*, 27(15):20412–20420.

[Yuan et al., 2005] Yuan, V., Bowman, J. D., Funk, D., Morgan, G., Rabie, R., Ragan, C., Quintana, J., and Stacy, H. (2005). Shock temperature measurement using neutron resonance spectroscopy. *Physical Review Letters*, 94(12):125504.

[Zeil et al., 2010] Zeil, K., Kraft, S., Bock, S., Bussmann, M., Cowan, T., Kluge, T., Metzkes, J., Richter, T., Sauerbrey, R., and Schramm, U. (2010). The scaling of proton energies in ultrashort pulse laser plasma acceleration. *New Journal of Physics*, 12(4):045015.

[Zepf et al., 2001] Zepf, M., Clark, E., Krushelnick, K., Beg, F., Escoda, C., Dangor, A., Santala, M., Tatarakis, M., Watts, I., Norreys, P., et al. (2001). Fast particle generation and energy transport in laser-solid interactions. *Physics of Plasmas*, 8(5):2323–2330.

[Ziegler et al., 2010] Ziegler, J. F., Ziegler, M. D., and Biersack, J. P. (2010). Srim–the stopping and range of ions in matter (2010). *Nuclear Instruments and Methods in Physics Research Section B: Beam Interactions with Materials and Atoms*, 268(11-12):1818–1823.

[Zulick et al., 2013] Zulick, C., Dollar, F., Chvykov, V., Davis, J., Kalinchenko, G., Maksimchuk, A., Petrov, G., Raymond, A., Thomas, A., Willingale, L., et al. (2013). Energetic neutron beams generated from femtosecond laser plasma interactions. *Applied Physics Letters*, 102(12):124101.

Curriculum Vitae

Personal Data

Name	**Marc Zimmer.**
Date of birth	**October, 8th, 1990.**
Place of birth	**Heppenheim.**
Citizenship	**German.**

Education

February, 2017– May, 2020	**Dr. rer. nat., Physics** , *Technische Universität Darmstadt*, *Grade: 1.0*.
October, 2014– September, 2016	**M.Sc, Physics,**, *Technische Universität Darmstadt*, *Grade: 1.4*, Master Thesis: The Neutralized Drift Compression Experiment for Short and Intense Ion Pulses, *Grade: 1.0*. (Lawrence Berkeley National Laboratory)
August, 2015– May, 2016	**Exchange Program**, *UC California*, Berkeley.
October, 2011– September, 2014	**B.Sc, Physics,**, *Technische Universität Darmstadt*, *Grade: 2.7*, Bachelor Thesis: Optimization of A Laser Frequency Stabilization Using Electromagnetically Induced Transparency, *Grade: 1.7*. (Institute of Applied Physics, TU Darmstadt)
May, 2010	**Abitur,**, *Lessing Gymnasium*, Lampertheim, *Grade: 1.8*.

Experimental Campaigns

Conducted

May, 2020	**Optimization of a Laser-Driven Neutron Source for Non-Destructive Material Testing**, PHELIX LASER, Darmstadt, 4 Weeks.
August, – September 2018	**Utilizing Laser-Driven Neutrons for Neutron Resonance Spectroscopy**, PHELIX LASER, Darmstadt, 3 Weeks.
November, – December 2017	**Development of an Epi-Thermal Laser-Driven Neutron Source**, PHELIX LASER, Darmstadt, 3 Weeks.

Participated

August, – September 2019	**Laser Ion Acceleration With Cryogenic Hydrogen Jets**, TEXAS PW LASER, Austin, USA, 8 Weeks.
August 2017	**Combining Laser Accelerated Ions With Traditional Accelerator Structures at the LIGHT-Project**, PHELIX LASER, Darmstadt, 3 Weeks.

April 2017 **Investigating the Influence of the Target Thickness on Laser Ion Generation by Using Liquid Crystal Targets**, PHELIX LASER, Darmstadt, 3 Weeks.

Publications

Zimmer, M., et al., *Development of a Setup for Material Identification Based on Laser-Driven Neutron Resonance Spectroscopy*, EPJ Web of Conferences. Vol. 231. EDP Sciences, 2020.

Zimmer, M., et al., *Prospects of Laser-Based Neutron Sources for Neutron Resonance Spectroscopy*, GSI-FAIR SCIENTIFIC REPORT, 2018.

Zimmer, M., et al., *Investigations on laser-based neutron sources for possible applications*, GSI-FAIR SCIENTIFIC REPORT, 2017.

Poole, P. L., et al., *Ion acceleration with high laser energy using variable thickness liquid crystal*, GSI-FAIR SCIENTIFIC REPORT, 2017.

Seidl, P. A., et al., *Irradiation of materials with short, intense ion pulses at NDCX-II*, Laser and Particle Beams 35.2, 2017.

Seidl, P. A., et al., *Recent Experiments At Ndcx-II: Irradiation Of Materials Using Short, Intense Ion Beams*, arXiv preprint arXiv:1610.05253, 2016.

Conferences

Talks

January 2020 **40th International Workshop on High Energy Density Physics with Intense Ion and Laser Beams**, *Hirschegg*, Austria.

January 2019 **39th International Workshop on High Energy Density Physics with Intense Ion and Laser Beams**, *Hirschegg*, Austria.

January 2018 **38th International Workshop on High Energy Density Physics with Intense Ion and Laser Beams**, *Hirschegg*, Austria.

Poster Presentation

July 2019 **8th International Meeting of the Union for Compact Accelerator-Driven Neutron Sources**, *Paris*, France.

September 2018 **Conference of the International Committee on Ultrahigh Intense Lasers**, *Lindau*, Germany.